NECMETTÍN ERBAKAN ÜNÍVERSÍTESÍ FEN VE MÜHENDISLÍK BILIMLERI DERGISI

NECMETTIN ERBAKAN UNIVERSITY JOURNAL OF SCIENCE AND ENGINEERING

Yıl/Year:2025 Cilt/Volume:7 Sayı/Issue:2

E-ISSN: 2667-7989





NECMETTİN ERBAKAN ÜNİVERSİTESİ FEN VE MÜHENDİSLİK BİLİMLERİ DERGİSİ NECMETTIN ERBAKAN UNIVERSITY JOURNAL OF SCIENCE AND ENGINEERING

E-ISSN: 2667-7989

Cilt/Volume: 7, Sayı/Issue: 2, (Ağustos/August, 2025)

Uluslararası Hakemli Dergi/International Referred Journal

İmtiyaz Sahibi/Holder of Concession

Necmettin Erbakan Üniversitesi Rektörü Rector of Necmettin Erbakan University Prof. Dr. Cem ZORLU

Baş Editör/Editor-in-Chief

Doç. Dr. Fatih ERCİ, Necmettin Erbakan Üniversitesi Assoc. Prof., Necmettin Erbakan University

Yardımcı Editörler/Associate Editors

Prof. Dr. Nihat AKGÜNEŞ, Necmettin Erbakan Üniversitesi *Prof., Necmettin Erbakan University*

Doç. Dr. Emrah MADENCİ, Necmettin Erbakan Üniversitesi Assoc. *Prof., Necmettin Erbakan University*

Dr. Ahmet Burçin BATIBAY Makine ve Kimya Endüstrisi A.Ş. *Ph.D. Machinery and Chemical Industry Inc.*

Yayına Hazırlık ve Mizanpaj Editörleri/Layout Editors

Dr. Behiç Selman ERDOĞDU, Necmettin Erbakan Üniversitesi (Res. Asst. Ph.D.), Necmettin Erbakan University

Dr. Öğr. Üyesi Merve ÖZCAN TÜRKMEN, Necmettin Erbakan Üniversitesi Asst. Prof., Necmettin Erbakan University

Arş. Gör. Canan SEVİNÇ ŞAŞMAZ, Necmettin Erbakan Üniversitesi (Res. Asst.), Necmettin Erbakan University

Arş. Gör. Halil İbrahim AYAZ, Necmettin Erbakan Üniversitesi (Res. Asst.), Necmettin Erbakan University

İstatistik Editörü/Statistical Editor

Doç. Dr. Ahmet PEKGÖR, Necmettin Erbakan Üniversitesi Assoc. Prof., Necmettin Erbakan University

Dil Editörü/Language Editor

Doç. Dr. Mehmet DEMİRTAŞ, Necmettin Erbakan Üniversitesi Assoc. Prof., Necmettin Erbakan University
Arş. Gör. Tuba ULUSOY, Necmettin Erbakan Üniversitesi (Res. Asst.), Necmettin Erbakan University

Sekreter/Secretary

Dr. Esra TANHAŞ (Res. Asst. Ph.D.), Necmettin Erbakan University Arş. Gör. Ömer Faruk ATİZ (Res. Asst.), Necmettin Erbakan University

Yazışma Adresi/Correspondence Address

Necmettin Erbakan Üniversitesi Rektörlüğü, 42090, Meram, Konya, Türkiye

Telefon/Phone: +90 (332) 221 05 00 web: www.dergipark.gov.tr/neufmbd e-posta/e-mail: neufmbd@erbakan.edu.tr

Necmettin Erbakan Üniversitesi Fen ve Mühendislik Bilimleri Dergisi, yılda üç kez yayınlanan uluslararası hakemli bir dergidir. Necmettin Erbakan University Journal of Science and Engineering is an international referred journal published three issues per year.

E-ISSN: 2667-7989

İÇİNDEKİLER/CONTENTS

Türkçe ve İngilizce Dillerinde Spam Posta Tespiti: Bireysel, Toplu ve Hibrit Yaklaşımları İçeren Yapay Zeka Tabanlı Tekniklerin Bütünsel Bir Çalışması Spam Mail Detection in Turkish and English Languages: A Holistic Study of AI-based Techniques including Individual, Ensemble and Hybrid Approaches CANDAN, Esma Nisa; KÜÇÜKİLHAN, Rehnüma; EROĞLU, Alperen.	Araştırma Makalesi Research Article	189-205
Gönderim Sınıfı Grubunda Denk Çapraz Homomorfizmler Equivalent Crossed Homomorphisms on The Mapping Class Group ÜNLÜ EROĞLU, Hatice.	Araștırma Makalesi Research Article	206-213
Hepatit-B İçin Yeni Bir Matematiksel Model ve Modelde Dikey Bulaşın Etkisi A New Mathematical Model for Hepatitis-B and the Effect of Vertical Transmission in the Model YAVUZ, Mehmet; BAYRAKTAR, Naime Büşra; AKYÜZ, Kübra; ÖZDEMİR, Feyza Nur.	Araştırma Makalesi Research Article	214-227
Fibonacci Kodlaması ve k-Zeckendorf Gösterimleri ile Yeni Bir Genetik Algoritma Modeli A Novel Genetic Algorithm Model with Fibonacci Encoding and k-Zeckendorf Representations GÖKTEPE, Yunus Emre; KÖKEN, Fikri; ERGUN, Halime.	Araştırma Makalesi Research Article	228-244
Scada Sistemi ve Görüntü İşleme Teknikleri Kullanarak Gerçek Zamanlı Aydınlatma Sisteminin Tasarımı Design of Real-Time Lighting System Using Scada System and Image Processing Techniques ALTUNKAYA, Murat; KARAALTUN, Muhammed.	Araștırma Makalesi Research Article	245-258
Ankastre Temel, Winkler ve Psödo-eşlenik Yöntemlerine Göre Üstyapı Performansının İncelenmesi Investigation of Superstructure Performance Based on the Fixed Base Foundation, Winkler, and Pseudo-Coupled Methods ECEMİŞ, Ali Serdar; YENGİNAR, Yavuz; ÖZKAN, İlyas.	Araștırma Makalesi Research Article	259-272
Güneş Enerji Santralinin Reaktif Güç Desteği için Kullanılması Using Solar Power Plant for Reactive Power Support KÖROĞLU, Harun; ALTUNKAYA, Sabri.	Araştırma Makalesi Research Article	273-285
Paratiroid Hormon Tayinine Yönelik IrO2 Nanopartikül Tabanlı Yatay Akış İmmünosensör Geliştirilmesi Development of IrO2 Nanoparticles-Based Lateral Flow Immunosensor for Determination of Parathyroid Hormone GÜMÜŞ, Eda; BİNGÖL, Haluk; ZOR, Erhan.	Araştırma Makalesi Research Article	286-293
Pestisit Tespiti için Konjuge Polimer Nanopartikül Tabanlı Biyosensörün Tasarımı ve Geliştirilmesi Design and Development of Conjugated Polymer Nanoparticles-Based Biosensor for Pesticide Detection YENİTERZİ, Dilara; SOYLER, Dilek; SÖYLEMEZ, Saniye.	Araştırma Makalesi Research Article	294-308

Necmettin Erbakan Üniversitesi/Fen ve Mühendislik Bilimleri Dergisi
Necmettin Erhakan University Journal of Science and Engineering

Cilt/Volume: 7, Say	yı/ <i>Issue</i> : 2, Ağustos	/ <i>August</i> , 2025
---------------------	-------------------------------	------------------------

E-ISSN: 2667-7989

Uzaktan Algılama Yağış Verileri Yardımıyla Kuraklık Aşma Olasılığı İndeksi'ni (KAOİ) Kullanarak Konya İli Kuraklık Analizi Drought Analysis of Konya Province using Drought Exceedance Probability Index (DEPI) with Remote Sensing Precipitation Data KARAÇOR, Fatih; TOPÇU, Emre.	Araștırma Makalesi Research Article	309-321
Poliol Sentezinde Metal Tuzlarının Gümüş Nanotel Morfolojisi Üzerindeki Etkisi Influence of Metal Salts on Silver Nanowire Morphology in Polyol Synthesis KARASAKAL, Mücahit; DEMİREL, İrem Sena; ERTUŞ, Emre Burak.	Araştırma Makalesi Research Article	322-330
Yapısal Çelik ve Bakır Alaşımlarında Çentik Darbe Testinin Sonlu Elemanlar Yöntemiyle Analizi Finite Element Analysis of Notch Impact Test in Structural Steel and Copper Alloys KORKMAZ, Sümeyye Erdem; GAVGALI, Esma.	Araştırma Makalesi Research Article	331-348

Dr. Öğr. Üyesi Vahit TONGUR

Dr. Muhammad Asyraf Muhammad Rizal

Necmettin Erbakan University Journal of Science and Engineering

Alan Editörleri/Editorial Board

Adana Alparslan Türkes Bilim ve Teknoloji Üniversitesi/Adana Alparslan Türkes Prof. Dr. Ahmet BEYCİOĞLU Science and Technology University Necmettin Erbakan Üniversitesi/Necmettin Erbakan University Prof. Dr. Ceyda ÖZFİDAN KONAKÇI Prof. Dr. Esra YALDIZ Necmettin Erbakan Üniversitesi/Necmettin Erbakan University Prof. Dr. Gökhan ZENGİN Selçuk Üniversitesi/Selçuk University Prof. Dr. Hüseyin BAYRAKÇEKEN Afyon Kocatepe Üniversitesi/Afyon Kocatepe University Prof. Dr. Hüseyin Zahit SELVİ Necmettin Erbakan Üniversitesi/Necmettin Erbakan University Prof. Dr. Mehmet Akif ERİŞMİŞ Necmettin Erbakan Üniversitesi/Necmettin Erbakan University Prof. Dr. Mehmet HACIBEYOĞLU Necmettin Erbakan Üniversitesi/Necmettin Erbakan University Prof. Dr. Mesut UYANER Necmettin Erbakan Üniversitesi/Necmettin Erbakan University Prof. Dr. Mustafa Kürşat DEMİR Necmettin Erbakan Üniversitesi/Necmettin Erbakan University Prof. Dr. Semra ARSLAN SELÇUK Gazi Üniversitesi/Gazi University Necmettin Erbakan Üniversitesi/Necmettin Erbakan University Prof. Dr. Senar AYDIN Prof. Dr. Ummahan EGE ARSLAN Eskişehir Osmangazi Üniversitesi/Eskisehir Osmangazi University Doç. Dr. Ali SARIBIYIK Sakarya Uygulamalı Bilimler Üniversitesi/Sakarya University of Applied Sciences Doç. Dr. Alper ALVER Aksaray Üniversitesi/Aksaray University Doç. Dr. Alper SİNAN Akdeniz Üniversitesi/Akdeniz University Doç. Dr. Aydın KARAKOCA Necmettin Erbakan Üniversitesi/Necmettin Erbakan University Doç. Dr. Bilal ERVURAL Necmettin Erbakan Üniversitesi/Necmettin Erbakan University Doç. Dr. Ceyhun YILMAZ Afyon Kocatepe Üniversitesi/Afyon Kocatepe University Doç. Dr. Derya BAL ALTUNTAŞ Recep Tayyip Erdoğan Üniversitesi/Recep Tayyip Erdoğan University Tekirdağ Namık Kemal Üniversitesi/Tekirdağ Namık Kemal University Doç. Dr. Emrehan YAVŞAN Doç. Dr. Fatma BAYRAM SARIİPEK Konya Teknik Üniversitesi/Konya Technical University Necmettin Erbakan Üniversitesi/Necmettin Erbakan University Doç. Dr. Murat KARAKOYUN Doç. Dr. Mustafa KUNTOĞLU Selçuk Üniversitesi/Selçuk University Doç. Dr. Mustafa YALÇIN Afyon Kocatepe Üniversitesi/Afyon Kocatepe University Doç. Dr. Süleyman DOĞU Necmettin Erbakan Üniversitesi/Necmettin Erbakan University Doç. Dr. Yasemin TABAK Tübitak Marmara Araştırma Merkezi/Tübitak Marmara Research Center Dr. Öğr. Üyesi Ali Serdar ECEMİŞ Necmettin Erbakan Üniversitesi/Necmettin Erbakan University Dr. Öğr. Üyesi Çiğdem AŞÇIOĞLU Afyon Kocatepe Üniversitesi/Afyon Kocatepe University Dr. Öğr. Üyesi Hatice Banu KESKİNKAYA Necmettin Erbakan Üniversitesi/Necmettin Erbakan University Dr. Öğr. Üyesi Mehmet Kürşat ÖKSÜZ Erzincan Binali Yıldırım Üniversitesi/Erzincan Binali Yıldırım University Dr. Öğr. Üyesi Rıza BÜYÜKZEREN Necmettin Erbakan Üniversitesi/Necmettin Erbakan University

Konya Teknik Üniversitesi/Konya Technical University

Universiti Teknologi Malaysia

E-ISSN: 2667-7989

Yayın ve Danışma Kurulu /Editorial and Advisory Board

Prof. Dr. Ahmet CAN	Necmettin Erbakan Üniversitesi/Necmettin Erbakan University
Prof. Dr. Aşır GENÇ	Necmettin Erbakan Üniversitesi/Necmettin Erbakan University
Prof. Dr. Atilla EVCİN	Afyon Kocatepe Üniversitesi/Afyon Kocatepe University
Prof. Dr. Didem BALKANLI	Yıldız Teknik Üniversitesi/Yıldız Technical University
Prof. Dr. Erdal KOCABAŞ	Necmettin Erbakan Üniversitesi/Necmettin Erbakan University
Prof. Dr. Haluk BİNGÖL	Necmettin Erbakan Üniversitesi/Necmettin Erbakan University
Prof. Dr. Hasan KOTAN	Bursa Teknik Üniversitesi/Bursa Technical University
Prof. Dr. Hicran AÇIKEL	Necmettin Erbakan Üniversitesi/Necmettin Erbakan University
Prof. Dr. Hidayet OĞUZ	Necmettin Erbakan Üniversitesi/Necmettin Erbakan University
Prof. Dr. İbrahim KALAYCI	Necmettin Erbakan Üniversitesi/Necmettin Erbakan University
Prof. Dr. Mehmet AKTAN	Necmettin Erbakan Üniversitesi/Necmettin Erbakan University
Prof. Dr. Mehmet KARALI	Necmettin Erbakan Üniversitesi/Necmettin Erbakan University
Prof. Dr. Nilgün ERTAŞ	Necmettin Erbakan Üniversitesi/Necmettin Erbakan University
Prof. Dr. Ömer IŞILDAK	Tokat Gaziosmanpaşa Üniversitesi/Tokat Gaziosmanpaşa University
Prof. Dr. Sabri ALPAYDIN	Necmettin Erbakan Üniversitesi/Necmettin Erbakan University
Prof. Dr. Sabri KOÇER	Necmettin Erbakan Üniversitesi/Necmettin Erbakan University
Prof. Dr. Süleyman KALELİ	Sakarya Üniversitesi/Sakarya University
Prof. Dr. Ümmügülsüm DAĞLIOĞLU	Necmettin Erbakan Üniversitesi/Necmettin Erbakan University
Dr. Öğr. Üyesi Hasan Ali AKYÜREK	Necmettin Erbakan Üniversitesi/Necmettin Erbakan University



Vol: 7 No: 2 Year: 2025

Araştırma Makalesi/Research Article

e-ISSN: 2667-7989

https://doi.org/10.47112/neufmbd.2025.85

Türkçe ve İngilizce Dillerinde Spam Posta Tespiti: Bireysel, Toplu ve Hibrit Yaklaşımları İçeren Yapay Zeka Tabanlı Tekniklerin Bütünsel Bir Çalışması

Esma Nisa CANDAN¹ D Rehnüma KÜÇÜKİLHAN² Alperen EROĞLU^{1*} D

¹ Necmettin Erbakan University, Faculty of Engineering, Department of Computer Engineering, Konya, Türkiye
² Afyon Kocatepe University, Faculty of Engineering, Department of Environmental Engineering, Afyon, Türkiye

Makale Bilgisi

Geliş Tarihi: 25.09.2024 Kabul Tarihi: 14.11.2024 Yayın Tarihi: 30.08.2025

Anahtar Kelimeler:

Hibrit Öğrenme, İngilizce Veri Setleri, Toplu Öğrenme, Türkçe Veri Setleri, Spam Mail.

ÖZET

Artan e-posta ve sosyal medya kullanımı nedeniyle spam sayısı artmış ve bu durumun sistemlere zarar vermeden etkili bir sekilde tespit edilmesi ve sınıflandırılması konusunda kritik bir zorluk olusturmustur. Bu makale, Türkçe ve İngilizce veri kümelerini kullanarak e-postaları spam veya ham olarak tespit etmek ve sınıflandırmak için en etkili yaklaşımları analiz etmek ve ortaya çıkarmak için bütünsel bir strateji sunmaktadır. Birleşik olarak oluşturulan yeni veri kümelerine ek olarak, farklı dillerde oluşturulan iki farklı veri kümesi kullanılmaktadır. Gelişmiş makine öğrenmesi ve derin öğrenme yaklaşımlarını temel alarak en iyi spam posta algılama yöntemlerini sunmak için karşılaştırmalı bir çalışma yapılmaktadır. Ayrıca yeni bir yaklaşım olarak spam posta tespiti için toplu ve hibrit öğrenme yöntemleri bir araya getirilmiştir. Optimize edilmiş özellik seçimi yaklaşımları ve ön işleme ile doğal dil işlemeyi ve geliştirilmiş öğrenme algoritmaları kullanılmaktadır. Literatürde yaygın olarak kullanılan Multinomial Naive Bayes, Destek Vektör Makinesi, Lojistik Regresyon, K-En Yakın Komşular, Karar Ağacı, Rastgele Orman, Oylama sınıflandırıcısı ve makine öğrenme algoritmaları olarak Yığınlama Sınıflandırıcısı ile Uzun Kısa Süreli Bellek, Çift Yönlü yöntemlerini karşılaştırmaktayız. Uzun Kısa Süreli Bellek, Transformatörlerden Çift Yönlü Kodlayıcı Gösterimleri ise derin öğrenme algoritmaları olarak kullanılmaktadır. 5 kat çapraz doğrulamaya ek olarak, veri kümeleri her model için 80:20 oranlarıyla eğitim verileri ve test verileri olarak bölünmüştür. İzgara Arama tekniği kullanılarak modellerin hiper parametreleri de optimize edilmektedir. Makine öğrenmesi yaklaşımlarına dayalı toplu öğrenme yöntemi, İngilizce Enron veri seti için %99,9 ile en iyi performansı sağlarken, basit ortalamaya dayalı hibrit toplu öğrenme yaklaşımı, UCI ve Kaggle'dan Türkçe veri seti için %98,43 ile en iyi doğruluk değerini vermektedir.

Spam Mail Detection in Turkish and English Languages: A Holistic Study of AI-based Techniques including Individual, Ensemble and Hybrid Approaches

Article Info

Received: 25.09.2024 Accepted: 14.11.2024 Published: 30.04.2025

Keywords:

English Datasets, Ensemble Learning, Hybrid Learning, Turkish Datasets, Spam Mail.

ABSTRACT

Spam has surged due to increased email and social media use, posing a critical challenge in effectively detecting and classifying this growing volume without causing harm to systems. This paper presents a holistic strategy to analyze and reveal the most efficient approaches for detecting and classifying e-mails as spam or ham by using Turkish and English datasets. We use two different datasets generated in different languages in addition to conjunctively generated new datasets. We make a comparative study to find out the best spam mail detection approaches based on our enhanced machine learning and deep learning methods. We also bring ensemble and hybrid learning methods together as a new approach for spam mail detection. We utilize natural language processing, and improved learning algorithms with optimized feature selection approaches and preprocessing. We compare various methods commonly used in the literature which are Multinomial Naive Bayes, Support Vector Machine, Logistic Regression, K-Nearest Neighbors, Decision Tree, Random Forest, Voting classifier, and Stacking classifier as machine learning algorithms, and Long Short Term Memory, Bidirectional Long Short Term Memory, Bidirectional Encoder Representations from Transformers as deep learning algorithms. We split the datasets as train data and test data with the 80:20 ratios in addition to 5-fold cross-validation for each model. We also optimize the hyperparameters of our models by using Grid Search. The ensemble method based on machine learning approaches provides the best performances which are the percentage of 99.9% for the English Enron dataset, and the hybrid ensemble approach based on simple average yields the best accuracy value of 98.43% for the Turkish dataset from UCI and Kaggle.

To cite this article:

Candan, E. N.; Küçükilhan, R. & Eroğlu, A. (2025). Spam Mail Detection in Turkish and English Languages: A Holistic Study of AI-based Techniques including Individual, Ensemble and Hybrid Approaches. *Necmettin Erbakan University Journal of Science and Engineering*, 7(2), 189-205. https://doi.org/10.47112/neufmbd.2025.85

*Corresponding Author: Alperen Eroğlu, aeroglu@erbakan.edu.tr



INTRODUCTION

Electronic mail (e-mail) is increasingly favored for communication by institutions, organizations, and individuals due to its efficiency and accessibility. The number of e-mail users is rising significantly, projected to reach 7.73 billion by 2026. While e-mails serve various purposes such as business processes, document sharing, and marketing, they pose risks like information theft and system vulnerabilities [1–3]. Spam e-mails, including harmful content and unwanted advertisements, contribute to network congestion and inefficiency. Despite advancements in spam detection, they still constitute 53% of worldwide e-mail traffic. Researchers propose combining machine and deep learning algorithms into network systems to address this issue for more effective spam detection and removal.

There are two common approaches to detect whether an e-mail is legitimate or not. The first one is based on non-Artificial Intelligent (AI) techniques, software frameworks such as server authorization methods, architectural modification-based statements, collaborative models, rule-based models, and content-dependent models [4]. The latter leverages AI-based approaches including machine and deep learning techniques. In recent years, machine and deep learning approaches have been used for classifying and detecting spam or ham e-mails [5], [6]. Big companies like Google and Yahoo utilize a machine learning-based spam mail filtering approach. The content and behavior of the unsolicited mail can be changed in time. Thus, instead of static solutions, our systems can learn and decide effectively and dynamically with a higher accuracy performance. It is possible to implement spam mail filters on different sides of the network such as a firewall filter, a mail server filter, a mail transfer server filter, a mail delivery agent filter, and a client-side filter. A spam mail filter can generally be deployed on a gateway, or a router, on the applications hosted by a cloud platform, and on the user's system [6, 7].

Machine and deep learning algorithms are beneficial solutions to optimize, categorize, and classify in different areas [8–10]. In this study, we propose an AI-based spam filtering solution by utilizing machine learning (ML) and deep learning (DL) approaches. We exploit natural language processing (NLP) to understand the content of e-mails and improve our spam mail filter accuracy. We use three different datasets. They are generated in Turkish and English language. We also take advantage of feature selection and optimization methods to enhance the accuracy performance of learning models. At this point, our contributions can be presented as follows:

We present a comprehensive and comparative study that analyzes ML and DL algorithms while considering hybrid and ensemble methods. We propose optimized solutions for spam mail detection including a novel hybrid ensemble method approach. We use Turkish and English imbalanced datasets. We also generate two new datasets by combining all Enron datasets into one and bringing together two Turkish data sets with a new one. The generated English dataset is more balanced in comparison to separate individual datasets. Hence, we consider both balanced and imbalanced datasets in our experiments. Different optimized feature selection approaches are leveraged to overcome overfitting problems and longer processing times so that we improve commonly used ML and DL algorithms in the literature. Our results also present the processing time for each technique. Different NLP solutions for modifying our data to enhance the performance of learning algorithms are utilized. To the best of our knowledge, there is a gap in the literature that aggregates and compares all these methods with a categorical point of view in addition to seeking out the best of them for different datasets. Therefore, we propose a holistic approach to spam mail detection solutions. We bridge this gap in this study by formulating recommendations for individual, ensemble, and hybrid methods by consolidating the most effective techniques and considering the running time details of each algorithm.

The rest of the paper is organized as follows. The successive session discusses a comprehensive literature review, and we present the common datasets with the newly generated datasets. The implementation of commonly used ML and DL algorithms and their comparisons are illustrated.

Moreover, we explain the steps beginning with preprocessing and splitting the datasets, feature extraction and selection, the structure for ML and DL models, and the model validation. In the Experimental Results section, we present the outcomes of our experiments using various techniques across different datasets. In the Discussion section, we reveal the best results of our solutions for datasets in different languages. In the Conclusion section, we summarize the study and discuss future work.

MATERIALS AND METHODS

Related Work

This section presents the state of the art regarding spam classification and detection of algorithms in different ways. We can roughly classify the related studies in the literature as individual, hybrid, and ensemble approaches as demonstrated in Table 1. The first category includes only ML and DL algorithms. The hybrid method including different methods comes together to propose more accurate models, on the contrary, the ensemble learning methods include the same category but different algorithms' voting or other weights. Based on the literature, most of the studies commonly develop their models using the following steps: data collection or dataset selection, data preprocessing, feature extraction and selection, training of models, and evaluation of the models. Most of the studies use accuracy, precision, recall, and F1 metrics to analyze and compare the performance of models. There are two kinds of validation methods such as cross-validation and splitting of the data as train and test.

Although many studies and algorithms have been put forward in spam email filtering, on the other hand, since spam contents have a very dynamic structure there is a need for efficient, reliable, and agile algorithmic approaches to detect new spam variants in different contexts [11]. Rustam et al. [11] make use of multiple features to increase the accuracy of the supervised ML algorithms. They utilize a composition of two feature selection methods which are the bag of words (BoW) and the term frequencyinverse document frequency (TF-IDF) feature selection methods. The authors consider imbalanced data and use a resampling approach against this issue. Random Forest (RF), Support Vector Machine (SVM), Gaussian Naive Bayes (GNB), Gradient Boosting Machine (GBM), and Logistic Regression (LR) are analyzed as machine learning models with several optimized hyperparameters. Long short-term memory (LSTM) and gated recurrent unit (GRU) are also applied for the spam mail classification. Two Kaggle datasets which are "the Spam or Ham - EMP Week 2 ML HW Dataset" and "the Spam filter Dataset" are utilized in addition to the combination of these two datasets. They use new data to validate and test the models' performances. Based on the results of that study, the LR and RF algorithms have the highest accuracy performance results which are 99% and 99.1%, respectively. In [6] evaluates the effectiveness of K-Nearest Neighbors (K-NN), Naive Bayes (NB), and SVM classifiers, the Multinomial Naive Bayes (MNB) algorithm achieving the highest accuracy performance at 96.2%.

To make an accurate detection of spam content, ML models require optimization techniques. In Gibson et al. [5], the bio-inspired metaheuristic approaches such as Genetic Algorithm (GA) and Particle Swarm Optimization (PSO) are leveraged to optimize the following machine learning algorithms: Multi-Layer Perceptron (MLP), NB, RF, SVM, and Decision Tree (DT). They analyzed the Ling-Spam dataset, 6 different Enron datasets, the PUA dataset, and the SpamAssassin dataset. To validate their results, they split their data into 70%-80% train and 25%-20% test data. According to the results, optimized MNB based on GA has the highest performance which is 100% when the SpamAssassin dataset is used. There are various datasets including text analysis approaches and content-based features for training spam and phishing mail filtering models. The result of that study classifies the data into three classes which are spam, ham, and phishing. Magdy et al. [7] use the SpamBase dataset, the CSDMC2010 dataset, and a combination of the SpamAssassin and Nazario datasets as benchmark datasets including content-based features since text analysis approaches require more time to process. They suggest a deep learning approach based on a neural network. They select their features by implementing Low variance,

Principal Component Analysis (PCA), and Chi-squared (CHI) techniques. To validate and analyze their method performance, they exploit a 10-fold cross-validation approach. Their model gives the highest result when Chi-squared is used as a feature selection approach and the Phishing Corpus dataset is utilized as the benchmark, which consists of three classes ham, spam, and phishing in comparison to other datasets. In addition to CHI, another study utilizes different feature selection methods such as information gain (IG), accuracy (ACC), document frequency thresholding (DF), and odds rate (OR) [12]. Synthetic-minority over-sampling technique (SMOTE) is also used for preprocessing [13].

Table 1 *A categorization and comparison table including state of the art individual, hybrid and ensemble approaches.*

Category of solution manner	Utilized Datasets	Used Algorithms/Classifiers	Best algorithms and Performances	Feature Extraction / Preprocessing methods	Validation	Ref
Individual (DL)	Enron dataset: 32638 emails for 150 users	Feed Forward Neural Network (FFNN), BERT.	k FFNN, 99.22% (F1-score) BoW TF-IDF IDF		80% training 20% testing. and 5-folds cross validation.	[14]
(Individual) ML	E-mail msg spam detection dataset from Kaggle	MNB, Bernoulli Naive Bayes (BNB), GNB, RF, SVM	MNB, 98.8%, (accuracy)	BoW	any random email (new data)	[15]
(Individual) ML and DL	Sms-spam collection dataset form Kaggle	NB, RF, Artificial Neural Networks (ANN), SVM, LSTM, Bi-LSTM	Bi-LSTM, 98.57%, (accuracy)	TF-IDF Word Embedding Text vectorization	NA	[16]
ML and DL (Individual)	The Enron email dataset	LSTM, Bi-LSTM, BERTSVM,K-NN, MNB, DT, LR, RF	BERT, 99.14%, (accuracy)	Count Vectorizer, TF-IDF	70% for training, 30% for testing	[17]
ML (Individual)	2006 Enron corpus dataset, 2007 Trec dataset	K-NN	K-NN, 93.18%, (accuracy)	Tokenization, Removing stop words, noise, and stemming	80% for training, 20% for testing	[18]
ML (Individual)	TurkishEmail, TrHamSpamEmai lv1.0	SVM, RF, NB, K-NN, C4.5, MLP, LR, Sequential minimal optimization (SMO)	MLP %98, (accuracy)	BoW, TF-IDF, CHI, IG, ACC, OR, DF	NA	[12]
ML, DL (Individual)	Various datasets are referenced	NB, DT, RF, SVM, Neural Networks (NN), Automatic Identification System (AIS)	NB 99.46%, (accuracy)	Vectorizer	Various methods	[19]
ML, DL (Individual)	Kaggle Dataset in English, and its translated version into URDU language	NB, SVM, LSTM, Convolutional Neural Networks (CNN)	LSTM, 98.4%, (accuracy)	Tokenization	80% for training, 20% for testing	[20]
ML (Hybrid)	SPAMBASE dataset from UCI	K-NN, RF, NB, Fuzzy K-NN (FKNN)	BGWOA-FKNN 97.61%, (accuracy)	Black widow Optimization Algorithm (BWO), Binary Grey Wolf Optimization (BGWO)	10-fold cross- validation	[21]
ML and DL (Hybrid)	Enron email dataset, SMS Spam Collection dataset	CNN, RF, SVM, LSTM with RNN, DT, GNB, XGB	CNN with the Glove model, 96.52%, (accuracy)	Count Vectorizer, TF-IDF, Word Embedding	a 10-folds cross-validation mode.	[22]
DL, ML (Hybrid)	TREC Public Spam, GenSpam, SA, Enron (EN), and LS.	SVM, LR, K-NN, RF, BERT + SVM, BERT + K-NN, BERT + LR, Federating Learning (FT) + Hierarchical Attention Network (HAN)	FT+HAN,	Word Embedding	10-fold cross validation, splitting train and test	[23]
DL, ML (Hybrid)	Enron, Dredze, TREC 2007	SVM, CNN, K-NN, multi-modal architecture based on model fusion (MMA-MF), Proximal Support Vector Machine (P-SVM)	99.16%, (accuracy)	Paragraph Vector, Doc2Vec DBoW	5-fold cross validation	[24]
ML (Hybrid)	Enron Spam dataset form UCI	GA, DT, K-NN, SVM, J-48, NB, GADT	GADT 95.5%, (accuracy)	BoW,TF-IDF, PCA	NA	[25]
ML, DL (Ensemble)	SMS spam collection from UCI	SVM, NB, K-NN, RF, CNN, LSTM, Deep Neural Networks (DNN) + Discounted cash flow (DCF)	DCF, 98.38%, (accuracy)	Word Embdedding, SMOTE	10-fold cross validation 80% for training, 20% for testing	[13]
Ensemble (ML)	Email Spam Classification Dataset, Spam filter dataset from Kaggle	DT, SVM, NB, MLP, VC	99% (accuracy)	NA	Three cases of train:test ratios - 70:30, 80:20, and 90:10	[26]
ML, (Ensemble)	SMS-Spam-Collection-Dataset from Kaggle,Twitter spam dataset from nclab	K-NN, NB, ETC, RF, SVC, LR, XGB, DT, the proposed VC	VC, 97.96%, (accuracy) ETC, 97.77% (accuracy)	Vectorizer	80% for training, 20% for testing	[27]
ML, DL, (Ensemble), (Hybrid) (Ensemble + Hybrid)	ENRON Dataset Turkish spam dataset from Kaggle Turkish spam dataset from UCI	K-NN, MNB, SVM, RF, SVM, LR, DT, BI ['] -LSTM, LSTM, BERT, BERT-TURK	K-NN+MNB with stacking, 99.9%, (accuracy) BERT-Turk + SVM with simple average, 98.43% (accuracy)	TF-IDF, BoW Tokenizer, Word2Vec, Keras, BERT-Turk	80% for training, % for testing 5-fold cross-validation	our study

The e-mail data classification such as normal, harassment, fraudulent, and suspicious is another important issue [28]. Some disadvantages of skipping meaningful information of some filtration and keyword-based search algorithms cause short sequence emails and extraneous problems. Thus, the study

proposes a multi-class email classification solution relying on LSTM based on a Gated Recurrent Neural Network (GRU) to overcome these limitations. In that study, some of the feature extraction techniques such as Word2Vec, TF-IDF, Vector Normalization, BoW, and embedding vector for the DL algorithm. This study presents a hyper-tuned DL scheme. In this study, the loss function is selected as Categorical cross-entropy and the value of the weights optimizer is chosen as the ADAM optimizer. The accuracy of the model is the percentage of 95%. A self-extended dataset is used including three original e-mail datasets, social media sources from Twitter, and criminal activities. For the validation part, they split their data into three sub-datasets which are training, validation, and test. The ratio of the three sub-datasets is 65, 10, and 25, respectively.

All in all, there are many state-of-the-art kinds of research presented in Table 1 by categorizing them. We provide a holistic approach to show the best algorithms by relying on individual methods including ML-based feature selection methods, hybrid and ensemble methods. ML-based feature selection methods called hybrid ensemble algorithms have the best performance solutions even if we have different data sets in different languages.

MI-Based and DI-Based Methods by Using Different Datasets In Turkish and English

In this study, we use several datasets, including the open-source six pieces of the Enron dataset for detecting spam emails in English, and open-source datasets from UCI and Kaggle for Turkish spam email detection. Subsequently, the dataset is preprocessed by employing the most suitable techniques. The preprocessed datasets are then transformed into numerical vectors using various methods such as BoW, TF-IDF, Word2Vec, and Glove. This transformation is carried out to make the data suitable for input into ML, DL models, and other different learning model implementations. We select various ML and DL algorithms demonstrating effective performance in practical applications, including document classification and spam filtering. ML approaches including the MNB algorithm [29-31], SVM [32], K-NN [33,34], DT [35], RF [35], and LR [36] algorithms as well as ensemble learning methods like VC and Stacking classifier (SC), are trained. DL algorithms such as LSTM [37, 38], Bi-LSTM [39], BERT [40, 41], and BERTurk [42] are employed, and their accuracy values are compared. All these steps are discussed in-depth in this paper. Figure 1 illustrates our methodology. We use the Google Colab platform to conduct our experiments. The system properties are like the following: Linux 5.15.120+ x86_64, 12 GB RAM, 110 GB Harddisk, Tesla T4 GPU, and Intel(R) Xeon(R) CPU @ 2.20GHz, Thread(s) per core: 2, Core(s) per socket: 1.

Datasets

English Datasets

The detection of spam emails in English is carried out using the open-source Enron dataset [43]. Within the Enron dataset, six separate datasets are chosen for analysis, categorized into spam and raw emails in varying quantities. Here's a breakdown of the Enron datasets: Enron 1 dataset comprises a total of 5,172 email texts, with 3,672 being raw emails and 1,500 being spam emails; Enron 2 dataset contains a total of 5,857 email texts, consisting of 4,361 raw emails and 1,496 spam emails; Enron 3 dataset includes a total of 5,512 email texts, with 4,012 being raw emails and 1,500 being spam emails; Enron 4 dataset encompasses a total of 6,000 email texts, with 4,500 being spam emails and 1,500 being raw emails; Enron 5 dataset consists of a total of 5,175 email texts, with 3,675 being spam emails and 1,500 being raw emails; Enron 6 dataset contains a total of 6,000 email texts, with 4,500 being spam emails and 1,500 being raw emails. Each of these datasets is used to analyze and detect spam emails.

The process for handling the English datasets begins with the extraction of data from compressed files. Then we read the email contents from text files and save them in comma-separated values (CSV) file format. During this process, we determine that there are no missing data points within the datasets.

However, duplicate text contents are identified as follows: 178 in the Enron 1 dataset, 33 in the Enron 2 dataset, 238 in the Enron 3 dataset, 149 in the Enron 4 dataset, 63 in the Enron 5 dataset, and 11 in the Enron 6 dataset. To ensure that these duplicate entries are systematically removed from the datasets, making them ready for preprocessing steps.

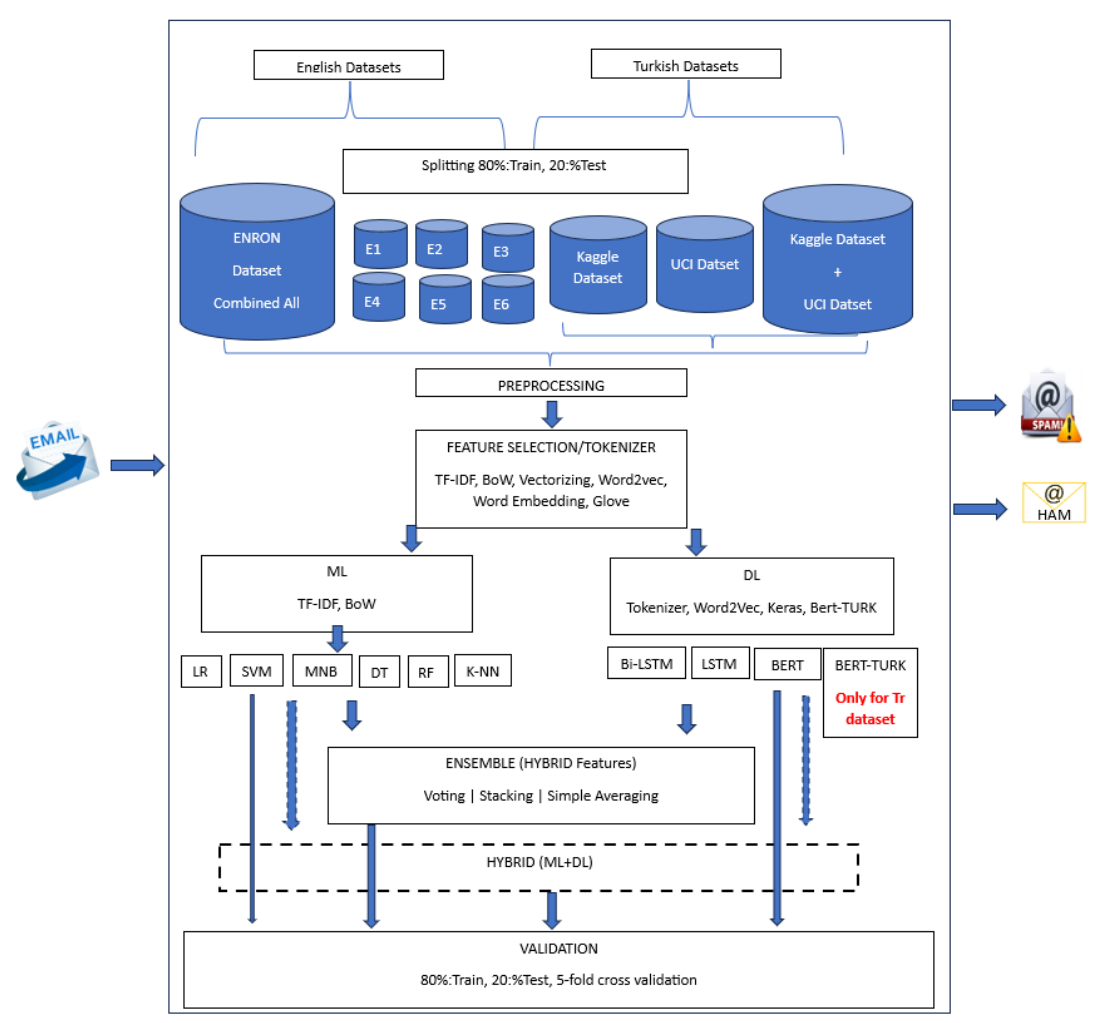


Figure 1
Proposed spam/ham mail detection methodology.

Turkish Datasets

To detect spam emails in Turkish, open-source datasets from Kaggle [44] and UCI [45] websites are utilized. The Kaggle dataset comprises a total of 1,015 email texts, with 514 categorized as spam and 501 as raw. In contrast, the UCI dataset contains 790 email contents, consisting of 324 spam emails and 466 raw emails. To facilitate the analysis, the content from the Kaggle dataset is extracted from text files and converted into CSV file format. However, the UCI dataset initially presented challenges as it could not be correctly read in CSV format. As a result, is processed to be converted back to CSV format to make it suitable for analysis. During the analysis, we determine that the UCI dataset has one row of missing data. The Kaggle dataset contains four repeated rows, and the UCI dataset has 71 repeated rows. The identified duplicate rows are removed from the dataset to eliminate such records that may potentially cause issues in future analyses and to prepare for preprocessing.

Data Preprocessing

The initial step in any ML or data analysis solution involves cleaning and processing the data. The execution of these procedures plays a key role in the success of the intended model. In this study, a

comprehensive exploration of commonly employed preprocessing steps including NLP tasks for textual data is conducted. These preprocessing procedures encompass the following steps which are the removal of stop words, and elimination of the symbols, signs, punctuation marks, and numerical values from the text to ensure uniform treatment of all text data. The others are like the following: creating regular expressions to handle special cases such as emails, URL domains, HTML tags, and codes, and then removing them from the dataset, discarding words that do not contribute to the meaningful content of the text, and converting words to lowercase. Each of the described steps is applied to every dataset individually. Subsequently, each of the English and Turkish datasets are separately merged and prepared for analysis. Once the datasets have undergone preprocessing, they are prepared for conversion into digital vectors, a crucial step in many NLP and ML tasks.

Feature Selection Methods

Text analysis is a significant domain for ML algorithms. However, these algorithms typically require fixed-size numerical feature vectors as input, whereas raw text documents come in variable lengths. To bridge this gap, several methods have been developed to extract numerical features from email content. Within the scope of this project, some of these methods, namely BoW, TF-IDF, Word2Vec, and Glove are employed. The BoW technique serves as a method for extracting features from text, which can then be utilized in ML algorithms. BoW is primarily used to determine whether known words are present in the text [46]. The TF-IDF method is a statistical approach employed to assess the significance of a word within an entire corpus of text [47]. Its importance increases proportionally to the frequency of the word's occurrence within a document [48]. Word2Vec is a transfer learning algorithm enabling the conversion of text data into input suitable for ML algorithms and facilitating model training [49]. Glove, Global Vectors for Word Representation, is a type of word embedding method. In Glove, each word is represented as a vector, and these vectors are computed based on the word's usage in language and its associations with other words within a specific context [50, 51].

In the conducted studies, models are trained using BoW and TF-IDF vectors with ML algorithms. Additionally, in the context of DL algorithms, models are trained using Word2Vec and Glove methods. Furthermore, uncased tokenizers, readily available in BERT models, and Keras tokenizer vectors from the Keras library are trained and evaluated. The results obtained from these different approaches are compared for the analysis.

Splitting of Datasets for Training and Test Steps

After performing all the preprocessing steps and being transformed into numerical vectors, the datasets are prepared for model training. They are split into two sets: an 80% training set and a 20% test set. This division allows for the training and evaluation of models using the data.

Evaluation Metrics

In the study, various classification performance evaluation metrics are utilized, including accuracy, recall, precision, and F1-score. These metrics rely on different aspects of model performance such as True Positives (TP), True Negatives (TN), False Positives (FP), False Negatives (FN). TP are values that are true and correctly predicted. The TN Values are not correct and are correctly predicted as such. The FP Values mean that are not correct but are incorrectly predicted as correct. The values of FN are correct but are incorrectly predicted as not correct. The representation of these components in a confusion matrix is illustrated in Table 2. This matrix provides a comprehensive view of the model's performance across various categories, facilitating the assessment of classification results.

Table 2Confusion matrix.

	Predicted (HAM) 0	Predicted (SPAM) 1
Actual (HAM) 0	TN	FP
Actual (SPAM) 1	FN	TP

This study uses accuracy, recall, precision, and F1-score as evaluation parameters to assess the performance of classification models, and these metrics can be calculated based on the values presented in the confusion matrix, as follows:

The value of accuracy is calculated by using (1):

$$Accuracy = \frac{(TP + TN)}{(TP + FP + TN + FN)}$$
(1)

We can find the value of recall by utilizing (2):

$$Recall = \frac{TP}{(TP + FN)}$$
 (2)

The value of precision is measured by (3):

$$Precision = \frac{TP}{(TP + FP)}$$
 (3)

F1-Score equals to (4):

$$F1-Score = \frac{2 \times (precision \times recall)}{(precision + recall)}$$
(4)

EXPERIMENTAL RESULTS

Machine Learning Results

In the Enron 1 dataset, LR and SVM models, trained with TF-IDF vectors, achieve an accuracy of 99.1%. The Enron 2 dataset has an accuracy of 99.74% result from a MNB model trained with TF-IDF vectors achieving. For the Enron 3 dataset, an MNB model trained with TF-IDF vectors reaches an accuracy of 99.62%. In the Enron 4 dataset, an LR model achieves an accuracy of 98.88%. For the Enron 5 dataset, a MNB model, trained with BoW vectors, attains an accuracy of 99.51%. On the Enron 6 dataset, the K-NN model, trained with TF-IDF vectors, reaches an accuracy of 98.08%. Finally, for the combined dataset, an SVM model, trained with TF-IDF vectors, achieves the highest accuracy of 99.51%.

Similarly, for the detection of spam emails in Turkish, the training process involved exploring all hyperparameter combinations, and subsequently, the models are retrained and tested using the hyperparameters that yield the best results. After conducting these tests, the model's performance is evaluated using various evaluation metrics. The best results of the ML models developed for Turkish and English spam email detection, along with their respective results, can be found in Table 3.

Deep Learning Results

In the Enron 1 dataset, the Bi-LSTM model, trained with Word2Vec vectors, achieves an accuracy of 97.49%. In the Enron 2 dataset, a Bi-LSTM model trained with Keras Tokenizer word vectors reaches an accuracy of 98.12%. The same accuracy is also attained by the Bi-LSTM model trained with Keras Tokenizer word vectors in the Enron 3 dataset. For the Enron 4 dataset, the Bi-LSTM model trained with Word2Vec vectors achieves an accuracy of 97.82%. In the Enron 5 dataset, a Bi-LSTM model

trained with Keras Tokenizer word vectors excels with an accuracy of 99.16%. The LSTM model training with Word2Vec vectors has the highest performance in the Enron 6 dataset, with an accuracy of 99.13%. In the combined dataset, the Bi-LSTM model training with Word2Vec vectors achieves the highest accuracy of 99.26%. Various models are created for each dataset for spam email detection in the Turkish language. The initial step involves preprocessing the data and converting it into numerical vectors using various methods such as Keras Tokenizer, Word2Vec, Glove, and BERT Tokenizer. After analyzing the results, all the datasets are merged, and model training is conducted once more. During the model training process, hyperparameters are tuned to attain the highest accuracy values. The best results of the models developed, and their respective outcomes can be found in Table 4.

Table 3 *ML Methods Results.*

Dataset	Model	Accuracy	Recall	Precision	F1-Score	Train Time (s)	Prediction Time (s)	Total Time (s)	Best Parameters
Enron1	LR TF-IDF	99.09%	99.09%	99.10%	99.10%	0.82	0.001	0.82	penalty: 12, solver: lbfgs
Enron2	MNB BoW	99.74%	99.74%	99.74%	99.74%	0.01	0.001	0.01	alpha: 0.01
Enron3	MNB TF-IDF	99.62%	99.62%	99.62%	99.62%	0.05	0.01	0.06	alpha: 0.001
Enron4	LR BoW	98.88%	98.88%	98.89%	98.88%	0.62	0.001	0.62	C: 100.0, penalty: 12, solver: lbfgs
Enron5	MNB BoW	99.51%	99.51%	99.51%	99.51%	0.02	0.001	0.02	alpha: 0.01
Enron6	K-NN TF- IDF	98.08%	98.08%	98.09%	98.06%	0.01	0.39	0.41	n neighbors: 3
Combined Enron Dataset	SVM TF-IDF	99.51%	99.51%	99.51%	99.51%	2433.18	42.38	2475.57	C: 10, gamma: 0.1, kernel:rbf
Kaggle	MNB TF-IDF	94.55%	94.55%	94.63%	94.53%	0.005	0.001	0.006	alpha: 0.01
UCI	LR TF-IDF	93.75%	93.75%	94.09%	93.68%	0.58	0.007	0.58	C: 1000.0, penalty: 12,solver: saga
Combined Turkish Dataset	MNB TF-IDF	95.08%	95.08%	95.13%	95.06%	0.01	0.03	0.01	alpha: 0.1

Table 4DL Methods Results

Dataset	Model	Tokenizer	Optimizer	Epoch	Batch	Train Time (s)	Prediction Time (s)	Total Time (s)	Accuracy	Loss
Enron1	BI -LSTM	Word2Vec	Adam	15	32	290	2	292	97.49%	0.06
Enron2	BI -LSTM	Keras Tokenizer	Adam	10	64	1013	12	1025	98.12%	0.07
Enron3	BI -LSTM	Word2Vec	Adam	10	32	209	2	211	97.82%	0.06
Enron4	BI -LSTM	Word2Vec	Adam	10	32	209	2	211	97.82%	0.06
Enron5	LSTM	Word2Vec	Adam	20	32	69	0	69	99.13%	0.03
Enron6	LSTM	Word2Vec	Adam	20	32	46	0	46	98.42%	0.05
Combined Enron Dataset	BI -LSTM	Word2Vec	Adam	20	32	2333	16	2349	99.22%	0.03
Kaggle	BERTurk	Bert Tokenizer	AdamW	5	16	150	10	160	97.24%	0.05
UCI	BERTurk	Bert Tokenizer	AdamW	10	16	110	10	120	96.07%	0.07
Combined Turkish	BERTurk	Bert Tokenizer	AdamW	12	16	319	24	343	97.72%	0.03

Hybrid, Ensemble, and the Combination of Those Learning Methods

In this section, we analyze the methods ensemble methods in addition to hybrid feature selection methods and hybrid methods including the best ML and DL algorithms.

Ensemble Learning is an ML approach designed to enhance overall prediction performance by aggregating the predictions of multiple models. This strategy aims to achieve more accurate predictions by leveraging the strengths of different models while mitigating their shortcomings. It operates on the concept that combining weak models can create a more powerful and robust predictive model. Ensemble Learning has various applications, including improving decision reliability, optimizing or near-optimizing feature selection, data fusion, incremental learning, handling non-stationary learning scenarios, and error correction [52]. The core idea behind this technique is rooted in the understanding that when individual forecasts are appropriately combined, the collective decision of the ensemble provides better overall accuracy than any individual committee member's prediction [53-55].

In the study, new models are trained by combining ML and DL models using voting, stacking, and simple average ensemble techniques. The VC is a type of ensemble learning technique that allows

for the combination of multiple diverse ML models. Once each model selected for ensemble learning is trained, their outputs are subjected to a voting process. This voting can be performed in two main ways: hard or soft. In the hard voting process, also known as majority voting, the final output is determined by taking most of the individual model outputs. In the soft voting approach, the output values are averaged, and the prediction corresponds to the output with the highest average. After completing the voting process, the ensemble produces a prediction result by aggregating the decisions of its constituent models. This technique is beneficial because it often results in improved prediction accuracy compared to using individual models in isolation [56]. The SC is an ensemble learning technique that combines multiple ML models. Once the selected models for ensemble learning are trained, their predictions are collected. Subsequently, the final predictions are generated using a meta-model, which is constructed based on the combined predictions of these models. The SC is particularly useful when different models have unique strengths and weaknesses, as it can exploit the complementary aspects of these models to improve overall prediction performance [57]. In the simple average ensemble method, the trained models can be combined to improve the predictions. In this method, first, the models to be predicted are trained. Then, the prediction results of the trained models are averaged. The resulting average value is considered as the result predicted by the model. After all model developments are completed with ML and DL algorithms, model developments are carried out by hybridizing the three ML algorithms that gave the best results for both Turkish and English data sets, DL algorithms, and finally ML and DL algorithms together. Voting and stacking ensemble methods are used in ML and ML hybrid models, the stacking ensemble method is used in DL and DL hybrid models, and the simple average ensemble method is used in ML and DL hybrid models.

Ensemble, Hybrid and Hybrid Ensemble Learning Results

For the Enron 1 dataset, the LR and MNB hybrid model using TF-IDF vectors created by stacking have the best outcomes. In the Enron 2 dataset, the LR model utilizing TF-IDF vectors depending on stacking gives the highest accuracy. The MNB and SVM hybrid model, along with LR trained with TF-IDF vectors using stacking, achieves the best results in the Enron 3 dataset. For the Enron 4 dataset, the MNB hybrid model and the LR and SVM hybrid model, both trained with TF-IDF vectors, provide the best results. The K-NN and MNB hybrid model using TF-IDF vectors delivers the top results In the Enron 5 dataset. For the Enron 6 dataset, the MNB and SVM hybrid model, based on TF-IDF vectors, provides the best performance. The MNB and SVM hybrid model, consisting of TF-IDF vectors, yields the best results for the combined dataset. These outcomes suggest that different hybrid models have superior performance on different datasets. It can be said that these hybrid approaches have led to increased accuracy in most datasets, with the MNB model performing exceptionally well in the Enron 2 dataset. This demonstrates the versatility of ensemble methods and hybridization in improving model performance across a range of data scenarios.

For the Kaggle dataset, the best performance belongs to the SVM and MNB hybrid model trained with TF-IDF vectors created through voting. However, for the UCI dataset, the LR and MNB hybrid model using TF-IDF vectors depending on voting delivered the highest accuracy. If we look at the results of the combined dataset, stacking with LR and MNB hybrid models trained with TF-IDF vectors resulted in the best performance. In the light of the results, it is observed that different hybrid models have more successful results for different datasets. In the case of the Kaggle and UCI datasets, the hybrid models achieve the same accuracy value as the MNB and LR models for each respective dataset, while underscoring the effectiveness of ensemble techniques. Additionally, the MNB model performed exceptionally well in the combined dataset. This demonstrates the flexibility and utility of hybridization and ensemble methods in achieving high accuracy across various data scenarios. The best ML ensemble models, and their respective outcomes can be found in Table 5.

Table 5 *ML-based ensemble model results.*

Dataset	Model	Ensemble	Accuracy	Recall	Precision	F1-Score	Train Time (s)	Prediction Time (s)	Total Time (s)
Enron1	LR + MNB TF-IDF	Stacking	99.19%	99.19%	99.21%	99.20%	320.23	1.60	321.84
Enron2	LR + MNB + SVM TF-IDF	Stacking	99.65%	99.65%	99.65%	99.65%	414.28	2.91	417.20
Enron3	LR + MNB TF-IDF	Stacking	99.71%	99.71%	99.71%	99.71%	72.22	0.02	72.25
Enron4	LR + SVM TF-IDF	Stacking	99.48%	99.48%	99.48%	99.48%	357.28	2.55	359.84
Enron5	KNN + MNB TF-IDF	Stacking	99.90%	99.90%	99.90%	99.90%	26.25	0.01	26.26
Enron6	KNN + MNB TF-IDF	Stacking	98.99%	98.99%	98.99%	98.99%	2.13	0.51	2.64
Combined Enron Dataset	SVM + MNB TF-IDF	Stacking	99.62%	99.62%	99.62%	99.62%	45.66	0.15	45.82
Kaggle	SVM + MNB TF-IDF	Voting	94.55%	94.55%	94.63%	94.53%	0.10	0.002	0.10
UCI	LR + MNB TF-IDF	Voting	93.75%	93.75%	94.09%	93.68%	0.16	0.001	0.17
Combined Turkish Dataset	LR + MNB TF-IDF	Stacking	94.79%	94.79%	94.82%	94.78%	0.16	0.01	0.17

The experimental results generated by one of the DL-based methods for the English language, which is the BERT + Bi-LSTM hybrid model has an accuracy value of 94.49% in the Enron 1 data set, 94.62% in the Enron 2 data set, and 95.83% and 97.97% accuracy in the Enron 3 and Enron 4 data sets, respectively. BERT + LSTM hybrid model with 97.20% accuracy on the Enron 5 dataset, BERT + LSTM hybrid model with 95.67% accuracy on the Enron 6 dataset, and BERT + Bi with 95.61% accuracy on the combined dataset. According to the results, the Bi-LSTM model provides the best performance. When analyzing the Turkish language, BERTurk + Bi-LSTM hybrid models show the best performance with an accuracy value of 87.19% in the Kaggle dataset, 89.02% in the UCI dataset, and 92.20% in the combined dataset, respectively. The best results of the DL ensemble models developed, and their respective outcomes can be found in Table 6.

Table 6 *DL-based ensemble model results.*

Dataset	Model	Tokenizer	Optimizer	Epoch	Batch	Train Time (s)	Prediction Time (s)	Total Time (s)	Accuracy	Loss
Enron1	BERT + BI -LSTM	BERT Tokenizer	Adam	20	32	1344	11	1355	94.49%	0.15
Enron2	BERT + BI - LSTM	BERT Tokenizer	Adam	10	64	1013	12	1025	98.12%	0.07
Enron3	BI -LSTM	BERT Tokenizer	Adam	20	32	1385	12	1397	95.83%	0.12
Enron4	BI -LSTM	BERT Tokenizer	Adam	15	32	1181	13	1194	97.67%	0.07
Enron5	LSTM	BERT Tokenizer	Adam	20	32	1325	11	1336	97.20%	0.09
Enron6	LSTM	BERT Tokenizer	Adam	20	32	1476	13	1489	95.67%	0.11
Combined Enron Dataset	BI -LSTM	BERT Tokenizer	Adam	17	32	6753	75	6828	95.61%	0.11
Kaggle	BERTurk	Bert Tokenizer	AdamW	20	32	75	0	75	87.19%	0.70
UCI	BERTurk	Bert Tokenizer	AdamW	20	32	65	0	65	89.02%	0.47
Combined Turkish Dataset	BERTurk	Bert Tokenizer	AdamW	20	32	97	0	97	92.20%	0.42

Table 7 *Hybrid ensemble model results.*

Dataset	Model	Accuracy	Recall	Precision	F1-Score	Train Time (s)	Prediction Time (s)	Total Time (s)
Enron1	LSTM + SVM	99.19%	99.34%	98.05%	98.69%	205.15	154.90	360.05
Enron2	LSTM + SVM	99.57%	99.31%	98.97%	99.14%	206.53	141.76	348.29
Enron3	LSTM + SVM	99.57%	99.31%	98.97%	99.14%	206.53	141.76	348.29
Enron4	LSTM + SVM	99.48%	100%	99.29%	99.64%	169.53	107.98	277.51
Enron5	LSTM + SVM	99.70%	100%	99.58%	99.79%	137.77	97.29	235.06
Enron6	LSTM + KNN	98.41%	99.77%	98.09%	98.92%	85.81	476.11	561.92
Combined Enron Dataset	Bi-LSTM + LR	99.39%	99.79%	99.01%	99.40%	2449.35	2029.55	4478.91
Kaggle	BERTurk + MNB	97.92%	99.41%	96.56%	97.96%	167.04	11.85	178.89
UCI	BERTurk + MNB	97.77%	98.83%	95.14%	96.95%	115.24	14.35	129.60
Combined Turkish Dataset	BERTurk + SVM	98.43%	98.82%	97.68%	98.25%	337.95	25.96	363.91

In the study conducted for the English language, the accuracy values are 99.19% in the Enron 1 data set, 99.57% in the Enron 2 data set, 99.14% in the Enron 3 data set, 99.48% in the Enron 4 data set, and 99.70% in the Enron 5 data set, respectively. The LSTM + SVM hybrid model shows the best performance, the LSTM + KNN hybrid model with an accuracy value of 98.41% on the Enron 6 dataset, and the Bi-LSTM + LR model with an accuracy value of 99.39% on the combined dataset. In the study

conducted for the Turkish language, BERTurk + MNB hybrid models showed the best performance with accuracy values of 97.92% and 97.77% in the Kaggle and UCI datasets, respectively, and BERTurk + SVM hybrid model with 98.43% accuracy in the combined dataset. The best results of the hybrid ensemble models developed, and their respective outcomes can be found in Table 7.

DISCUSSION AND PERFORMANCE EVALUATION

In this study, ML and DL algorithms are employed to address real-world problems, specifically related to spam email detection. The algorithms selected for this research are developed as potential solutions for the classification problem concerning spam emails. This study focuses on several key aspects, including pre-processing steps, vectorization of data, and the impact of the raw or spam ratio on performance. Experiments are conducted using a total of 1085 Turkish email texts and 33,716 English email texts. The datasets are open access. Each of these datasets is subjected to several key steps such as pre-processing and vectorization before being applied to various models. We extensively discuss these crucial steps in the Methodology section. To ensure accuracy in the comparison of these models, ML algorithms are assessed according to precision, recall, F1-score, and accuracy metrics, while DL algorithms are evaluated based on accuracy and loss values. The results are systematically recorded, and statistical information is employed to analyze and compare the findings. Based on the performance results obtained, the study conducts comparisons using different methods and presents comprehensive evaluations. This research contributes to the understanding of how various factors, including data preprocessing and vectorization, can impact the performance of ML and DL models in the context of spam email detection.

For English datasets, the best results are obtained while using one of the ML algorithms which is MNB models trained with TF-IDF vectors. Among the DL algorithms, it has been observed that Bi-LSTM models using Word2Vec vectors give the best results. Among the ensemble learning methods, the stacking method created with ML algorithms has been shown to produce the best results. Thus, spam mail detection in English is solved with 99.9% as the highest accuracy value, with at least 97% accuracy performance.

According to the Turkish data sets, the best results are obtained in spam mail detection with MNB models trained with TF-IDF vectors, one of the ML algorithms. Among the DL algorithms, it has been observed that BERTurk models trained with BERTurk tokenizer vectors give the best results. Among the ensemble learning methods, the simple average method created with ML and DL algorithms has achieved the best results. Thus, spam mail detection in the Turkish language is solved with 98.4% accuracy, with at least 93% accuracy value.

All in all, although this study does not produce a generic solution for spam mail detection on the languages used, the obtained results show that especially hybrid and ensemble learning methods and some ML algorithms provide more successful outcomes.

CONCLUSION

In recent years, the prevalence of spam emails has increased significantly due to the widespread use of email in business and personal communication, as well as the growth of social media platforms. Effectively detecting and categorizing this rising volume of spam emails is a critical concern to safeguard systems and prevent issues like fraudulent activities. This paper conducts a comparative analysis and literature review to identify the most efficient methods for distinguishing between spam and legitimate emails, using datasets in both Turkish and English. In addition to existing datasets, we've also created new datasets in these languages. In this study, we present a comparative and comprehensive study taking advantage of various approaches which are ML, DL, hybrid, and ensemble methods. These

methods are combined with NLP techniques, enhanced learning algorithms, optimized feature selection, and preprocessing. We compare our solutions with commonly used methods in the field such as MNB, SVM, LR, K-NN, DT, RF, VC, SC, and DL algorithms like LSTM, Bi-LSTM, BERT, and BERTurk. The results are validated by splitting the datasets into training and testing data with an 80:20 ratio and using 5-fold cross-validation for each model. Additionally, the hyperparameters of our models are fine-tuned using Grid search. The best feature selection method for the Enron dataset is the TF-IDF approach, while the simple average ensemble learning approach is for the Turkish dataset. The findings reveal that ensemble methods based on ML achieve the best performance, achieving an accuracy rate of 99.9% for the English dataset. In comparison, a hybrid ensemble approach with a simple average produces the highest accuracy of 98.43% for the Turkish dataset.

These proposed methods are well-suited for various platforms, including email and social media, to effectively detect and categorize spam content. In future work more efficient and real-time models can be proposed by using transfer learning approaches, large language models (LLMs), and federated learning approaches to detect spam mail so we can decrease the overhead of this problem on the Internet.

Author Contributions

Research Design (CRediT 1) E.N.C. (%34) – R.K. (%33) – A.E. (%33)

Data Collection (CRediT 2) E.N.C. (%34) – R.K. (%33) – A.E. (%33)

Research - Data Analysis - Validation (CRediT 3-4-6-11) E.N.C. (%39) – R.K. (%38) – A.E. (%23)

Writing the Article (CRediT 12-13) E.N.C. (%39) – R.K. (%23) – A.E. (%38)

Revision and Improvement of the Text (CRediT 14) E.N.C. (%39) – R.K. (%23) – A.E. (%38)

Conflict of interest

The authors declare that they have no conflict of interest.

REFERENCES

- [1] J. Doshi, K. Parmar, R. Sanghavi, N. Shekokar, A comprehensive dual-layer architecture for phishing and spam email detection, *Computer & Security*. 133 (2023), 103378. doi:10.1016/j.cose.2023.103378
- [2] N. Saidani, K. Adi, MS. Allili, A semantic-based classification approach for an enhanced spam detection. *Computer & Security*. 94 (2020), 101716. doi:10.1016/j.cose.2020.101716
- [3] B. Feng, Q. Fu, M. Dong, D. Guo, Q. Li, Multistage and elastic spam detection in mobile social networks through deep learning, *IEEE Network*. 32(4) (2018), 15-21. doi:10.1109/MNET.2018.1700406
- [4] A. Karim, S. Azam, B. Shanmugam, K. Kannoorpatti, M. Alazab, A comprehensive survey for intelligent spam email detection, *IEEE Access*. 7 (2019), 168261-168295. doi:10.1109/ACCESS.2019.2954791
- [5] S. Gibson, B. Issac, L. Zhang, SM. Jacob, Detecting spam email with machine learning optimized with bio-inspired metaheuristic algorithms, *IEEE Access*. 8 (2020), 187914-187932. doi:10.1109/ACCESS.2020.3030751
- [6] S. Rapacz, P. Chołda, M. Natkaniec, A method for fast selection of machine-learning classifiers for spam filtering, *Electronics*. 10(17) (2021), 2083. doi:10.3390/electronics10172083
- [7] S. Magdy, Y. Abouelseoud, M. Mikhail, Efficient spam and phishing email filtering based on deep learning, *Computer Networks*. 206 (2022), 108826. doi:10.1016/j.comnet.2022.108826
- [8] F. Ozen, R. Ortac Kabaoglu, T. V. Mumcu, Deep Learning Based Temperature and Humidity Prediction, *Necmettin Erbakan University Journal of Science and Engineering*. 5(2) (2023). 219-229. doi:10.47112/neufmbd.2023.20
- [9] M. Hacıbeyoglu, M. Çelik, Ö. Erdaş Çiçek, Energy Efficiency Estimation in Buildings with K Nearest Neighbor Algorithm, *Necmettin Erbakan University Journal of Science and Engineering*, 5 (2) (2023), 65-74. doi:10.47112/neufmbd.2023.10
- [10] A. Pektaş, O. İnan, Application of Tree Seed Algorithm on Clustering Problems, *Necmettin Erbakan University Journal of Science and Engineering*. 4(1) (2022), 1-10. doi:10.47112/neufmbd.2022.8
- [11] F. Rustam, N. Saher, A. Mehmood, E. Lee, S. Washington, I. Ashraf, Detecting ham and spam emails using feature union and supervised machine learning models, *Multimedia Tools and Applications*. 82 (2023), 26545–26561. doi: 10.1007/s11042-023-14814-2
- [12] E. E. Eryılmaz, D. Ö. Şahin, E. Kılıç, Türkçe İstenmeyen E-postaların Farklı Öznitelik Seçim Yöntemleri Kullanılarak Makine Öğrenmesi Algoritmaları ile Tespit Edilmesi, *Türkiye Bilişim Vakfı-Bilgisayar Bilimleri ve Mühendisliği Dergisi*. 13(2) (2020), 57-77.
- [13] M. A. Shaaban, Y. F. Hassan, S. K. Guirguis, Deep convolutional forest: a dynamic deep ensemble approach for spam detection in text, *Complex & Intelligent Systems*. 8(6) (2022), 4897-4909. doi:10.1007/s40747-022-00741-6
- [14] S. Kaddoura, O. Alfandi, N. Dahmani, A spam email detection mechanism for English language text emails using a deep learning approach, In: 29th International Conference on Enabling Technologies: Infrastructure for Collaborative Enterprises (WETICE), IEEE, Bayonne, France, 2020: 193-198. doi:10.1109/WETICE49692.2020.00045
- [15] T. Toma, S. Hassan, M. Arifuzzaman, An analysis of supervised machine learning algorithms for spam email detection, In: *International Conference on Automation, Control, and Mechatronics for Industry 4.0 (ACMI), IEEE,* Rajshahi, Bangladesh, 2021: 1-5. doi:10.1109/ACMI53878.2021.9528108
- [16] C. M. Shaik, N. M. Penumaka, S. K. Abbireddy, V. Kumar, S. Aravinth, Bi-LSTM and conventional classifiers for email spam filtering, In: *Third International Conference on Artificial*

- *Intelligence and Smart Energy (ICAIS)*, *IEEE*, Coimbatore, India, 2023: 1350-1355. doi:10.1109/ICAIS56108.2023.10073776
- [17] K. Debnath, N. Kar. Email spam detection using deep learning approach, In: *International Conference on Machine Learning, Big Data, Cloud and Parallel Computing (COM-IT-CON)*, *IEEE*, Faridabad, India, 2022: 37-41. doi:10.1109/COM-IT-CON54601.2022.9850588
- [18] A. R. Yeruva, D. Kamboj, P. Shankar, U. S. Aswal, A. K. Rao, C. Somu, E-mail spam detection using machine learning—KNN, In: *5th International Conference on Contemporary Computing and Informatics (IC3I), IEEE*, Uttar Pradesh, India, 2022: 1024-1028. doi:10.1109/IC3I56241.2022.10072628
- [19] N. Ahmed, R. Amin, H. Aldabbas, D. Koundal, B. Alouffi, T. Shah, Machine learning techniques for spam detection in email and IoT platforms: Analysis and research challenges, *Security and Communication Networks*. (1) (2022), 1-19. doi:10.1155/2024/7538203
- [20] Z. B. Siddique, M. A. Khan, I. U. Din, A. Almogren, I. Mohiuddin, S. Nazir, Machine learning-based detection of spam emails, *Scientific Programming*. (1) (2021), 1-11. doi:10.1155/2021/6508784
- [21] Z. Hassani, V. Hajihashemi, K. Borna, I. S. Dehmajnoonie, A classification method for E-mail spam using a hybrid approach for feature selection optimization, *Journal of Sciences, Islamic Republic of Iran.* 31(2), (2020), 165-173.
- [22] A. Sheneamer, Comparison of deep and traditional learning methods for email spam filtering, *International Journal of Advanced Computer Science and Applications (IJACSA)*. 12(1) (2021), 560-565. doi: 10.14569/IJACSA.2021.0120164
- [23] S. Zavrak, S. Yilmaz, Email spam detection using hierarchical attention hybrid deep learning method, *Expert Systems with Applications*. 233 (2023), 120977. doi: 10.1016/j.eswa.2023.120977
- [24] G. Hnini, J. Riffi, M. A. Mahraz, A. Yahyaouy, H. Tairi, MMPC-RF: a deep multimodal feature-level fusion architecture for hybrid spam E-mail detection, *Applied Sciences*. 11(24) (2021), 11968. doi: 10.3390/app112411968
- [25] A. I. Taloba, S. S. Ismail, An intelligent hybrid technique of decision tree and genetic algorithm for e-mail spam detection, *In: IEEE 2019 Ninth International Conference on Intelligent Computing and Information Systems (ICICIS)*, *IEEE*, Cairo, Egypt, 2019: 99-104. doi:10.1109/ICICIS46948.2019.9014756
- [26] K. Meena, S. R. Upadhyaya, A Privacy-Preserving machine learning ensemble for spam detection, *In: IEEE 5th International Conference on Inventive Research in Computing Applications (ICIRCA)*, *IEEE*, Coimbatore, India, 2023: 255-259.
- [27] M. Sumathi, S. Raja, Machine learning algorithm-based spam detection in social networks, *Social Network Analysis and Mining*. 13(1) (2023), 104. doi:10.1007/s13278-023-01108-6
- [28] M. Hina, M. Ali, A. R. Javed, F. Ghabban, L. A. Khan, Z. Jalil, SeFACED: Semantic-based forensic analysis and classification of e-mail data using deep learning, *IEEE Access*. 9 (2021), 98398-98411. doi:10.1109/ACCESS.2021.3095730
- [29] S. Xu, Y. Li, W. Zheng, Bayesian multinomial naïve bayes classifier to text classification, *In: International Conference on Multimedia and Ubiquitous* Engineering, *Springer*, Singapore 2017: 347–352. doi:10.1007/978-981-10-5041-1 57
- [30] R. O. Olanrewaju, S. A. Olanrewaju, L. A. Nafiu, Multinomial naïve bayes classifier: bayesian versus nonparametric classifier approach, *European Journal of Statistics*. 2 (8) (2022), 1-13. doi:10.28924/ada/stat.2.8
- [31] U. K. B. Saravanan, M. Vijay, T. Shreedhar, G. Rajasekar, R. Yashwanth, P. Shakthipriya, Multinomial Naive Bayes Based Machine Learning Analysis of Twitter Sentiment, *In: IEEE 2nd International Conference on Edge Computing and Applications (ICECAA)*. Namakkal, India, 2023: 429-434. doi:10.1109/ICECAA58104.2023.10212150.

- [32] Y. K. Zamil, S. A. Ali, M. A. Naser, Spam image email filtering using k-nn and svm, *International Journal of Electrical and Computer Engineering*. 9(1) (2019), 245-254. doi:10.11591/ijece.v9i1. 245-254.
- [33] B. Trstenjak, S. Mikac, D. Donko, Knn with tf-idf based framework for text categorization, *Procedia Engineering*. 69 (2014), 1356-1364. doi:10.1016/j.proeng.2014.03.129
- [34] Z. Yong, L. Youwen, X. Shixiong, An improved knn text classification algorithm based on clustering, *Journal of Computers*, 4(3) (2009), 230-237. doi:10.4304/jcp.4.3.230-237
- [35] S. S. Ismail, R. F. Mansour, A. El-Aziz, M. Rasha, A. I. Taloba, Efficient e-mail spam detection strategy using genetic decision tree processing with NLP features, *Computational Intelligence and Neuroscience*. (2022), 1-16. doi:10.1155/2022/7710005.
- [36] D. Jurafsky, J. H. Martin, Speech and Language Processing: An Introduction to Natural Language Processing, Computational Linguistics, and Speech Recognition with Language Models, (2024). https://web.stanford.edu/~jurafsky/slp3/5.pdf (accessed 21 September 2024).
- [37] S. Jamshidi, M. Mohammadi, S. Bagheri, H. E. Najafabadi, A. Rezvanian, M. Gheisari, M. Ghaderzadeh, A. S. Shahabi, Z. Wu, Effective text classification using BERT, MTM LSTM, and DT. *Data & Knowledge Engineering*. 151 (2024), 102306. doi:10.1016/j.datak.2024.102306.
- [38] Y. Yu, X. Si, C. Hu, J. Zhang, A review of recurrent neural networks: LSTM cells and network architectures, *Neural Computation*. 31 (7) (2019), 1235-1270. doi:10.1162/neco a 01199
- [39] A. Purwarianti, I. A. P. A. Crisdayanti, Improving Bi-LSTM performance for Indonesian sentiment analysis using para44 graph vector, *In: IEEE 2019 International Conference of Advanced Informatics: Concepts, Theory and Applications (ICAICTA)*, Bandung, Indonesia, 2019: 1-5. doi:10.1109/ICAICTA.2019.8904199.
- [40] Y. Xiong, N. Wei, K. Qiao, Z. Li and Z. Li, Exploring Consumption Intent in Live E-Commerce Barrage: A Text Feature-Based Approach Using BERT-BiLSTM Model, *IEEE Access*, 12 (2024), 69288-69298. doi: 10.1109/ACCESS.2024.3399095.
- [41] J. Wallat, F. Beringer, A. Anand, V. Anand, Probing BERT for Ranking Abilities. *In: Kamps, J., et al. Advances in Information Retrieval. ECIR 2023. Lecture Notes in Computer Science*, Springer, Cham, 2024: 13981. doi:10.1007/978-3-031-28238-6 17
- [42] B. Aytan, C. O. Sakar, Comparison of transformer-based models trained in turkish and different languages on turkish natural language processing problems, *In: 2022 30th Signal Processing and Communications Applications Conference (SIU)*, Safranbolu, Turkey, 2022: 1-4. doi:10.1109/SIU55565.2022.9864818
- [43] E. Corp, W. W. Cohen. Enron Email Dataset, (2015). https://www.loc.gov/item/2018487913/ (accessed 23 September 2024).
- [44] H. Simsek, E. Aydemir. Classification of unwanted e-mails (spam) with turkish text by different algorithms in weka program, *Journal of Soft Computing and Artificial Intelligence*, 3 (2022), 1-4. doi:10.55195/jscai.1104694
- [45] UCI Machine Learning Repository. Turkish Spam V01 dataset, (2019). https://archive.ics.uci.edu/dataset/530/turkish+spam+v01 [accessed 15 December 2023].
- [46] W. Qader, M. Ameen, B. Ahmed, An overview of bag of words; importance, implementation, applications, and challenges, *In: 2019 International Engineering Conference (IEC)*, Erbil, Iraq, 2019: 200-204. doi:10.1109/IEC47844.2019.8950616
- [47] L. Havrlant, V. Kreinovich, A simple probabilistic explanation of term frequency-inverse document frequency (tf-idf) heuristic (and variations motivated by this explanation), *International Journal of General Systems*. 46 (2017), 27-36. doi:10.1080/03081079.2017.1291635
- [48] A. Jalilifard, V. F. Carida, A. F. Mansano, R. S. Cristo, F. P. C. Fonseca, Semantic sensitive tf-

- idf to determine word relevance in documents, *In: Advances in Computing and Network Communications*, 2021: 327–337. doi:10.1007/978-981-33-6987-0
- [49] F. Zhang, W. Song, Product improvement in a big data environment: A novel method based on text mining and large group decision making, *Expert Systems with Applications*, 245 (2024), 123015, doi:10.1016/j.eswa.2023.123015.
- [50] J. Pennington, R. Socher, C. Manning, Glove: global vectors for word representation, *In: Proceedings of the 2014 Conference on Empirical Methods in Natural Language Processing (EMNLP)*, Doha, Qatar, 2014: 1532–1543. doi:10.3115/v1/D14-1162
- [51] Z. Hua, Y. Tong, Y. Zheng, Y. Li, and Y. Zhang, PPGlove: Privacy-Preserving Glove for Training Word Vectors in the Dark, *IEEE Transactions on Information Forensics and Security*. 19 (2024), 3644-3658. doi:10.1109/TIFS.2024.3364080
- [52] P. Bountakas, C. Xenakis, HELPHED: Hybrid ensemble learning phishing email detection, Journal of Network and Computer Applications. 210 (2023), 103545. doi:10.1016/j.jnca.2022.103545
- [53] O. Sagi, L. Rokach, Ensemble learning: a survey, *Wiley Interdisciplinary Reviews: Data Mining and Knowledge Discovery.* 8 (4) (2018), e1249. doi:10.1002/widm.1249
- [54] G. Wang, J. Sun, J. Ma, K. Xu, J. Gu, Sentiment classification: the contribution of ensemble learning, *Decision Support Systems*. 57 (2014), 77-93. doi:10.1016/j.dss.2013.08.002
- [55] M. A. Ganaie, M. Hu, A. K. Malik, M. Tanveer, P. N. Suganthan, Ensemble deep learning: a review, *Engineering Applications of Artificial Intelligence*. 115 (2022), 105151. doi:10.1016/j.engappai.2022.105151.
- [56] N. C. Yang, K. L. Sung, Non-intrusive load classification and recognition using soft-voting ensemble learning algorithm with decision tree, k-nearest neighbor algorithm and multilayer perceptron, *IEEE Access*. 11 (2023), 94506-94520. doi:/10.1109/ACCESS.2023.3311641
- [57] A. Ghourabi, M. Alohaly, Enhancing spam message classification and detection using transformer-based embedding and ensemble learning, *Sensors*. 23(8) (2023), 3861. doi:10.3390/s23083861



Vol: 7 No:2 Year: 2025

Araştırma Makalesi/Research Article

e-ISSN: 2667-7989

https://doi.org/10.47112/neufmbd.2025.86

Gönderim Sınıfı Grubunda Denk Çapraz Homomorfizmler

Hatice ÜNLÜ EROĞLU 1* 📵

¹ Necmettin Erbakan University, Faculty of Science, Department of Mathematics and Computer Sciences, Konya, Türkiye

Makale Bilgisi ÖZET

Geliş Tarihi: 01.10.2024 Kabul Tarihi: 08.12.2024 Yayın Tarihi: 31.08.2025

Anahtar Kelimeler: Çapraz homomorfizm, Dolanım sayısı, Gönderim sınıfı grubu.

Bir yüzeyin gönderim sınıfı grubu, yön koruyan kendisine giden diffeomorfizmalarının izotopi sınıflarını tanımlayan bir grup olup, matematiğin pek çok alanında, özellikle topoloji, cebir ve geometride önemli bir rol oynar. Topolojide, gönderim sınıfı grupları 3-manifoldların ve lif demetlerin incelenmesinde önemlidir; cebir ve geometri alanlarında ise otomorfizm teorisi, modül uzayları ve yüzeyler üzerindeki kompleks yapılar ile yakın bir ilişkiye sahiptir. Gönderim sınıfı grupları konusunda ilginç bir bakış açısı, gönderim sınıfı gruplarının kohomoloji sınıflarının incelenmesini içerir. Yönlendirilebilir yüzeylerin gönderim sınıfı gruplarının kohomoloji sınıfları, yüzey demetlerinin karakteristik sınıfları olarak düşünülebilir. Earle, Morita, Furuta ve Trapp tarafından verilen, yönlendirilebilir yüzeylerin gönderim sınıfı gruplarının kohomoloji sınıfının çeşitli inşaları vardır. Bu inşalar çok farklı görünmektedir. Bu nedenle, çeşitli yazarlar bu yapıları karşılaştırarak aralarındaki ilişkileri daha iyi anlamak için çaba sarf ettiler. Furuta tarafından önerilen ve Trapp tarafından sunulan gönderim sınıfı gruplarının kohomoloji sınıflarını veren çapraz homomorfizmler dolanım sayıları ile ilişkilidir. Bu çalışmada, bu iki farklı yapı arasındaki ilişkiyi gösteriyoruz.

Equivalent Crossed Homomorphisms on The Mapping Class Group

Article Info ABSTRACT

Received: 01.10.2024 Accepted: 08.12.2024 Published: 31.08.2025

Keywords:

Crossed homomorphism, Winding number, Mapping class group. The mapping class group of a surface, which describes the isotopy classes of orientation-preserving self-diffeomorphisms, plays an important role in many areas of mathematics, particularly in topology, algebra and geometry. In topology, mapping class groups are essential for studying 3-manifolds and fiber bundles, while in algebra and geometry, they are closely related to the theory of automorphisms, moduli spaces, and complex structures on surfaces. An interesting perspective on mapping class groups involves the study of their cohomology classes. Cohomology classes of the mapping class groups of orientable surfaces can be considered as characteristic classes of surface bundles. There are several constructions of the cohomology class of the mapping class groups of orientable surfaces given by Earle, Morita, Furuta, and Trapp. These constructions seem very different. Therefore, various authors have made efforts to better understand the relationships between these constructions by comparing them. The crossed homomorphisms which yield the cohomology classes of the mapping class groups, as proposed by Furuta and presented by Trapp, are related to winding numbers. In this study, we show the relation between these two different constructions.

To cite this article:

Ünlü Eroğlu, H. (2025). Equivalent crossed homomorphisms on the mapping class group. *Necmettin Erbakan University Journal of Science and Engineering*, 7(2), 206-213. https://doi.org/10.47112/neufmbd.2025.86

*Corresponding Author: Hatice Ünlü Eroğlu, hueroglu@erbakan.edu.tr



INTRODUCTION

Let $\Sigma_{g,1}$ be a compact connected oriented smooth surface of genus g with 1 boundary component and $\Sigma_{g,*}$ be a surface obtained by attaching a disc to the boundary $\partial \Sigma_{g,1}$ with a fixed point *. The mapping class groups of $\Sigma_{g,1}$ and $\Sigma_{g,*}$ are the groups of all isotopy classes of orientation preserving self-diffeomorphisms, with the former fixing the boundary pointwise and the latter fixing the marked point *, respectively. Let $MCG(\Sigma_{g,1})$ and $MCG(\Sigma_{g,*})$ denote the mapping class groups of $\Sigma_{g,1}$ and $\Sigma_{g,*}$, respectively [1].

Various crossed homomorphisms from $MCG(\Sigma_{g,1})$ to $H_1(\Sigma_{g,1}, \mathbb{Z})$ were constructed to get a generator of the first cohomology class of the mapping class group. Earle [2] first constructed a crossed homomorphism $MCG(\Sigma_{g,*}) \to \frac{1}{2g-2} H_1(\Sigma_g; \mathbb{Z})$ for $g \ge 2$ and a crossed homomorphism $MCG(\Sigma_{g,*}) \to H_1(\Sigma_g; \mathbb{Z})$ can be obtained after the multiplication by (2g-2).

Morita [3] proved the following isomorphisms:

$$H^1\left(MCG(\Sigma_{g,1}); H^1(\Sigma_g; \mathbb{Z})\right) \cong H^1\left(MCG(\Sigma_{g,*}); H^1(\Sigma_g; \mathbb{Z})\right) \cong \mathbb{Z}.$$

Moreover, Morita [3] gave a combinatorial construction of a crossed homomorphism representing a generator of $H^1\left(MCG(\Sigma_{g,1}); H^1(\Sigma_g; \mathbb{Z})\right)$. Kuno [4] compared Earle's and Morita's constructions. Recently, Chen [5] and Maruyama [6] constructed new crossed homomorphisms.

Trapp and Furuta also constructed crossed homomorphisms representing a generator of $H^1\left(MCG\left(\Sigma_{g,1}\right); H^1\left(\Sigma_g; \mathbb{Z}\right)\right)$ using winding numbers. In this paper, we provide a survey of different constructions given by Trapp [7] and proposed by Furuta [8]. We also show that both constructions are equivalent by using difference cocycles after we present an overview to provide the necessary background information.

MATERIALS AND METHODS

This section is devoted to the basic definitions which will be needed in the next section. We define crossed homomorphisms, the winding number of a smooth curve, and the difference cocycle. We refer the reader to [9] for any unexplained terminology on the homology and cohomology of surfaces. In this paper, we are interested in homologies and cohomologies with $\mathbb Z$ coefficients, so we will no longer emphize the coefficients.

Crossed Homomorphism

Let us recall the definition of the first cohomology group $H^1(MCG(\Sigma_{g,1}); H^1(\Sigma_{g,1}))$ of $MCG(\Sigma_{g,1})$ with coefficients in $H^1(\Sigma_{g,1})$ [10].

There is an action of $MCG(\Sigma_{g,1})$ on $H_1(\Sigma_{g,1})$ via the symplectic representation ρ , which takes an element of $MCG(\Sigma_{g,1})$ to an automorphism of $H_1(\Sigma_{g,1})$ preserving the intersection form. If we identify $H^1(\Sigma_{g,1})$ with $Hom(H_1(\Sigma_{g,1}), \mathbb{Z})$, the action of $MCG(\Sigma_{g,1})$ on $H^1(\Sigma_{g,1})$ is defined to be $\phi_1 f(x) = f((\phi_1)_*^{-1}(x)) = f(\rho(\phi_1^{-1}(x)))$, where $\phi_1 \in MCG(\Sigma_{g,1})$, $f \in H^1(\Sigma_{g,1})$, $x \in H_1(\Sigma_{g,1})$, and $(\phi_1)_*$ is the induced homomorphism from ϕ_1 .

A crossed homomorphism ψ is a function $\psi: MCG(\Sigma_{g,1}) \to H^1(\Sigma_{g,1})$ such that $\psi(\mu_1\mu_2) = \psi(\mu_1) + \mu_1 \psi(\mu_2)$ for all μ_1 , $\mu_2 \in MCG(\Sigma_{g,1})$. Let $Z^1(MCG(\Sigma_{g,1}); H^1(\Sigma_{g,1}))$ denote the set of all crossed homomorphisms $\psi: MCG(\Sigma_{g,1}) \to H^1(\Sigma_{g,1})$.

Let us define a function $\psi_m : MCG(\Sigma_{g,1}) \to H^1(\Sigma_{g,1})$ such that $\psi_m(\mu_1) = \mu_1 \ m - m$, where m is a fixed element of $H^1(\Sigma_{g,1})$. This defined function ψ_m is called a *principal crossed homomorphism*. Let us denote the set of all such principal crossed homomorphisms by $B^1(MCG(\Sigma_{g,1}); H^1(\Sigma_{g,1}))$.

The first cohomology group of $MCG(\Sigma_{g,1})$ with coefficients in $H^1(\Sigma_{g,1})$ is defined as the quotient

$$H^{1}\left(MCG(\Sigma_{g,1}); \ H^{1}(\Sigma_{g,1})\right) := \frac{Z^{1}\left(MCG(\Sigma_{g,1}); \ H^{1}(\Sigma_{g,1})\right)}{B^{1}\left(MCG(\Sigma_{g,1}); \ H^{1}(\Sigma_{g,1})\right)}$$

Similarly, we can define $H^1(MCG(\Sigma_{g,1}); H_1(\Sigma_{g,1}))$.

Winding Number

In this subsection, we provide the definition of the winding number [11]. Intuitively, the winding number of a smooth oriented closed curve is the number of rotations made by its tangent vector with respect to a nonvanishing vector field X, as the curve is traversed once in the positive direction.

Assume that $\Sigma_{g,1}$ is given some Riemannian structure. Let $T^1\Sigma_{g,1}$ be the unit tangent bundle of $\Sigma_{g,1}$ and $prj: T^1\Sigma_{g,1} \to \Sigma_{g,1}$ be the natural projection defined by prj(t,v) = t for each unit vector $v \in T_t\Sigma_{g,1}$ and $t \in \Sigma_{g,1}$, where $T_t\Sigma_{g,1}$ is the tangent space over the point t. Let $\beta: S^1 \to \Sigma_{g,1}$ be a smooth oriented closed curve with $\beta(S^1) = \gamma$ based at the point t and continuously varying non-zero tangents exist at all points of γ . The continuous map β induces a pullback over S^1 from $T^1\Sigma_{g,1}$ to $\Sigma_{g,1}$. That is, if $prj^{\beta}: S^1 \times S^1 \to S^1$ is the first projection map, then there exists a map F taking the fiber of $S^1 \times S^1$ over each point $a \in S^1$ isomorphically onto the fiber of $T^1\Sigma_{g,1}$ over $\beta(a)$ such that the following diagram is commutative:

$$S^{1} \times S^{1} \xrightarrow{F} T^{1} \Sigma_{g,1}$$

$$prj^{\beta} \qquad \qquad prj$$

$$S^{1} \xrightarrow{\beta} \Sigma_{g,1}$$

$$(1)$$

Here, the total space is $S^1 \times S^1$, as $\beta(S^1) = \gamma$ is an orientation preserving curve.

Since the surface $\Sigma_{g,1}$ has a nonempty boundary, a nonvanishing vector field X on $\Sigma_{g,1}$ exists. If a nonvanishing vector field X is given, there is a section $X^{\beta} \colon S^{1} \to S^{1} \times S^{1}$ such that $F \circ X^{\beta} = \tilde{X} \circ \beta$, where $\tilde{X}(t) \coloneqq X(t)/\|X(t)\|_{t}$ for $t \in \Sigma_{g,1}$ and $\|X(t)\|_{t}$ denotes the norm of X(t) on $T_{t}\Sigma_{g,1}$. This section is defined so that $X^{\beta}(a) = (a, \tilde{X}(\beta(a)))$ for every $a \in S^{1}$.

Now by considering the tangent map $d\beta: TS^1 \to T\Sigma_{g,1}$, we can define $d_0\beta: S^1 \to T^1\Sigma_{g,1}$ as follows:

$$d_0\beta(a) = \frac{d\beta(a,1)}{\|d\beta(a,1)\|_{\beta(a)}}.$$

This defined map $d_0\beta$ pulls back to a unique section $Y^\beta: S^1 \to S^1 \times S^1$ which satisfies the equality $F \circ Y^\beta = d_0\beta$.

Assume that $X^{\beta}(a) = Y^{\beta}(a) = a_0$ for a point $a \in S^1$. Then X^{β} and Y^{β} represent elements of

 $\pi_1(S^1 \times S^1, a_0)$. The projection map prj^{β} induces the homomorphism $prj_*^{\beta}: \pi_1(S^1 \times S^1, a_0) \to \pi_1(S^1, a)$. Clearly, $prj_*^{\beta}(X^{\beta}) = prj_*^{\beta}(Y^{\beta})$. Therefore, we see that $Y^{\beta}(X^{\beta})^{-1}$ is an element of the kernel of prj_*^{β} . Let A_0 denote the fiber over $a \in S^1$, and $i^{\beta}: A_0 \to S^1 \times S^1$ be the inclusion map. By the exactness of the following sequence

$$0 \to \pi_1(A_0, a_0) \xrightarrow{i_*^{\beta}} \pi_1(S^1 \times S^1, a_0) \xrightarrow{prj_*^{\beta}} \pi_1(S^1, a), \tag{2}$$

we get

$$i_*^{\beta}(w^{\beta}) = Y^{\beta}(X^{\beta})^{-1}$$

for some unique $w^{\beta} \in \pi_1(A_0, a_0)$. Indeed, the exactness of the sequence (2) implies that i_*^{β} is one to one and there exists an element w^{β} of $\pi_1(A_0, a_0)$ such that the image of w^{β} is $Y^{\beta}(X^{\beta})^{-1}$, which is an element of the kernel of prj_*^{β} . Because of the injectivity of i_*^{β} , w^{β} is unique. A choice of the orientation of $T_t\Sigma_{g,1}$ for $t\in\Sigma_{g,1}$ gives us an orientation of A_0 . Hence, we can regard w^{β} as an integer, which is defined to be the winding number $wind(\gamma, X)$ of γ with respect to X.

Difference Cocycle

In this subsection, the difference cocycle introduced by Chillingworth [11] is constructed. To see that we get the same integer in the image of the difference cocycle for the different smooth representatives of a homology class, we present an example.

For a Riemannian metric on $\Sigma_{g,1}$ and two nonvanishing vector fields X_1 and X_2 on $\Sigma_{g,1}$, one can define sections $\widetilde{X_1}$ and $\widetilde{X_2}$ from $\Sigma_{g,1}$ to $T^1\Sigma_{g,1}$ by $\widetilde{X_1}(t) \coloneqq X_1(t)/\|X_1(t)\|_t$ and $\widetilde{X_2}(t) \coloneqq X_2(t)/\|X_2(t)\|_t$ for $t \in \Sigma_{g,1}$. Let $\gamma = \beta(S^1)$ be an oriented closed curve and let us consider the commutative diagram (1) exhibited in the construction of the winding number. Suppose that $X_1(t) = X_2(t)$ for some $t \in \Sigma_{g,1}$. The composition maps $\widetilde{X_1}\beta$ and $\widetilde{X_2}\beta$ pull back to unique sections $X_1^\beta, X_2^\beta \colon S^1 \to S^1 \times S^1$, respectively. From the exact sequence (2), we obtain $i_*^\beta(u^\beta) = X_1^\beta\left(X_2^\beta\right)^{-1}$ for a unique $u^\beta \in \pi_1(A_0, a_0) \cong \mathbb{Z}$ and u^β can be identified with an integer which is the total number of times that X_1 rotates relative to the X_2 as γ traversed once.

Definition [11] Let $\gamma_1, \gamma_2, ..., \gamma_{2g}$ be smooth simple closed curves on $\Sigma_{g,1}$, based at t, and their homotopy classes generate $\pi_1(\Sigma_{g,1}, t)$. Then $\{[\gamma_1], [\gamma_2], ..., [\gamma_{2g}]\}$ form a basis of $H_1(\Sigma_{g,1})$. A difference cocycle is a homomorphism

$$d(X_1, X_2): H_1(\Sigma_{g,1}) \longrightarrow \mathbb{Z}$$

defined by $d(X_1, X_2)[\gamma_i] = u^{\beta_i}$, where $\gamma_i = \beta_i(S^1)$.

Given an oriented closed curve $\gamma = \beta(S^1)$, we have $u^{\beta} = d(X_1, X_2)[\gamma]$. Because γ is homotopic to a product of γ_i or γ_i^{-1} .

Chillingworth [11] obtains that $d(X_1, X_2)[\gamma] = wind(\gamma, X_2) - wind(\gamma, X_1)$ for a smooth oriented closed curve γ .

Notice that the image of $[\gamma]$ under $d(X_1, X_2)$ does not change for different choices of representatives. To be clear, let us consider the following example.

Example

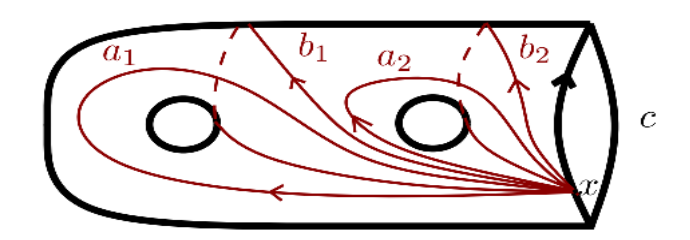


Figure 1
Orientable genus-2 surface with one boundary.

Consider a cellular decomposition of $\Sigma_{2,1}$. Let x be a 0-cell on the boundary of $\Sigma_{2,1}$ and a_1, b_1, a_2, b_2, c be 1-cells as depicted in Figure 1. The unique 2-cell $\Sigma_{2,1} \setminus \{a_1, b_1, a_2, b_2, c\}$ will be denoted by A. Let $\langle x \rangle$, $\langle a_1, b_1, a_2, b_2, c \rangle$, and $\langle A \rangle$ be the free abelian groups generated by $\{x\}$, $\{a_1, b_1, a_2, b_2, c\}$, and $\{A\}$, respectively. We have the following cellular chain complex:

$$0 \longrightarrow \langle A \rangle \xrightarrow{\partial_2} \langle a_1, b_1, a_2, b_2, c \rangle \xrightarrow{0} \langle x \rangle \longrightarrow 0.$$

In the above chain complex ∂_2 denotes the boundary map and the image of it is $\partial_2(A) = c$.

For two nonvanishing vector fields X_1 and X_2 on $\Sigma_{2,1}$, $d(X_1,X_2)$ is defined on the free abelian group $\langle a_1,b_1,a_2,b_2,c\rangle$ and its image is an integer. Now, we aim to show that it induces a homomorphism from $H_1(\Sigma_{2,1})$ to \mathbb{Z} . Therefore, we need to get $d(X_1,X_2)(c)=0$, because the boundary of the 2-cell A is c.

By Lemma 5.7 in [11], we have $wind(c, X_1) = wind(c, X_2)$. By Lemma 4.1 in [11], $d(X_1, X_2)(c) = wind(c, X_2) - wind(c, X_1) = 0$ is obtained. Similarly, one can show that $d(X_1, X_2)(\gamma) = 0$ for any separating curve γ . By the universal property of quotient groups, we get a homomorphism $d(X_1, X_2)$: $H_1(\Sigma_{2,1}) \to \mathbb{Z}$, as desired.

MAIN RESULT

This section is devoted to two crossed homomorphisms defined by Trapp and proposed by Furuta, and it is shown that these definitions are equivalent.

Trapp [7] defined a map

$$\tau_X: MCG(\Sigma_{g,1}) \longrightarrow H^1(\Sigma_{g,1})$$

such that $\tau_X(f)[\gamma] = wind(f\gamma, X) - wind(\gamma, X)$ for any $f \in MCG(\Sigma_{g,1})$, $[\gamma] \in H_1(\Sigma_{g,1})$ and a nonvanishing vector field X on $\Sigma_{g,1}$. Let $\rho \colon MCG(\Sigma_{g,1}) \longrightarrow Sp(2g; \mathbb{Z})$ be the symplectic representation. Trapp showed that τ_X is a crossed homomorphism by getting the following formula:

$$\tau_X(fh) = \tau_X(f)\rho(h) + \tau_X(h),$$

for any $f, h \in MCG(\Sigma_{g,1})$.

Lemma The cohomology class $\tau_X(f)$ is equal to the difference cocycle $d(X, f^{-1}X)$ for any $f \in MCG(\Sigma_{g,1})$ and a nonvanishing vector field X on $\Sigma_{g,1}$.

Proof. Let $[\gamma] \in H_1(\Sigma_{g,1})$. From the fact that $wind(f\gamma, fX) = wind(\gamma, X)$, we have $wind(f\gamma, X) = wind(\gamma, f^{-1}X)$ and this implies that $\tau_X(f)$ is equal to $d(X, f^{-1}X)$ as follows:

$$\tau_X(f)[\gamma] = wind(f\gamma, X) - wind(\gamma, X) = wind(\gamma, f^{-1}X) - wind(\gamma, X) = d(X, f^{-1}X)[\gamma].$$

We now outline Furuta's crossed homomorphism [8].

Recall that $\Sigma_{g,1}$ is given a Riemannian structure. Let X be a nonvanishing vector field on $\Sigma_{g,1}$ and $f \in MCG(\Sigma_{g,1})$. Since X is nonvanishing, fX is also a nonvanishing vector field. Let S^1 denote the set of angles mod 2π . Let a fixed orientation be chosen on $\Sigma_{g,1}$. Furuta defined a map

$$\psi_f: \Sigma_{g,1} \longrightarrow S^1$$

such that $\psi_f(p) := \angle(X_p, (f \ X)_p)$ is the angle mod 2π from X_p to $(f \ X)_p$. Let the cohomology class $\psi_f^*([S^1]) \in H^1(\Sigma_{g,1})$ be denoted by $[\psi_f]$. Here $[S^1]$ indicates the generator of $H^1(S^1)$. The Poincaré dual of $[\psi_f]$ gives us a homology class $m_X(f) \in H_1(\Sigma_{g,1})$. In summary, Furuta obtained a map m_X : $\mathrm{MCG}(\Sigma_{g,1}) \to H_1(\Sigma_{g,1})$ depending on X. In [8], it is proved that m_X : $\mathrm{MCG}(\Sigma_{g,1}) \to H_1(\Sigma_{g,1})$ is a crossed homomorphism. It is also shown that its cohomology class $[m_X]$ is independent of X and is a generator of $H^1(\mathrm{MCG}(\Sigma_{g,1}); H_1(\Sigma_{g,1}))$. Moreover, it can be seen that the map Ψ_X : $\mathrm{MCG}(\Sigma_{g,1}) \to H^1(\Sigma_{g,1})$ defined by $\Psi_X(f) = [\psi_f]$ is also a crossed homomorphism.

Now our task is to give the relation between these two above crossed homomorphisms.

Theorem Let X be a nonvanishing vector field on $\Sigma_{g,1}$. Then we have $\tau_X(f)[\gamma] = \Psi_X(f^{-1})[\gamma] = [\psi_{f^{-1}}][\gamma]$ for any $f \in MCG(\Sigma_{g,1})$ and $[\gamma] \in H_1(\Sigma_{g,1})$.

Proof. Let $\beta: S^1 \to \Sigma_{g,1}$ be a smooth closed oriented curve with $\beta(S^1) = \gamma$ and continuously varying non-zero tangents exist at all points of γ . Consider the commutative diagram (1) which is depicted in the winding number subsection.

Let \tilde{X} and $f^{-1}X$ be the unit vector fields induced by X and $f^{-1}X$, respectively. There exist sections X^{β} and $(f^{-1}X)^{\beta}$ such that $F \circ X^{\beta} = \tilde{X} \circ \beta$ and $F \circ (f^{-1}X)^{\beta} = f^{-1}X \circ \beta$. Suppose that \tilde{X} and $f^{-1}X$ rotate k and l-times, respectively, around the fiber on $T^1\Sigma_{g,1}$ restricted to γ . Then by the construction of the difference cocycle, X^{β} and $(f^{-1}X)^{\beta}$ are homotopic to maps sending θ to $(\theta, k\theta)$ and θ to $(\theta, l\theta)$, respectively. After the compositions of X^{β} and $(f^{-1}X)^{\beta}$ with the second projection map $pr_2: S^1 \times S^1 \to S^1$, we get $pr_2 \circ X^{\beta}: S^1 \to S^1$ taking θ to $k\theta$ and $pr_2 \circ (f^{-1}X)^{\beta}: S^1 \to S^1$ taking θ to $l\theta$. Therefore, the image of $[\gamma]$ under $d(X, f^{-1}X)$ can be regarded as the degree of the map $S^1 \to S^1$ sending θ to $(k-l)\theta$.

Now recall the map $\psi_{f^{-1}}: \Sigma_{g,1} \to S^1$ defined by $\psi_{f^{-1}}(p) = \angle(X)_p, (f^{-1}X)_p)$. From the restriction of the map $\psi_{f^{-1}}$ to γ we have a map denoted by $\psi_{f^{-1}} \circ \beta: S^1 \to S^1$. Since we assumed that \widetilde{X} and $\widetilde{f^{-1}X}$ rotate k and l-times, respectively, around the fiber on $T^1\Sigma_{g,1}$ restricted to γ , by the definition of $\psi_{f^{-1}}$ the composition map $\psi_{f^{-1}} \circ \beta$ is homotopic to a map sending θ to $(k-l)\theta$. Therefore, we have $d(X, f^{-1}X)[\gamma] = \deg(\psi_{f^{-1}} \circ \beta)$.

Our next step is to show the equality $[\psi_{f^{-1}}][\gamma] = \deg(\psi_{f^{-1}} \circ \beta)$ in an explicit way. After identifying $H^1(\Sigma_{g,1})$ with $\operatorname{Hom}(H_1(\Sigma_{g,1}), \mathbb{Z})$, the cohomology class $[\psi_{f^{-1}}]$ is obtained from the induced map $(\psi_{f^{-1}})_*$. Indeed, the induced map $(\psi_{f^{-1}})_*$: $H_1(\Sigma_{g,1}) \to H_1(S^1)$ will give us a cohomology class after identifying $H_1(S^1)$ with \mathbb{Z} . Let us consider the following sequence:

$$H_1(S^1) \overset{\beta_*}{\to} H_1(\Sigma_{g,1}) \overset{\left(\psi_{f^{-1}}\right)_*}{\longrightarrow} H_1(S^1) \cong \mathbb{Z}.$$

The isomorphism in the above sequence comes from the cohomology class $[S^1] \in H^1(S^1)$. If [a] is a generator of $H_1(S^1)$, we have

$$(\psi_{f^{-1}} \circ \beta)_*([a]) = (\psi_{f^{-1}})_* \circ \beta_*([a]) = (\psi_{f^{-1}})_*([\gamma]).$$

Consequently, we obtain

$$[\psi_{f^{-1}}][\gamma] = (\psi_{f^{-1}})_{\alpha}([\gamma]) = (\psi_{f^{-1}} \circ \beta)_{\alpha}([a]) = \deg(\psi_{f^{-1}} \circ \beta) = d(X, f^{-1}X)[\gamma] = \tau_X(f)[\gamma],$$

for any smooth representative γ .

Corollary Let X be a nonvanishing vector field on $\Sigma_{g,1}$ and $f \in MCG(\Sigma_{g,1})$. If $n_X(f)$ is the Poincaré dual of $\tau_X(f)$ defined by Trapp, then $n_X: MCG(\Sigma_{g,1}) \to H_1(\Sigma_{g,1})$ depends only on X and it is also a crossed homomorphism. Moreover, the cohomology class $[n_X] \in H^1(MCG(\Sigma_{g,1}); H_1(\Sigma_{g,1}))$ is independent of X.

Proof. Recall that the Poincaré dual of $[\psi_{f^{-1}}]$ is $m_X(f^{-1}) \in H_1(\Sigma_{g,1})$ and the cohomology class $[m_X]$ is a generator of $H^1(MCG(\Sigma_{g,1}); H_1(\Sigma_{g,1}))$. In [8], it is also proved that m_X is a crossed homomorphism. By the previous theorem, we obtain $[\psi_{f^{-1}}][\gamma] = \tau_X(f)[\gamma]$. Therefore, the homology class $n_X(f)$ is equal to $m_X(f^{-1})$, which completes the proof.

DISCUSSION AND CONCLUSIONS

In this study, we obtain the equivalence of two crossed homomorphisms defined by Trapp and proposed by Furuta. Morita was aware of the equivalence, but to our knowledge, there is no explicit proof showing this equivalence. We fill this gap with this study. In the construction of difference cocycles, algebraic and geometric features are used. Moreover, crossed homomorphisms and winding numbers can be applied in other areas of mathematics such as Banach spaces. Therefore, we can consider this subject as an interdisciplinary subject in mathematics [12-14]. For future work, it can be constructed other crossed homomorphisms on the mapping class group of an orientable surface that contains more than one boundary component with the help of difference cocycles.

Ethical Statement

This study is derived from the Ph.D thesis titled "Generalized Chillingworth Classes on Subsurface Torelli Groups", submitted in August 2018 under the supervision of Prof. Dr. Mustafa KORKMAZ. It has also been developed and partially modified from the content of the paper titled "Crossed Homomorphisms on The Mapping Class Group", which was presented orally at the 6th Workshop of Association for Turkish Women in Maths but was not published in full text.

Author Contributions

Research Design (CRediT 1) H.Ü.E.: (%100)

Data Collection (CRediT 2) H.Ü.E.: (%100)

Research - Data Analysis – Validation (CRediT 3-4-6-11) H.Ü.E.: (%100)

Writing the Article (CRediT 12-13) H.Ü.E.: (%100)

Revision and Improvement of the Text (CRediT 14) H.Ü.E.: (%100)

Financing

This research did not receive any specific grant from funding agencies in the public, commercial, or not-for-profit sectors.

Sustainable Development Goals (SDG)

Sustainable Development Goals:Not supported.

REFERENCES

- [1] B. Farb, D. Margalit, A primer on mapping class groups, *Princeton University Press*, Princeton, 2012. doi:10.1515/9781400839049
- [2] C. J. Earle, Families of Riemann surfaces and Jacobi varieties. *Annals of Mathematics*. 107(2), (1978), 255–286. doi:10.2307/1971144
- [3] S. Morita, Families of Jacobian manifolds and characteristic classes of surface bundles. I., *Annales de L' Institut Fourier (Grenoble)*. 39(3) (1989), 777–810. doi:10.5802/aif.1188
- [4] Y. Kuno, A combinatorial formula for Earle's twisted 1-cocycle on the mapping class group $\mathcal{M}_{g,*}$, Mathematical Proceedings of the Cambridge Philosophical Society. 146(1) (2009), 109–118. doi:10.1017/S0305004108001680
- [5] L. Chen, Circle action of the punctured mapping class group and cross homomorphism, (2023). arXiv preprint arXiv:2301.06247.
- [6] S. Maruyama, A crossed homomorphism for groups acting on the circle, *Journal of Topology and Analysis*. doi:10.1142/S1793525324500092
- [7] R. Trapp, A linear representation of the mapping class group \mathcal{M} and the theory of the winding numbers, *Topology and its Applications*. 43(1992), 47-64. doi:10.1016/0166-8641(92)90153-Q
- [8] S. Morita, Casson invariant, signature defect of framed manifolds and the secondary characteristic classes of surface bundles, *Journal of Differential Geometry*. 47(3) (1997), 560-599. doi:10.4310/jdg/1214460550
- [9] A. Hatcher, Algebraic Topology, Cambridge University Press, Cambridge, 2002.
- [10] K. S. Brown, Cohomology of Groups, *Springer-Verlag*, New York, 1982. doi:10.1007/978-1-4684-9327-6
- [11] D. R. J. Chillingworth, Winding numbers on surfaces, I, *Mathematische Annalen*. 196 (1972), 218–249.
- [12] A. K. Çopur, Some results on an iterative algorithm associated with enriched contractions in Banach spaces, *Necmettin Erbakan University Journal of Science and Engineering*. 5(2) (2023), 162-172. doi:10.47112/neufmbd.2023.16
- [13] S. Pak, Ö. Gürmen Alansal, U. Cesur, Pseudo 2- Çaprazlanmış Modüller ve Pseudo 3-Çaprazlanmış Modüller, *Necmettin Erbakan University Journal of Science and Engineering*. 2(2) (2020), 22-37.
- [14] M. Erdoğdu, A. Yavuz, Geometric Analysis of the NLS Surface with the Pseodu Null Darboux Frame of Spacelike Curve, *Necmettin Erbakan University Journal of Science and Engineering*. 6(1) (2024), 188-198. doi:10.47112/neufmbd.2024.42



Vol: 7 No: 2 Year: 2025

Araştırma Makalesi/Research Article

e-ISSN: 2667-7989

https://doi.org/10.47112/neufmbd.2025.87

Hepatit-B İçin Yeni Bir Matematiksel Model ve Modelde Dikey Bulaşın Etkisi

Mehmet YAVUZ 1,2* D Naime Büşra BAYRAKTAR 1 D Kübra AKYÜZ 1 D Feyza Nur ÖZDEMİR ³ D

³ Necmettin Erbakan University, Graduate School of Natural and Applied Sciences, Department of Computer Engineering, Konya, Türkiye

Makale Bilgisi	ÖZET
Geliş Tarihi: 23.05.2024 Kabul Tarihi: 18.12.2024 Yayın Tarihi: 31.08.2025	Bu makalede, Hepatit virüsünün bulaşma dinamiklerini araştırmak için Hepatit B'nin yeni bir matematiksel modeli oluşturulmuştur. Model, dikey bulaşmayı dikkate alarak geliştirilmiştir. Modelde, duyarlı, latent, akut, taşıyıcı, iyileşen ve aşılanmış popülasyonlar dikkate alınmıştır. Ayrıca, pozitiflik ve hastalıksız denge noktası belirlenmiştir. Son olarak, sayısal sonuçlar elde edilmiş ve hastalığın gelecekteki seyrini tahmin etmek için biyolojik yorumları yapılmıştır.
Anahtar Kelimeler: Hepatit-B virüsü,	
Matematiksel modelleme, Göç faktörü,	
Dikey geçiş.	

A New Mathematical Model for Hepatitis-B and the Effect of Vertical Transmission in the Model

Article Info	ABSTRACT
Received: 23.05.2024 Accepted: 18.12.2024 Published: 31.08.2025	In this paper, a new mathematical model of Hepatitis B is constructed to investigate the dynamics of the transmission of the Hepatitis virus. The model is developed by considering the vertical transmission. In the model, susceptible, latent, acute, carrier, recovered, and vaccinated populations are taken into account. Moreover, positivity is performed, and disease-free equilibrium point is calculated. Finally, the numerical results and their biological interpretations
Keywords:	are performed to estimate the future directions of the disease.
Hepatitis-B virus,	•
Mathematical modeling,	
Migration factor,	
Vertical transmission.	

Yavuz, M., Bayraktar, N.B., Akyüz, K. & Özdemir, F.N. (2025). A new mathematical model for Hepatitis-B and the effect of vertical transmission in the model. Necmettin Erbakan University Journal of Science and Engineering, 7(2), 214-227. https://doi.org/10.47112/neufmbd.2025.87

*Sorumlu Yazar: Mehmet Yavuz, mehmetyavuz@erbakan.edu.tr



¹ Necmettin Erbakan University, Faculty of Science, Department of Mathematics and Computer Sciences, Konya, Türkiye

² Kyrgyz-Turkish Manas University, Faculty of Science, Department of Applied Mathematics and Informatics, Bishkek, Kyrgyzstan

INTRODUCTION

Infectious diseases have caused problems for humanity throughout history. From past to present, infectious diseases that have caused social, economic and cultural losses have also caused mass deaths. In the historical process, it is known that infectious diseases such as plague, smallpox, typhus, typhoid, cholera, influenza, malaria and Hepatitis-B cause the death of many people. Various solutions and effects on the transmission routes and course of these diseases, which pose problems for humanity, are being investigated. For this reason, in recent years, especially with a major process such as a pandemic, studies on infectious disease research have begun to appear widely in the literature [54–57]. One of the infectious diseases that has been a problem throughout history is Hepatitis-B disease. Hepatitis-B is a liver infection caused by Hepatitis-B virus (HBV). It poses a global health problem because it causes many deaths [1, 2].

HBV disease, which causes elevated liver enzymes, is an infectious disease that is transmitted through body fluids, blood and mucosal contact. In some individuals infected with HBV, the disease can survive silently in the body. The virus can also manifest itself in some individuals. Hepatitis-B disease is divided into acute and chronic. Acute HBV is a short-term illness that occurs within the first 6 months after exposure to the Hepatitis-B virus. Even if the virus does not cause any symptoms in these people, the risk of being a carrier and transmitting the infection continues. Among the symptoms observed in individuals, complaints such as fever, fatigue, loss of appetite, nausea or vomiting, muscle, joint and stomach pain are observed. Chronic HBV infection is the form of the Hepatitis-B virus that cannot be eliminated and can cause bad consequences such as liver damage (cirrhosis), liver cancer and death [3]. While there is no known treatment for acute HBV, the disease can be controlled with the help of various medications in chronic HBV. HBV can be transmitted horizontally or vertically between individuals. Transmission between individuals through blood or water, sexual contact, or reuse of unsafe syringes is called horizontal transmission, while transmission of the virus from an HBV-infected mother to her newborn baby is called vertical transmission.

Mathematical modeling in infectious diseases is an important method to examine the course of diseases. Mathematical models provide information about the estimated number of cases of infectious diseases and the estimated number of deaths from the disease [4]. Moreover, mathematical modeling also helps determine parameters and solution methods to alleviate the disease [5]. Therefore, mathematical modeling of the disease has become a highly preferred subject to determine the course of infectious diseases.

Many studies have been conducted in the literature on the mathematical modeling of HBV, one of the infectious diseases. Bashir and Umar [6] established a new mathematical model by combining three control strategies known as treatment, vaccination and media campaign in order to reduce the spread of HBV. Combining the three interventions was shown to improve the outcome of the study as much as possible. Kiemtore et al. [7] conducted a study in Africa, one of the places in the world where HBV is most likely to occur. They developed a model that included vaccination and treatment of HBV in the Burkina Faso population. They estimated the disease parameters using Gray Wolf Optimization (GWO). Li and Chai [8], developed a mathematical model that models the drug resistance treatment of HBV. Their aim was to investigate the reason for the decrease in drug resistance of the disease as a result of the mutation of HBV over time. As a result, it has been revealed that if the virus resistance of the disease is high in the body, combined drug treatment shortens the clearance time of the resistant HBV virus.

Liu et al. [9] designed a fractional model for Hepatitis-B. They created a non-linear epidemic model by investigating the stages of transmission of HBV. They formulated the model with the vaccine effect using the Atangana-Baleanu derivative (AB derivative). As a result, it has been demonstrated that

vaccination is a method that can end the HBV epidemic process. Elaiw et al. [10] pointed out that there may be model inaccuracies that may arise when modeling HBV disease, and they modeled the disease with a non-linear ordinary differential equation. Possible disruptions and uncertainties were reflected in the model as social limited disruptions. They expanded their model by adding two types of drug therapies used to prevent new infections. Khan et al. [11] established an HBV model and conducted a sensitivity analysis of the model by examining its existence and positivity. They performed numerical simulations to analyze parameter sensitivities. de Villiers et al. [12] compared two deterministic HBV models, the Imperial HBV model and CDA. Additionally, the effect of the birth dose of HBV vaccine was investigated. They contributed to the literature by revealing some differences between the two models.

Preventing the HBV epidemic in Ghana and the Brong Ahafo region is a major challenge due to limited resources in these regions. Otoo et al. [13] drew attention to this problem and formulated a model that explains the spread of HBV. They proposed an intervention that would minimize the impact of the epidemic. As a result, they have shown that it is possible to combat the spread of the disease by vaccinating susceptible people and treating infected people. Cardoso et al. [14] explained the dynamics of HBV with a fractional model. They presented the main results of this model. They calculated the equilibrium point and basic reproduction number. Finally, by performing numerical simulations, they demonstrated that the model converged to an equilibrium point. Farman et al. [15] created a time-spanning and non-linear model of HBV. They used fractional parameters to develop the system. Finally, they applied numerical simulation. In this way, they investigated the effect of the system parameter on the spread of the disease. Reinharz et al. [16] developed a multicompartmental model that included infected human hepatocytes and total intracellular HBV DNA per infected human hepatocyte. They also modeled HBV kinetics during 14-day treatment of Humanized Chimeric Mice. As a result of the study, they obtained new information about HBV DNA dynamics in infected human hepatocytes.

There are many models in the form of in vivo model systems to demonstrate the progression of HBV in different animal species. Ortega-Priet et al. [17] drew attention to this situation and conducted a study examining in vivo model systems to examine the HBV life cycle. They examined models such as the chimpanzee model, tree mouse model and carrier animal models of HBV. Khan et al. [18] considered various stages of HBV using generalized saturated incidence. They created a model to demonstrate HBV dynamics and control strategies. They investigated the time dynamics and stability conditions of the model. Finally, they updated their models to increase the number of the recovered population and minimize the infected population. Friedman and Siewe [19], discussed the treatment of chronic HBV with the combination of IFN-alpha and adefovir. In their study, they investigated what the optimal ratio between IFN-alpha and adefovir should be for the best results. They designed a model of HBV pathogenesis using a partial differential equation system.

Oludoun et al. [20] formulated a model to examine the impact of testing and treatment on HBV and to analyze the transmission process. They used the Next Generation Matrix method for the basic reproduction number. As a result, they revealed that testing in cases of acute HBV and chronic unconsciousness will contribute to controlling the disease. Moreover, a number of illustrative applications have been performed in terms of the investigations on HBV, COVID-19 [21–25], HIV-AIDS [26–28], SARS-CoV [29–32], tuberculosis [33–36], Malaria [37–40], other infectious diseases [41–46] and prey-predator competition research that successfully explain mathematical modelling [47–50].

In this study, mathematical modeling was used to examine the effect of vertical transmission and migration parameters of HBV on the course of HBV infectious disease. In the mathematical model consisting of 6 compartments, susceptible population, latent population, acute population, carrier

population, protected infected (in the sense of recovered) and vaccinated population were used.

The rest of the study is organized as follows: Numerical results and discussion are presented in Section 4, and the conclusion is explained in Section 5.

DERIVATION OF THE MATHEMATICAL MODEL FOR HBV INFECTION

In this section, the basic SLACPV mathematical model for the effect of HBV on vertical transmission and migration factor is proposed and analyzed. Total population, susceptible population S(t), latent population L(t), acute population A(t), carrier population C(t), protective rescued P(t) and vaccinated population V(t) is divided into six mutually exclusive parts.

The parameters provided constitute elements of a mathematical model describing the transmission dynamics of Hepatitis-B virus (HBV). Λ denotes the recruitment rate of individuals into the susceptible population, while ς represents the rate of immunity decrease due to vaccination. μ stands for the natural mortality rate, and β signifies the transmission rate. ϕ indicates reduced transmission compared to acute infection, and ω represents the rate of babies born infected from mothers. ϑ signifies the proportion of infected mothers transmitting HBV to their offspring. ϖ is the vaccination rate, ξ is the recovery rate from acute infection, and f is the recovery rate of carriers. p denotes the transition rate from acute to carrier status, and μ_0 is the HBV-related death rate. g represents the rate of new individuals joining the community through migration. b signifies the transition rate from susceptible to latent infection, l is the vaccine leakage rate, and k is the transition rate from latent to acute infection. ω is the rate of babies born infected. These parameters collectively depict the interplay of various processes in HBV transmission dynamics, aiding in understanding and predicting disease spread and control measures. The same situation is represented by a schematic diagram and stated in Section 2. The equation system of the given schematic diagram is given in Eq. (1)

Hence, by considering this assumption the rate of change of susceptible, latent, acute, carrier, protected infected (protective rescued) and vaccinated population is described in the following nonlinear system of differential equations.

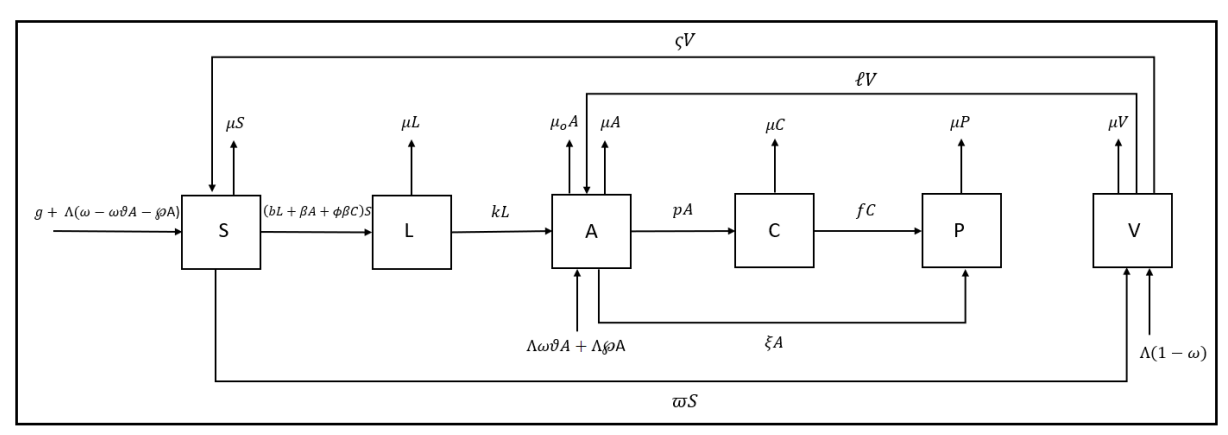


Figure 1
Schematic diagram of the SLACPV model.

$$\frac{dS}{dt} = \Lambda\omega(1 - \vartheta A) - (bL)S + \varsigma V - (\mu + \beta A + \phi \beta C + \varpi)S + g - \Lambda \wp A,$$

$$\frac{dL}{dt} = (\beta A + \phi \beta C)S - \mu L + (bL)S - kL,$$

$$\frac{dA}{dt} = \Lambda\omega \vartheta A - \mu A - \mu_o A - pA - \xi A + kL + \ell V + \Lambda \wp A,$$
(1)

$$\frac{dC}{dt} = pA - fC - \mu C,$$

$$\frac{dP}{dt} = \xi A - \mu P + fC,$$

$$\frac{dV}{dt} = \Lambda(1 - \omega) + \overline{\omega}S - \mu V - \varsigma V - \ell V,$$
(1)

with initial conditions $S(0) = S_0 \ge 0$, $L(0) = L_0 \ge 0$, $A(0) = A_0 \ge 0$, $C(0) = C_0 \ge 0$, $P(0) = P_0 \ge 0$, $V(0) = V_0 \ge 0$. The used model parameters and their biological description are listed in Table 1.

QUALITATIVE ANALYSIS OF THE MODEL

Equilibria of the Model

In this subsection, we evaluate the disease-free equilibrium (DFE) and its stability to study the steady-state behaviour of the model constructed for the HBV disease model. In order to achieve this, we reconsider the following system of equations:

$$\Lambda\omega(1-\vartheta A) - (bL)S + \varsigma V - (\mu + \beta A + \phi \beta C + \varpi)S + g - \Lambda \wp A = 0,$$

$$(\beta A + \phi \beta C)S - \mu L + (bL)S - kL = 0,$$

$$\Lambda\omega\vartheta A - \mu A - \mu_o A - pA - \xi A + kL + \ell V + \Lambda \wp A = 0,$$

$$pA - fC - \mu C = 0,$$

$$\xi A - \mu P + fC = 0,$$

$$\Lambda(1-\omega) + \varpi S - \mu V - \varsigma V - \ell V = 0,$$
(2)

By solving the last equation, we get the following DFE point:

$$\Psi^{0} = (S_{0}, L_{0}, A_{0}, C_{0}, P_{0}, V_{0}) = (S_{0}, 0, 0, 0, 0, 0), \tag{3}$$

where

$$S_0 = \frac{\Lambda\omega + g}{\mu + \varpi}$$

or

$$S_0 = \frac{\Lambda(\omega - 1)}{\varpi}.$$

NUMERICAL RESULT AND DISCUSSION

In this study, we want to examine the effect of HBV on the course of the disease by establishing a new model that takes into account the vertical transmission and migration parameters. For this, we are building a mathematical model with 6 compartments: susceptible population S(t), latent population L(t), acute population A(t), carrier population C(t), protected infected (protective rescued) P(t) and vaccinated population V(t). We use the 4th order Runge-Kutta method to obtain numerical solutions of the model within these compartments. In general, m-order Runge-Kutta method has the following advantages:

• To calculate the approximate value of the Y_{i+1} solution, it is found by calculating only the Y_i value. That's why the one-step method is the most important method of its kind.

• When m = 4, it turns into the method called classical Runge Kutta. This method is the most used method [51].

After performing the numerical solutions of the relevant model, we obtain some results. We use the literature [52, 53] for some of our parameters used in the model and estimate many of them. Our parameter estimates are shown in Table 1:

Table 1Parameters used for the HBV model.

Par.	Biological description	Value	Sources
Λ	Recruitment rate	0.22996	fitted
ς	Rate of decrease in immunity due to the effect of the vaccine	0.1546	fitted
μ	Natural mortality rate	3.4857e-05	[52]
β	Transmission rate	0.001	fitted
ϕ	Reduced transmission rate relative to acute	0.21	fitted
ω	The rate of births without successful insemination	0.003	fitted
	(babies born sick after insemination from mothers)		
ϑ	Infected rate of mothers with HBV acute virus	0.02456	fitted
ϖ	Vaccination rate	0.21	fitted
ξ	Recovery rate of individuals with acute infection	0.17	fitted
f	Recovery rate of individuals in the carrier class	0.2124	fitted
p	Transition rate from Acute to Carrier	0.1349	fitted
μ_o	Death rate from HBV disease	0.1025	fitted
g	Rate of community coming from outside	0.3899	fitted
b	Transition rate from susceptible to latent	0.002	fitted
ℓ	Vaccine leakage rate	0.1356	fitted
k	Transition rate from latent to acute	0.1174	fitted
80	Rate of babies born infected	0.2438	fitted
S(0)	Initial Susceptible population	6000	fitted
L(0)	Initial Latent population	500	fitted
A(0)	Initial Acute population	1497	[53]
C(0)	Initial Carrier population	100	fitted
P(0)	Initial protected infected population	150	fitted
V(0)	Initial Vaccinated population	300	fitted

In this investigation we have performed all numerical results and finding by benefiting from Matlab R2023b Software. Below, we examine the development and change of some populations in our model over time. In Figure 2, we examine the change and development of acute individuals, vaccinated individuals and recovered individuals over time.

In Figure 3, we examine the effect of individuals in the latent phase on acute individuals and recovering individuals. In addition, on these populations, the mortality rate from HBV disease in Figure 4, the recovery rate of individuals with acute infection in Figure 5, the transmission rate in Figure 6 and in Figure 7 we also examine the change in vaccination rate over time.

It has been observed that when the number of vaccinated individuals is kept at a minimum level, the number of infected individuals decreases, and the number of protected individuals reaches a maximum.

The Protected Infected population increased as a result of the decrease in Latent and Acute individuals towards the end of the process. This positively affected the course of the disease.

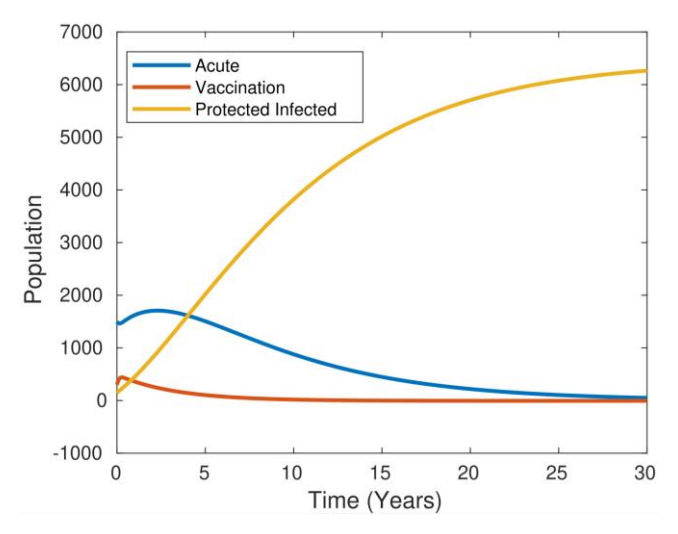


Figure 2Status of Acute, Vaccination, Protected Infected populations relative to each other.

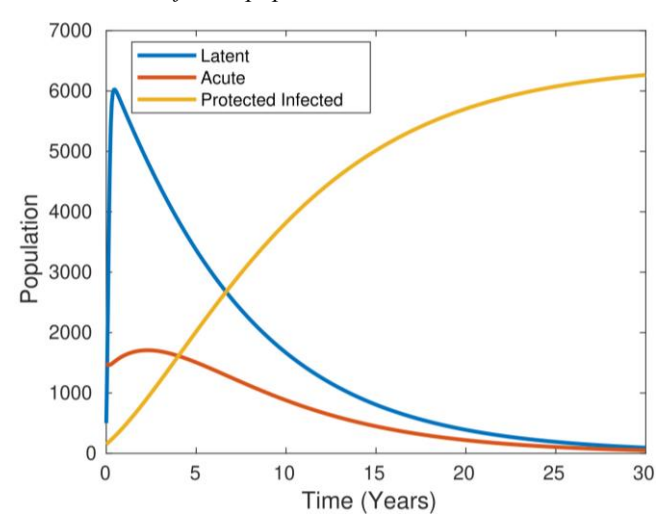


Figure 3 *Latent Status of Latent, Acute, Protected Infected populations relative to each other.*

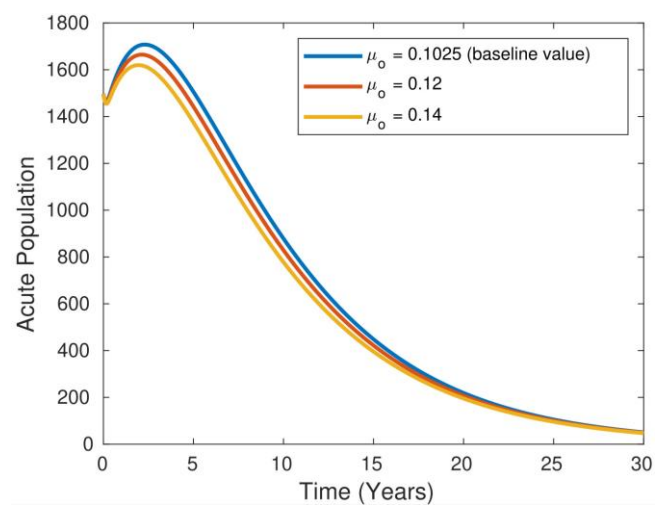


Figure 4
The mortality rate from HBV disease.

The graph in Figure 4 depicts the mortality rates attributable to HBV (Hepatitis B Virus) over a specific period of time (30 years). Trends in the graph indicate the change in death rates from HBV

disease over time. The reasons for sudden decreases or fluctuations in a certain period in the graph are; epidemics, changes in health policies or difficulties in access. A clear downward trend is observed in the death rates caused by HBV disease over time. This decline is generally due to factors such as the expansion of vaccination programs, improvements in treatment options, and effective implementation of health education.

The graph in Figure 5 shows the recovery rates of individuals with acute infectious disease over 30 years. Examining the changes in the trends in the graph over time is important for the management and treatment of the disease. It is necessary to determine the underlying reasons for a significant increase or decrease in recovery rates in a certain period. These reasons include factors such as the nature of the disease, treatment methods used, access to healthcare and patients' lifestyle. Additionally, information can be obtained about the change in recovery rates by demographic characteristics by examining the change in recovery rates. Evaluating the impact of factors such as age, gender, geographical location or underlying health condition on recovery rates is important to understand how the disease is affected among different groups. There is a clear trend in the graph, so appropriate strategies are being developed to understand the reasons for this trend and increase recovery rates. This is a critical step for improving health policies and health services and improving patients' quality of life.

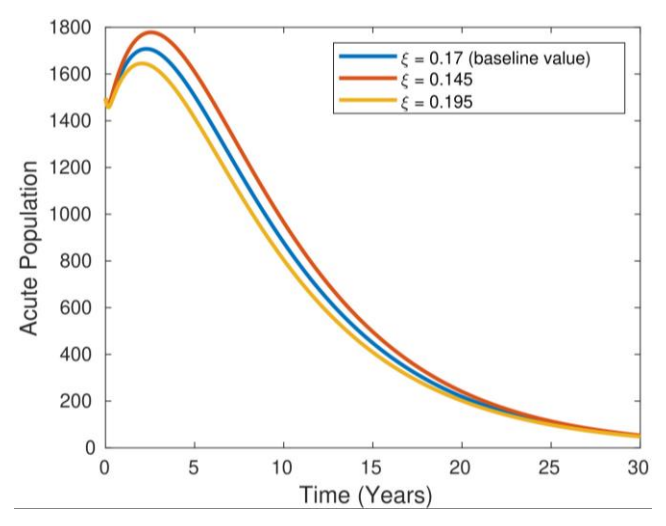


Figure 5 *The recovery rate of individuals with acute infection disease.*

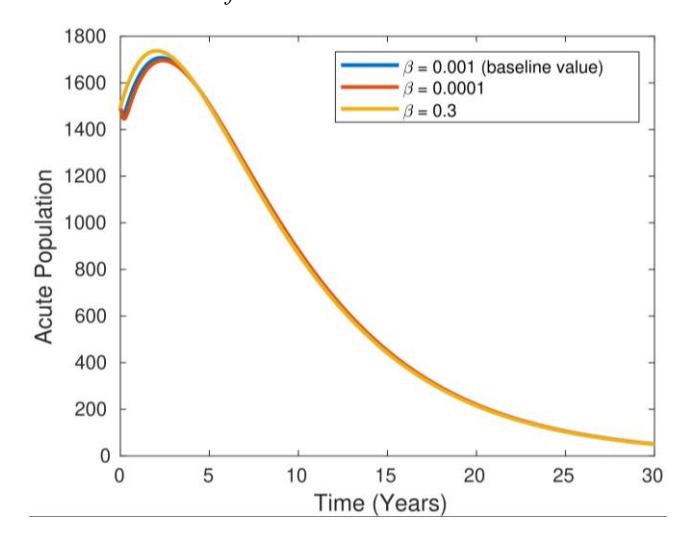


Figure 6 *The transmission rate of the HBV virus.*

The graph in Figure 6 depicts the change in the transmission rate of the HBV virus over a certain

period of time. An important point is that the continuous, graphical changes increase over time. For example, it is necessary to determine the underlying causes of sudden increases or decreases in transactions over a certain period. These include factors such as epidemics, changes in health policies, changes in the development of society, or a new treatment or vaccine. In addition, a clear formation is seen in the graph, and it is necessary to examine how the events progress. It should also be determined how long the increases or decreases continue over 30 years and what factors they depend on. The results of such analyzes should evaluate health policies and interventions. Finally, appropriate strategies are developed to understand the reasons for this trend and prevent similar situations from occurring in the future. These strategies control the spread of the disease.

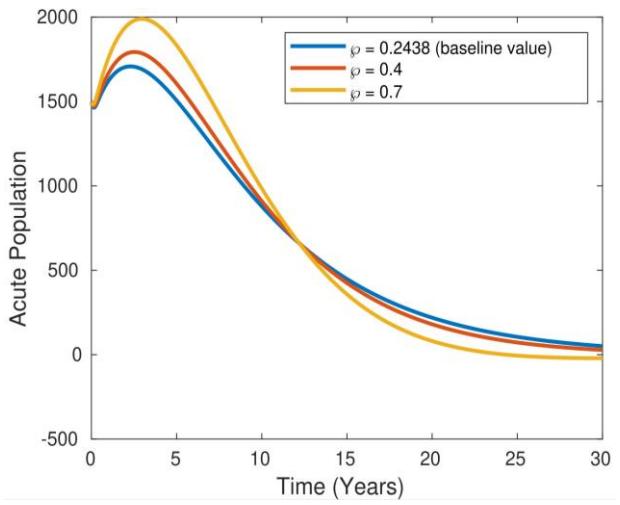


Figure 7
Rate of babies born infected.

The graph in Figure 7 shows the change in the rate of infected babies over time over 30 years. It is important to know the reasons behind the increase or decrease in the rates of babies born in certain periods of these data. The reason for the increase at the beginning of this process is due to the high vertical transmission rate of HBV. In the middle of the process, a clear intersection can be seen on the graph. The reason for this intersection is that the vertical transmission of HBV is under control. After this point, a significant decrease is observed in the graph. Appropriate strategies are developed to understand the reasons for this trend and prevent similar situations from occurring in the future. As a result of these strategies, vertical transmission of the disease is controlled. As a result of these analyses, the number of healthy babies is expected to increase.

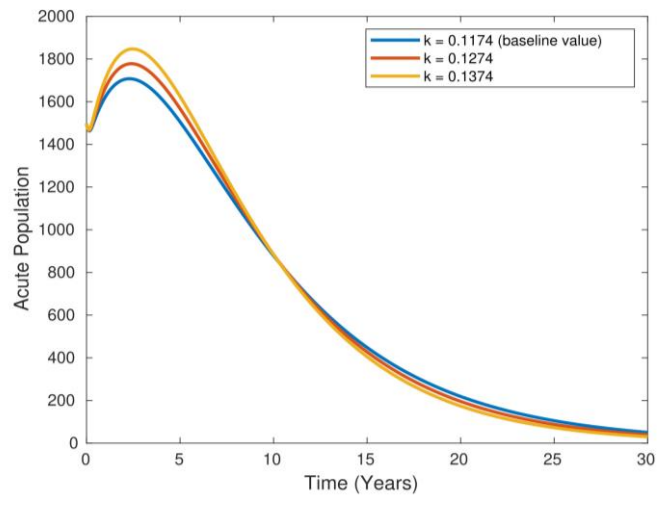


Figure 8 *Acute population dynamics according to various values of k.*

CONCLUSION

In this paper, we have developed a new Hepatitis-B mathematical model containing a vertical transmission from mothers to newborn babies. Also, we have evaluated the disease-free equilibrium point. In the numerical simulation section of the article presents the results obtained throughout our study process. The effectiveness of this model and its performance by developing a new expanding structure that models Hepatitis-B by selecting the appropriate effect for the model. In the modelling of the results we obtained, it is seen that the course of Hepatitis-B disease is modelled by predicting it and predictions about its process are obtained. Non-negative solutions have been obtained to ensure biological augmentation of our system of equations of the model.

Ethical Statement

This study is an original research article designed and developed by the authors.

Author Contributions

```
Research Design (CRediT 1) M.Y. (%60) – N.B.B. (%15) – K.A. (%15) – F.N.Ö. (%15) 
Data Collection (CRediT 2) M.Y. (%10) – N.B.B. (%30) – K.A. (%30) – F.N.Ö. (%30) 
Research - Data Analysis - Validation (CRediT 3-4-6-11) M.Y. (%25) – N.B.B. (%25) – K.A. (%25) – F.N.Ö. (%25) 
Writing the Article (CRediT 12-13) M.Y. (%25) – N.B.B. (%25) – K.A. (%25) – F.N.Ö. (%25)
```

Writing the Article (CRediT 12-13) M.Y. (%25) – N.B.B. (%25) – K.A. (%25) – F.N.O. (%25) Revision and Improvement of the Text (CRediT 14) M.Y. (%25) – N.B.B. (%25) – K.A. (%25) – F.N.Ö. (%25)

Financing

This research was supported by Scientific and Technological Research Council of Türkiye (TÜBİTAK) under the undergraduate research project.

Conflict of Interest

The authors declare no conflict of interest.

Data Availability Statement

No Data associated in the manuscript.

Sustainable Development Goals (SDG)

Sustainable Development Goals: 3 Good health and well-being

REFERENCES

- [1] S.M. Ciupe, R.M. Ribeiro, P.W. Nelson, G. Dusheiko, A.S. Perelson, The role of cells refractory to productive infection in acute hepatitis B viral dynamics, *Proceedings of the National Academy of Sciences*. 104(12) (2007), 5050-5055. doi: 10.1073/pnas.0603626104
- [2] F.F. Chenar, Y.N. Kyrychko, K.B. Blyuss, Mathematical model of immune response to hepatitis B, *Journal of Theoretical Biology*. 447 (2018), 98-110. doi: 10.1016/j.jtbi.2018.03.025
- [3] Acıbadem Yayın Kurulu, (2021). https://www.acibadem.com.tr/ilgi-alani/hepatit-b/ (erişim 10 Mayıs 2024).
- [4] A. Çilli, K. Ergen, Salgın hastalıkların tahmininde kullanılan SI ve SIS modellerin uygulamaları, Bitlis Eren Üniversitesi Fen Bilimleri Dergisi. 8(3) (2019), 755-761. doi: 10.17798/bitlisfen.522533
- [5] A. Costa, M. Pires, R. Resque, S.S.M.S. Almeida, Mathematical modeling of the infectious diseases: key concepts and applications, *Journal of Infectious Diseases and Epidemiology*. 7(5) (2021), 209. doi: 10.23937/2474-3658/1510209
- [6] U.S. Bashir, A. Umar, Mathematical analysis of hepatitis B virus model with interventions in Taraba state, Nigeria. *International Journal of Development Mathematics (IJDM)*. 1 (1) (2024). doi: 10.62054/ijdm/0101.14
- [7] A. Kiemtore, W.O. Sawadogo, I. Zangré, P.O.F. Ouedraogo, I. Mouaouia, Estimation of parameters for the mathematical model of the spread of hepatitis B in Burkina Faso using grey wolf optimizer, *International Journal of Analysis and Applications*. 22 (2024), 48-48. doi: 10.28924/2291-8639-22-2024-48
- [8] D.M. Li, B. Chai, A dynamic model of hepatitis B virus with drug-resistant treatment, *AIMS Mathematics*. 5(5) (2020), 4734-4753. doi: 10.3934/math.2020303
- [9] P. Liu, A. Din, R. Zarin, Numerical dynamics and fractional modeling of Hepatitis B virus model with non-singular and non-local kernels, *Results in Physics*. 39 (2022), 105757. doi: 10.1016/j.rinp.2022.105757
- [10] A.M. Elaiw, M.A. Alghamdi, S. Aly, Hepatitis B virus dynamics: modeling, analysis, and optimal treatment scheduling, *Discrete Dynamics in Nature and Society*. 1 (2013). doi: 10.1155/2013/712829
- [11] T. Khan, S. Ahmad, G. Zaman, Modeling and qualitative analysis of a hepatitis B epidemic model, *Chaos: An Interdisciplinary Journal of Nonlinear Science*. 29(10) (2019). doi: 10.1063/1.5111699
- [12] M.J. de Villiers, I. Gamkrelidze, T.B. Hallett, S. Nayagam, H. Razavi, D. Razavi-Shearer, Modelling hepatitis B virus infection and impact of timely birth dose vaccine: a comparison of two simulation models, *PLoS One.* 15 (8) (2020). e0237525 doi: 10.1371/journal.pone.0237525
- [13] D. Otoo, I.O. Abeasi, S. Osman, E.K. Donkoh, Mathematical modeling and analysis of the dynamics of hepatitis b with optimal control, *Communications in Mathematical Biology and Neuroscience*. (2021). doi: 10.28919/cmbn/5733
- [14] L.C. Cardoso, R.F. Camargo, F.L.P. dos Santos, J.P.C. Dos Santos, (2021). Global stability analysis of a fractional differential system in hepatitis B. Chaos, *Solitons & Fractals*. 143 (2021). 110619. doi: 10.1016/j.chaos.2020.110619
- [15] M. Farman, A. Ahmad, H. Muslim, M.O. Ahmad, (2019). Dynamical behavior of hepatitis B fractional-order model with modeling and simulation, *Journal of Biochemical Technology*. 10(3) (2019), 11-17.
- [16] V. Reinharz, Y. Ishida, M. Tsuge, K. Durso-Cain, T.L. Chung, C. Tateno, et al. Understanding hepatitis B virus dynamics and the antiviral effect of interferon alpha treatment in humanized chimeric mice, *Journal of Virology*. 95(14) (2021), 10-1128. doi: 10.1128/jvi.00492-20

- [17] A.M. Ortega-Prieto, C. Cherry, H. Gunn, M. Dorner, In vivo model systems for hepatitis B virus research, *ACS Infectious Diseases*. 5(5) (2018), 688-702. doi: 10.1021/acsinfecdis.8b00223
- [18] T. Khan, F.A. Rihan, M. Ibrahim, S. Li, A.M. Alamri, S.A. AlQahtani, Modeling different infectious phases of hepatitis B with generalized saturated incidence: An analysis and control, *Mathematical Biosciences and Engineering*. 21(4) (2024), 5207-5226. doi: 10.3934/mbe.2024230
- [19] A. Friedman, N. Siewe, Chronic hepatitis B virus and liver fibrosis: A mathematical model, *PLoS One*. 13(4) (2018), e0195037. doi: 10.1371/journal.pone.0195037
- [20] O. Oludoun, O. Adebimpe, J. Ndako, M. Adeniyi, O. Abiodun, B. Gbadamosi, The impact of testing and treatment on the dynamics of Hepatitis B virus, *F1000Research*. 10 (2021). doi: 10.12688/f1000research.72865.1
- [21] R. Ikram, A. Khan, M. Zahri, A. Saeed, M. Yavuz, P. Kumam, Extinction and stationary distribution of a stochastic COVID-19 epidemic model with time-delay, *Computers in Biology and Medicine*. 141 (2022), 105115. doi: 10.1016/j.compbiomed.2021.105115
- [22] I.U. Haq, N. Ali, and K. S. Nisar, An optimal control strategy and Grünwald-Letnikov finite-difference numerical scheme for the fractional-order COVID-19 model, *Mathematical Modelling and Numerical Simulation with Applications*. 2(2) (2022), 108-116. doi: 10.53391/mmnsa.2022.009
- [23] H. Joshi, B.K. Jha, and M. Yavuz, Modelling and analysis of fractional-order vacci-nation model for control of COVID-19 outbreak using real data, *Mathematical Biosciences and Engineering*. 20(1) (2022), 213-240. doi: 10.3934/mbe.2023010
- [24] H. Joshi, M. Yavuz, S. Townley, and B. K. Jha, Stability analysis of a non-singular fractional-order covid-19 model with nonlinear incidence and treatment rate, *Physica Scripta*. 98(4) (2023), 045216. doi: 10.1088/1402-4896/acbe7a
- [25] M. Yavuz, F.Ö. Coşar, F. Günay, F.N. Özdemir, A new mathematical modeling of the COVID-19 pandemic including the vaccination campaign, *Open Journal of Modelling and Simulation*. 9(3) (2021), 299-321. doi: 10.4236/ojmsi.2021.93020
- [26] A.S. Waziri, E.S. Massawe, O.D. Makinde, Mathematical modelling of HIV/AIDS dynamics with treatment and vertical transmission, *Journal Applied Mathematics*. 2(3) (2012), 77-89. doi: 10.5923/j.am.20120203.06
- [27] D. Wodarz, M.A. Nowak, Mathematical models of HIV pathogenesis and treatment, *BioEssays*. 24(12) (2002), 1178-1187. doi: 10.1002/bies.10196
- [28] T.K. Ayele, E.F.D. Goufo, S. Mugisha, Mathematical modeling of HIV/AIDS with optimal control: a case study in Ethiopia, *Results in Physics*. 26 (2021), 104263. doi: 10.1016/j.rinp.2021.104263
- [29] S. Wang, Y. Pan, Q. Wang, H. Miao, A.N. Brown, L. Rong, Modeling the viral dynamics of SARS-CoV-2 infection, *Mathematical Biosciences*. 328 (2020), 108438. doi: 10.1016/j.mbs.2020.108438
- [30] S.M. Ciupe, N. Tuncer, Identifiability of parameters in mathematical models of SARS-CoV-2 infections in humans, *Scientific Reports*. 12(1) (2022), 14637. doi: 10.1038/s41598-022-18683-x
- [31] G. Gonzalez-Parra, D. Martínez-Rodríguez, R.J. Villanueva-Micó, Impact of a new SARS-CoV-2 variant on the population: A mathematical modeling approach, *Mathematical and Computational Applications*, 26(2) (2021). 25. doi: 10.3390/mca26020025
- [32] A. Atifa, M.A. Khan, K. Iskakova, F.S. Al-Duais, I. Ahmad, Mathematical modeling and analysis of the SARS-Cov-2 disease with reinfection, *Computational Biology and Chemistry*. 98 (2022), 107678. doi: 10.1016/j.compbiolchem.2022.107678
- [33] M. Yavuz, F. Özköse, M. Akman, Z.T. Tastan, A new mathematical model for tuberculosis

- epidemic under the consciousness effect, *Mathematical Modelling and Control*. 3(2) (2023), 88-103. doi: 10.3934/mmc.2023009
- [34] E.D. Ginting, D. Aldila, I.H. Febriana, A deterministic compartment model for analyzing tuberculosis dynamics considering vaccination and reinfection, *Healthcare Analytics*. 5 (2024), 100341. doi: 10.1016/j.health.2024.100341
- [35] J. Wang, G. Lyu, Analysis of an age-space structured tuberculosis model with treatment and relapse, *Studies in Applied Mathematics*. 153(1) (2024), e12700. doi: 10.1111/sapm.12700
- [36] E.M. Delgado Moya, J.A. Ordoñez, F. Alves Rubio, M. Niskier Sanchez, R.B. de Oliveira, R. Volmir Anderle, D. Rasella, A Mathematical Model for the Impact of 3HP and Social Programme Implementation on the Incidence and Mortality of Tuberculosis: Study in Brazil, *Bulletin of Mathematical Biology*. 86(6) (2024), 1-25. doi: 10.1007/s11538-024-01285-1
- [37] A.A. Gebremeskel, H.E. Krogstad, Mathematical modelling of endemic malaria transmission, *American Journal of Applied Mathematics*. 3(2) (2015), 36-46. doi: 10.11648/j.ajam.20150302.12
- [38] S.I. Oke, M.M. Ojo, M.O. Adeniyi, M.B. Matadi, Mathematical modeling of malaria disease with control strategy, *Communications in Mathematical Biology and Neuroscience*. (2020), Article-ID: 43. doi: 10.28919/cmbn/4513
- [39] M. Osman, I. Adu, Simple mathematical model for malaria transmission, *Journal of Advances in Mathematics and Computer Science*. 25(6) (2017), 1-24. doi: 10.9734/JAMCS/2017/37843
- [40] S. Olaniyi, O.S. Obabiyi, Mathematical model for malaria transmission dynamics in human and mosquito populations with nonlinear forces of infection, *International Journal of Pure and Applied Mathematics*. 88(1) (2013), 125-156. doi: http://dx.doi.org/10.12732/ijpam.v88i1.10
- [41] P. A. Naik, Z. Eskandari, M. Yavuz, & Z. Huang, Bifurcation results and chaos in a two-dimensional predator-prey model incorporating Holling-type response function on the predator, *Discrete and Continuous Dynamical Systems-S.* (2024). doi: 10.3934/dcdss.2024045
- [42] D. Ghosh, P.K. Santra, G.S. Mahapatra, A three-component prey-predator system with interval number, *Mathematical Modelling and Numerical Simulation with Applications*. 3(1) (2023), 1-16. doi: 10.53391/mmnsa.1273908
- [43] P.A. Naik, Z. Eskandari, H.E. Shahkari, K.M. Owolabi, Bifurcation analysis of a discrete-time prey-predator model, *Bulletin of Biomathematics*. 1(2) (2023), 111-123. doi:10.59292/bulletinbiomath.2023006
- [44] J. Danane, M. Yavuz, M. Yıldız, Stochastic modeling of three-species Prey–Predator model driven by L'evy Jump with Mixed Holling-II and Bedding-ton–DeAngelis functional responses, *Fractal and Fractional*. 7(10) (2023), 751.doi: 10.3390/fractalfract7100751
- [45] O.M. Tessa, Mathematical model for control of measles by vaccination. *In Proceedings of Mali Symposium on Applied Sciences*, 2006: pp. 31-36.
- [46] K.A.M. Gaythorpe, C.L. Trotter, B. Lopman, M. Steele, A.J.K. Conlan, Norovirus transmission dynamics: a modelling review, *Epidemiology & Infection*. 146(2) (2018), 147-158.doi:10.1017/S0950268817002692
- [47] I.U. Haq., M. Yavuz, N. Ali, A. Akgül, A SARS-CoV-2 fractional-order mathematical model via the modified Euler method, *Mathematical and Computational Applications*. 27(5) (2022), 82. doi: 10.3390/mca27050082
- [48] N. Kar, N. Ozalp, A fractional mathematical model approach on glioblas-toma growth: tumor visibility timing and patient survival, *Mathematical Modelling and Numerical Simulation with Applications*. 4(1) (2024), 66-85. doi:10.53391/mmnsa.1438916
- [49] B. Bolaji, T. Onoja, C. Agbata, B. I. Omede, U. B. Odionyenma, Dynamical analysis of HIV-TB co-infection transmission model in the presence of treatment for TB, *Bulletin of Biomathematics*. 2(1) (2024), 21-56. doi:10.59292/bulletinbiomath.2024002

- [50] F. Evirgen, E. Uçar, S. Uçar, N. Özdemir, Modelling influenza A disease dynamics under Caputo-Fabrizio fractional derivative with distinct contact rates, *Mathematical Modelling and Numerical Simulation with Applications*. 3(1) (2023), 58-73. doi:10.53391/mmnsa.1274004
- [51] N.E. Binbay, H.B. Gümgüm, Block denklemlerinin nümerik yöntemlerle çözümü, Fen Bilimleri ve Matematik Alanında Araştırma Makaleleri. (2019), 155-183.
- [52] https://data.tuik.gov.tr/Bulten/Index?p=Olum-ve-Olum-Nedeni-Istatistikleri-2021-45715#:~:text=Bin%20ki%C5%9Fi%20ba%C5%9F%C4%B1na%20d%C3%BC%C5%9Fen%20%C3%B6l%C3%BCm,ba%C5%9F%C4%B1na%206%2C7%20%C3%B6l%C3%BCm%20d%C3%BC%C5%9Ft%C3%BC. Access Date: 11 April 2024
- [53] https://www.cdc.gov/hepatitis/statistics/2015surveillance/index.htm#tabs-5-3 Access Date: 11 April 2024
- [54] Ö.A. Gümüs, Q. Cui, G.M. Selvam, A. Vianny, Global stability and bifurcation analysis of a discrete time SIR epidemic model, *Miskolc Mathematical Notes*. 23(1) (2022), 193-210. doi: 10.18514/mmn.2022.3417
- [55] S.H. Streipert, G.S. Wolkowicz, An augmented phase plane approach for discrete planar maps: Introducing next-iterate operators. *Mathematical Biosciences*, 355 (2023), 108924. doi: 10.1016/j.mbs.2022.108924
- [56] L. Boulaasair, H. Bouzahir, M. Yavuz, Global mathematical analysis of a patchy epidemic model, *An International Journal of Optimization and Control: Theories & Applications (IJOCTA)*. 14(4) (2024), 365-377. doi: 10.11121/ijocta.1558
- [57] S. Bhatter, S. Kumawat, B. Bhatia, S.D. Purohit, Analysis of COVID-19 epidemic with intervention impacts by a fractional operator, *An International Journal of Optimization and Control: Theories & Applications (IJOCTA)*. 14 (3) (2024), 261-275. doi: 10.11121/ijocta.1515



Vol: 7 No:2 Year: 2025

Araştırma Makalesi/Research Article

e-ISSN: 2667-7989

https://doi.org/10.47112/neufmbd.2025.88

Fibonacci Kodlaması ve k-Zeckendorf Gösterimleri ile Yeni Bir Genetik Algoritma Modeli

Yunus Emre GÖKTEPE 1* 📵 Fikri KÖKEN 1 📵 Halime ERGÜN 1 📵

¹ Necmettin Erbakan University, Seydisehir Ahmet Cengiz Faculty of Engineering, Department of Computer Engineering, Konya, Türkiye

Makale Bilgisi

Geliş Tarihi: 03.11.2024 Kabul Tarihi: 15.12.2024 Yayın Tarihi: 31.08.2025

Anahtar Kelimeler:

Fibonacci sayıları, Genetik algoritma, Optimizasyon, Zeckendorf gösterimleri.

ÖZET

Bu çalışma, karmaşık optimizasyon problemlerini çözmenin verimliliğini artırmak için Fibonacci kodlamasını ve k-Zeckendorf gösterimlerini kullanan yeni bir genetik algoritma (GA) modeli sunmaktadır. Geleneksel GA, kromozomları temsil etmek için ikili veya sayısal kodlamayı kullanır, ancak bu çalışma Fibonacci dizisine ve Zeckendorf teoremine dayanan alternatif bir yaklaşım önermektedir. Bu gösterimleri GA çerçevesine dahil ederek, model arama sürecini iyileştirmeyi ve daha etkili çözümlere yol açmayı amaçlamaktadır. Bu yaklaşımın önemi, GA'ların performansını etkileyen kritik bir faktör olan kromozom gösterimini iyileştirme yeteneğinde yatmaktadır. Yeni kodlama şemaları, algoritmanın keşif ve yararlanma aşamalarını geliştirerek, optimum çözümlere doğru daha verimli bir yakınsama sağlar. Model iki zorlu problemde test edilmiştir: yüksek dereceli bir polinomun optimum değerini bulma ve dikdörtgen prizmanın hacmini optimize etme. Sonuçlar, önerilen yöntemin standart GA'dan daha başarılı olduğunu göstermektedir. Bu araştırma, alternatif kromozom gösterimlerinin GA performansını önemli ölçüde etkileyebileceğini göstermektedir. Ayrıca, özellikle karmaşık polinom denklemleri ve geometrik kısıtlamaları içeren optimizasyon problemleri için yeni bir çerçeve sağlar. GA'ların daha faklı optimizasyon problemlerine uygulanabileceğini gösterir ve hesaplamalı matematik ve mühendislik tasarımındaki potansiyelini vurgular.

A Novel Genetic Algorithm Model with Fibonacci Encoding and k-Zeckendorf Representations

Article Info

ABSTRACT

Received: 03.11.2024 Accepted: 15.12.2024 Published: 31.08.2025

Keywords:

Fibonacci numbers, Genetic algorithm, Optimization, Zeckendorf representations. This study presents a new genetic algorithm (GA) model that uses Fibonacci coding and k-Zeckendorf representations to improve the efficiency of solving complex optimization problems. Traditional GA uses binary or numerical coding to represent chromosomes, but this study proposes an alternative approach based on Fibonacci sequence and Zeckendorf theorem. By incorporating these representations into the GA framework, it aims to improve the model search process and lead to more efficient solutions. The importance of this approach lies in its ability to improve the chromosome representation, which is a critical factor affecting the performance of GAs. The new coding schemes improve the exploration and exploitation phases of the algorithm, allowing for more efficient convergence towards optimal solutions. The model is tested on two challenging problems: finding the optimum value of a high-degree polynomial and optimizing the volume of a rectangular prism. The results show that the proposed method outperforms the standard GA. This research shows that alternative chromosome representations can significantly affect GA performance. It also provides a new framework for optimization problems, especially those involving complex polynomial equations and geometric constraints. It shows that GAs can be applied to more diverse optimization problems and highlights their potential in computational mathematics and engineering design.

To cite this article:

Göktepe, Y.E., Köken, F. & Ergün, H. (2025). A novel genetic algorithm model with Fibonacci encoding and *k*-Zeckendorf representations. *Necmettin Erbakan University Journal of Science and Engineering*, 7(2), 228-244. https://doi.org/10.47112/neufmbd.2025.88

*Corresponding Author: Yunus Emre Göktepe, ygoktepe@erbakan.edu.tr



INTRODUCTION

Inspired by the principles of natural selection and genetics, genetic algorithms (GAs) operate by iteratively generating a population of potential solutions represented as chromosomes. These chromosomes undergo selection, crossover, and mutation operations to produce new offspring that inherit beneficial traits from their parents. Through this iterative process, the population evolves over generations, gradually improving the quality of solutions until an optimal or near-optimal solution is found [1].

GA offers a robust approach to optimization problems, offering approximate solutions and addressing challenges that may arise during the search process. Optimization refers to the minimization (or maximization) of a specific objective function of multiple decision variables while satisfying functional constraints. Mathematical optimization involves selecting the best element from a given set of available alternatives based on specific criteria. In its simplest form, an optimization problem entails systematically selecting input values from a given set and calculating the function's value to either maximize or minimize a real function. Optimization involves the use of specific techniques to evaluate the most cost-effective and efficient solution for a problem or process design [2–4]. GAs have been widely implemented in various domains for optimization.

A GA-based optimization model was proposed by Srimathi et al. to address resource constraints and activity conflicts in construction projects. Researchers from different fields use genetic algorithms to solve optimization problems. The model uses the selection, mutation, and crossover processes of GA to create a conflict-free schedule. It is noted that the proposed model can be adapted to optimize construction programs and consider additional factors [5].

Ulkir and Akgün investigated the surface roughness of the samples fabricated from polyethylene terephthalate glycol (PETG). They generated a dataset of 25 samples by varying four factors at three levels using a 3D printer. Subsequently, they trained a bidirectional feedback neural network (CFNN) with this dataset and optimized the parameters of the CFNN using genetic algorithms (GA). This study primarily aims to predict and optimize surface roughness in additive manufacturing (AM) using machine learning (ML) techniques [6].

Genetic algorithms represent individuals within a population as chromosomes and apply genetic operators such as selection, crossover, and mutation based on their fitness values. In this way, the population gradually approaches the best solution over time. The performance of the genetic algorithms depends on the choice of chromosome representation. Chromosome representation is one of the most important components of genetic algorithms because it reflects the characteristics of the problem domain under investigation and influences the effectiveness of genetic operators. The most commonly used method for chromosome representation uses bit strings or numerical values. Therefore, there is a need to explore alternative chromosome representation methods.

An optimization method using Fibonacci and genetic algorithm has been proposed to develop a method to reduce maintenance costs in wind turbines. In only the first layer of their proposed model, the researchers used the Fibonacci search algorithm to optimize the number of maintenances in a given lifetime. In the second layer, they applied a genetic algorithm to determine preventive maintenance times and which component to preserve in each preventive maintenance activity [7].

Fibonacci numbers have found applications in various fields, including plant biology, animal population dynamics, art, and music. In mathematics and computer science, Fibonacci numbers possess intriguing properties and are used in diverse applications. They have been employed in image processing, data compression, encryption, and coding theory [8–10]. In computer science, Fibonacci numbers play a significant role in the analysis of algorithm complexity and the design of efficient data

structures. Their wide range of applications has made them a popular topic of study in mathematics and computer science [11,12].

Genetic algorithm and Fibonacci Q-matrix were used for the image encryption problem and an algorithm consisting of diffusion-mixing-diffusion-optimization layers was proposed. Experimental results and security analyses demonstrate that the algorithm exhibits not only high security but also a certain level of robustness suitable for practical applications, along with real-time performance [13].

The objective of this study was to examine the impact of representing chromosomes using Fibonacci numbers on the performance of genetic algorithms. To achieve this, we tested the proposed methods on two different problems. The first problem involved finding the roots of a fourth-degree polynomial, whereas the second problem involved maximizing the volume by bending the edges of a flat plate. These problems are commonly used in the genetic algorithm literature. We compared the performance of the proposed methods with that of the standard genetic algorithm. In addition, we analysed the effect of chromosome length and the parameter k on performance. The results of our study demonstrate that representing chromosomes using Fibonacci numbers yields better results than the standard genetic algorithm.

In the literature, no study has examined Fibonacci integration sequences into chromosomal representations used in genetic algorithms. This novel approach remains unexplored and presents a potential area for research within the field of computational genetics. This study fills this research gap by showcasing the performance enhancement achieved using Fibonacci numbers in chromosome representation. The contributions of this study can be summarized as follows: Proposal of a genetic algorithm model that incorporates Fibonacci numbers and Zeckendorf and *k*-Zeckendorf representations. Definition of the components of the proposed model, including chromosome representation, fitness evaluation, chromosome selection, crossover, and mutation. Application of the proposed model to various optimization problems and comparison of the results with those obtained using traditional genetic algorithm methods. The experimental findings demonstrate the superior accuracy of the proposed model compared with alternative approaches.

MATERIALS AND METHODS

In this section, an in-depth explanation of Fibonacci base and Zeckendorf representations is given and how these values are calculated is shown. Also, the structure of the Genetic algorithm is mentioned and the proposed method is introduced in detail.

Fibonacci Representations

It is known [14] that the Fibonacci sequence $\{F_n\}$ is defined recursively as follows:

$$F_n = \begin{cases} 0, & \text{if } n = 0\\ 1, & \text{if } n = 1\\ F_{n-1} + F_{n-2}, & \text{if } n > 1 \end{cases}$$
 (1)

Leaving the first Fibonacci number, the remaining 12 numbers and their corresponding indices are as follows:

Table 1 *The nth Fibonacci numbers.*

Every positive integer N can be written as

$$N = F_{k_1} + F_{k_2} + \dots + F_{k_r}, \qquad k_1 > k_2 > \dots > k_r \ge 2 \tag{2}$$

which is called a Fibonacci representation of N. There are other ways of representing N as the Fibonacci representation. Zeckendorf's theorem is a reasonably well-known result concerning the possibility of writing positive integers as a sum of distinct Fibonacci numbers provided the k_j satisfy the inequalities $k_j - k_{j+1} \ge 2$, $(j = 1, 2, ..., r - 1), k_r \ge 2$. This representation is called Zeckendorf's Fibonacci representation [15,16].

The most well-known method for representing non-negative integers using just the digits {0,1} is of course by way of the minimal system. However, there are other ways of representing integers using just {0,1} for which the corresponding situation is not quite so obvious. One such system is Zeckendorf's Fibonacci representation.

Zeckendorf's Representation with Fibonacci Bases

Zeckendorf's theorem states that every positive integer can be represented uniquely as the sum of one or more distinct Fibonacci numbers. This representation is achieved in such a way that the sum excludes any two consecutive Fibonacci numbers [15].

The Zeckendorf theorem presents an alternative to the binary number system, which is useful in applications such as data transmission and compression [17].

Zeckendorf's Fibonacci encoding uses Zeckendorf's Fibonacci representation: Any positive integer $N = (...d_3d_2d_1)_{fib}$ can be represented as follows:

$$N = \sum_{i=1}^{n} d_i F_{k_i} \tag{3}$$

where F_{k_i} , $k_1 \ge 2$ is the k_i^{th} Fibonacci number, $k_i - k_{i-1} \ge 2$, $d_i \in \{0,1\}$, $d_n = 1$. The Zeckendorf's Fibonacci coding is denoted by $N = (d_i)_{fib}$.

It is seen that for $N \le 34$, an 8-bit $\{0,1\}$ array is generated. For example, the Zeckendorf's Fibonacci representation for N = 23 is 21 + 0 + 0 + 0 + 0 + 2 + 0 and $N = (1000010)_{fib}$.

A number representation system is typically most useful when it has a unique representation for every integer. Zeckendorf's Fibonacci encoding achieves this by avoiding consecutive 1's. However, we saw that although each number does have such a sum, some numbers have more than one sum, and so their representation is not unique.

Let's slightly modify Zeckendorf's Fibonacci encoding to give a new form {0,1} with a single representation.

In [18] a Zeckendorf-Wythoff sequence is defined, where each row is a Fibonacci sequence. The Zeckendorf-Wythoff sequence is designed to divide positive integers into columns ordered by their Zeckendorf representation. If the largest (smallest) Fibonacci number used in the Zeckendorf representation of N is F_k , N starts (ends) with F_k . The k column of the Zeckendorf-Wythoff sequence is composed of the integers N in ascending order, whose Zeckendorf representation ends with F_{k+1} .

Each row of the sequence is composed of N integers with Zeckendorf representations of the same form, i.e., any two consecutive numbers in the row have the indices of the Fibonacci numbers F_k corresponding to the digits used in the Zeckendorf representations with a difference of one [15,16].

The Zeckendorf-Wythoff sequence arranged in 12 columns is shown in Table 2 because we used 8-, 12-, and 14-bit arrays. The 14-bit representation is omitted for brevity.

 Table 2

 Zeckendorf-Wythoff sequence

$w_{i,j}$	1	2	3	4	5	6	7	8	9	10	11	12
$\overline{w_{1,j}}$	1	2	3	5	8	13	21	34	55	89	144	233
$w_{2,j}$	4	7	11	18	29	47	76	123	199	322	521	843
$w_{3,j}$	6	10	16	26	42	68	110	178	288	466	754	1220
:	:	:	:	:	:	:	:	:	:	:	:	:
$w_{13,j}$	33	54	87	141	228	369	597	966	1563	2529	4092	6621
:	:	:	:	:	:	:	:	÷	:	:	÷	:
$w_{56,j}$	145	235	380	615	995	1610	2605	4215	6820	11035	17855	28890
	:	:	:	:	:	:	:	:	:	:	:	:

Some general properties of the sequence are revealed from the Zeckendorf representations. Let $N = w_{ij}$ be the element in the i -th row and j -th column of the Zeckendorf-Wythoff sequence. The first element in column j is considered $w_{1,j} = F_{j+1}$ and the Zeckendorf representation of each integer listed in column j results in F_{j+1} . It can be exemplified:

$$w_{2,j} = F_{j+1} + F_{j+3}$$

$$w_{13,j} = F_{j+1} + F_{j+3} + F_{j+5} + F_{j+7}$$

$$w_{56,j} = F_{j+1} + F_{j+11}$$
(4)

Moreover, each of the indices of the Fibonacci numbers used in the Zeckendorf representation of $w_{i,j+1}$ is the sum of the Fibonacci numbers with one more index than the corresponding indices in the Zeckendorf representation of $w_{i,j}$.

Each row can be seen as a generalized Fibonacci sequence $w_{3,j} = 2F_{j+3}$ or $w_{13,j} = 3F_{j+2} + 9F_{j+3}$. In $w_{i,j}$, each positive integer occurs exactly once, and each consecutive element in the first column is the smallest unused integer [19].

Let R(N) is the number of representations of the non-negative integer N as the sum of different Fibonacci numbers. It is given that for integers N in odd columns of a row, successive values of R(N) form an arithmetic progression and R(N-1) is a constant. Furthermore, if there is an N element of the form $F_n < N < F_{n+1} - 1$ given in a column of the Zeckendorf-Wythoff sequence, then $N + F_{n+k}$, $k \ge 2$ is an element in the same column. Then properties of the Zeckendorf representations and Wythoff pairs are then applied to count R(N) [15,16].

Because each row contains the generalized Fibonacci sequence of positive integers, $R(N) = R(w_{i,j} - 1)$ will be a constant for the integers N in any given row for sufficiently large j.

The number of representations of N as sums of different Fibonacci numbers can be written from the Zeckendorf representation of N such that; if the Zeckendorf representation of N ends with F_k , $k \ge 2$, then a constant q.

$$R(N) = R(N-1)R(F_k) - q, 0 \le q \le R(N-1)$$
(5)

where $R(F_k) = \left[\frac{k}{2}\right]$ and $R(F_k - 1) = 1, k \ge 1$, and [x] is the greatest integer less than a real number x.

Table 3 lists the number of different Fibonacci representations of numbers N according to columns in Table 2.

Table 3 R(N) for N in Table 2

j	1	2	3	4	5	6	7	8	9	10	11	12
$R(F_{j+1})$	1	1	2	2	3	3	4	4	5	5	6	6
$R(w_{2,i})$	1	1	3	3	5	5	7	7	9	9	11	11
$R(w_{3,j})$	2	2	4	4	6	6	8	8	10	10	12	12

An alternative canonical representation can be derived to express any given number as a summation of Fibonacci numbers, while also allowing for the use of consecutive Fibonacci numbers in the same sum. This requirement can be satisfied by employing a base system with Fibonacci numbers as placeholders, allowing for the occurrence of adjacent numbers. This condition is justified by the fact that the sum of any two consecutive Fibonacci numbers corresponds to the subsequent Fibonacci number. As a result, the representation $(..100..)_{fib}$ can always be substituted with $(..011..)_{fib}$. In this investigation, each number $(..100..)_{fib}$ was transformed into $(..011..)_{fib}$. This representation not only serves as a canonical form but also offers a more compact alternative to Zeckendorf's Fibonacci encoding.

To convince yourself that every number can be represented in this system, write down the *k*-Zeckendorf representations of some numbers for 10 bits. It starts as follows:

 Table 4

 Representations of k-Zeckendorf using Zeckendorf's Fibonacci coding

N	Zeckendorf's code	1-Zeckendorf's code	2-Zeckendorf's code	3-Zeckendorf's code	4-Zeckendorf's code
3	100	011			
5	1000	0110			
8	10000	01100	01011		
13	100000	011000	010110		
21	1000000	0110000	0101100	0101011	
34	10000000	01100000	01011000	01010110	
55	100000000	011000000	010110000	010101100	010101011
89	1000000000	0110000000	0101100000	0101011000	0101010110

It is seen that the least number of Fibonacci numbers is the number of 1s in the Zeckendorf's Fibonacci coding, since the Zeckendorf's theorem guarantees the least number of Fibonacci's and is also called the minimal Fibonacci representation.

Genetic Algorithms in Optimization

Genetic algorithms represent a computational methodology that emulates natural evolutionary processes and are widely employed to address search and optimization challenges. The genetic algorithm technique was first proposed by Professor John Holland [20]. Because of its broad perspective and applicability, it has been applied to many optimization and search problems.

The genetic algorithm technique is an iterative optimization method. It works by simultaneously considering a certain number of possible solutions for a given problem in each iteration. It starts working with randomly generated solutions called chromosomes. It continues to search for the best by using the genetic operators of reproduction, crossover, and mutation in each iteration.

The structure of a genetic algorithm mainly consists of chromosome encoding, fitness calculation, chromosome selection, and recombination [21].

A genetic algorithm considers a population of individuals representing possible solutions to a problem. These individuals, called chromosomes, are formed by the combination of a certain number of genes. The structure created by expressing these genes with letters, numbers, or other representations is

called chromosome encoding.

Determining how suitable the chromosomes in the population are for the problem being examined is done by fitness calculation. The calculated value provides information about the quality of the chromosome and determines the probability of its transmission to the next generation during the selection stages. For example, the One-Max problem, which is a frequently used test problem, tries to maximize the number of 1 bit in a chromosome of a certain length. The fitness value for this problem is simply the number of 1s in the bit string of the chromosome.

In the chromosome selection part of the genetic algorithm, chromosomes whose quality is determined through fitness functions are selected for recombination. Chromosomes with high fitness values are more likely to be selected for recombination. The most commonly used methods are roulette wheel selection, tournament selection, and random stochastic selection [22].

Recombination involves improving the number of chromosomes coming from the selection phase using genetic algorithms. The aim of this study was to preserve the genetic information available and transmit it by providing a certain amount of mixture while creating a new generation. Thus, chromosomes with higher fitness values can be obtained. The two most important operators used at this stage are genetic crossover and mutation. Mixing of selected parent chromosomes based on one or more determined points is called crossover. Mutation acts on individual chromosomes and changes a specified gene.

The GA code will continue iteratively until a specified stopping criterion is met. The population obtained after the recombination steps was evaluated using the fitness function. This is because the new population obtained at this stage is accepted as the input population for the next iteration. The pseudocode of the basic genetic algorithm consisting of the aforementioned stages can be given as shown in Algorithm 1.

Algo	Algorithm 1. Pseudocode for the genetic algorithm							
1	Begin							
2	Initialize the population							
3	Evaluate the population							
4	While not (stop condition reached)							
5	Chromosome selection							
6	Perform the crossover operator							
7	Perform the mutation operator							
8	Evaluate the population							
9	Return best chromosomes							
10	End							

Proposed Method

The genetic algorithm attempts to obtain the result by searching for the most appropriate chromosomes through candidate solutions. For a given problem to be solved using a GA approach, possible solution candidates must be represented in accordance with the problem.

In this study, our proposed genetic algorithm approach facilitates the representation of chromosomes using Fibonacci numbers. Initially, we generated the initial population from randomly chosen values. There are two different versions of the proposed genetic algorithm model, based on the differentiation of the selected chromosome representation method. To express the chromosomes within this population using Fibonacci numbers, we derived both Zeckendorf and *k*-Zeckendorf representations. Subsequently, we computed the fitness values of the chromosomes. Iteratively, we executed steps involving chromosome selection, operation of genetic operators, and generation of a new offspring until the stipulated termination criterion was met. After fulfilling the termination criterion, we presented the best-performing chromosome alongside its corresponding optimal fitness values as the

model output. The flowchart of the proposed model is shown in Figure 1.

Figure 1
Flowchart of the proposed model.

The proposed model performs specific calculations for whichever of the two different representations (Zeckendorf / k-Zeckendorf) is chosen and continues to work on this representation throughout all iterations. As shown in Figure 1, the Zeckendorf/k-Zeckendorf representations are calculated for each individual in the initial randomly generated population. The pseudocode of the model is given in Algorithm 2. The for loop, which starts in the third step of Algorithm 2, involves calculating the representations for all chromosomes in the population.

Output of the best chromosome and fitness

The code in the 4th step of Algorithm 2 indicates the Zeckendorf representation of a chromosome. The pseudocode that corresponds to this step and calculates the Zeckendorf representations of a chromosome is given in algorithm 3. In this code, the Zeckendorf representation of the chromosome is kept in a variable that is initialized to null. The chromosome value was compared with all Fibonacci numbers from largest to smallest within the cycle. In each cycle, the Fibonacci number with a maximum value less than or equal to the chromosome value is searched. At the end of the for loop, the unique Zeckendorf representation for the chromosome is calculated. Because this code is in the for loop of Algorithm 2, it performs these calculations for the entire population.

Algorithm 2. Pseudocode for the proposed algorithm

```
Begin
2
           Generate a random initial population
3
           For each chromosome in the population
4
              Calculate Zeckendorf representations of chromosomes
5
              If model = k-Zeckendorf, then
6
                  Find k-Zeckendorf representations
7
              Calculate the fitness function of all chromosomes
8
           While not (stop condition reached)
9
              Execute the chromosome selection step
10
              Perform the crossover operator
              Define mutation rate using Fibonacci numbers
11
12
              Perform the mutation operator
13
              Evaluate the population
14
           Obtain chromosome values from the Zeckendorf / k-Zeckendorf representations
           Return best chromosome/chromosomes
15
16
       End
```

Algorithm 3. Pseudocode for calculating Zeckendorf representations

```
2
            Initialize var to maintain Zeckendorf representation of the given chromosome
3
            For each item in the Fibonacci array
4
               If chromosome > item, then
5
                   Insert "1" into var
6
                   Decreased value of the chromosome by item
7
               Else
8
                   Insert "1" into var
            Return var
10
        End
```

If the proposed model works on k-Zeckendorf representations, the function of finding k-Zeckendorf representations works in the sixth step of algorithm 2. The pseudocode of the program running in this function is given in algorithm 4.

Algorithm 4. Pseudocode to find k-Zeckendorf representations

The basic logic of the *k*-Zeckendorf representation is that the bit with the largest value in the chromosome is distributed to the two bits before it. This process is performed by assigning the value of the bit with the largest value to the two largest bits that are smaller than itself. In this way, in most cases, the chromosome can be expressed with a smaller number of bits without losing its value.

By distributing one bit within the chromosome to two smaller bits, a different representation of the same chromosome is obtained. After such a change, repeated distribution of another gene within the same chromosome may be possible. This means that a new and different representation can be obtained for the same chromosome. At this point, our approach for obtaining the *k*-Zeckendorf representation is based on all possible distributions. As a result of this process, the last representation with no possibility of a new distribution is accepted as the expression of the chromosome.

After this point, the fitness values of the chromosomes are calculated. Chromosome selection was

performed according to the roulette wheel method. The crossover genetic operator is run on the selected chromosomes.

The golden ratio was used to determine the mutation rate. The formula for the golden ratio is expressed as $\alpha = (1 + \sqrt{5})/2$, which corresponds to the value $\cong 1.618$. Because the mutation rate should be less than 1, we used this value as $1/\alpha$. At each iteration, we calculate the mutation rate by multiplying it by the reciprocal of the variable α , denoted as $1/\alpha$. As the iterations progress, it is expected that the chromosomes will approach the ideal point. In this way, as we get closer to the target, fewer mutations will be made compared with the first iterations.

When the termination criterion is met, iterations are concluded, and the output includes the best chromosome (closest to the target) and the corresponding highest fitness value.

The genetic algorithm model with Fibonacci numbers and Zeckendorf representations used in this study was implemented in Python.

EXPERIMENTAL RESULTS

In the course of this investigation, efforts were made to enhance the genetic algorithm optimization method. Chromosomal representations were generated using Fibonacci numbers. The outcomes derived from this approach were assessed through a comparative analysis with those obtained using the standard genetic algorithm.

For this purpose, polynomials of high degree [23] and maximum volume problems [24] are considered.

Polynomials of the High Degree

Exploration of maximum and minimum points in polynomial functions is an extensively studied topic in the field of mathematics. Notably, the identification of extrema becomes progressively more challenging and resource-intensive when dealing with higher-degree polynomials [23].

The general expression for polynomials is given by Equation 6. By selecting coefficients (denoted as 'a') and values for the variable 'x' from the set of real numbers, a polynomial of the desired degree can be obtained.

$$P_n(x) = a_n x^n + a_{n-1} x^{n-1} + \dots + a_1 x + a_0, a_n, x \in \mathbb{R}, a_n \neq 0$$
 (6)

In this study, two polynomials of the fourth and fifth degrees were evaluated. The coefficients of the polynomials were chosen randomly, resulting in the formulation of the polynomials as shown in Equations 7 and 8. These polynomials were then used as input for the model.

$$P_4(x) = 5x^4 - 7x^3 + 3x^2 - 8x + 11 \tag{7}$$

$$P_5(x) = 6x^5 - 3x^4 + 4x^3 - 2x^2 + 9x - 7 \tag{8}$$

Maximum Volume Problem

The problem at hand is the optimization of a rectangular prism's dimensions in order to achieve the maximum volume, given a limited amount of material for its construction. This situation commonly arises when faced with the task of creating a rectangular container, such as a box, using a fixed area of material, as depicted in Figure 2.

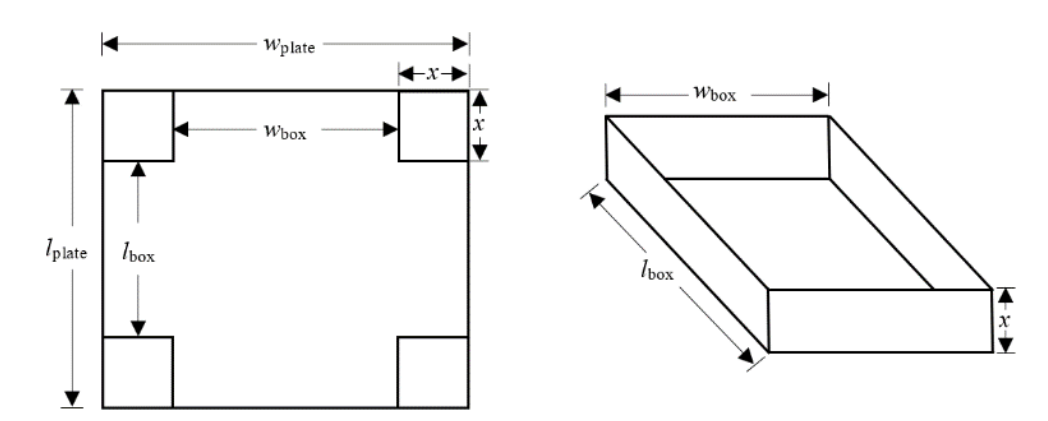


Figure 2Shema Maximum volume problem (a) equal squares of side length x from each corner of the cardboard, (b) folding these edges.

The goal is to maximize the volume of the box by cutting equal squares with side length x from each corner of a rectangular piece of cardboard with dimensions a inches and b inches, and then folding the resulting sides, as illustrated in Figure 2.

Consider a rectangular box characterized by the dimension length l, width w, and height x, yielding a volume V = l*w*x. Assuming a predetermined amount of material, the construction of the box entails cutting squares of side length x from each corner of a rectangular sheet. Subsequently, the residual material is folded to form the box. Expressing the volume in terms of x yields the formulation given in Equation 9.

$$V(x) = x * (l - 2 * x) * (w - 2 * x)$$
(9)

The determination of the optimal value of x that maximizes the volume of the box can be calculated using the principals of calculus.

Expressing the volume V(x) of the box as a function of x, we obtain $V(x) = 4x^3 - 2(l+w)x^2 + lwx$ which can be considered as the problem of finding the value that x can take to have the maximum volume.

If $l = F_n$ and $w = F_{n+1}$ are selected, a golden rectangle can be constructed, and we have:

$$V(x) = 4x^3 - 2F_{n+2}x^2 + F_nF_{n+1}x$$
(10)

then it is worked on a golden rectangle, where F_nF_{n+1} is golden rectangle numbers A001654.

A similar rectangle can be constructed when $l = F_n$ and $w = F_{n+2}$ are taken as:

$$V(x) = 4x^3 - 2L_{n+1}x^2 + F_n F_{n+2}x$$
(11)

where L_n is the Lucas number.

Comparison of Experimental Results

We initially assessed the efficacy of the proposed approach using a sample problem featuring a fourth-order polynomial. We tested the genetic algorithm and the proposed approaches separately for polynomial solutions using 8-bit, 12-bit, and 14-bit long chromosomes.

The results obtained by solving the fourth-order sample polynomial problem created with randomly selected coefficients and given in Equation 7 are shown in Table 5.

Table 5Comparison of the results obtained using the proposed method for a fourth-degree polynomial problem with those obtained from the genetic algorithm.

Solution method	Coding base	Value of the best chromosome	Maximum fitness value	Increase in fitness according to the genetic algorithm
Comotio algorithms	8-bit	250	$1,94*10^{10}$	-
Genetic algorithm	12-bit	4063	$1,36*10^{15}$	-
(standard solution)	14-bit	16244	$3,48*10^{17}$	-
Genetic algorithm	8-bit	255	$2,1*10^{10}$	8,3%
with Zeckendorf	12-bit	4084	$1,39*10^{15}$	2,08%
representations	14-bit	16374	$3,59*10^{17}$	3,24%
Genetic algorithm	8-bit	255	$2,1*10^{10}$	8,3%
with k-Zeckendorf	12-bit	4095	$1,41*10^{15}$	3,19%
representations	14-bit	16382	$3,6*10^{17}$	3,44%

As shown in Table 5, when 8-bit chromosomes are used, the best chromosome values obtained for the genetic algorithm, Zeckendorf, and k-Zeckendorf approaches are 250, 255, and 255, respectively. The maximum fitness values are 1.941010, 2.11010, and 2.11010, respectively. Considering the maximum fitness values obtained, the Zeckendorf and k-Zeckendorf approaches gave 8.3% better results than the genetic algorithm. When 12-bit chromosomes were employed, the Zeckendorf and k-Zeckendorf approaches yielded maximum fitness values that were 2.08% and 3.19% better than those obtained with the genetic algorithm, respectively. Similarly, with the use of 14-bit chromosomes, both the Zeckendorf and k-Zeckendorf approaches exhibited superior performance compared with the genetic algorithm, achieving 3.24% and 3.44% better maximum fitness values, respectively.

The results obtained by solving the fifth-degree sample polynomial problem, which was developed with randomly selected coefficients as presented in Equation 8, are depicted in Table 6.

Table 6Comparison of the results obtained using the proposed method for a fifth-degree polynomial problem with those obtained from the genetic algorithm.

Solution method	Coding base	Value of the best chromosome	Maximum fitness value	Increase in fitness according to the genetic algorithm
Canatia algorithm	Coding base Value of the best chromosome Maximum fitness value according to the genetic algorithm			
Genetic algorithm	12-bit	4053	$6,56*10^{18}$	-
(standard solution)	14-bit	16157	$6,61*10^{21}$	-
Genetic algorithm	8-bit	254	$6,33*10^{12}$	8,3%
with Zeckendorf	12-bit	4081	$6,79*10^{18}$	3,5%
representations	14-bit	16377	$7,07*10^{21}$	7%
Genetic algorithm	8-bit	255	$6,46*10^{12}$	10,4%
with k-Zeckendorf	12-bit	4087	$6,84*10^{18}$	4,27%
representations	14-bit	16383	$7,08*10^{21}$	7,2%

As indicated in Table 6, the Zeckendorf and k-Zeckendorf approaches demonstrated superior performance, exhibiting improvements ranging from 3.5% to 10.4% for problems that can be represented by a fifth-degree polynomial.

In the maximum volume problem, the objective is to bend the edges of a flat plate to maximize the volume relative to its dimensions. In this context, the model was executed for three sample sheets characterized by side length ratios of 1/2, 1/3, and 1/8. The dimensions of these sheets are specified as 4096x8192, 1024x3072, and 2048x16384, respectively. The outcomes derived for these sample sheets are illustrated in Table 7.

Table 7Comparison of the results obtained by the proposed method for the maximum volume problem with those obtained from the genetic algorithm.

		Genetic algorithm (standard solution)		with Ze	algorithm ckendorf entations	Genetic algorithm with k-Zeckendorf representations		
Sheet size	Optimum bending length	Obtained fitness value	Error rate (deviation from optimum)	Obtained fitness value	Error rate (deviation from optimum)	Obtained fitness value	Error rate (deviation from optimum)	
4096x8192	865,6	851	1,69%	878	1,43%	868	0,28%	
1024x3072	231,1	235	1,68%	234	1,24%	231	0,05%	
2048x16384	495,0	486	1,82%	490	1,01%	496	0,20%	

As indicated in Table 7, the anticipated optimal bending points for plates of sizes 4096x8192, 1024x3072, and 2048x16384 are 866, 231, and 495, respectively. However, the genetic algorithm method yielded a bending point of 851 for the 4096x8192 plate. On the other hand, our Zeckendorf approach identified it as 878, and the *k*-Zeckendorf approach determined it to be 868.

Evaluating these outcomes in terms of deviation (error) rates from the optimal point of 851, we observe error rates of 1.69%, 1.43%, and 0.28% for the genetic algorithm, Zeckendorf, and k-Zeckendorf approaches, respectively, for the 4096x8192 plate. For the 1024x3072 plate, the error rates were 1.68%, 1.24%, and 0.05%, respectively. Meanwhile, for the 2048x16384 plate, the error rates were 1.82%, 1.01%, and 0.20%, respectively.

In addition, the maximum volume problem was tested on a sample golden rectangle formed by selecting the coefficients from the Fibonacci numbers, as given in Equation 10, and on rectangular plates formed by selecting the coefficients from the Fibonacci and Lukas numbers, as given in Equation 11, and the results were evaluated. When the Fibonacci numbers f_{19} , f_{20} , and f_{21} are selected for the coefficients according to Equation 10, the equation in Equation 12 is obtained.

$$V(x) = 4x^3 - 2F_{21}x^2 + F_{19}F_{20}x (12)$$

When Equation 11 is used, the f_{19} and f_{21} fibonacci numbers and the lukas number l_{20} are determined as coefficients, and the equation in Equation 13 is obtained.

$$V(x) = 4x^3 - 2L_{20}x^2 + F_{19}F_{21}x$$
 (13)

The outcomes derived from these special rectangle sheets are presented in Table 8.

Table 8Comparison of the results obtained using the proposed method for the maximum volume problem of special rectangles with those obtained from the genetic algorithm.

			algorithm d solution)	with Ze	algorithm ckendorf entations	Genetic algorithm with k-Zeckendorf representations		
Special rectangles	Optimum bending length	Obtained fitness value	Error rate (deviation from optimum)	Obtained fitness value	Error rate (deviation from optimum)	Obtained fitness value	Error rate (deviation from optimum)	
Equation 12	838,9	831	0,94%	836	0,35%	840	0,13%	
Equation 13	926,6	933	0,69%	924	0,28%	927	0,04%	

As indicated in Table 8, the expected optimal bending points for the golden rectangle determined by Equation 12 and the special rectangle determined by Equation 13 are 838.9 and 926.6, respectively.

The 0.94% deviation rate obtained with the standard genetic algorithm method for the golden rectangle was reduced to 0.35% with the Zeckendorf approach and 0.13% with the k-Zeckendorf approach. Similarly, for the special rectangle specified in Equation 13, the 0.69% deviation rate obtained by the genetic algorithm method was reduced to 0.28% with the Zeckendorf approach and 0.04% with the k-Zeckendorf approach.

Similarly, for the special rectangle specified in Equation 13, the 0.69% deviation rate obtained by the genetic algorithm method was reduced to 0.28% with the Zeckendorf approach and 0.04% with the k-Zeckendorf approach.

These findings indicate that the proposed Zeckendorf and *k*-Zeckendorf methods outperform the genetic algorithm approach because they exhibit lower error rates across the evaluated plate sizes.

We initially assessed the efficacy of the proposed approach using a sample problem featuring a fourth-order polynomial. We tested the genetic algorithm and the proposed approaches separately for polynomial solutions using 8-bit, 12-bit, and 14-bit long chromosomes. The results obtained by solving the fourth-order sample polynomial problem created with randomly selected coefficients and given in Equation 7 are shown in Table 9.

Table 9Comparison of the results obtained using the proposed method for a fourth-degree polynomial problem with those obtained from the genetic algorithm.

Solution method	Coefficien ts	Value of the best chromosome	Maximum fitness value	Increase in fitness according to the genetic algorithm
Constin algorithm	8-bit	250	$1,94*10^{10}$	_
Genetic algorithm	12-bit	4063	$1,36*10^{15}$	-
(standard solution)	14-bit	16244	$3,48*10^{17}$	-
Genetic algorithm	8-bit	255	$2,1*10^{10}$	8,3%
with Zeckendorf	12-bit	4084	$1,39*10^{15}$	2,08%
representations	14-bit	16374	$3,59*10^{17}$	3,24%
Genetic algorithm	8-bit	255	$2,1*10^{10}$	8,3%
with k-Zeckendorf	12-bit	4095	$1,41*10^{15}$	3,19%
representations	14-bit	16382	$3,6*10^{17}$	3,44%

The obtained results demonstrate that the proposed genetic algorithm models exhibit better performance than the standard genetic algorithm. These models facilitate the representation of chromosomes using Fibonacci numbers.

There are certain limitations and challenges in this study. First, the proposed genetic algorithm models were tested on only two distinct problems: the fourth-degree polynomial problem and the maximum volume problem. These problems represent only a few among the wide range of problems for which genetic algorithms can be applied. Therefore, it is necessary to test the effectiveness of the proposed models on other problems. Second, note that the proposed genetic algorithm models are dependent on the parameters of the Zeckendorf and *k*-Zeckendorf representations. These parameters involve Fibonacci selection numbers and determination of the value of k. Further research is needed to investigate how these parameters affect the performance of the proposed models and how they can be optimized.

CONCLUSION

In this study, we investigated the use of genetic algorithms (GAs) for optimization by leveraging their capacity to simulate the evolutionary processes found in nature. GAs have been widely applied to diverse search and optimization challenges because of their adaptability and efficacy. The fundamental structure of GA encompasses several essential elements, including chromosome encoding, fitness

evaluation, chromosome selection, and recombination. These elements iteratively collaborate to explore and identify optimal solutions for a given problem.

Our study introduced a novel approach that employs Fibonacci numbers for chromosome representation within GAs. This approach offers two distinct representations: Zeckendorf and k-Zeckendorf, each offering unique advantages. Through experimental analysis, we demonstrated the efficacy of our approach by comparing it with standard GA solutions for polynomial optimization and maximum volume problems.

The results of our experiments reveal that the Zeckendorf and k-Zeckendorf methodologies surpass the standard GA in terms of fitness values and error rates across the evaluated problems. The adoption of Fibonacci numbers as the foundation for chromosome representation presents a promising avenue for enhancing the performance of GAs in optimization tasks.

In summary, the adoption of Fibonacci numbers for chromosome representation in GA exhibits considerable potential for advancing optimization outcomes. Continued research in this area may yield further advancements in optimization algorithms' efficiency and efficacy.

Ethical Statement

This study is an original research article designed and developed by the authors.

Ethics Committee Approval

This study does not require any ethics committee approval.

Author Contributions

```
Research Design (CRediT 1) Y.E.G.: (%20) – F.K. (%40) – H.E. (%40)
```

Data Collection (CRediT 2) Y.E.G.: (%30) – F.K. (%40) – H.E. (%30)

Research - Data Analysis – Validation (CRediT 3-4-6-11) Y.E.G.: (%70) – H.E. (%30)

Writing the Article (CRediT 12-13) Y.E.G.: (%40) – F.K. (%20) – H.E. (%40)

Revision and Improvement of the Text (CRediT 14) Y.E.G.: (%60) – F.K. (%20) – H.E. (%20)

Financing

This research did not receive any specific grant from funding agencies in the public, commercial, or not-for-profit sectors.

Conflict of Interest

The authors declare no conflict of interest.

Sustainable Development Goals (SDG)

Sustainable Development Goals: 8 Decent work and economic growth.

REFERENCES

- [1] M. Mitchell, An Introduction to Genetic Algorithms, MIT Press, 1998.
- [2] A.O. Faouri, P. Kasap, Maximum likelihood estimation for the Nakagami distribution using particle swarm optimization algorithm with applications, *Necmettin Erbakan University Journal of Science and Engineering*. 5(2) (2023), 209-218. doi:10.47112/neufmbd.2023.19.
- [3] A. Pektaş, İ. Onur, Ağaç tohum algoritmasının kümeleme problemlerine uygulanması, *Necmettin Erbakan University Journal of Science and Engineering.* 4 (2022), 1-10.
- [4] A. Ünlü, İ. İlhan, A novel hybrid gray wolf optimization algorithm with harmony search to solve multi-level image thresholding problem, *Necmettin Erbakan University Journal of Science and Engineering*. 5(2) (2023), 230-245. doi:10.47112/neufmbd.2023.21.
- [5] K.R. Srimathi, A. Padmarekha, K.S. Anandh, Automated construction schedule optimisation using genetic algorithm, *Asian Journal of Civil Engineering*. 24 (2023), 3521-3528. doi:10.1007/s42107-023-00729-8.
- [6] O. Ulkir, G. Akgun, Predicting and optimising the surface roughness of additive manufactured parts using an artificial neural network model and genetic algorithm, *Science and Technology of Welding and Joining*. 28 (2023), 548-557. doi:10.1080/13621718.2023.2200572.
- [7] E. Singh, S.S. Afshari, X. Liang, Wind turbine optimal preventive maintenance scheduling using Fibonacci search and genetic algorithm, *Journal of Dynamics, Monitoring and Diagnostics*. 2 (2023), 157-169.
- [8] M. Basu, M. Das, Uses of second order variant Fibonacci universal code in cryptography, *Control and Cybernetics*. 45 (2016), 239-251.
- [9] A. Rehman, T. Saba, T. Mahmood, Z. Mehmood, M. Shah, A. Anjum, Data hiding technique in steganography for information security using number theory, *Journal of Information Science*. 45 (2019), 767-778. doi:10.1177/0165551518816303.
- [10] L. Wu, H. Cai, Novel stream ciphering algorithm for big data images using Zeckendorf representation, *Wireless Communications and Mobile Computing*. 2021 (2021), 1-19. doi:10.1155/2021/4637876.
- [11] M.S. Taha, M.S.M. Rahem, M.M. Hashim, H.N. Khalid, High payload image steganography scheme with minimum distortion based on distinction grade value method, *Multimedia Tools and Applications*. 81 (2022), 25913-25946. doi:10.1007/s11042-022-12691-9.
- [12] Y. Wu, L. Wu, H. Cai, Cloud-edge data encryption in the internet of vehicles using Zeckendorf representation, *Journal of Cloud Computing*. 12 (2023), 39. doi:10.1186/s13677-023-00417-7.
- [13] Z. Liang, Q. Qin, C. Zhou, An image encryption algorithm based on Fibonacci Q-matrix and genetic algorithm, *Neural Computing and Applications*. 34 (2022), 19313-19341.
- [14] T. Koshy, Fibonacci and Lucas Numbers with Applications, Volume 2, *John Wiley & Sons*, 2019.
- [15] C. Kimberling, The Zeckendorf array equals the Wythoff array, *Fibonacci Quarterly*. 33 (1995), 3-8.
- [16] C. Kimberling, Edouard Zeckendorf, Fibonacci Quarterly. 36 (1998) 416-418.
- [17] P. Pooksombat, P. Udomkavanich, W. Kositwattanarerk, Multidimensional Fibonacci Coding, (2017). http://arxiv.org/abs/1706.06655 (erişim 09 Mart 2024).
- [18] M. Bicknell-Johnson, The Zeckendorf-Wythoff Array Applied to Counting the Number of Representations of N as Sums of Distinct Fibonacci Numbers, in: F.T. Howard (Ed.), *Applications of Fibonacci Numbers, Springer Netherlands*, Dordrecht, 1999: ss. 53-60.
- [19] W. Lang, ed., The Wythoff and the Zeckendorf Representations of Numbers Are Equivalent,

- Kluwer Academic Publishers, Dordrecht, 1996. doi:10.1007/978-94-009-0223-7.
- [20] J.H. Holland, Adaptation in Natural and Artificial Systems: An Introductory Analysis with Applications to Biology, Control, and Artificial Intelligence, *The MIT Press*, 1992. doi:10.7551/mitpress/1090.001.0001.
- [21] J. McCall, Genetic algorithms for modelling and optimisation, *Journal of Computational and Applied Mathematics*. 184 (2005), 205-222. doi:10.1016/j.cam.2004.07.034.
- [22] D. Dumitrescu, B. Lazzerini, L.C. Jain, A. Dumitrescu, Evolutionary Computation, *CRC Press*, 2000.
- [23] T. DeAlwis, Maximizing or minimizing polynomials using algebraic inequalities, in: *Proceedings of the 9th Asian Technological Conference on Mathematics*, 2004: ss. 88-97. https://atcm.mathandtech.org/EP/2004/2004I328/fullpaper.pdf (erişim 21 Mart 2024).
- [24] A. Mikhalev, I.V. Oseledets, Rectangular maximum-volume submatrices and their applications, *Linear Algebra and its Applications*. 538 (2018), 187-211. doi:10.1016/j.laa.2017.10.014.



Vol: 7 No: 2 Year: 2025

Araştırma Makalesi/Research Article

e-ISSN: 2667-7989

https://doi.org/10.47112/neufmbd.2025.89

SCADA Sistemi ve Görüntü İşleme Teknikleri Kullanarak Gerçek Zamanlı Aydınlatma Sisteminin Tasarımı

Murat ALTUNKAYA 1* 🕞 Muhammed KARAALTUN 2 🕞

^{1*} Ramadan Mühendislik San. Tic. Ltd. Şti, Midyat, Mardin, Türkiye

² Necmettin Erbakan University, Faculty of Engineering, Department of Computer Engineering, Konya, Türkiye

Makale Bilgisi

ÖZET

Geliş Tarihi: 31.07.2024 Kabul Tarihi: 20.11.2024 Yayın Tarihi: 31.08.2025

Anahtar Kelimeler:

Aydınlatma Armatürleri, Görüntü İşleme Teknikleri, Mobil Teknolojiler, SCADA, Web.

SCADA terimi, İngilizce "Supervisory Control and Data Acquisition" kelimelerinin ilk harflerini temsil eder. SCADA sistemleri tek bir kontrol noktasından, otomasyon sistemlerinin fonksiyonlarını kontrol etmek ve izlemek için kullanılan sistemlerdir. SCADA sistemleri, doğal gaz, petrol, su dağıtım otomasyonları, hava kirliliği kontrolü ve benzeri alanlarda çok başarılı bir şekilde kullanılmaktadır. Bu çalışmada, SCADA sistemi, şehirler arası yollar ile birlikte şehir içi parklar ve sokakların aydınlatma sistemlerinde kullanılmıştır. SCADA sistemi sokak, park ve şehirlerarası yollarında kullanılan aydınlatma armatürlerinin gereksiz zamanlarda çalışmasını engellemiş ve aydınlatma armatürlerinde meydana gelen arızaların tespitini kolaylaştırmıştır. Parkların aydınlatma sistemlerinde insanların tespiti için gerçek zamanlı görüntü işleme teknikleri kullanılması, sistemin en kritik ve yenilikçi özelliklerinden biridir. Bu özellik, ortamda insan varlığını anlık olarak algılayarak, aydınlatmanın gereksiz yere açık kalmasını engeller ve enerji verimliliğini sağlar. Gerçek zamanlı görüntü işleme sayesinde, aydınlatma ihtiyaç duyulduğunda aydınlatma devreye girer, bu hem enerji tasarrufu sağlar hem de güvenliği artırır. Bu özellik, akıllı şehir uygulamaları kapsamında önemli olup, kullanıcıların güvenliğini sağlarken çevresel etkileri de en aza indirir. Bu sayede, tasarlanan SCADA sistemi, modern aydınlatma çözümleri için etkili bir örnek teşkil etmektedir. Bu sistemi gerçekleştirmek için şehirler arası yollar ile birlikte şehir içinde bulunan sokaklar ve parklar için bir prototip hazırlanmıştır. Hazırlanan bu prototip donanım ve yazılım olmak üzere iki ana bileşenden oluşmaktadır. Donanım kısmında mikrodenetleyici olarak Arduino Mega2560 Pro Mini kullanılmıştır. Ayrıca TCA9548a Mux modülü, PCD8574 I2C modülü, LDR sensörü, LED ve kamera donanımları sırasıyla pinlerin çoğaltması, ledler ile Mux modülü arasında haberleşmenin sağlanması, ışık şiddetinin ölçülmesi, aydınlatma ve insan tespitinin yapılması için kullanılmıştır. Yazılım kısmında sistemin web tasarımı için ASP.Net MVC, mobil uygulaması için Flutter ve veri tabanı için ise MySQL kullanılmıştır. Tasarlanan sistem, test amaçlı web ve mobil uygulamalar üzerinden izlenmiş ve kontrolleri başarılı bir şekilde sağlanmıştır. Ayrıca tasarlanan sistemde gerçek zamanlı insan tespiti modelinin eğitim başarısının 0.99 ve test başarısının farklı çevre koşulları dikkate alındığında aydınlık ortamda 0.98, karanlık ortamda ise 0.94 olduğu görülmektedir.

Design of Real-Time Lighting System Using SCADA System and Image Processing Techniques

Article Info

ABSTRACT

Received: 31.07.2024 Accepted: 20.11.2024 Published: 31.08.2025

Keywords:

Image Processing Techniques, Lighting Fixtures, Mobile Technologies, SCADA, Web.

The term SCADA stands for "Supervisory Control and Data Acquisition". SCADA systems are used to control and monitor the functions of automation systems from a single control point. These systems have been successfully used in areas such as natural gas, petroleum, water distribution automation, air pollution control, and similar fields. In this study, a SCADA system is utilized to light urban parks and streets, along with intercity roads. By using the SCADA system, unnecessary operation of lighting fixtures on streets, parks, and intercity roads is prevented, and the detection of faults in lighting fixtures is facilitated. Using real-time image processing techniques to detect people in park lighting systems is one of the system's most critical and innovative features. This capability instantly detects human presence, preventing unnecessary lighting and promoting energy efficiency. Through real-time image processing, lighting is activated only when needed, which not only conserves energy but also enhances security. This feature is significant within smart city applications, as it ensures user safety while minimizing environmental impact. Consequently, the designed SCADA system serves as an effective model for modern lighting solutions. A prototype is prepared for streets and parks in the city, along with intercity roads to implement this system. This prototype consists of two main components: hardware and software. Arduino Mega2560 Pro Mini microcontroller is used as the hardware component. Furthermore, the TCA9548a Mux module, PCD8574 I2C module, LDR sensor, LED, and camera equipment are used for pin expansion, communication between LEDs and Mux module, measuring light intensity, and for lighting and human detection, respectively. For the software part, ASP.Net MVC, Flutter, and MySQL are used for web design, mobile applications, and databases, respectively. The designed system is monitored through web and mobile applications for testing purposes, and its control is achieved successfully. In addition, in the designed system, it is seen that the training accuracy of the real-time human detection model is 0.99 and the testing accuracy is 0.98 in the light environment and 0.94 in the dark environment, considering different environmental conditions.

To cite this article:

Altunkaya, M. & Karaaltun, M. (2025). Design of Real-Time Lighting System Using SCADA System and Image Processing Techniques. *Necmettin Erbakan University Journal of Science and Engineering*, 7(2), 245-258. https://doi.org/10.47112/neufmbd.2025.89

*Corresponding Author: Murat Altunkaya, murataltunkayaa@gmail.com



INTRODUCTION

Image processing techniques and applications have gained significant importance in recent times. Image processing techniques are actively used in various fields such as security, health, defense industry, automotive, surveillance, entertainment, media, robotics, and technology [1][2]. Image processing techniques are powerful tools used to analyze, process, and make real-time decisions using captured images [3][4]. These techniques enable the analysis of environmental conditions using camera images [5]. SCADA (Supervisory Control and Data Acquisition) systems are structures composed of hardware and software elements designed to comprehensively investigate, track, and supervise companies' operational and automation processes through an integrated database [6]. Implementing SCADA enables companies to collect, analyze, report, and alarm real-time data during production processes in their manufacturing facilities[6]. Modern lighting systems have evolved to meet various needs such as increasing energy efficiency, providing comfort, and enhancing safety. Traditional lighting systems typically operate at fixed illumination levels, while next-generation lighting systems adjust illumination based on the dynamic characteristics of the environment [7]. They have developed an IoT-based smart lighting system, which utilizes motion and LED fixture sensors to transmit data to a cloud system via Esp8266 (Wi-Fi module). They control the system through the ThingSpeak platform [8]. They have also created an IoT-based smart street lighting system to save energy. The system enables remote management of streetlamps using TCP/IP connectivity. It is controlled using Wi-Fi and includes a real database, offering web-based control and monitoring screens to users accessing it via the internet, along with lighting management software on the server [9]. Wireless communication is achieved using RS232 and GPRS modules. The smart city control software (SCM) includes the LIGHTiST software module, which enables centralized monitoring and control of the lighting system, maintenance and fault tracking, and real-time monitoring and control of energy and alarm data collected from the field [10]. An IoTbased smart streetlamp control system was designed aiming to reduce electricity consumption and minimize human effort. The system utilizes LED, LDR, and IR sensors [11], [12]. Image processing techniques are powerful tools for analyzing, processing, and making real-time decisions based on captured images. These techniques can analyze images obtained through cameras to determine whether there are people present in the environment and adjust the lighting system accordingly. This allows for rapid and effective adaptation to changing light conditions in the environment. Real-time remote lighting systems offer many advantages. Firstly, users are relieved from manually adjusting illumination levels. With image processing algorithms, the system can automatically adjust the lighting system based on the detected presence of people in the environment. This ensures energy efficiency compared to traditional lighting methods. Data obtained through image processing techniques accurately determine the realtime light requirements of the environment, preventing unnecessary energy consumption. This contributes to reducing energy costs and increasing environmental sustainability. In this study, a realtime remote lighting system using image processing techniques is proposed. Using image processing techniques, the prototype is developed to remotely control and monitor lighting systems in various urban areas such as streets, parks, and roads. The prototype ensures ease of maintenance in case of fixture malfunctions and prevents unnecessary energy consumption. The first part of this study provides information about SCADA, lighting, and image processing techniques. The second part provides general information about SCADA, lighting, image processing techniques, and the design of the prototype system. The third part provides information about the design of the prototype system. The fourth part presents information about the developed prototype and the real-time remote lighting system using image processing techniques. The final section presents the conclusions.

MATERIALS AND METHODS

The methods and hardware system of this study are explained under this heading.

Urban and Interurban Lighting Systems

Lighting systems are of great importance in cities and on intercity roads. These systems are utilized to enhance traffic safety, enable road users to perceive road conditions during nighttime or adverse weather conditions and create a secure environment in urban areas. Urban lighting systems are employed to illuminate streets, avenues, intersections, pedestrian crossings, recreational areas, underpasses, and parking lots in urban environments. These systems facilitate pedestrians and drivers to have better visibility of roads during nighttime or low-light conditions [7]. Interurban lighting systems, on the other hand, are utilized for long distances such as highways between cities, tunnels, and main roads. These systems are designed to provide adequate visibility to drivers during long-distance journeys. Highway lighting systems typically require higher light levels as vehicles traveling at higher speeds necessitate longer visibility distances. Advanced technologies contribute to the effectiveness and energy efficiency of interurban lighting systems, preventing unnecessary energy consumption while ensuring adequate visibility for drivers [13]. Smart lighting systems offer solutions for controlling electricity consumption and management of lighting fixtures, thereby promoting energy savings [14].

Human Perception Process

Image processing techniques are computational methods developed alongside advancements in computer technology, with a wide range of practical applications. This methodology involves converting a moving or stationary image captured with a camera, camcorder, or scanner into a digital format, followed by interpreting this digital data through various algorithms. Numerous libraries, developed in different programming languages, support this field. OpenCV, an open-source computer vision library is widely utilized in image processing applications and is often used in conjunction with PyTorch to develop deep learning-based solutions [15]. Technological advancements have popularized image processing techniques in fields such as defense, healthcare, agriculture, and lighting, where they are applied in tasks ranging from object detection to controlling specific illumination features [16][17]. OpenCV is designed for real-time image processing and is frequently chosen for applications such as object recognition, human detection, face recognition, and motion analysis due to its broad functionality. PyTorch, optimized for deep learning algorithms, provides a flexible framework for developing complex models and achieves high accuracy in tasks like human detection and object recognition through neural networks. processing, In object detection for image torchvision.models.detection.fasterrcnn resnet50 fpn (pretrained=True) composite model which consists of Region-based Convolutional Neural Networks (Faster R-CNN), ResNet-50, and Feature Pyramid Network (FPN) is used for the human detection process. This model offers a powerful deep learning-based solution for high-accuracy projects. Thanks to the Faster R-CNN algorithm, this model achieves faster and more accurate results than prior R-CNN methods [18]. ResNet-50, a deep convolutional neural network with residual connections, serves as the feature extractor, addressing the "vanishing gradient" issue in deep models [19]. Key features of the Faster R-CNN model include the RPN for generating candidate objects, a classifier for label assignment, and bounding box regression for precise object localization [20]. The FPN structure allows for efficient multi-scale feature extraction, facilitating better detection of objects of varying sizes by combining features at different resolutions, thus enhancing accuracy for both large and small objects [21]. The pretrained=True option leverages the COCO (Common Objects in Context) dataset's pre-trained weights. COCO, with approximately 80 classes, is widely used in object detection applications [22]. In this study, the COCO 2017 dataset, split into the train (118,287 images), test (40,670 images), and validation (5,000 images) sets, was used primarily for human detection among other classes. The combination of Faster R-CNN for object detection and ResNet-50 for feature extraction provides a powerful solution in this domain. The Faster R-CNN ResNet-50 FPN composite model is extensively utilized in applications requiring high accuracy and where real-time processing is not a strict requirement, although real-time performance can be achieved under certain conditions.

In this study, the torchvision.models.detection.fasterrcnn_resnet50_fpn(pretrained=True) composite model was selected to carry out the human detection process on image data. This model, built on the Faster R-CNN algorithm, is known for its high accuracy and notable speed advantage, making it a strong solution for object detection. The model was trained on the COCO dataset, allowing it to achieve high accuracy on the dataset through transfer learning. To apply the model in this project, the images in the COCO dataset were resized to a specific dimension and converted to the appropriate formats. Then, the Faster R-CNN model was configured and utilized for the human detection process, the steps of the human detection process are given below.

- **Step 1**: Data Preparation: The image in the frame variable is resized to the desired size dimensions and each image is transformed into the data structure required by the model using OpenCV libraries.
- **Step 2**: Model Usage: The composite model torchvision.models.detection.fasterrcnn_resnet50_fpn (pretrained=True) is used to classify and detect humans.
- **Step 3**: Accuracy Analysis: The model's training and testing accuracy, including the classes and bounding boxes, were analyzed to verify the accuracy of the human detection process.

The model's results were obtained in the form of bounding boxes and probability scores indicating the type and location of objects in the image. Furthermore, the model's performance was evaluated by conducting a detailed accuracy analysis on the detected humans. A test example of the prototype is presented in Figure 1.



Figure 1 *A test example of the prototype.*

SCADA System

SCADA [23] systems are structured from hardware and software components to comprehensively research and monitor companies' operational and automation processes, maintaining an integrated database [23]. Implementing SCADA enables companies to collect real-time data during production processes, analyze it, report issues through alarms, and generate reports [24]. SCADA systems efficiently perform tasks such as remote adjustment of settings in widely dispersed production facilities from a central control point, displaying alarms in the system, remotely turning the system on and off, and collecting information from the system [25].

Structure of the SCADA System

Remote Terminal Unit (RTU); these are the units that make data collection and monitoring

terminals.

Communication System

These are systems that enable information or messages to be sent crosswise from one point to another point.

Master Terminal Unit (MTU)

It can be expressed as a place where production facilities distributed over a wide geographical area can be remotely controlled, monitored, and managed with computers [26]. The structure of the SCADA System is shown in Figure 2.

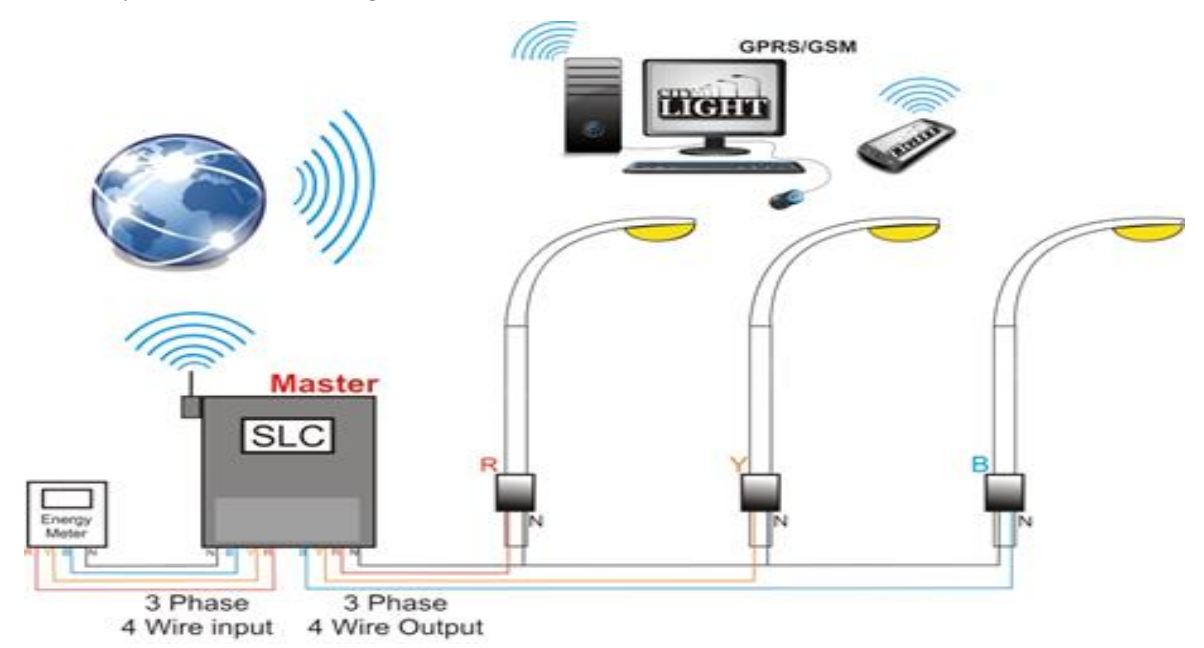


Figure 2
Structure of the SCADA system [27].

Control: In SCADA systems, control operations can be performed manually or automatically from control panels, central control rooms, remote terminal units, computer screens, and master terminal units [28]

Monitoring: Monitoring operations in SCADA systems can be conducted from central control rooms, control panels, remote terminal units, computer screens, and master terminal units [29].

Data Acquisition: Data acquisition in SCADA systems refers to the process of collecting data from sensors and transmitters prepared according to the structure of the production facility during the development of application software [30].

Data Recording and Storage: In SCADA systems, data recording and storage operations involve automatically recording data from sensors and transmitters into a database prepared according to the structure of the production facility during the development of application software.

Alarm: SCADA systems require continuous monitoring of processes and data, and in case of reaching undesired conditions, they are equipped with an alarm system where various settings are configured to notify system administrators and technicians [31][32].

Real-Time Remote Lighting System Using Image Processing Techniques

The prototype and software, which are developed for the real-time remote lighting system in this

study, are detailed under this heading.

Designing the Prototype System and Lighting System

After designing the prototype system, the parts were cut with a laser, and the system was assembled. Once the assembly process of the system was completed, the LEDs of the lighting fixtures were installed, and their assemblies were made. The image of the prepared prototype system and lighting fixtures is given in Figure 3. In the prepared prototype, lighting systems for parks, roads, and streets were developed. Illumination is a factor directly affecting human life and the process of illuminating certain areas. Lighting that is designed for everyday needs allows the human eye to perceive normal objects more easily. Lighting is necessary for reasons such as insufficient daylight, ensuring safety and security at night, and carrying out outdoor activities. In the prepared prototype, excessive lighting in street, park, and road lighting poles (fixtures) is prevented, as excessive lighting can cause discomfort to the eyes and lead to light pollution. To avoid energy waste, energy-saving bulbs are used instead of fluorescent lamps in streets, parks, and avenues. In outdoor lighting, the fixed opening and closing hours of fixtures lead to significant energy waste as lighting is not always needed. After dusk, the number of traffic accidents resulting in injuries or fatalities increases due to poorly lit streets. The prepared Real-Time Remote Lighting System Using Image Processing Techniques will help prevent this.



Figure 3 *Prototype system and lighting fixtures.*

Software System

In this section, the SCADA software system, which is used in the lighting system of the designed prototype, is explained. In the prepared prototype, the control and monitoring of road, building, and park lighting systems are controlled with SCADA software. In the created prototype, the lighting system is activated according to the status of daylight. Furthermore, lighting is automatically turned on and off depending on human density, which is checked by the camera integrated into the lighting system. For example, the system automatically works when humans are detected with the camera whereas the lighting system is automatically turned off when there are no people in the environment. Operating the system in this way saves energy. At the same time, in the prepared lighting system, faulty luminaires or whether they are working or not are shown on the system, and the data is recorded in the real-time database. Since the faults occurring in the luminaires in the system are known, they can be repaired

quickly. Since it is known where the maintenance personnel will go, both time and transportation costs will be saved. The image of the prepared prototype system and lighting fixtures in their open state is given in Figure 4.



Figure 4

Open state of prototype system and lighting fixtures.

The luminaires in the prototype are controlled by the microcontroller according to the information sent from the system. The entire system is controlled from the web and mobile applications without the need for physical intervention. The system administrator or authorized user can view the faults in the system from anywhere or obtain reports from the printer. In this project, the features of the created SCADA software are presented in the following section.

User Management

In the prototype lighting system, rights can be defined according to users' authorization for management, control, maintenance, monitoring, and other tasks using SCADA software. The system administrator has rights to add and authorize users, while other users have rights at the given authorization level. The user login page and user addition pages are shown in Figure 5. Users can perform operations based on the roles given by the administrator who added them using their email and passwords.



Figure 5
User login page and user addition.

Graphics Management

The high quality of the system monitoring and surveillance provides convenience to users when using the software of the prepared prototype. The interface showing all areas is illustrated in Figure 6.

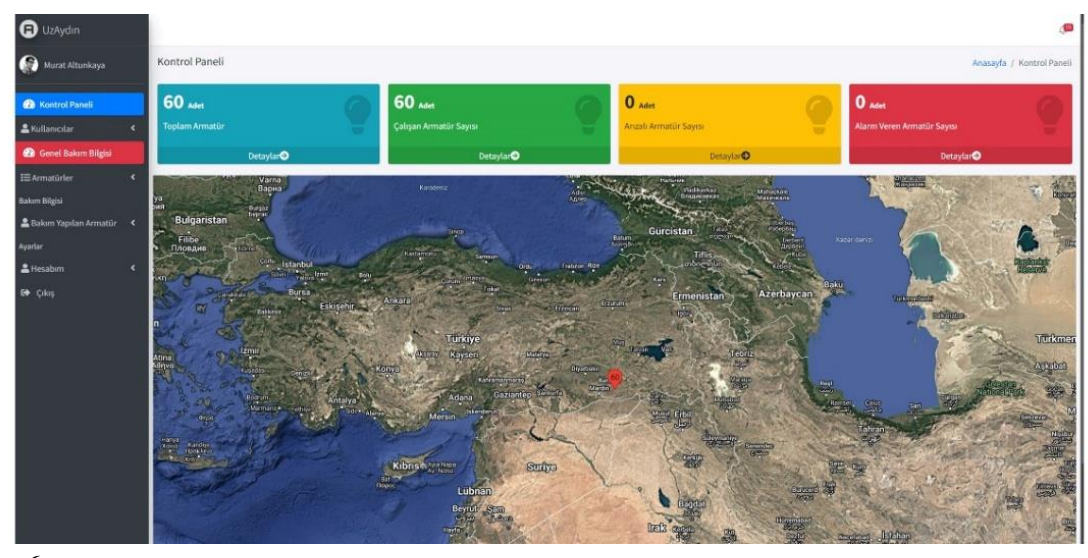


Figure 6
Interface showing the areas.

In the interface shown in Figure 6, the statuses and locations of all fixtures in the system are provided. Providing their locations on the map will assist maintenance personnel in quickly addressing any faults.

Database Management

The real-time data of the lighting fixtures in the developed prototype are recorded in the database through the software prepared for the system. The data from the system is stored in the database on the server via web API. The server interface showing the Database and tables is illustrated in Figure 7.

In the software prepared for the prototype, log records of all operations performed in the system are taken. Moreover, the times and dates when the lighting fixtures in the prototype are operational are recorded in the system.

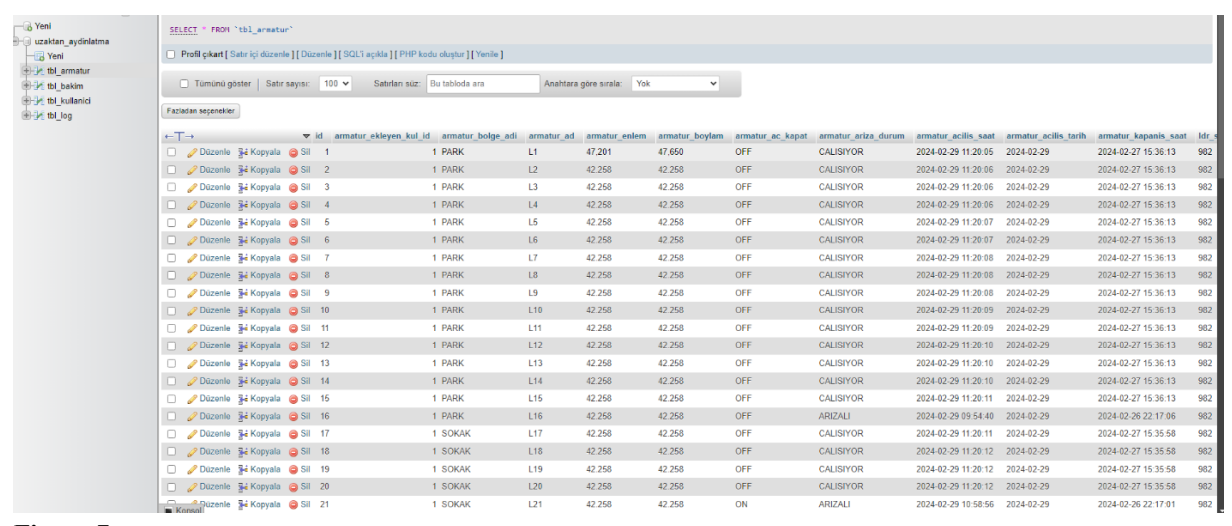


Figure 7 *Database and tables.*

Alarm Management

In the software prepared for the prototype, malfunctions or warnings of the lighting fixtures in the system are recorded in the database, and their locations on the map are shown. Alarm management screen of the system is shown Figure 8.



Figure 8
Alarm management screen.

The system sends automatic notifications to users with authorization for alarms generated within the system. Also, maintenance personnel, having access to all information about the lighting fixture associated with the alarm displayed on their screen, can directly proceed to the location of the lighting fixture triggering the alarm.

Report Management

In the software prepared for the prototype, the data of the lighting fixtures in the system, including faults or warnings, are recorded in the database, and authorized users can print them from anywhere using a printer. Figure 9 shows the lighting fixtures in the system that trigger alarms.

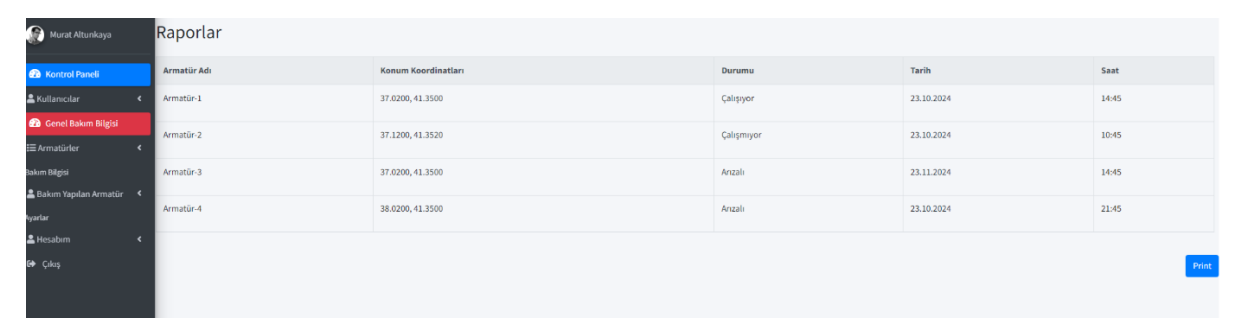


Figure 9 *Report screen of alarm-triggering lighting fixtures.*

As shown in Figure 9, in addition to alarm-triggering lighting fixtures, reporting of all data present in the system can be obtained. Reports can be generated on a daily or monthly basis.

RESULTS AND DISCUSSION

In this study, a SCADA and image processing-based lighting system was successfully developed for intercity roads, urban parks, and streets. A prototype was developed to assess the SCADA and image processing-based lighting system. The prototype was operational for a total of 80 hours, during which the on/off status of the luminaires was monitored. According to the data collected in the database, it was observed that the luminaires were activated at the correct times, and their deactivation contributed to energy savings. Furthermore, it was verified that the microcontroller and sensors functioned effectively, and the data was logged into the database without any issues. The SCADA system improved maintenance processes and enhanced operational efficiency through its fault detection capabilities. Users were able to monitor and control the system in real-time via mobile and web-based interfaces, allowing for immediate intervention in case of any problems. Thanks to fault detection, operational issues were resolved quickly.

The developed SCADA and image processing-based lighting system provides a valuable solution for smart cities in terms of energy efficiency. Real-time human detection technologies and LDR sensors

help prevent unnecessary energy consumption, resulting in significant energy savings. During the 80-hour operational period, the system's reliability and performance were tested. It was observed that the luminaires were turned on and off at the correct times. For testing purposes, the cables of some luminaires were deliberately cut to simulate faults, and the system successfully detected and managed these issues. One of the key advantages of this system is its scalability. The SCADA system can be easily integrated into infrastructures of various sizes, making it suitable for lighting management in large cities. However, it is important to consider that environmental factors, such as extreme weather conditions, can negatively affect sensor performance. Therefore, it is recommended that sensors used in outdoor environments be made more durable or that additional measures be developed to address such challenges.

This study presents an effective prototype for energy savings and safe lighting management, while also laying the groundwork for future developments and expansion. Figure 10 shows the number of luminaires according to fault conditions, and the statuses of selected sample luminaires are provided in Figure 11.

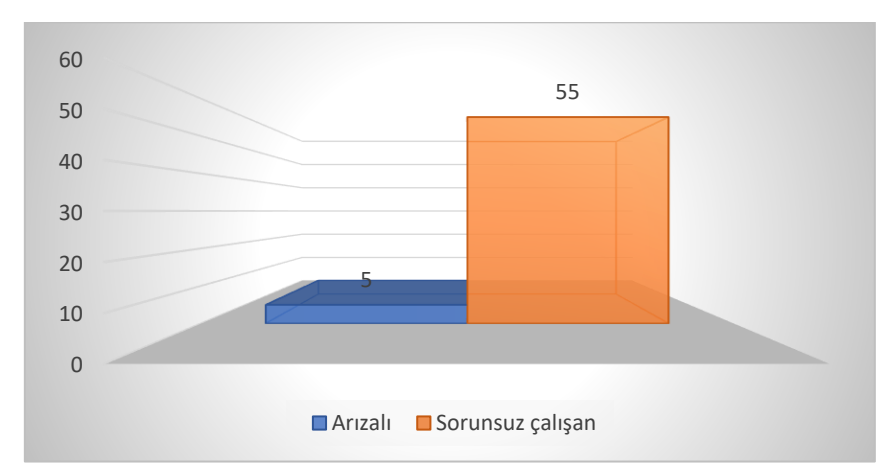


Figure 10 *Number of luminaires according to fault conditions.*

Bölge Adı	Armatür Adı	Enlem	Boylam	Açma/Ka pama Durumu	Arıza Durumu	Açılış Saati	Açılış Tarihi	Kapanış Saati	Kapanış Tarihi	LDR Sensör	Kamera Değer
PARK	L14	42.258	42.258	Kapalı	CALISIYOR	19:00	20.10.2024	05:45	20.10.2024	982	İnsan Yok
PARK	L15	42.258	42.258	Kapalı	CALISIYOR	19:00	20.10.2024	05:45	20.10.2024	982	İnsan Yok
PARK	L16	42.258	42.258	Kapalı	ARIZALI	19:00	20.10.2024	05:45	20.10.2024	982	İnsan Yok
SOKAK	L17	42.258	42.258	Kapalı	CALISIYOR	19:00	20.10.2024	05:45	20.10.2024	982	İnsan Yok
SOKAK	L18	42.258	42.258	Kapalı	CALISIYOR	19:00	20.10.2024	05:45	20.10.2024	982	İnsan Yok
SOKAK	L19	42.258	42.258	Kapalı	CALISIYOR	19:00	20.10.2024	05:45	20.10.2024	982	İnsan Yok
SOKAK	L20	42.258	42.258	Kapalı	CALISIYOR	19:00	20.10.2024	05:45	20.10.2024	982	İnsan Yok
SOKAK	L21	42.258	42.258	Kapalı	ARIZALI	19:00	20.10.2024	05:45	20.10.2024	982	İnsan Yok
SOKAK	L36	42.258	42.258	Kapalı	ARIZALI	19:00	20.10.2024	05:45	20.10.2024	982	İnsan Yok
OTOYOL	L53	42.258	42.258	Kapalı	CALISIYOR	19:00	20.10.2024	05:45	20.10.2024	982	İnsan Yok
OTOYOL	L54	42.258	42.258	Kapalı	CALISIYOR	19:00	20.10.2024	05:45	20.10.2024	982	İnsan Yok
OTOYOL	L55	42.258	42.258	Kapalı	CALISIYOR	19:00	20.10.2024	05:45	20.10.2024	982	İnsan Yok
OTOYOL	L56	42.258	42.258	Kapalı	ARIZALI	19:00	20.10.2024	05:45	20.10.2024	982	İnsan Yok

Figure 11

The situations of some sample luminaires are given.

In this study, the performance of the torchvision.models.detection.fasterrcnn_resnet50_fpn (pretrained=True) composite model used to classify and detect humans was evaluated in terms of Accuracy, Precision, and Recall evaluation metrics. Accuracy is the ratio between the correctly classified samples and the total number of samples in the evaluation dataset. Precision measures the number of correct samples retrieved divided by all retrieved samples. Lastly, Recall measures the number of correct samples retrieved divided by all correct samples [31]. These evaluation metrics are given in Equation 1.

$$Accuracy = \frac{TP + TN}{TP + FP + TN + FN}$$

$$Precision = \frac{TP}{TP + FP}$$

$$Recall = \frac{TP}{TP + FN}$$
(1)

In Equation 1, TP, TN, FP, and FN represent true positive, true negative, false positive, and false negative, respectively. Accuracy, Precision, and Recall values of the model in different light conditions are given in Table 1.

Table 1 *Performance values of the model in different light conditions.*

Environment	Accuracy	Precision	Recall	
Train	0.99	0.99	0.99	
Test (Light)	0.98	0.98	0.98	
Test (Dark)	0.94	0.91	0.94	

The results in Table 1 demonstrate that the accuracy of the model in the training set is 0.99. Additionally, when different environmental conditions are examined on the test set, it is seen that the accuracy of the model is 0.98 in the light environment and the accuracy of the model is dropped to 0.94 in the dark environment. Figure 12 demonstrates the real-time testing of the trained model for human detection in light and dark environments.



Light environment

Dark environment

Figure 12
Real-time human detection.

As seen in Figure 12, the trained model was able to identify all human pictures in the image in the bright environment; however, the model trained in the dark environment could not exhibit the same performance. As a result, the designed system monitors and controls parks and roads in real-time with very good success and intervenes immediately in case of any problems.

CONCLUSIONS

Image processing techniques and real-time remote lighting systems are widely used in many fields, and these applications are rapidly increasing every day. In this study, the real-time remote monitoring and control of street, road, and park lighting fixtures in the prototype are achieved with the real-time remote lighting system. Software suitable for the system is developed using .NET MVC for the web part and Flutter for the mobile part of the Real-Time Remote Lighting System. The real-time remote lighting system software includes features such as user management, database management, alarm management, and report management. In conclusion, integration of the real-time remote lighting system with the prototype has enabled monitoring, maintenance, and rapid and accurate transmission of problems occurring in street, road, and park lighting fixtures to the system. The real-time remote lighting system using image processing techniques has not only achieved energy savings but also reduced maintenance costs.

Ethical statement

This article is extracted from my master thesis dissertation entitled "Scada Sistemi ve Görüntü İşleme Teknikleri Kullanarak Gerçek Zamanlı Aydınlatma Sisteminin Tasarımı", which was presented on 29.02.2024 supervised by Muhammed KARAALTUN.

Conflict of interest

The authors have no conflicts of interest to disclose for this study.

Author Contributions

Research Design (CRediT 1) M.A. (%50) – M.K. (%50)

Data Collection (CRediT 2) M.A. (%40) - M.K. (%40)

Research - Data Analysis - Validation (CRediT 3-4-6-11) M.A. (%50) - M.K. (%30)

Writing the Article (CRediT 12-13) M.A. (%50) - M.K. (%40)

Revision and Improvement of the Text (CRediT 14) M.A. (%40) - M.K. (%40).

REFERENCES

- [1] A. Yankı, M. Elmaci, V. Aslantaş, Image processing and deep learning based smart door lock system using face recognition, *Electronic Letters on Science and Engineering* . 20 (2024), 11–36.
- [2] E. E. Elmas, M. Alkan, insansız hava araçlarıyla hareketli nesnelerin tespit ve takibi, *Gazi Üniversitesi Fen Bilimleri Dergisi Part C: Tasarım ve Teknoloji*. 10 (2022), 1111–1126. doi:10.29109/gujsc.1199340
- [3] O. Ç. Şimşek, E. Kızılkaya Aydoğan, Y. Delice, Denim kumaşların görüntü tahminlemesinde üretim parametreleri ve görüntü işleme tekniklerinin kullanılması, *International Journal of 3D Printing Technologies and Digital Industry*. 8 (2024), 104–113. doi:10.46519/ij3dptdi.1337641
- [4] O. İnam, D. Somer, G. Üney, and A. Soylu, Calculation of the choroidal vascularity index and tissue distribution indexes in different retinal and choroidal regions by employing digital image processing techniques in optical coherence tomography images, *Genel Tip Dergisi*. 33 (2023), 785–795. doi:10.54005/geneltip.1349861
- [5] F. G. Tan, A. Sinan Yüksel, E. Aydemir, M. Ersoy, Derin öğrenme teknikleri ile nesne tespiti ve takibi üzerine bir inceleme, *European Journal of Science and Technology*. 25 (2021), 159–171. doi:10.31590/ejosat.878552
- [6] G. Zecevic, Web based interface to SCADA system, POWERCON 1998- 1998 International Conference on Power System Technology, Proceedings. 2 (1998), 1218–1221. doi:10.1109/ICPST.1998.729279
- [7] M. H. İbrahim, SCADA sistemi: Şehir içi ve şehirlerarası yolların aydınlatma sisteminin kontrolü ve otomasyonu, *Cukurova University Journal of the Faculty of Engineering*. 37 (2022), 991–999.
- [8] T. Özseven, N. Sağlam, IoT based street lighting and computer aided control, *Turkish Journal of Nature and Science*. 10 (2021), 265–274. doi:10.46810/tdfd.997116
- [9] C. Perdahçı, Z. Ünal, B. Bıkmaz, IOT Tabanlı Akıllı Yol Aydınlatma Sistemi içinde: *VI. Elektrik Tesisat Ulusal Kongre ve Sergisi*, İzmir, 2019: ss. 1–10.
- [10] H. Çelik, B. Büyükkınacı, M. B. Yurtseveni, Aydınlatma Otomasyon Teknikleri: Cendere Caddesi Örneği, *IX. Ulusal Aydınlatma Sempozyumu*, 2017 : ss. 1–10.
- [11] S. M. Sorif, D. Saha, P. Dutta, Smart street light management system with automatic brightness adjustment using bolt IoT platform, 2021 IEEE International IOT, Electronics and Mechatronics Conference, IEMTRONICS 2021 Proceedings, 2021: ss. 1–4. doi:10.1109/IEMTRONICS52119.2021.9422668
- [12] O. F. Farsakoglu, I. Atik, H. Yusuf, H. Kilis, LED aydınlatma sistemlerinin çevre kirliliğini azaltmadaki etkileri, *Yüzüncü Yıl Üniversitesi Fen Bilimleri Enstitüsü Dergisi* 19 (2014), 94–103.
- [13] E. Yılmaz, O. Erden, N. Kocadağ, Sokak aydınlatması dönüşümü fayda maliyet analizi üzerine bir mühendislik ekonomisi çalışması, *Gazi Journal of Engineering Sciences*. 5 (2019), 280–289. doi:10.30855/gmbd.2019.03.09.
- [14] T. P. Nam, N. Van Doai, Application of Intelligent Lighting Control for Street Lighting System, 2019 International Conference on System Science and Engineering (ICSSE), 2019: ss. 53–56. doi:10.1109/ICSSE.2019.8823357.
- [15] A. Eldem, H. Eldem, A. Palalı, Görüntü işleme teknikleriyle yüz algılama sistemi geliştirme, *Bitlis Eren Üniversitesi Fen Bilimleri Dergisi*. 6 (2017), 44–48.
- [16] B. Demir, N. Çetin, Z. A. KUŞ, Görüntü işleme tekniği ile yabancı ot renk özelliklerinin belirlenmesi, *Alınteri Zirai Bilimler Dergisi*. 31 (2016), 59–64.

- [17] B. Şin, İ. Kadioğlu, İnsansız hava aracı (İHA) ve görüntü işleme teknikleri kullanılarak yabancı ot tespitinin yapılması, *Turkish Journal of Weed Science*. 22 (2019), 211–217.
- [18] E. Güney, C. Bayılmış, An implementation of traffic signs and road objects detection using faster R-CNN, *Sakarya University Journal Of Computer And Information Sciences*. 5 (2021), 216–224. doi:10.35377/saucis.05.02.1073355
- [19] C. Topcu, P. Güneş, Bitki hastalıklarını tespitte derin öğrenme: ResNet modelinin etkinliği, *Anadolu bil meslek yüksekokulu dergisi*. 19 (2024), 31–65. doi:10.17932/iau.abmyod.2006.005/abmyod_v19i69002
- [20] A. Mawlood, A.G Abdulghani, G.G.M. Dalveren, Moving object detection in video with algorithms YOLO and Faster R-CNN in different conditions, *European Journal of Science and Technology*. 33 (2022), 40–65. doi:10.31590/ejosat.1013049.
- [21] M. Canayaz, A. Milanlioglu, S. Şehribanoğlu, A. Yalın, A. Yokuş, A comparative study of segmentation algorithms for intracerebral hemorrhage detection, *Firat University Journal of Experimental and Computational Engineering*. 3 (2024), 75–94. doi:10.62520/fujece.1423648.
- [22] B. Özcan, H. Bakır, Yapay Zeka Destekli Beyin Görüntüleri Üzerinde Tümör Tespiti, International Conference on Pioneer and Innovative Studies (ICPIS). 1 (2023), 297–306.
- [23] S. Gündoğdu, Ö. Şahin, Su dağıtım sistemlerinde scada uygulaması, *DEÜ Mühendislik Fakültesi Fen ve Mühendislik Dergisi*. 10 (2008), 23–32.
- [24] B. Citkuseva-Dimitrovska, E.Z.O. Flyght, and U.G. Stefanov, SCADA System for Process Data Exchange in Master Slave RF and Iot Network, *The Eurasia Proceedings of Science, Technology, Engineering & Mathematics (EPSTEM)*. 28 (2024), 554–564.
- [25] O. Duymazlar, D. Engin, Design, Application and analysis of an OPC-based SCADA System, *Politeknik Dergisi*. 26 (2023), 991–999. doi:10.2339/politeknik.1029629.
- [26] H.C. Bayrakçı, H. Büyükpatpat, PLC ve scada kontrol yöntemleri ile sıvı dolum otomasyonu, *European Journal of Science and Technology*. 27 (2021), 283–291. doi:10.31590/ejosat.877004
- [27] Street Light Management System Manufacturer, Supplier, Exporter from Vadodara, (2024). https://www.instrumentuniversal.com/street-light-management-system-2538636.html (erişim 11 Haziran 2024).
- [28] D. Bailey, E. Wright, *Practical SCADA for industry*. Elsevier Oxford, 2006. [Çevrimiçi]. Erişim adresi: https://s2.smu.edu/~nair/ftp/senior_design/scada/Practical_SCADA_for_Industry.pdf
- [29] M. Vanderzee, D. Fisher, G. Powley, R. Mohammad, SCADA: Supervisory Control and Data Acquisition, *Oil and Gas Pipelines: Integrity and Safety Handbook*, Wiley, 2015: ss. 13–26. doi:10.1002/9781119019213.CH02
- [30] F.J. Maseda, I. López, I. Martija, P. Alkorta, A. J. Garrido, I. Garrido, Sensors data analysis in supervisory control and data acquisition (Scada) systems to foresee failures with an undetermined origin, *Sensors*. 21 (2021). doi:10.3390/s21082762
- [31] M. Vakili, M. Ghamsari, M. Rezaei, Performance analysis and comparison of machine and deep learning algorithms for IoT data classification, (2023). https://arxiv.org/abs/2305.12345 (erişim 15 Temmuz 2024).
- [32] M. Karaçor, K. Keleş, Otomasyon Sistemlerinin Bileşenleri, VI. Otomasyon Sempozyumu, Samsun, 2007: ss. 1–10.



Vol: 7 No:2 Year: 2025

Araştırma Makalesi/Research Article

e-ISSN: 2667-7989

https://doi.org/10.47112/neufmbd.2025.90

Ankastre Temel, Winkler ve Psödo-eşlenik Yöntemlerine Göre Üstyapı Performansının İncelenmesi

Ali Serdar ECEMİŞ 1* D Yavuz YENGİNAR 1 D İlyas ÖZKAN 1 D

¹ Necmettin Erbakan University, Faculty of Engineering, Department of Civil Engineering, Konya, Türkiye

Makale Bilgisi

Geliş Tarihi: 04.07.2024 Kabul Tarihi: 20.01.2025 Yayın Tarihi: 31.08.2025

Anahtar Kelimeler:

Ankastre temel, Deprem, Psodo-eşlenik yöntem, Winkler yöntemi, Yapı-zemin etkileşimi. Bu çalışmada, orta sıkı kumlu zemin üzerine oturan 5 katlı bir binanın performansı ankastre temel, Winkler ve Pseudo-eşlenik yöntemleriyle analiz edilmiştir. Yapının periyodu, kolonlara etki eden eksenel yükler ve kesme kuvvetleri, deprem kuvvetleri, kat yer değiştirmeleri, temel taban basıncı ve yer değiştirme değerleri statik ve dinamik yükleme durumlarında belirlenmiştir. Yapısal mühendislikte kullanılan temel çözüm yöntemi, çeşitli yükleme koşullarında binaların dinamik ve statik davranışlarını derinden etkilemektedir. Winkler ve Pseudo-eşlenik yöntemlerinin ankastre temele göre karşılaştırılmasıyla, birkaç önemli fark ortaya çıkmıştır: Winkler ve Pseudo-eşlenik yöntemlerinde bina periyotları birbirine yakın iken ankastre temel çözümünde periyot %6,7 daha fazla olmaktadır. Ölü ve hareketli yük (G+Q) altında kolonlara etki eden eksenel yükler temel analiz yönteminden oldukça az etkilenmektedir, ancak deprem (EQx) yükü altında Winkler ve Pseudoeşlenik yöntemleri, ankastre temel yöntemine göre 1. ve 5. kat kolonlarındaki eksenel yükleri önemli ölçüde azalmaktadır. Köşe kolonlarındaki kesme kuvvetleri Winkler ve Pseudo-eşlenik yöntemlerinde %46 daha düşük elde edilmiştir. Ayrıca, bu yöntemler deprem kuvvetinde %7 artış ve ankastre temel yöntemine göre %4,7 daha az kat yer değiştirmesi sonucunu vermiştir. Maksimum temel basıncı, oturma ve farklı oturmanın konumu, kullanılan temel analiz yöntemine bağlı olarak değişmektedir. Bu bulgular, özellikle deprem olayları gibi farklı yükleme senaryoları altında yapısal stabilite, performans ve dayanıklılığın optimize edilmesinde temel seçiminin kritik rolünü vurgulamaktadır.

Investigation of Superstructure Performance Based on the Fixed Base Foundation, Winkler, and Pseudo-Coupled Methods

Article Info

Received: 04.07.2024 Accepted: 20.01.2025 Published: 31.08.2025

Keywords:

Earthquake, Fixed-base foundation, Pseudo-coupled method, Soil-structure interaction Winkler method.

ABSTRACT

ÖZET

In the present study, the performance of 5-story building resting on medium dense sandy soil was analyzed by fixed-base, Winkler and Pseudo-coupled methods. The period of structure, axial loads and shear forces acting on columns, earthquake forces, story displacements, foundation base pressure and settlement values were determined in static and dynamic loading cases. The choice of foundation solution method in structural engineering profoundly influences the dynamic and static behavior of buildings under various loading conditions. Comparing Winkler and Pseudo-coupled methods to the fixed-base foundation, several key differences emerge: building periods are closer together in Winkler and Pseudo-coupled methods, with fixed-base periods being 6.7% longer. Axial loads on columns under gravity plus live load (G+Q) are minimally affected by the foundation method, but under earthquake (EQx) loading, Winkler and Pseudo-coupled methods significantly reduce axial loads on 1st and 5th floor columns compared to the fixed-base method. Shear forces on corner columns are 46% lower with Winkler and Pseudo-coupled methods. Moreover, these methods result in a 7% increase in earthquake force and 4.7% less story displacement than the fixed-base method. Additionally, the location of maximum base pressure, settlement, and differential settlement varies depending on the foundation analysis method employed. These findings emphasize the critical role of foundation selection in optimizing structural stability, performance, and resilience under different loading scenarios, particularly seismic events.

To cite this article:

Ecemiş, A.S., Yenginar, Y. & Özkan, İ. (2025). Investigation of superstructure performance based on the fixed base foundation, Winkler, and pseudo-coupled methods. *Necmettin Erbakan University Journal of Science and Engineering*, 7(2), 259-272. https://doi.org/10.47112/neufmbd.2025.90

*Corresponding Author: Ali Serdar Ecemiş, asecemis@erbakan.edu.tr



INTRODUCTION

The stability and structural integrity of any building rely fundamentally on the efficacy of its foundation system [1]. In civil engineering, the choice of foundation analysis method plays a pivotal role in ensuring the safety and longevity of structures, particularly in the context of varying soil conditions, structural loads, and environmental factors [2,3,4]. Among the myriad techniques available, three prominent methodologies stand out: the fixed base method [5,6], the Winkler method [7,8,9], and the pseudo-coupled approach [10]. Each of these methods offers distinct advantages and considerations in analyzing foundation behavior and subsequently influencing the stability and performance of the superstructure they support.

The fixed base method represents a classical approach to foundation analysis, assuming a rigid connection between the foundation and the underlying soil. This method simplifies the analysis by negating the effects of soil-structure interaction, thereby treating the structure as isolated from its supporting medium [11,12]. While this assumption facilitates straightforward analysis and design processes, it may lead to inaccuracies in predicting structural response, particularly in situations where soil characteristics significantly influence structural behavior [13,14].

In contrast, the Winkler method acknowledges the interaction between the structure and the underlying soil through a simplified representation of soil behavior [15,16,17]. It divides the soil into discrete springs or elements, each characterized by stiffness parameters such as the modulus of subgrade reaction. By incorporating soil-structure interaction in this manner, the Winkler method offers a more realistic representation of foundation behavior compared to the fixed base approach [18,19,20]. However, its accuracy is contingent upon appropriate selection and calibration of soil parameters, which can pose challenges in practice, especially for heterogeneous soil profiles [18,21].

In the analysis of building structures, the fixed-base assumption can be preferred. However, since this method typically neglects soil effects, it may lead to inaccurate modeling of dynamic behavior. Fixed-base analysis often underestimates the natural period of the building while overestimating its frequency. In contrast, when soil springs are introduced using the Winkler method, dynamic behaviors, such as the increase in the natural period due to poor soil conditions, are more realistically represented. Neglecting soil effects, particularly for weak soils, can result in incorrect calculation of seismic loads. Therefore, the Winkler method provides more accurate results and should be favored over the fixed-base assumption in building design and analysis [22].

The pseudo-coupled method represents a more advanced approach that seeks to reconcile the advantages of both the fixed base and Winkler methods while mitigating their respective limitations. This method employs numerical techniques, such as finite element analysis, to simulate the interaction between the structure and the underlying soil in a more comprehensive manner [10]. By considering the dynamic and nonlinear behavior of both the structure and the soil, the pseudo-coupled method offers enhanced accuracy in predicting foundation response and superstructure stability under various loading conditions [21,23,24]. However, its implementation may require specialized expertise and computational resources, making it less accessible for routine engineering applications.

The Winkler and Pseudo-coupled methods differ in their handling of raft foundation settlements and soil-structure interaction. The Winkler method is simpler and effective for rigid foundations, particularly on D-class soils, where settlements are nearly uniform. In contrast, the Pseudo-coupled method is more suitable for flexible foundations or rigid foundations on stronger C-class soils, as it accounts for differential settlements by dividing the raft foundation into multiple regions. Increasing the number of regions in the Pseudo-coupled method improves accuracy, reducing both settlement and differential settlement values. Both methods rely heavily on the accurate determination of the subgrade

reaction coefficient, which directly affects settlement behavior. While the Winkler method offers simplicity, the Pseudo-coupled approach provides greater precision, especially for complex soil conditions [9].

Understanding the effects of foundation analyses with fixed base, Winkler, and pseudo-coupled methods is crucial for ensuring the safety, efficiency, and cost-effectiveness of structural designs. By elucidating the interplay between these methodologies and their impact on superstructure stability, engineers can make informed decisions in selecting the most appropriate foundation analysis technique for a given project, thereby optimizing the performance and resilience of built infrastructure in diverse geotechnical environments.

In the present study, the performance of 5-story building resting on medium dense sandy soil was analyzed by fixed-base, Winkler and Pseudo-coupled methods. The period of structure, axial loads and shear forces acting on columns, earthquake forces, story displacements, foundation base pressure and settlement values were determined in static and dynamic loading cases.

MATERIALS AND METHODS

Site Conditions

A location was chosen in Hatay, one of the provinces most affected by the Kahramanmaraş earthquake on February 6, 2023 to determine local ground properties. The selected location (latitude: 36.198535, longitudal:36.159735) belongs to one of the buildings located by the Asi River in the center of Hatay.

The sediments in the Antakya region primarily consist of clay, sand, and gravel within alluvial deposits. The local soil class is generally weak, with some areas classified as ZD [25].

A medium dense sandy soil profile with infinite depth was designed under the structure. Geotechnical properties and seismic parameters of the soil are given in Table 1.

Table 1 *Geotechnical and seismic properties of local soil.*

Property	Value
Standard penetration blow count, N _{SPT}	15.0
Bulk unit weight, γ_n (kN/m ³)	17.3
Poisson ratio, v	0.3
Oedometric Modulus, E (MPa)	18.6
Coefficient of subgrade, k (kN/m³)	18000
Local soil class (TBEC, 2019)	ZD
Local soil class (EN 1998-1, 2004)	C
Short period design spectral acceleration coefficient, S _{DS}	1.1399
Short period map spectral acceleration coefficient, S _S	1.0590
Map spectral acceleration coefficient for 1.0 second period, S ₁	0.2760
Design spectral acceleration coefficient for 1.0 second period, S _{D1}	0.5652
Local soil impact coefficient for short period region, Fs	1.0764
Local soil impact coefficient for 1.0 second period, F ₁	2.0480

Structure information

In the central area of Hatay, a variety of buildings of varying heights could be found at the located along the banks of the Asi River. Notably, the 5-story structures exhibited superior seismic performance during the February 6 earthquake when compared to taller buildings [26]. In the study, the performance of 5-story building is investigated based on the foundation analyses methods. The properties of building are presented in Table 2. The building is symmetrical and has a square raft foundation. The 3D visual

and typical floor and foundation plan of the building modeled with Etabs program, which analyzes with finite element method, are presented in Figure 1 and Figure 2.

Table 2 *The properties of building.*

Number of Story	5
Story Height (m)	3
Structure Height (m)	15
Span X-Y (m)	5.75
Number of Span X-Y	6
Building Dimensions (m)	34.50 x 34.50
Column Dimensions (m)	50 x 50
Beam Dimensions (m)	40 x 60
Slab Thickness (m)	0.150
Dead Load (kN/m ²)	2.50
Live Load (kN/m ²)	3.50
Concrete Class	C30/37
Reinforcement	B420C
Analysis type	Vertical+Horizontal
Load-bearing system behavior coefficient, R	8.00
Resistance excess coefficient, D	3.00
Building importance coefficient, I	1.00

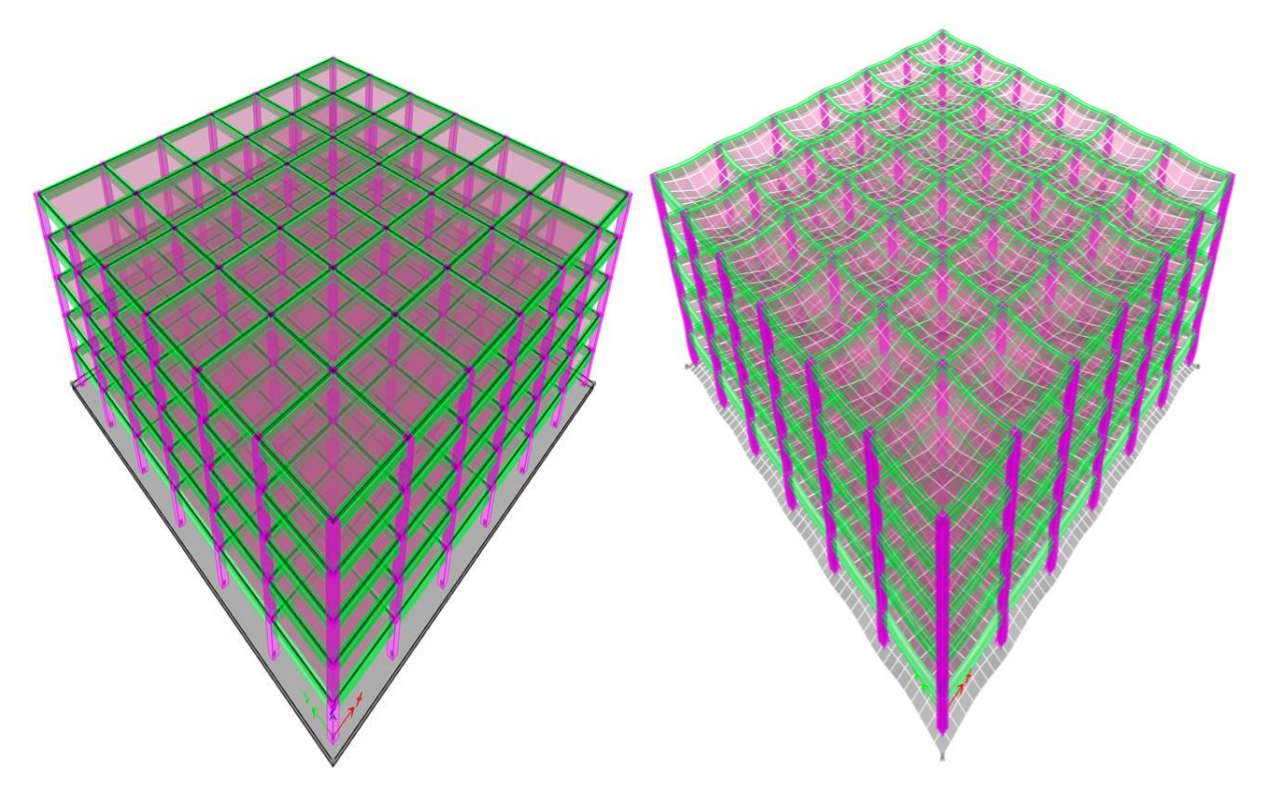


Figure 1
The perspective and meshed view of building.

In the analyzes, the effective section stiffnesses, which are required to be used in TBDY 2018, were taken into consideration. The effective section stiffness multipliers for horizontal and vertical elements are shown in Table 3.

 Table 3

 Effective section stiffness multipliers.

Reinforced Concrete Structural System Element	Effective Cross Section Stiffness Multiplier		
Slab (In plane)	Axial	Shear	
Slab	0.25	0.25	
Slab (Out of Plane)	Bending	Shear	
Slab	0.25	1.00	
Frame	Bending	Shear	
Beam	0.35	1.00	
Column	0.70	1.00	

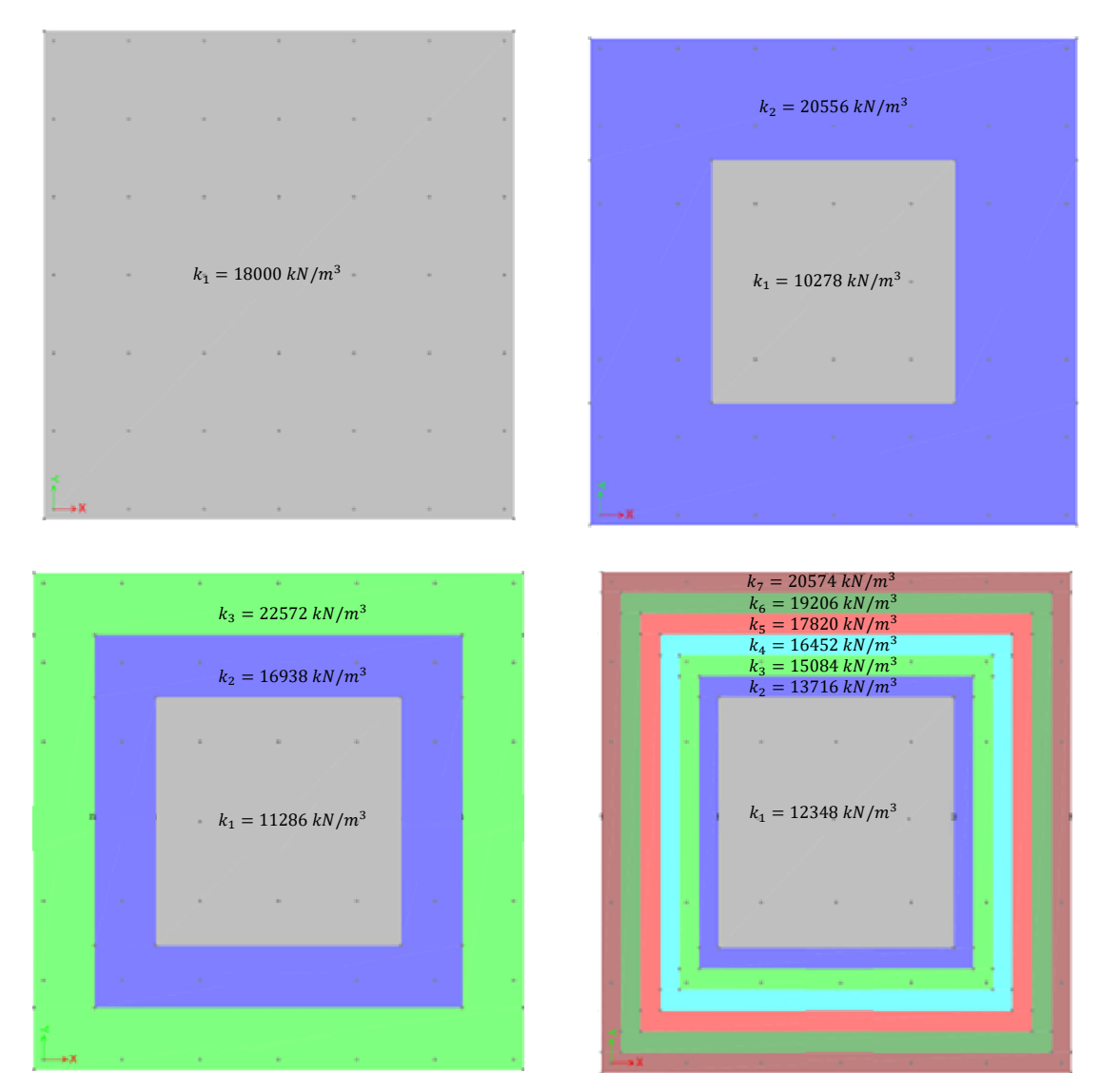


Figure 2
The foundation modelling and assigned area springs of models.

Methodology

The foundation of building has a width and length of 34.5m and 34.5 m, respectively. A soil has an 18000 kN/m³ of subgrade reaction is defined under the foundation. The foundation is analyzed based on the fixed base, Winkler, and Pseudo-coupled methods.

In the fixed base analysis, any soil is not defined under the foundation and therefore the soil-structure interaction is not existing.

In the Winkler method [9], the soil under the foundation is modeled with springs of equivalent stiffness. The spring coefficient corresponds to the subgrade coefficient of the soil (k_s), and it is assumed that each spring operates independently of each other. The soil subgrade coefficient is obtained by dividing the stress applied to the soil by the amount of settlement that occurs (see Eq. 1). The stress occurring in the foundation base arises from the loads transferred from the superstructure to the foundation (dead load, live load, earthquake forces, etc.). As long as the soil subgrade coefficient and foundation base pressure are known, settlements under the foundation can be determined. Analysis of the soil-structure interaction examines the settlement profile under the foundation and the resulting changes in the performance of the superstructure. However, modeling the soil under the foundation with equivalent springs in the Winkler method provides only an approximate solution for soil-structure interaction. It is known that the actual settlement profile varies according to differences in soil-foundation stiffness. To address this limitation of the Winkler method, the pseudo-coupled method was developed.

$$k_s = \frac{q_0}{s} \tag{1}$$

where, k_s is subgrade coefficient of soil, q₀ is base pressure of foundation, s is the settlement.

In the pseudo-coupled method, the foundation is divided into different regions and a different bearing coefficient is defined under each region. While the foundation is divided into different regions, the edge lengths of the innermost region are half of the foundation edges in both directions. In addition, the subgrade coefficient of the outer zone is defined to be twice that of the inner one. In this method, the settlement profile can be obtained more realistically as the subgrade coefficient increases from the center of the foundation to the outside.

In the analysis of the structure-foundation system, while the foundation is a single area (1 area) in the Winkler method, it is divided into 2, 3, 7 areas in the Pseudo coupled method (Figure 3). In different foundation modifications, the subgrade coefficient values to be used for each area were calculated with Equations 2 and 3. The area of each region and the subgrade coefficient values are presented in Table 4.

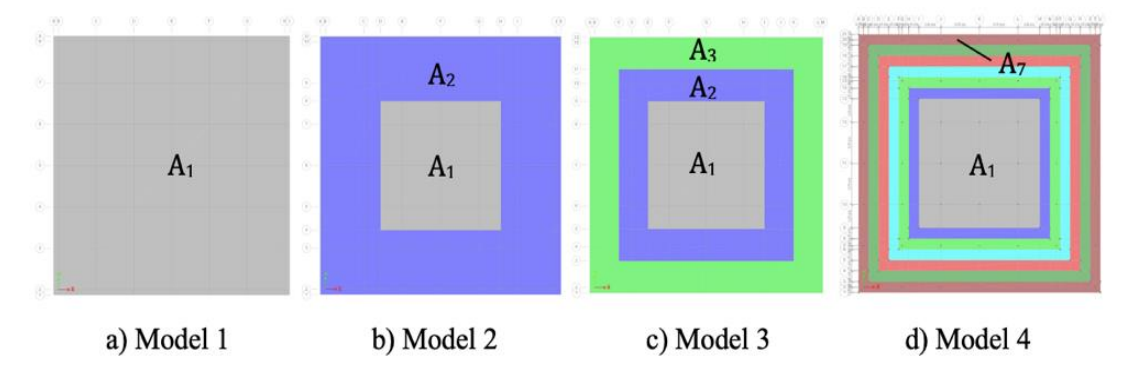


Figure 3Foundation modifications based on different analysis method: a) The Winkler Method (1 area) and Pseudo-Coupled Method by b) 2 regions, c) 3 regions, and d) 7 regions

$$k_1 \cdot A_1 + k_2 \cdot A_2 + \dots + k_n \cdot A_n = k_{avg} \cdot A_{total}$$
 (2)

$$k_1 = \dots = \frac{(x-1) \cdot k_{x-n}}{2x-6} = \dots = \frac{(x-1) \cdot k_{x-3}}{2x-5} = \frac{(x-1) \cdot k_{x-2}}{2x-4} = \frac{(x-1) \cdot k_{x-1}}{2x-3} = \frac{k_x}{2}$$
(3)

where k_n is the coefficient of subgrade reaction at the region n, A_n is the area of region n, k_{avg} is a value of the coefficient of subgrade reaction used in the Winkler method, and A_{total} is the total area of the raft foundation, x and n are positive integer, $x \ge 2$ and $x \ge n$.

 Table 4.

 The area and subgrade coefficient values of each region

Dogion	Area, A (m ²)			Subgrade coefficient, ks (kN/m³)				
Region	Model 1	Model 2	Model 3	Model 4	Model 1	Model 2	Model 3	Model 4
1	1296	324	324	324	18000	10278	11286	12348
2	-	972	405	117	-	20556	16938	13716
3	-	-	567	135	-	-	22572	15084
4	-	-	-	153	-	-	-	16452
5	-	-	-	171	-	-	-	17820
6	-	-	-	189	-	-	-	19206
7	-	-	-	207	-	-	-	20574

The structure-foundation system was analyzed in G+Q and E loading cases separately. The effect of the loading combinations of G+Q and 1.4G+1.6Q cases on the superstructure in percentages is same. Therefore, G+Q and EQx loading cases were investigated separately to see the effect of each loading. Axial force, shear force, moment, base pressure and settlement values were determined for the columns of C25, C28, and C7 at the center, edge and corner points of the foundation, respectively. The earthquake force was considered only in the x direction since the structure is symmetrical.

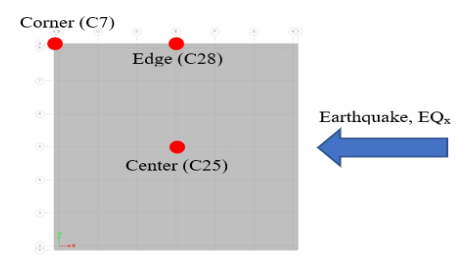


Figure 4
The location of columns and the direction of the earthquake.

RESULTS

Periods

Buildings vibrate according to their rigidity and the loads (earthquake, wind, etc.) they are exposed to. These vibrations occur within a specific time frame and sequence. The period of time until the structure returns to its previous state after undergoing a unit displacement, i.e., vibration, from its current position to the right or left, is termed the structure period. This period varies depending on the characteristics of the structural system of each building. The two most important factors determining the period are the mass and rigidity of the structure. Consequently, the force acting on the structure depends on both the mass and acceleration of the structure. The building period calculated by program was obtained as 0.907 s for the fixed-based solution, 0.967 s for the Winkler method, and 0.959-0.966 s for the pseudo-coupled methods. Since the building is symmetrical, the period values of the 1st and 2nd modes in the x and y directions are equal in all models. The 3rd mode was obtained as a torsional mode (Figure 5). The period values calculated by the program and used in the calculation of the base shear force are also given in Figure 5. It has been observed that the analysis method of the building foundation does not considerably affect the period of the superstructure since it is mostly affected by the weight and rigidity of the structure. In addition, the lowest period is obtained in fixed-base foundation since there is no soil-structure interaction. However, in the Winkler and Pseudo-coupled methods, structure period increases since the subsoil conditions are taken into consideration due by soil-structure interaction. Settlements under the foundation base increases the periods.

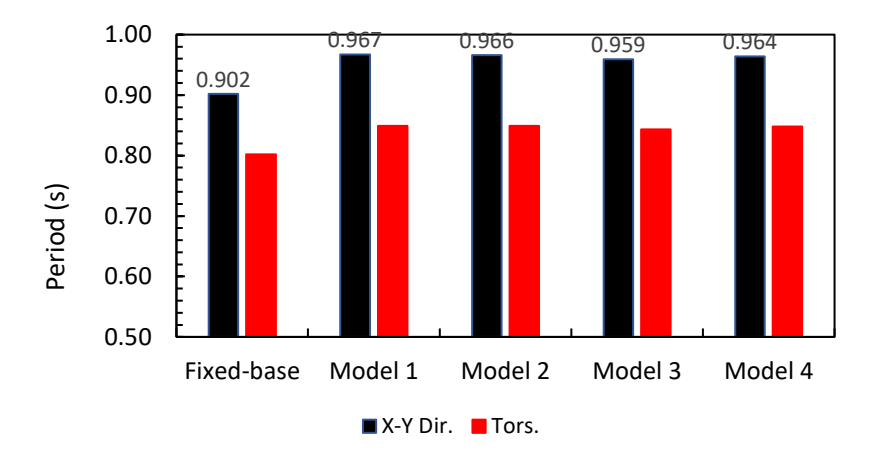


Figure 5
Structure periods.

Axial loads

Axial loads at columns of C7, C28, C25 for G+Q loading cases and C7 column for EQx loading case are presented in Figure 6. In the G+Q loading cases, there is a 2-3% difference between axial loads on columns depending on the foundation analysis methods. In the static loading case, axial loads on columns depends on the structural loads and soil-structure interactions do not affect the axial load distribution on the structure even if the foundation is analyzed by fixed-base, Winkler, and Pseudocoupled methods.

Axial load distribution at each story on columns of C25 (edge column) and C28 (center column) is same for G+Q and EQx loading cases because these columns are located on the center axis of floor plan, that is earthquake force is not applied. There is a 4.2% difference between axial loads of EQx loading case since soil-structure interaction is considered by Winkler and Pseudo-coupled methods (Figure 6d). However, axial load increases 83% and 30% at stories 5 and 1, respectively, for fixed-base solution compared with the Winkler and Pseudo-coupled methods. Considering soil-structure interaction in EQx loading cases decreases axial loads on each story.

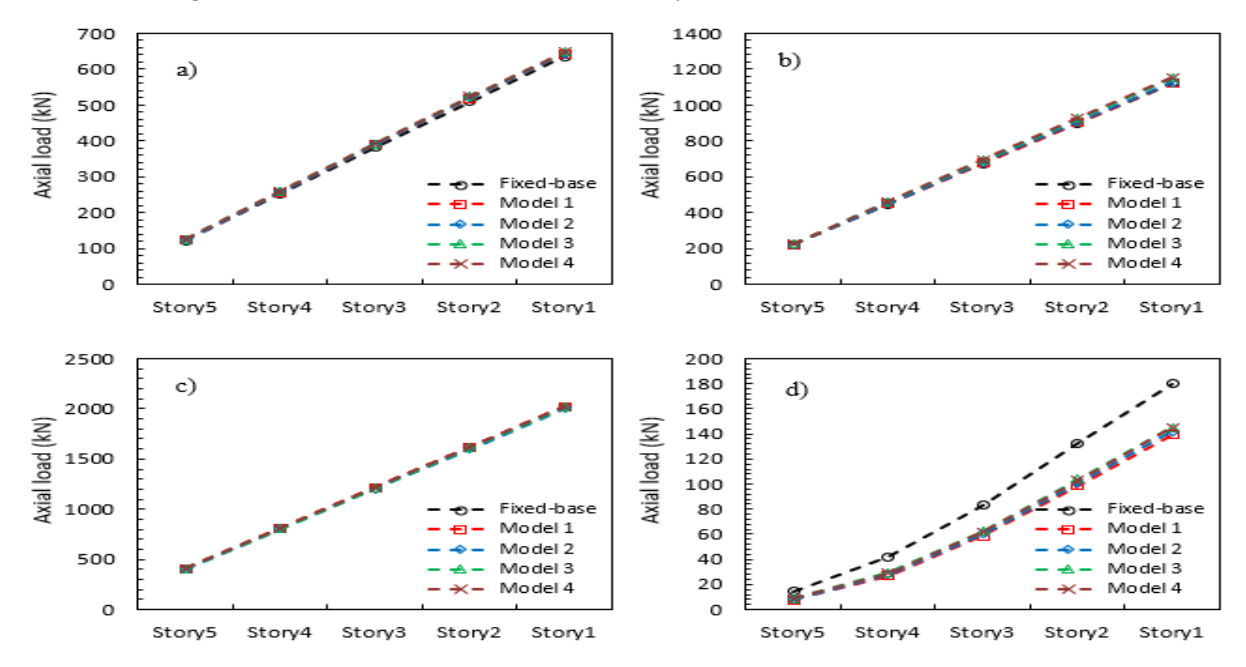


Figure 6Axial loads at columns of a) C7, b) C28, c) C25 for G+Q loading cases and d) C7 column for EQx loading case

Shear force

Shear forces at columns of C7, C28, C25 for EQx loading case are presented in Figure 7. Shear forces at the columns on the symmetry axis (C25 and C28) are very close even if the foundation analysis methods are different. However, shear force at the corner column (C7) is obtained greater for fixed-base solution (no soil-structure interaction) than Winkler and Pseudo-coupled methods. Considering soil-structure interaction decreases the shear forces acting on each story. In addition, increasing ratio of shear force from story 5 to story 1 decreases in the Winkler and Pseudo-coupled methods, but it increases in the fixed-base solution. Shear force of C7 column at story 1 in fixed-base solution is 46% greater than Winkler and Pseudo-coupled methods.

Earthquake forces and story displacements

Earthquake forces acting on each story and the displacements occurs resulting of these earthquake forces are presented in Figure 8. In the fixed-base foundation, earthquake forces acting at the story 5 is largest and 7% greater than soil-structure systems (Winkler and Pseudo-coupled methods). However, displacement of story 5 due to fixed-base solution is 4.7% smaller than Winkler and Pseudo-coupled methods. Soil-structure systems are less affected by earthquake forces but capable of large deformations.

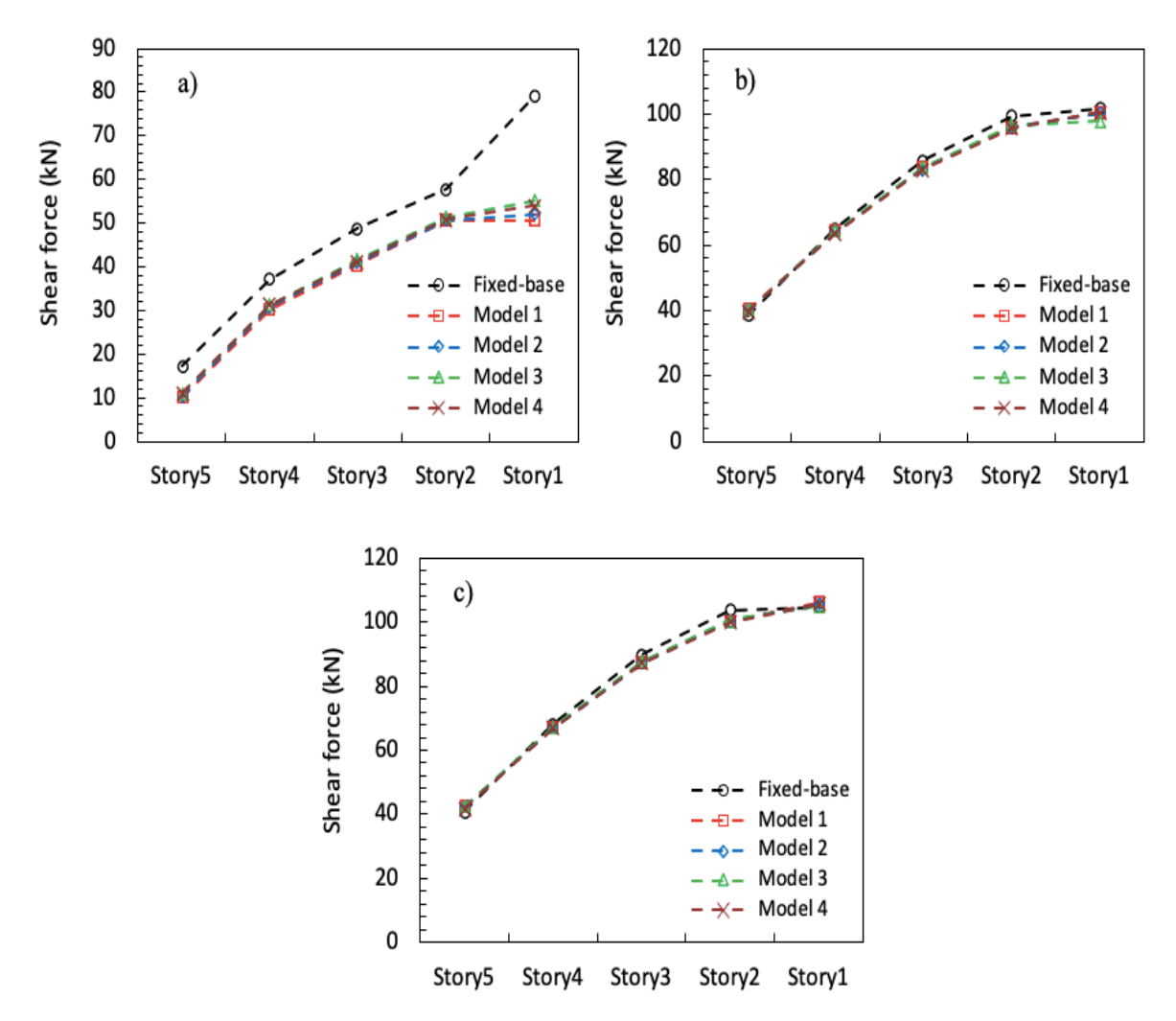


Figure 7
Shear forces at columns of a) C7, b) C28, c) C25 for EQx loading cases)

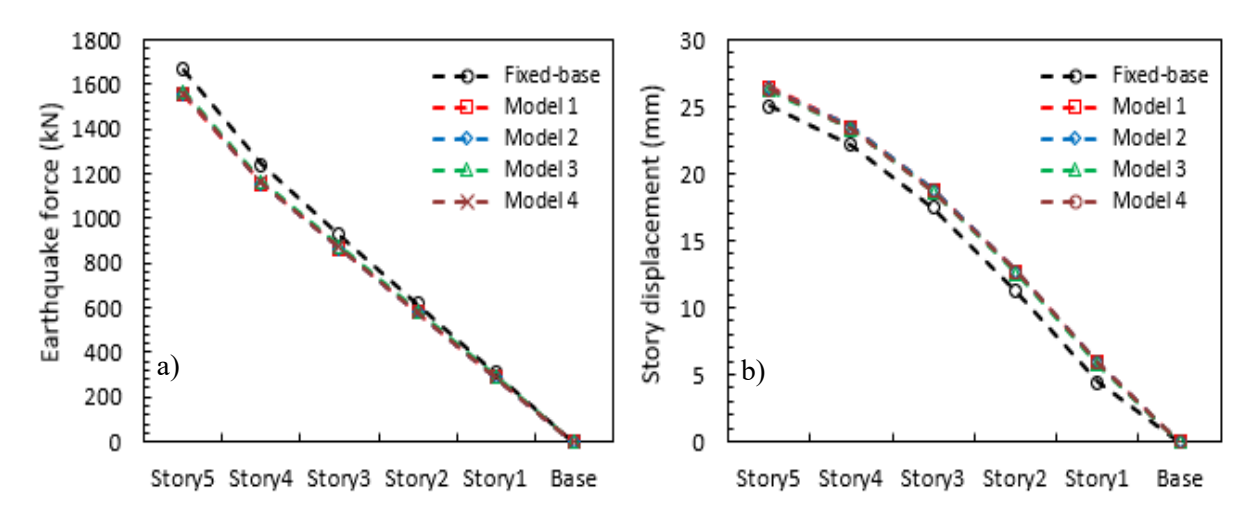


Figure 8
Shear forces at columns of a) C7, b) C28, c) C25 for EQx loading cases

Base Pressure

Base pressures at column bottom for G+Q and G+Q+EQx loading cases were presented in Figure 9. In the fixed-base solution, base pressures at any point of foundation are not exist since there is no subsoil or foundation.

In the Winkler solution for G+Q loading case, there is a 10% difference between the base pressures under the corner (C7), edge (C25) and center (C28) columns, while in the Pseudo-coupled method there is a 45% difference. In the Pseudo-coupled method, the base pressures under the corner and edge columns are lower than in the Winkler method, while they are higher under the center column. The reason for this difference is that in the Pseudo-coupled method, the subgrade coefficient increases at a certain rate as moving away from the center to the corner/edge. Additionally, as the number of areas increases (from Model 2 to Model 4), bottom pressures decrease.

For the G+Q+EQx loading case, the base pressures occurring under the edge and center column are the same as for the G+Q loading. In the Winkler solution, the base pressure under the corner column is maximum, while in the Pseudo-coupled method, the order of the base pressures from largest to smallest is center, corner and edge.

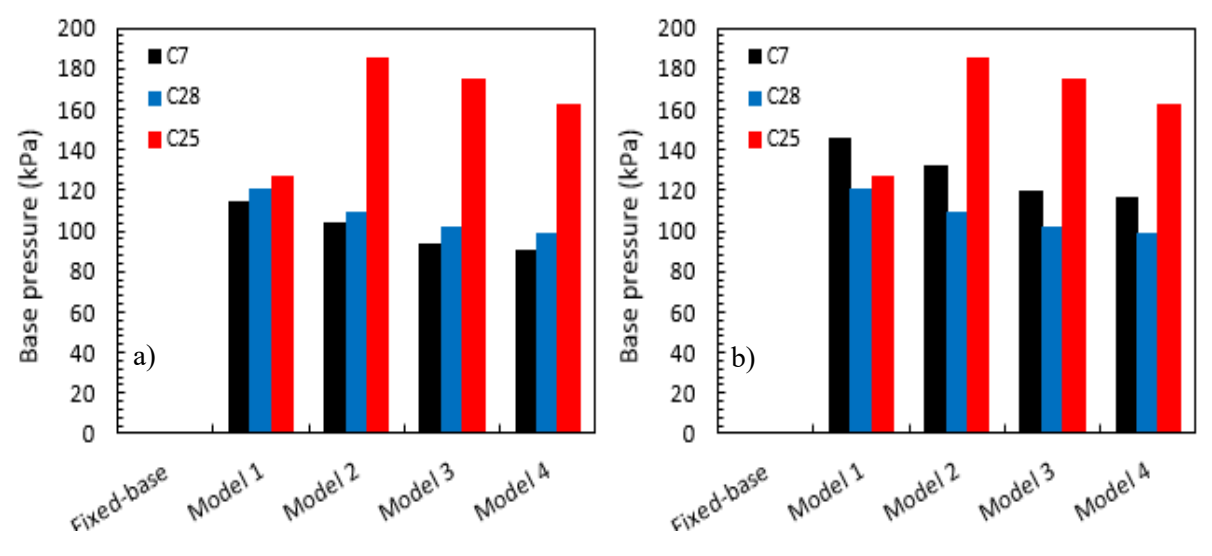


Figure 9
Base pressures at column bottom for a) G+Q and b) G+Q+EQx loading cases

Settlement

Settlements at column bottom for G+Q and G+Q+EQx loading cases were presented in Figure 10. In the fixed-base solution, settlements at any point of foundation are not exist since there is no subsoil or foundation.

In the Winkler and Pseudo-coupled methods, maximum and minimum settlements are observed at center and corner columns in G+Q loading case while at corner and edge columns, respectively, in G+Q+EQx loading case. Additionally, as the number of areas increases (from Model 2 to Model 4), settlements under column base decrease. Total settlement value for any structure should not be greater than 60mm for structural safety [27]. The building satisfies the total settlement criteria since it was at most 10mm (Figure 10a).

Differantial settlement is the difference between maximum and minimum settlement values. Differantial settlement value for any structure should not be greater than 20-30mm for structural safety [27]. Hence, differantial settlement values obtained from Winkler method is 0.71 mm and 1.39 mm in G+Q and G+Q+EQx loading cases, respectively (Figure 10b). In the Pseudo-coupled methods, differantial settlement values are 4.54 mm, 5.49 mm, 4.00 mm for Model 2, Model 3 and Model 4, respectively, for G+Q loading case. In addition, differantial settlement values decreases to 4.22 mm, 4.05mm, 3.54 mm for Model 2, Model 3 and Model 4, respectively, for G+Q+EQx loading case.

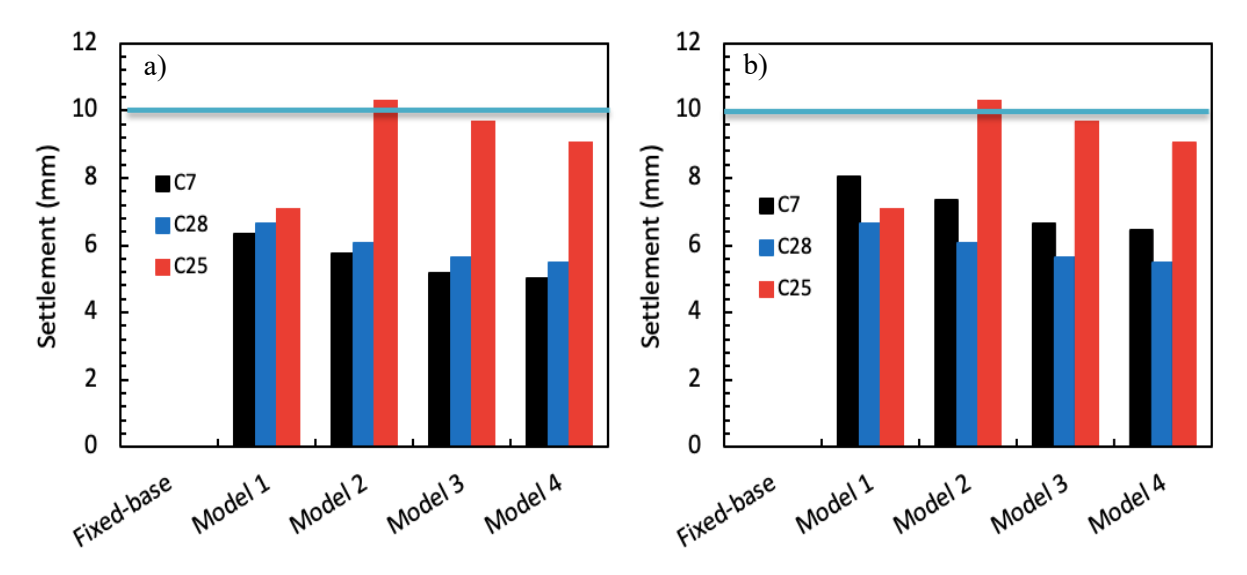


Figure 10Settlements at column bottom for a) G+Q and b) G+Q+EQx loading cases)

CONCLUSION

In the present study, the foundation system of 5-story building resting on medium dense sandy soil was analyzed considering fixed-base, Winkler and Pseudo-coupled methods. Main findings of the study are listed below.

- The periods of building are obtained closer in Winkler and Pseudo-coupled methods but 6.7% smaller in the fixed base foundation.
- Axial loads acting on building columns in G+Q loading case are not affected much by the foundation solution method. However, in EQx loading case, the axial loads on the columns on the 1st and 5th floors are 30% and 82% less, respectively, in Winkler and Pseudo-coupled methods compared to the fixed-base foundation solution.
- In Winkler and Pseudo-coupled methods, the shear force on the corner columns is 46% less than

in the fixed-base foundation.

- In Winkler and Pseudo-coupled methods, the earthquake force is 7% greater and story displacement is 4.7% less than in the fixed-base foundation.
- The location where the maximum base pressure, settlement, and differential settlement occurs change according to the foundation analyses methods.

In the present study, a symmetrical building was analyzed with the different methods. In the symmetric building, maximum base pressure is at the center of foundation. Therefore, Winkler and Pseudo-coupled methods give similar results on soil and structure system. However, in most case, raft foundations are loaded eccentrically due to the architectural designs or non-symmetrical geometry of buildings. Based on the authors' experience, excessive base pressures or settlements were observed at the edge/corner of the foundations in the eccentrically loading structures if the Winkler method uses. This phenomenon creates difficulties in geotechnical designs. In the eccentrically loading structures, Pseudo-coupled method balanced the base pressures at the center point and corner/edge points of the foundation. Therefore, the authors suggest that foundation solution methods should be applied for the buildings having different geometries, eccentricity, and foundation depth.

Ethical Statement

This study is an original research article designed and developed by the authors.

Author Contributions

Research Design A.S.E (%33), Y.Y. (%33), İ.Ö. (%33)

Data Collection A.S.E (%20), Y.Y. (%20), İ.Ö. (%60)

Research - Data Analysis - Validation A.S.E (%60), Y.Y. (%20), İ.Ö. (%20)

Writing the Article A.S.E (%20), Y.Y. (%60), İ.Ö. (%20)

Revision and Improvement of the Text A.S.E (%33), Y.Y. (%33), İ.Ö. (%33)

Financing

This research did not receive any specific grant from funding agencies in the public, commercial, or not-for-profit sectors.

Conflict of Interest

The authors have no conflicts of interest to disclose for this study.

Sustainable Development Goals (SDG)

Sustainable Development Goals: Not supported.

REFERENCES

- [1] X.-Y. Cao, D. Shen, D.-C. Feng, C.-L. Wang, Z. Qu, G. Wu, Seismic retrofitting of existing frame buildings through externally attached sub-structures: State of the art review and future perspectives, *Journal of Building Engineering*. 57 (2022), 104904.
- [2] H. Hao, K. Bi, W. Chen, T.M. Pham, J. Li, Towards next generation design of sustainable, durable, multi-hazard resistant, resilient, and smart civil engineering structures, *Engineering Structures*. 277 (2023), 115477.
- [3] G. Lazorenko, A. Kasprzhitskii, Z. Khakiev, V. Yavna, Dynamic behavior and stability of soil foundation in heavy haul railway tracks: A review, *Construction and Building Materials*. 205 (2019), 111-136.
- [4] Y. Guzel, F. Güzel, Considerations of Design Response Spectrum Involving Site Effect: Application to the Kocaeli Region, Türkiye, *Necmettin Erbakan Üniversitesi Fen ve Mühendislik Bilimleri Dergisi*. (2024). doi:10.47112/neufmbd.2024.31.
- [5] X. Wu, Y. Hu, Y. Li, J. Yang, L. Duan, T. Wang, T. Adcock, Z. Jiang, Z. Gao, Z. Lin, Foundations of offshore wind turbines: A review, *Renewable and Sustainable Energy Reviews*. 104 (2019), 379-393.
- [6] A.W. Lacey, W. Chen, H. Hao, K. Bi, Structural response of modular buildings—an overview, *Journal of building engineering*. 16 (2018), 45-56.
- [7] B.M. EL-garhy, M.M. osman, Winkler Coefficient for Beams on Elastic Foundation, *ERJ. Engineering Research Journal*. 25 (2002), 1-18. doi:10.21608/erjm.2002.70869.
- [8] N. Allotey, M. Hesham El Naggar, Analytical moment–rotation curves for rigid foundations based on a Winkler model, *Soil Dynamics and Earthquake Engineering*. 23 (2003), 367-381. doi:10.1016/S0267-7261(03)00034-4.
- [9] E. Winkler, Die Lehrevonder Elasticitaetund Festigkeit, , içinde: Prag. Dominicus, 1867: s. 182.
- [10] İ. Özkan, Y. Yenginar, A.S. Ecemiş, Analysis of raft foundation on sandy soils by Winkler and Pseudo-coupled methods, *Eskişehir Osmangazi Üniversitesi Mühendislik ve Mimarlık Fakültesi Dergisi*. 31 (2023), 675-688. doi:10.31796/ogummf.1224081.
- [11] H. Díaz, C.G. Soares, Review of the current status, technology and future trends of offshore wind farms, *Ocean Engineering*. 209 (2020), 107381.
- [12] T.P. Doğan, I.H. Erkan, Evaluation of the Nonlinear Seismic Responses of High-Rise Reinforced Concrete Buildings with Different Foundations and Structural Plans—Considering Soil-Structure Interactions, *Buildings*. 14 (2024), 1686. doi:10.3390/buildings14061686.
- [13] H. Tahghighi, A. Mohammadi, Numerical evaluation of soil–structure interaction effects on the seismic performance and vulnerability of reinforced concrete buildings, *International Journal of Geomechanics*. 20 (2020), 04020072.
- [14] J.M. Carbonell, L. Monforte, M.O. Ciantia, M. Arroyo, A. Gens, Geotechnical particle finite element method for modeling of soil-structure interaction under large deformation conditions, *Journal of Rock Mechanics and Geotechnical Engineering*. 14 (2022), 967-983.
- [15] S. Grecu, L.B. Ibsen, A. Barari, Winkler springs for axial response of suction bucket foundations in cohesionless soil, *Soils and Foundations*. 61 (2021), 64-79.
- [16] S.K. Suryasentana, H.J. Burd, B.W. Byrne, A. Shonberg, A Winkler model for suction caisson foundations in homogeneous and non-homogeneous linear elastic soil, *Géotechnique*. 72 (2022), 407-423.
- [17] Z. Zhang, M. Huang, C. Xu, Y. Jiang, W. Wang, Simplified solution for tunnel-soil-pile interaction in Pasternak's foundation model, *Tunnelling and Underground Space Technology*. 78 (2018), 146-158.

- [18] L. Pantelidis, The equivalent modulus of elasticity of layered soil mediums for designing shallow foundations with the Winkler spring hypothesis: A critical review, *Engineering Structures*. 201 (2019), 109452.
- [19] H. Asadi-Ghoozhdi, R. Attarnejad, A Winkler-based model for inelastic response of soil—structure systems with embedded foundation considering kinematic and inertial interaction effects, *Structures*. *Elsevier*, 28 (2020), 589-603.
- [20] S. Carbonari, J.D.R. Bordón, L.A. Padrón, M. Morici, F. Dezi, J.J. Aznárez, G. Leoni, O. Maeso, Winkler model for predicting the dynamic response of caisson foundations, *Earthquake Engineering & Structural Dynamics*. 51 (2022), 3069-3096.
- [21] S.J. Brandenberg, M.G. Durante, G. Mylonakis, J.P. Stewart, Winkler solution for seismic earth pressures exerted on flexible walls by vertically inhomogeneous soil, *Journal of Geotechnical and Geoenvironmental Engineering*. 146 (2020) 04020127.
- [22] Y. Yönet, Yapı-Zemin Etkileşiminin Binaların Deprem Davranışına Etkisinin Sonlu Elemanlar Yöntemiyle İncelenmesi, Yüksek Lisans Tezi, Necmettin Erbakan Üniversitesi Fen Bilimleri Enstitüsü, İnşaat Mühendisliği Anabilim Dalı, Konya, 2022.
- [23] G. Özyurt, Use of spatially variable subgrade modulus for improved accuracy in structural modeling of raft foundations, Orta Doğu Teknik Üniversitesi Fen Bilimleri Enstitüsü, İnşaat Mühendisliği Anabilim Dalı, Ankara, 2023.
- [24] J.W. Ringsberg, C.G. Soares, Advances in the Analysis and Design of Marine Structures, *CRC Press Taylor & Francis Group*, 2023.
- [25] İ. Vapur, İ.F. Kara, E. Akın, Kahramanmaraş ve Hatay depremlerinin Antakya ve Samandağ ilçelerindeki yapısal etkileri ve çözüm önerileri, *Ömer Halisdemir Üniversitesi Mühendislik Bilimleri Dergisi*. (2023). doi:10.28948/ngumuh.1293147.
- [26] T. Wang, J. Chen, Y. Zhou, X. Wang, X. Lin, X. Wang, Q. Shang, Preliminary investigation of building damage in Hatay under February 6, Turkey earthquakes, *Earthquake Engineering and Engineering Vibration*. 22 (2023), 853-866. doi:10.1007/s11803-023-2201-0.
- [27] EN 1998-1, Eurocode 8: Design of structures for earthquake resistance Part 1: General rules, seismic actions and rules for buildings, European Standard, rue de Stassart, Brussels, 2004.



Vol: 7 No:2 Year: 2025

Araştırma Makalesi/Research Article

e-ISSN: 2667-7989

https://doi.org/10.47112/neufmbd.2025.91

Güneş Enerji Santralinin Reaktif Güç Desteği için Kullanılması

Harun KÖROĞLU ¹ D Sabri ALTUNKAYA ^{2*} D

¹ R&D Unit, Inavitas Energy, Ankara, Türkiye

² Necmettin Erbakan University, Faculty of Engineering, Department of Electrical and Electronics Engineering, Konya, Türkiye

Makale Bilgisi ÖZET Enerji üretim, iletim ve dağıtım sistemlerinde reaktif güç kompanzasyonu için yatırım Gelis Tarihi: 28.06.2024 yapılmaktadır. Mevcutta elektrik dağıtım şirketleri reaktif güç kompanzasyonu için reaktör, Kabul Tarihi: 20.11.2024 kapasitör ve manyetik kontrollü reaktör yatrımı yapmaktadır. İletim şirketleri ise bu yatırımlara Yayın Tarihi: 31.08.2025 ek olarak mevcutta bulunann üretim santrallerinden yan hizmetler kapsamında reaktif güç desteği almaktadır. Günümüzde güneş enerji santrali (GES), rüzgâr enerji santrali (RES) gibi dağıtık üretim tesislerinin artmasıyla birlikte dağıtım şebekesine bağlı enerji akışı çift yönlü **Anahtar Kelimeler:** hale gelmistir. GES ve RES gibi dağıtık üretim tesislerinde üretim olmadığı saatlerde GES Kompanzasyon, iletkenlerden kaynaklı kapasitif reaktifin artmasına ve üretimin artması ise bölgede gerilim yükselmesine neden olur. Bu çalışmada dağıtık enerji kaynaklarının dezavantajlarını avantaja Reaktif güç desteği. çevirmek, kompanzasyon yatırım maliyetlerini azaltmak amacıyla GES'lerin reaktif güç kompanzasyonu için kullanılabilirliği araştırılmıştır. Bunun için bir elektrik dağıtım bölgesinde bulunan bir trafo merkezine bağlı bir GES'nden reaktif güç desteği alınması için gerekli simülasyon çalışmaları yapılmıştır. Daha sonra bölgedeki GES'nden yedi saat boyunca reaktif güç desteği alınarak deneysel çalışmalar yapılmıştır. Sonuç olarak GES'nden alınan reaktif güç desteği sayesinde kompanzasyon yatırımlarının azalacağı vurgulanmıştır.

Using Solar Power Plant for Reactive Power Support

Article Info ABSTRACT

Received: 28.06.2024 Accepted: 20.11.2024 Published: 31.08.2025

Keywords:

SPP,

Compensation, Reactive power support. Reactive power compensation investments are made for energy production, transmission and distribution systems. Currently, electricity distribution companies invest in reactors, capacitors and magnetically controlled reactors for reactive power compensation. With these investments, transmission companies receive reactive power support from existing production plants within the scope of ancillary services. Nowadays, with the increase in distributed generation facilities such as solar power plants (SPPs) and wind power plants (WPP), the energy flow connected to the distribution grid has become bidirectional. In distributed generation facilities such as SPP and WPP, during hours when there is no production, the capacitive reactive originating from the conductors increases and the increase in production causes voltage rise in the region. In this study, the usability of SPPs for reactive power compensation was investigated in order to turn the disadvantages of distributed energy resources into advantages and to reduce compensation investment costs. For this purpose, necessary simulation studies were carried out to obtain reactive power support from a solar power plant connected to a transformer center in a electricity distribution region. Later, experimental studies were carried out by receiving reactive power support from the solar power plant in the region for seven hours. As a result, it has been emphasized that the reactive power support received from the solar power plant will reduce compensation investments.

To cite this article:

Köroğlu, H. & Altunkaya, S. (2025). Using solar power plant for reactive power support. *Necmettin Erbakan University Journal of Science and Engineering*, 7(2), 273-285. https://doi.org/10.47112/neufmbd.2025.91

*Corresponding Author: Sabri Altunkaya, sabrialtunkaya@gmail.com



INTRODUCTION

The main task of electricity distribution companies is to transport the energy received from the transmission level to the end user in a quality and sustainable manner. At all voltage levels in the electrical power system, the voltage value must remain within the specified operating range. The increasing penetration of renewable energy sources and the increasing variability and subsequent uncertainty in the electrical grid cause various operational concerns. [1]. Distributed energy sources, by their nature, may cause voltage level distortions due to their inability to produce energy continuously due to their intermittent operation, and capacitive reactance increases due to the conductors going to the distributed source during periods when they are not producing. In order to operate electricity distribution grids more stable and securely, the concept of obtaining ancillary services from renewable energy sources connected to the distribution grid has become more popular with the increase in renewable energy potential. The trend of obtaining reactive power support from existing renewable energy sources is becoming increasingly widespread in the world. Obtaining ancillary services from generation plants connected to the distribution grid established for electricity generation will provide technical and economic benefits [2]. STATCOM applications are mostly due to the high cost of using power electronic components. In the future, low-cost reliable switches must be used to generate the required reactive power. STATCOM can be integrated into the grid to provide an adaptable reactive power source for loads. Inverters can be called STATCOM products from existing sources [3]. STATCOM is becoming increasingly popular among electrical engineers both at home and abroad due to its many features [4]. Inverters installed with distributed generation systems and rooftop solar systems can support ancillary services such as reactive power compensation, voltage regulation, flicker control, active power filtering and harmonic reduction [5-7]. Variable speed generators and wind turbines have the potential to add inertia to the grid, reduce power losses, provide voltage regulation of the system and assist in frequency control [8-10]. Therefore, in order to control the voltage to compensate for the effects of renewable power plants connected to the distribution grid with compensation investments, it is necessary to first use the reactive power features of inverter-controlled power plants and then check other options. Inverter-based power plants can respond very quickly to regulations in reactive power demands and disruptions in grid voltage [11]. However, while the reactive power support range from PV-based power plants is 5-10% within the power, it can be received at 100% at night [12]. During the night when there is no active power, DC-DC conversion is not used. However, an improved control scheme with an energy storage system can allow the inverter to operate in reactive power mode even without the PV panels harvesting solar energy. The inverter can then be programmed to operate as a VAR compensator to deliver only the required reactive power, which will then regulate the voltage at the load end [13]. By controlling the reactive power, compensation investments made every year will be significantly reduced [14]. In addition, by controlling the voltage, technical losses will be reduced, and energy efficiency will be increased. In this way, grid security will be improved, and voltage limit, line capacity, WPP penetration, capacitor penetration will be increased [15]. While receiving reactive power support as a ancillary service from distributed generation plants, should care to take the necessary reactive power support on whichever feeder the need is. For example, when the transmission transformer requirement is capacitive reactive, this support should not be taken from a feeder with capacitive reactive load, and if care is taken to get it from the feeder with inductive load, feeder-based technical losses will be reduced. Likewise, changes in the reactive power control values of distributed generation sources will significantly increase the voltage quality and security of the grid [16]. Photovoltaic (PV) power plants are a key factor in their integration with the electricity distribution grid. PV plant is a special form of distributed energy resources that can affect the electrical distribution grid and substation. There is a wide variety of compensation products considering the way they deal with the reactive power problem. Inverters, which are among these compensation systems, can provide reactive power according to

demand as automatic control of the power factor [17]. In this study, simulation and experimental studies of obtaining reactive power from PV power plants were carried out by using inverters in PV power plants. Simulation studies show that the problems experienced with the commissioning of a biogas power plant in a selected transmission transformer center have been eliminated thanks to the reactive power support received from the solar power plant. Thus, when reactive power support is received from existing production plants, renewable energy penetration will increase even more. In addition, the most important difference of this study from other studies is that the technical losses between the existing methods and the reactive support from the inverter are given mathematically.

MATERIALS AND METHODS

Study Area

According to Article 14 (Compensation of Reactive Energy) of the Electricity Grid Regulation, the ratio of the inductive reactive energy drawn from the system monthly to the active energy drawn from the system cannot exceed 20%, and the ratio of the capacitive reactive energy given to the system monthly to the active energy drawn from the system cannot exceed 15% [18]. Among the substations from which an electricity distribution company receives energy, a substation was selected whose reactive power was determined not to be within the limit values in the legislation. There are 2 similar 100 MVA transformers in this substation and it is a region where seasonal consumption is intense and distributed generation resources are common. A biogas production plant with an installed power of 10 MW was later added to a transformer in this substation. With the connection of this production plant from the distribution grid to the substation, the system's reactive power ratio was increased and the need for reactive power compensation arose.

A distribution grid receives energy from the substation connected to the transmission operator. Feeders at 31,5 kV voltage level coming from the transformers in this substation enter the distribution center entrance cell of the distribution company. Feeders leaving the distribution center either go to another distribution center or to a transformer to be transmitted to the end user. In this transformer, it is converted from 31,5 kV voltage level to 400 V voltage level and transmitted to electricity consumers. The single line diagram of the feeder coming out of the substation for the pilot region we chose in our study is shown in Figure 1. In this feeder, the transformer center reaches the Solar Power Plant building at the end of the 15-kilometer line.

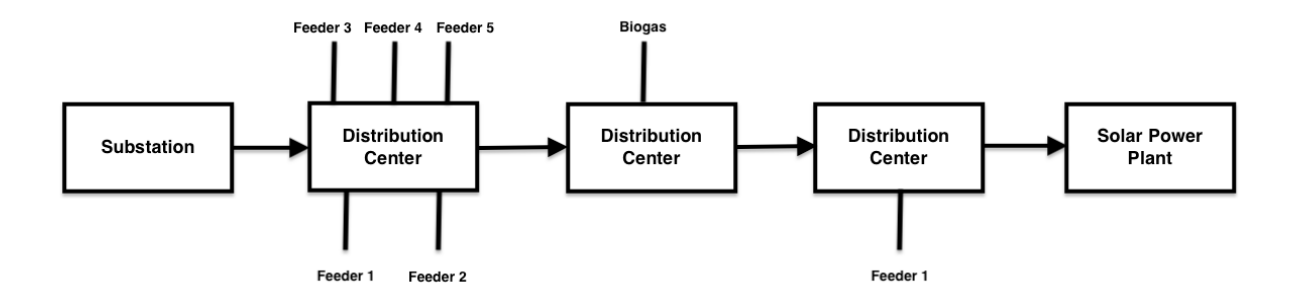


Figure 1
Single line diagram of the supported solar power plant [19].

The power plant from which we will receive reactive power support has 6 solar power plants with a power of 1 MWp and a total installed power of 6 MWp. Each power plant has 3572 solar energy panels with a power of 335 Wp. Each power plant has a PVS800 model 1 MWp central type inverter from ABB and is suitable for receiving reactive support. When field type solar power plants in the distribution region are examined, 1250 kVA transformers and 1 MWp inverters with a total power are used in solar power plants with a typical installed power of 1 MWp. While solar power plants produce at full load;

Although the transformer power is sufficient to obtain reactive power control with a power factor of ± 0.8 , inverter powers may be insufficient. Reactive power support ancillarly service can be received from these types of solar power plants when they do not produce at full load.

In order to receive reactive support from solar power plants, the active and reactive power flow in the grid must be effectively monitored and a communication infrastructure must be established. An uninterrupted and high-quality communication infrastructure will enable more flexible operation of distributed energy resources. Remote terminal unit (RTU) installations have been completed from field type SPPs in the electricity distribution region. Effective monitoring can be achieved by connecting the RTU installed in the field to the SCADA control center of electricity distribution company. Within the scope of the study, solar power inverters were manually controlled from the SCADA system according to the reactive power requirement in the substation on the feeder to which they were connected.

Inverters

One way to get maximum benefit from PV plants is to increase the functions performed by the inverter. In addition to the primary task of the inverter, conversion, it also performs multiple functions, including both reactive and real power control. The inverter works as a static compensator (STATCOM) device to generate reactive power to meet the demand generated from the loads and delivers active power to the grid. Inverters can provide reactive power according to demand by changing the power factor. Reactive power demand is provided according to the rule in the graph in Figure 2. In order to receive reactive power support from the inverter, if there is active production P in the production plant, reactive power support with the Qmax value according to the graph can be received. When a renewable source is not available, the inverter only acts as a reactive power compensator and provides improvement in power factor [20, 21].

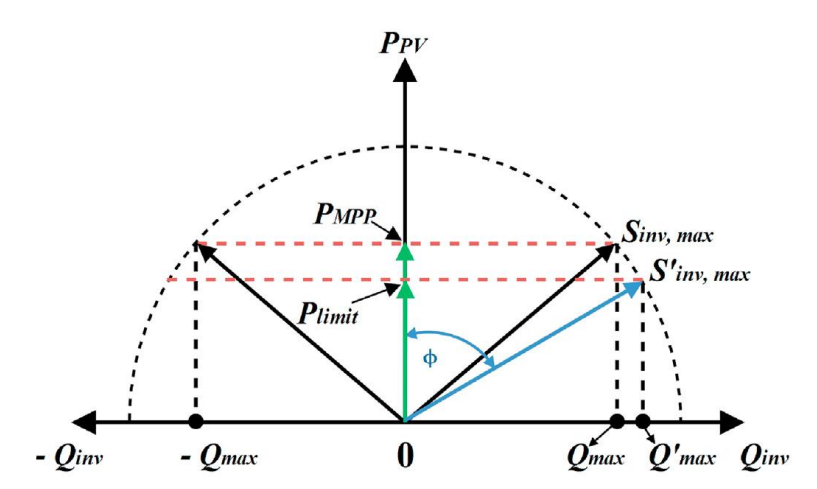


Figure 2 *Active power- reactive power capacity table for PV power plant inverter [21].*

The equivalent circuit of the grid-connected PV system in Figure 3 consists of a PV array with a capacitor connected in parallel with a diode as the main switch. The capacitor is connected to the power input of the inverter. The inverter output is connected to the grid through the RL filter.

Analysis Program

Within the scope of this study, the DigSilent program, which is a power systems analysis program, was used. Using the analysis program, the load was run on the distribution company feeder using the substation meter data and the approximation ratio of the results of the program was determined. According to the substation meter data and the power system analysis program, the substation in need of reactive power support was determined. The impact of renewable energy sources on this substation

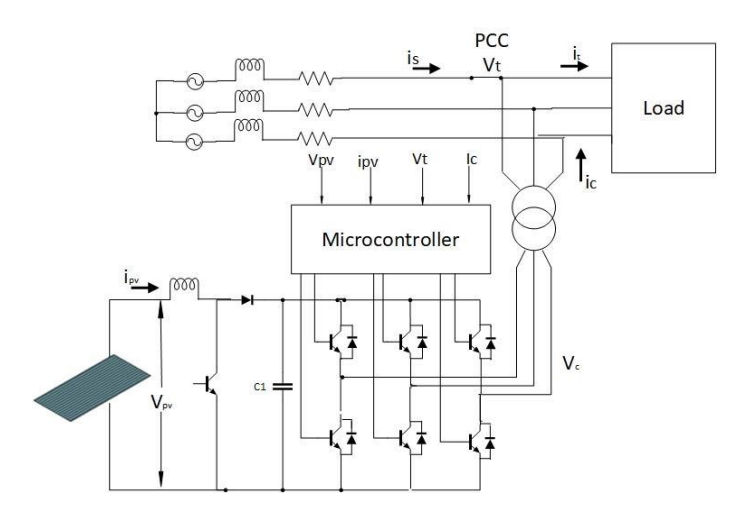


Figure 3
Grid-connected three-phase inverter PV system [22].

and the analysis of the reactive power support to be received from these sources are included under the experimental study title.

RESULTS

System Simulations

System simulations of the feeders of the substation we chose for three cases were carried out with the DigSilent power systems analysis program. In the first two simulations, the reactive power needs of the system were analyzed before and after adding the biogas production facility, while in the third simulation, the reactive power need required for the transformer center to remain within the specified reactive power limits was analyzed after the biogas production facility was connected. In the simulations, data obtained from the real-time transformer center were used to analyze the data. Initially, the accuracy of these data was confirmed by comparing the transformer center values with the simulation results.

Simulation 1: Current Situation

In the first simulation, existing reactive power simulations were performed before connecting the biogas production facility to investigate whether the system needed reagents and whether it met the demands of electricity distribution company. According to the load profile data of the transmission transformer located in the distribution region, which we determined above, the load was run using the power systems analysis program (Figure 4). When the biogas production plant was not in operation, the reactive power ratio we saw in the transmission transformer load profile data was compared with the result of the power systems analysis program. As a result of the simulation, the active power absorbed in the transmission transformer is 12,03 MWp, while the capacitive reactive power appears to be 1,4 MVAr. When the reactive power ratio of the transmission transformer is calculated according to Equation 1, it appears to be 11% capacitive reactive. Since it has a value lower than the 15% limit range, there is no need for an additional compensation investment, according to the regulation.

Reactive Power Ratio =
$$tg\delta = \frac{Q}{P} = \frac{1.4}{12.03} = 0.11$$
 (1)

Simulation 2: Commissioning of the Biogas Production Plant

In the second simulation, reactive power demands in the new situation were examined by performing reactive power simulations after the biogas production facility was included in the substation. The first simulation was repeated after a 10 MWp biogas production power plant was

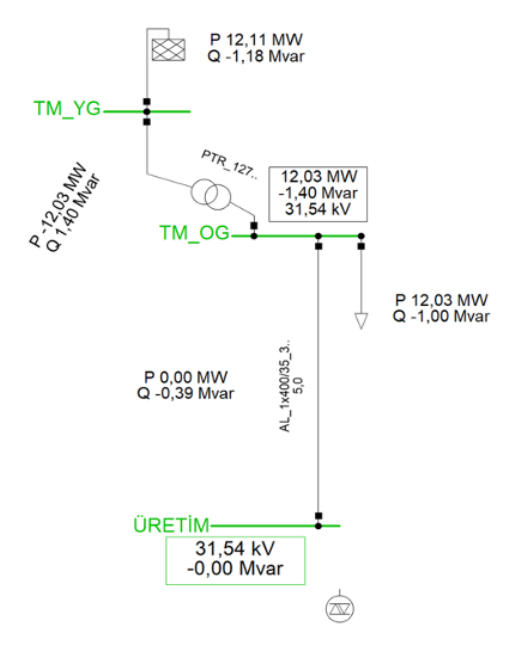


Figure 4Substation analysis study when the biogas production facility is not in operation [19].

commissioned at the substation. When the biogas production plant comes into operation, according to the analysis results, it is understood that 2,09 MW active and 1,33 MVAr capacitive reactive power is drawn in the transmission transformer (Figure 5). When the reactive power ratio is calculated according to Equation 2, it is seen that the reactive power ratio is 64% when the generation plant comes into operation. This calculated value is above the 15% limit value within the scope of the regulation.

Reactive Power Ratio =
$$tg\delta = \frac{Q}{P} = \frac{1,33}{2,09} = 0,64V(x) = x * (l - 2 * x) * (w - 2 * x)$$
 (2)

$$\begin{array}{c}
P2.17 \text{ MW} \\
Q-1,28 \text{ Mvar}
\end{array}$$

$$\begin{array}{c}
P2.17 \text{ MW} \\
Q-1,28 \text{ Mvar}
\end{array}$$

$$\begin{array}{c}
P12.04 \text{ MW} \\
Q-1,000 \text{ Mvar}
\end{array}$$

Figure 5Substation analysis study while the biogas production facility is in operation [19].

Simulation 3: Determination of Compensation Investment Needs

When the load profile data was analyzed based on one-year data after the biogas production plant was put into operation (Figure 6), it was found that a 1,32 MVAr reactor investment was required to keep the capacitive reactive ratio within 15% limits.

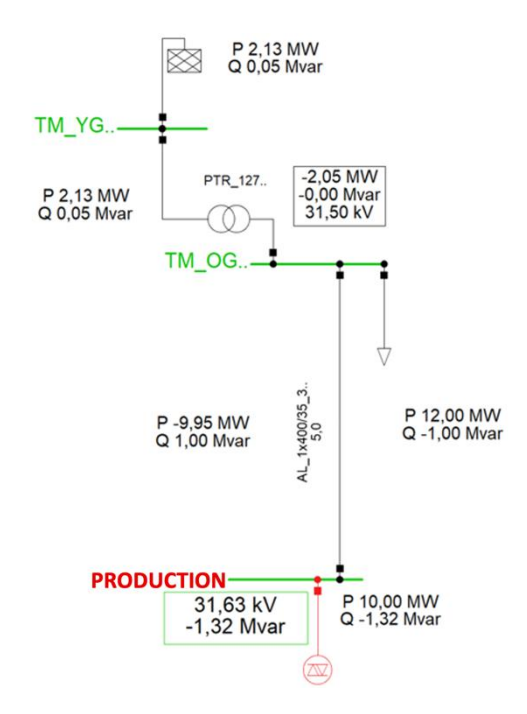


Figure 6Determination of compensation investment need while the biogas production facility is in operation [19].

For the three simulation studies conducted above, the net active power drawn from the substitutions, the reactive power found in the substitutions, and the reactive power ratio in the grid are shown in Table 1.

Table 1Summary information of simulation studies.

Simulation	Explanation	Net Active Power in Transformer (MW)	Net Reactive Power in Transformer (MVAr)	Reactive Power Ratio
Simulation 1	Current Situation	12,03	1,4	0,11
Simulation 2	Commissioning of the biogas production plant	2,09	1,33	0,64
Simulation 3	Determination of compensation investment needs	2,05	0	0

Implementation of Pilot Application

After the preparations for the pilot application were completed, the pilot application was carried out between 16.01.2024 at 19:00 and 17.01.2024 at 02:00. Since there was no production after sunset on 15.01.2024 in the transformer, whose active power curve was the same the day before and the day after, it was observed that the capacitive reactive increase in the grid originating from the production plant conductor. After sunset at 19.00 on 16.01.2024, reactive power support started to be received from the SPP inverter. The support process ended at 02.00 on 17.01.2024. As soon as the support process was completed, the value that appeared inductive in the load profile suddenly turned out to be capacitive. In the pilot application, a total of 2,4 MVAr inductive reactive support was provided to the system, 400 kVAr from each of the 6 inverters in the solar power plant site.

Figure 7 shows the measured instantaneous power values of the transmission transformer. When Figure 7 is examined, active power decreases from 7,6 MW to 0,2 MW between 19.00 in the evening and 09.00 in the morning, the day before the pilot study. Likewise, in the transmission transformer data, the capacitive reactive power value reaches up to 1,8 MVAr. In the evening of the same transmission

transformer, between 19.00 and 02.00, when we receive reactive power support from inverters, the active power value decreases from 7,6 MW to 4,8 MW. However, since we receive reactive power support, the amount of reactive power drawn from the system does not increase in the capacitive direction as it did the previous day, on the contrary, it increases slightly in the reactive direction. Thus, the system, which had 1,8 MVAr capacitive reactive power the day before, goes in the opposite direction, and the transformer is loaded inductively, and approximately 0,4 MVAr inductive reactive power appears in the system. This 6-hour support shows that this support will be sufficient for a 6-month period in which the production-consumption trend of the transmission transformer will not change during the winter period. Finally, when inductive reactive power support from solar inverters is stopped, capacitive power is generated in the system again between 02.00 and 08.00.

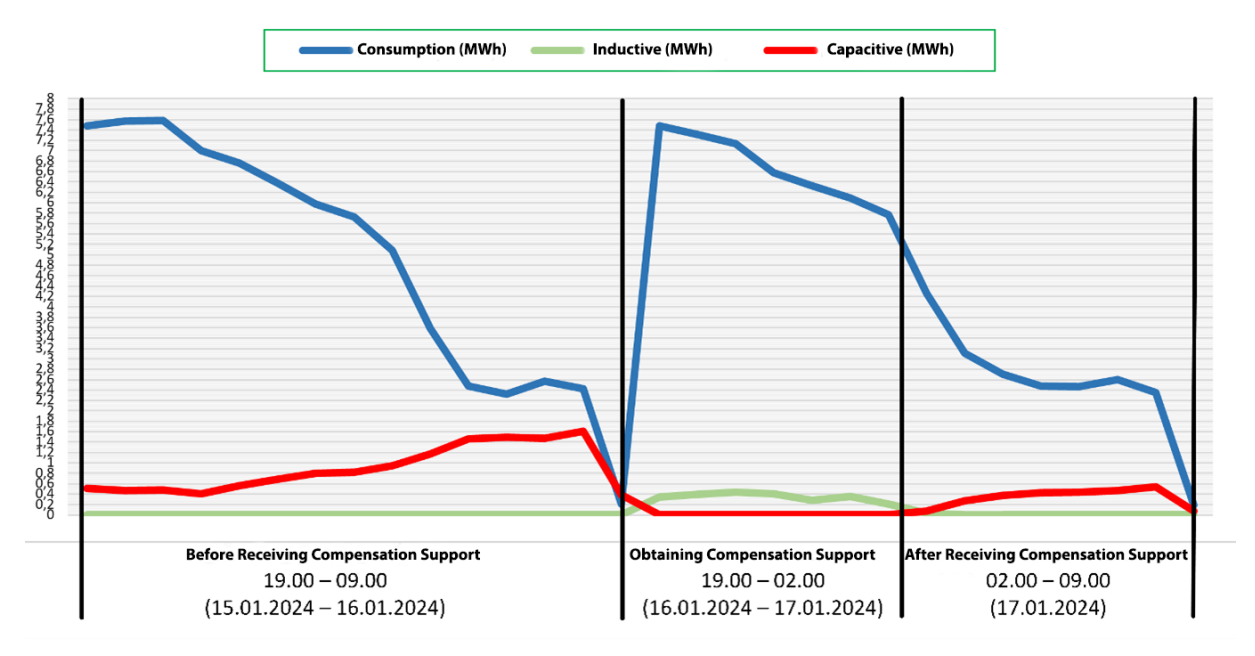


Figure 7
Transmission transformer load profile (Change in Substation Meter Values as a Result of Inductive Reactive Support from Solar Inverter)[19].

In addition, according to the trend graph of an inverter at the time of receiving support, when a command was sent to receive 400 KVAr inductive reactive power support, the inverter responded in a very short time. According to the SCADA screenshot in Figure 8, the inverter provided continuous reactive power support.

Cost Analysis: Meeting the Compensation Needs of Electricity Distribution Region in 2023 from Solar Power Plants

As a result of the analysis carried out in the distribution region of electricity distribution company, the compensation needs for the substations from which energy is received were determined. In line with these findings, it was revealed that 16 different substation reactors needed to be invested. Table 2 shows the power and investment costs of 25 reactor investments that need to be made for these 16 different substations. A total of 65,6 MVAr reactor power and a cost of \$1.890.223 is needed for 25 reactor investments. The solar power plants located on the feeders connected to the substations in this region have a total production capacity of 1054,73 MW. In addition, the required reactor power value for each

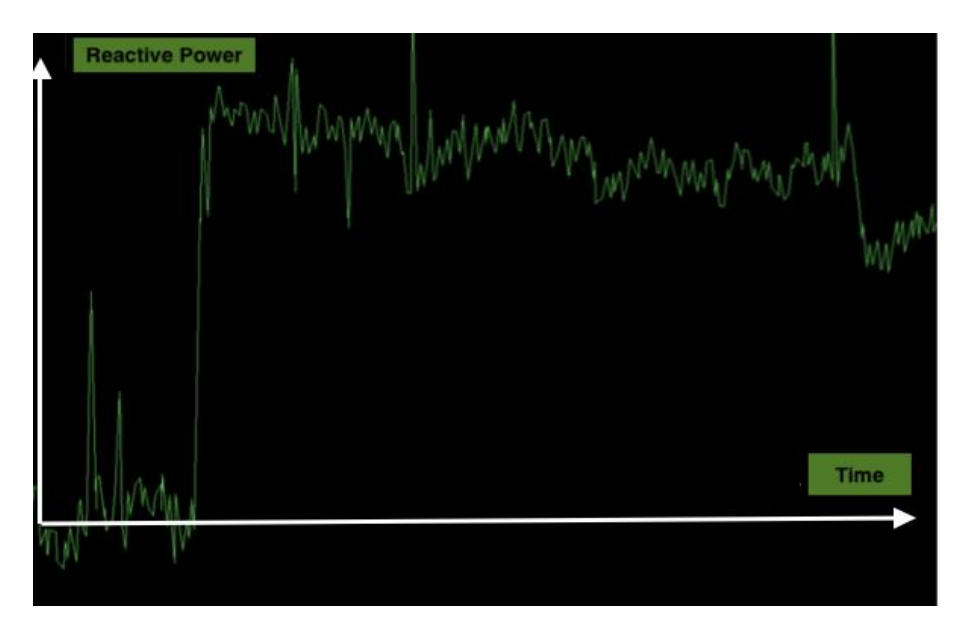


Figure 8 *Trend of receiving reactive power support of an inverter.*

feeder is less than the reactor power we can get from the solar power plant connected to the relevant feeder. Therefore, all of the reactor power required for each transformer can be provided by solar power plants. In this case, the \$1.9 million cost benefit required for the reactor investment can be achieved when reactive support is received from the solar power plant instead of the compensation systems that need to be installed only for 2023.

Table 2Compensation investment needs for the electricity distribution region in 2023 and installed plants connected to relevant transformers.

Substation	Shunt Reactor (MVAr)	Investment Cost	Solar Power Plant Installed Power Connected to The Electricity Distribution Grid (MW)
TM 1- TRA	2,4	\$ 75.351	15,34
TM 1- TRB	1,8	\$ 69.527	13,34
TM 2- TRA	3,6	\$ 69.368	
TM 2- TRA	2,4	\$ 72.158	55,38
TM 2- TRB	1,8	\$ 69.527	
TM 3- TRA	3,6	\$ 98.672	89,78
TM 4- TRA	1,8	\$ 69.527	53,11
TM 5- TRA	2,4	\$ 75.351	61,7
TM 6- TRA	1,8	\$ 71.742	88,79
TM 6- TRB	1,8	\$ 71.742	00,79
TM 7- TRA	3,6	\$ 88.302	67,34
TM 7- TRB	2,4	\$ 75.351	07,34
TM 8- TRA	2,4	\$ 69.731	75,84
TM 8- TRB	2,4	\$ 75.351	73,04
TM 9- TRA	2,4	\$ 51.451	134,33
TM 9- TRB	2,4	\$ 75.351	134,33
TM 10- TRA	3,6	\$ 51.451	73,15
TM 10- TRB	2,4	\$ 75.351	73,13
TM 11- TRA	5	\$ 105.692	38,95
TM 12- TRA	2,4	\$ 75.799	59,05
TM 13- TRA	2,4	\$ 76.174	101,85
TM 14- TRA	2,4	\$ 93.268	79,5
TM 14- TRB	2,4	\$ 75.351	17,3
TM 15- TRA	2,4	\$ 64.103	14,35
TM 16- TRA	3,6	\$ 94.535	46,3
TOTAL	65,6	\$ 1.890.223	1054,73

Technical Loss Analysis: Meeting the Compensation Need of Electricity Distribution Region in 2023 from Solar Power Plants Technical Loss Analysis

Within the scope of this study, the effects of receiving reactive power support from solar power plants and making reactor investments on the grid were examined and compared. Using the meter data on the inlet side of the reactor connected to the grid and the index values in the meter data at the reactor exit, the technical loss rate was calculated as 5,35%. Likewise, when reactive support is received from the solar power inverter, the technical loss rate calculated using the values taken while the inverter is on and the values taken when the inverter is off, in line with the values taken from the technical quality recorder data, is 2,65%.

The average consumptions for these two applications, when 2400 kVAr reactive power support is received from both the reactor and the solar power inverter, are as in Table 3. For both supports, according to 8760 hours of data, a technical loss cost of approximately 8,5 million TL arises (calculation was made by taking 2023 electricity generation company and market average: 1097 ½/MWh).

Table 3
Lost Energy Cost in 2023.

Active Power (MW)	Loss Rate Difference Between Reactor and Solar Inverter	Lost Power (MW)	8760 Hours of Lost Energy (MWh)	Lost Energy Cost in 2023 (b)
35,28	2,50%	0,882	7726,32	₺8.475.773

According to this technical loss study conducted for only a single transmission transformer, a total technical loss cost of 8,5 million & occurs in a year. When this is done in the compensation systems connected to all transformers in the substations in our country, the costs resulting from technical losses will be much higher.

DISCUSSION AND CONCLUSIONS

The problem caused by the increase in capacitive reactivity as a result of the introduction of renewable energy sources was solved by obtaining inductive support from a solar power plant connected to the same substation. As can be seen from the performance expected from SPPs, reactive power support is a well-known method to ensure voltage regulation and most of the new generation vehicles based on power electronics are well suited for this purpose. For this reason, it has been proven to benefit from the reactive capacities of solar power inverters as well as reactive power compensation investments to ensure reactive power flow limits. Electricity distribution companies make compensation investments in order to avoid substation-based reactive penalties. These investments are made not on a feeder basis, but only to keep the substation's reactive power within its limits. For example, a substation needs inductive reactive power support. If this need is supplied by an inductively loaded feeder, it will cause an increase in technical loss. The substation may be kept within the limit values, but feeder-based losses will increase. However, if this is done by taking solar power plants, technical losses can be further reduced by providing both transformer-based and feeder-based compensation.

With the reactive power support that can be provided from renewable energy sources, especially inverter-controlled facilities, which have recently increased in electricity distribution company, the grid voltage will be effectively controlled in the +/- direction, and the compensation investments made every year will be significantly reduced. Operational problems encountered as a result of the increase in distributed generation resources will be reduced and renewable energy integration will increase. In addition, another important result of effectively controlling the voltage profile is that it has been proven that it will enable the optimization of technical losses, and help increase grid efficiency, according to the comparison of reactive support received from the reactor and solar power inverter. Finally, in the

current situation, compensation facilities are connected to a feeder of the substation. Electricity distribution companies only make compensation investments to avoid reactive penalties. For example, let's assume that a substation needs an inductive reagent. In this case, inductive support is received from the reactor connected to a feeder. But perhaps the feeder connected to the reactor is inductively loaded. In order to remain at the reactive limit value, the substation receives inductive support from the inductively loaded feeder, causing technical losses to increase even more. When reactive support from generation plants connected to the distribution grid becomes widespread, these will be analyzed on a feeder basis, so the substation will remain within the reactive limit range, and technical loss optimization will be made by receiving support from the relevant feeder according to the reactive needs of the substation feeder outputs.

Ethical Statement

This study was produced from the master's thesis titled "Providing Reactive Power Support From Solar Power Source In Electricity Distribution Grid" submitted on 04.07.2024 under the supervision of Sabri Altunkaya.

Ethics Committee Approval

This study does not require any ethics committee approval.

Author Contributions

Research Design (CRediT 1): H.K. (%60) – S.A. (%40)

Data Collection (CRediT 2): H.K. (%100)

Research - Data Analysis - Validation (CRediT 3-4-6-11): H.K. (%80) – S.A. (%20)

Writing the Article (CRediT 12-13): S.A. (%100)

Revision and Improvement of the Text (CRediT 14): S.A. (%100)

Financing

This research did not receive any specific grant from funding agencies in the public, commercial, or not-for-profit sectors.

Conflict of Interest

The authors have no conflicts of interest to disclose for this study.

Sustainable Development Goals (SDG)

Sustainable Development Goals: 7 Affordable and clean energy.

REFERENCES

- [1] S. Sreekumar, D.S. Kumar and J.S. Savier, A case study on self healing of smart grid with islanding and inverter volt–VAr function, *IEEE Transactions on Industry Applications*. 56 (2020), 5408-5416. doi:10.1109/TIA.2020.3011664
- [2] B.E. Tankut. Voltage Regulation for Grid Connected Photovoltaic Systems using Reactive Power, Yüksek Lisans Tezi, Hasan Kalyoncu Üniversitesi Fen Bilimleri Enstitüsü, Elektronik ve Bilgisayar Mühendisliği Ana Bilim Dalı, Gaziantep, 2019
- [3] T.A. Boghdady and Y.A. Mohamed, Reactive power compensation using STATCOM in a PV grid connected system with a modified MPPT method, *Ain Shams Engineering Journal*. 14 (2023), 102060. doi:10.1016/j.asej.2022.102060
- [4] A.A. Suryawanshi and A. Tapde, Maximizing solar power output with pv-statcom for reactive power compensation in on-grid systems, *International Journal of Intelligent Systems and Applications in Engineering*. 12 (2024), 3382-3387.
- [5] P. Jahangiri and D.C. Aliprantis, Distributed Volt/VAr control by PV inverters, *IEEE Transactions on Power Systems*. 28 (2013), 3429-3439. doi:10.1109/TPWRS.2013.2256375
- [6] M.S.I. Tarek, A. Siam, M. Zia and M.M. Rahman. A Novel Five-Level Inverter Topology with Reactive Power Control for Grid-Connected PV System. In: 2018 International Conference on Smart Grid and Clean Energy Technologies (ICSGCE). Kajang, Malaysia, 2018. doi:10.1109/ICSGCE.2018.8556812
- [7] W. Zhong, G. Tzounas and F. Milano, Improving the power system dynamic response through a combined voltage-frequency control of distributed energy resources, *IEEE Transactions on Power Systems*. 37 (2022), 4375-4384. doi:10.1109/TPWRS.2022.3148243
- [8] G. Lalor, A. Mullane and M.O. Malley, Frequency control and wind turbine technologies, *IEEE Transactions on Power Systems*. 20 (2005), 1905-1913. doi:10.1109/TPWRS.2005.857393
- [9] A.J. Lamadrid and T. Mount, Ancillary services in systems with high penetrations of renewable energy sources, the case of ramping, *Energy Economics*. 34 (2012), 1959-1971. doi: 10.1016/j.eneco.2012.08.011
- [10] N.K. Roy, H.R. Pota and M.J. Hossain, Reactive power management of distribution networks with wind generation for improving voltage stability, *Renewable Energy*. 58 (2013), 85-94. doi:10.1016/j.renene.2013.02.030
- [11] A. Chatterjee, K. Mohanty, V.S. Kommukuri and K. Thakre, Design and experimental investigation of digital model predictive current controller for single phase grid integrated photovoltaic systems. *Renewable Energy*. 108 (2017), 438-448. doi:10.1016/j.renene.2017.02.057
- [12] R. Krishan, S.K. Singh, S. Patnaik, S. Verma. Reactive Power Control Strategies for Solar Inverters to Increase the Penetration Level of RE in Power Grid. In: 2nd International Conference on Large-Scale Grid Integration of Renewable Energy in India. New Delhi, India, 2019.
- [13] K. Tharuka Lulbadda and U. Hemapala, Use of solar PV inverters during night-time for voltage regulation and stability of the utility grid, *Clean Energy*. 6 (2022), 646-658. doi:10.1093/ce/zkac042
- [14] A.M. Howlader, S. Sadoyama, L.R. Roose and S. Sepasi, Distributed voltage regulation using Volt-Var controls of a smart PV inverter in a smart grid: An experimental study, *Renewable Energy*. 127 (2018), 145-157. doi:10.1016/j.renene.2018.04.058
- [15] P. Kayal and C.K. Chanda, Strategic approach for reinforcement of intermittent renewable energy sources and capacitor bank for sustainable electric power distribution system, *International Journal of Electrical Power & Energy Systems.* 83 (2016), 335-351.

- doi:10.1016/j.ijepes.2016.04.029
- [16] A. Joseph, K. Smedley and S. Mehraeen, Secure power distribution against reactive power control malfunction in DER units, *IEEE Transactions on Power Delivery*. 36 (2021), 1552-1561. doi:10.1109/TPWRD.2020.3011376
- [17] F. Bernáth and P. Mastný, Power factor compensation of photovoltaic power plant, *Electroscope* 5 (2012)
- [18] Anonim, Elektrik Şebeke Yönetmeliği, https://www.epdk.gov.tr/Detay/Icerik/3-6730/elektrik-sebeke- (accessed 12 January 2024).
- [19] H. Köroğlu. Elektrik Dağıtım Şebekesinde Güneş Enerji Santralinden Reaktif Güç Desteği Sağlanması, Yüksek Lisans Tezi, Necmettin Erbakan Üniversitesi Fen Bilimleri Enstitüsü, Elektrik Elektronik Mühendisliği Ana Bilim Dalı, Konya, 2024
- [20] M. Flota-Bañuelos, M. Espinosa-Trujillo, J. Cruz-Chan and T. Kamal, Experimental study of an inverter control for reactive power compensation in a grid-connected solar photovoltaic system using sliding mode control, *Energies*. 16 (2023), 853. doi:10.3390/en16020853
- [21] V. Kumar and M. Singh, Reactive power compensation using derated power generation mode of modified P&O algorithm in grid-interfaced PV system, *Renewable Energy*.178 (2021), 108-117.
- [22] A. Dhaneria. Grid Connected PV System with Reactive Power Compensation for the Grid. In: 2020 IEEE Power & Energy Society Innovative Smart Grid Technologies Conference (ISGT). Washington, DC, USA, 2020. doi: 10.1109/ISGT45199.2020.9087728



Vol: 7 No:2 Year: 2025

Araştırma Makalesi/Research Article

e-ISSN: 2667-7989

https://doi.org/10.47112/neufmbd.2025.92

Paratiroid Hormon Tayinine Yönelik IrO₂ Nanopartikül Tabanlı Yatay Akış İmmünosensör Geliştirilmesi

Eda GÜMÜŞ 1* D Haluk BİNGÖL 1,2 D Erhan ZOR 1,3 D

Makale Bilgisi ÖZET Biyosensörlerin hayatımıza getirdiği kolaylıklar, biyosensör teknolojisinin gün geçtikçe Geliş Tarihi: 12.12.2024 gelişmesini sağlayacak yeni çalışmaların önünü açmaktadır. Optik sensörler ile birçok alanda Kabul Tarihi: 24.02.2025 kalitatif ve kantitatif analizler yapılmaktadır. Bu alanlar arasında sağlık sektöründe önemli olan Yayın Tarihi: 31.08.2025 hormon testleri de dikkat çekmektedir. Bu çalışmada, kandaki kalsiyum dengesini koruyarak bazı metabolik faaliyetlerde önemli bir role sahip olan paratiroid hormonunun (PTH) kağıt bazlı yatay akış testi (LFA) ile tayin edilmesi amaçlanmıştır. Kandaki PTH seviyesi birçok paratiroid **Anahtar Kelimeler:** kaynaklı hastalık ve kanser teşhisi için önem arz etmektedir. Geliştirilen iridyum oksit Yatay akıs immünosensör, nanopartikül (IrO2NPs) esaslı LFA ile PTH tayini ve tespiti gerçekleştirilmiştir. Aynı zamanda, Kağıt-bazlı biyosensör, PTH tespiti için IrO₂NPs kullanılarak LFA geliştirilen ilk çalışmadır. PTH tayini için tasarlanan İridyum oksit nanopartikül, IrO₂NPs bazlı LFA'nın teşhis ve tayin alt sınırı (LOD ve LOQ) sırasıyla 3,92 ng/mL ve 11,88 Paratiroid hormon. ng/mL olarak hesaplanmıştır.

Development of IrO₂ Nanoparticles-Based Lateral Flow Immunosensor for Determination of Parathyroid Hormone

Article Info ABSTRACT

Received: 12.12.2024 Accepted: 24.02.2025 Published: 31.08.2025

Keywords:

Lateral flow immunosensor, Paper-based biosensor, Iridium oxide nanoparticle, Parathyroid hormone. The conveniences that biosensors bring to our lives pave the way for new studies that will enable biosensor technology to develop day by day. Qualitative and quantitative analyses are conducted in many areas with optical sensors. Among these areas, hormone tests, which are important in terms of health, also attract attention. This study aims to detect parathyroid hormone (PTH), which has an important role in some metabolic activities by maintaining calcium balance in the blood, by paper-based lateral flow analysis. PTH levels in the blood are important for the diagnosis of many parathyroid-related diseases and cancer. PTH was determined by the developed iridium oxide nanoparticles-based (IrO₂NPs) LFA. At the same time, this is the first study to develop an LFA for the detection of PTH using IrO₂NPs. The limit of detection and quantification (LOD and LOQ) of IrO₂NPs-based LFA designed for PTH determination were calculated as 3.92 ng/mL and 11.88 ng/mL, respectively.

To cite this article:

Gümüş, E., Bingöl, H. & Zor, E. (2025). Development of iridium oxide nanoparticles-based lateral flow immunosensor for determination of parathyroid hormone. *Necmettin Erbakan University Journal of Science and Engineering, 7*(2), 286-293. https://doi.org/10.47112/neufmbd.2025.92

*Corresponding Author: Eda Gümüş, edagumus@erbakan.edu.tr



¹ Necmettin Erbakan University, Science and Technology Research and Application Center (BİTAM), Konya, Türkiye

² Necmettin Erbakan University, Faculty of Engineering, Department of Basic Sciences, Konya, Türkiye

³ Necmettin Erbakan University, Ahmet Keleşoğlu Faculty of Education, Department of Science Education, Konya, Türkiye

INTRODUCTION

Parathyroid hormone (PTH), a single-chain peptide hormone consisting of 84 amino acids, is synthesized by parathyroid primary cells [1]. Its half-life is short, between 2-4 days. PTH increases the amount of calcium in the blood by triggering the formation of calcium from the bone and ensuring its reabsorption [2]. PTH generally helps the body absorb calcium from the kidneys, excrete phosphorus, and increase the formation mechanism of vitamin D. This hormone is also called "intact parathyroid hormone" and it plays a key role in metabolic activities in the liver and kidneys of the body [2–6].

Determination of PTH levels in blood is used to monitor parathyroid diseases such as osteoporosis and malignant hypercalcemia. PTH levels in blood are also important in determining some types of cancer, such as prostate cancer and breast cancer. When breast cancer and prostate cancer metastasize to the bone, an increase in the levels of PTH in the blood is observed. Therefore, determining the PTH levels is important and various analytical approaches were developed by using fluorometric, electrochemical and chromatographic [7] methods for PTH detection. Since PTH has a short half-life, the PTH levels in the blood decrease from its normal levels of 11-54 pg/mL in a short time after the parathyroid tissue is removed [8–10]. Therefore, rapid test kits are important to detect the PTH level in a short time.

Lateral flow assay (LFA) is a simple paper-based platform offered in strip format. LFA is one of the broadly used point-of-care technologies (POCT) because it provides robustness, high sensitivity, and easy and fast performance [11,12]. LFA consists of a chromatographic system that occurs through the separation of the components in the mixture resulting from differences in their movements in the reaction membrane and the specific antibody-to-antigen immunochemical reaction [13,14]. LFA consists of four parts: sample pad, conjugate pad, reaction pad (test membrane) and adsorbent pad [14,15]. This POCT platform provides results in a few minutes and is obtained with end-user intervention. It is preferred in many fields such as food safety, biomedicine, environmental health and quality control due to its simple production and low cost [16].

The use of nanomaterials in biosensor applications has become very common in recent years. They are widely preferred because of their high surface area, high activity, high catalytic effects, surface reactions, and high bio-detection [17]. Various nanomaterials such as plasmonic nanoparticles, quantum dots and other nanoparticles are used in paper-based immunochromatographic assays [18]. Particularly, AuNPs are widely used nanomaterials in LFA technology due to their high biocompatibility and high optical properties. However, in the case of the determination of analytes with low detection limits, their low sensitivity is thought to hinder future applications. Recently, iridium oxide nanoparticles (IrO₂NPs) have emerged as remarkable metal oxides that are widely used in electrocatalytic [19,20] and antitumor applications [21,22] due to their considerable large surface area, high chemical stability, high catalytic properties as well as corrosion resistance [23]. Besides, IrO₂NPs have been also used as an alternative to AuNPs in LFA to detect human immunoglobulin. The features of this nanomaterial, such as its unique sharp dark blue color, as well as its biocompatibility with antibodies and its advantage in conjugation thanks to its large surface area [24] have increased the reason to choose these nanoparticles [25–30].

In this study, considering all these advantages of IrO₂NPs, we developed a cost-effective, fast and robust biosensor for PTH determination. The optimization of each LFA component was conducted. The assay was created by determining the optimum quantity of BSA (1%, 3% and %5) and Tween-20 (0.01%, 0.025%, 0.050%, 0.075%, and 0.100%) in the optimization of the membrane, conjugate pad and sample pad. To find the optimum condition, the flow rate of iridium oxide nanoparticles on the membrane surface was taken into consideration. Then, qualitative and quantitative determination of PTH was performed in the LFA under the optimum conditions. LOD and LOQ values for PTH determination were calculated as 3.92 ng/mL and 11.88 ng/mL, respectively. This study is the first work to develop an

LFA for the determination of PTH using IrO₂NPs.

MATERIALS AND METHODS

Materials and Equipment

The sample pad (CFSP001700), glass fiber (GFCP000800), test membrane (HF090MC100), and adsorbent pad (CFSP001700) used in the LFA design were purchased from Millipore. K₂IrCl₆ (450162) used for IrO₂NPs synthesis was obtained from Sigma Aldrich. PTH hormone (P7036) was purchased from Sigma-Aldrich, polyclonal parathyroid hormone antibody (ab40630), polyclonal goat antibody (ab6702), and monoclonal parathyroid hormone antibody (ab154792) were purchased from Abcam.

Field Emission Scanning Electron Microscope (ZEISS GeminiSEM 500) with the Scanning transmission electron microscopy (STEM) detector was performed for the characterization of IrO₂NPs. Spectroscopic measurements were carried out with an Ultraviolet, Visible and Near Infrared Spectrometer (Shimadzu UV-3600 Plus). Spraying of test and control lines on the membrane surface was achieved with the Linomat 5 (CAMAG) device. Signal intensities on the test and control lines were measured with a colorimetric reader (Qiagen LR3).

Synthesis, Characterization, and Functionalization of Iridium Oxide Nanoparticles

For the synthesis of IrO₂NPs, all glass materials and magnetic stirrer were cleaned with HNO₃/HCl=1:3 (v/v), pure water, and dried in an oven to prevent pollution that could disrupt particle formation and size distribution. IrO₂NPs synthesis was carried out according to the Harriman and Thomas [30] method. For this, 30 mg K₂IrCl₆ was added to the aqueous solution (50 mL) of 3.80 mM sodium citrate sesquihydrate. The pH of the resulting solution (brown color) was adjusted to 7.5 using NaOH and boiled under reflux with constant stirring. This process was continued until the color of the brown solution changed to light blue. The pH of the solution, which was left to cool at room temperature, was adjusted to 7.5. Then, after boiling under reflux in the presence of oxygen gas for 2 hours, the process was completed when the solution turned dark blue (Figure 1) [24,30]. The solution was stored at 4°C, wrapped in aluminium foil.

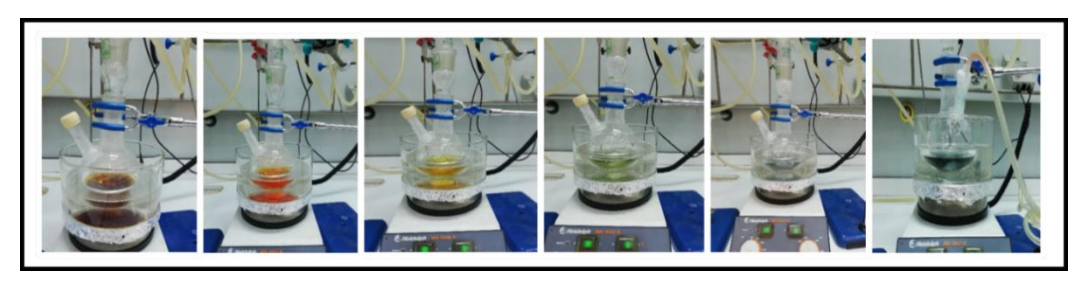


Figure 1
Synthesis of IrO₂NPs.

STEM images for the characterization of the IrO₂NPs were taken by FESEM. In the functionalization step of IrO₂NPs surfaces with antibodies, 100 μ L of anti-PTH antibody (250 μ g/mL) from goat was added to 1.5 mL of IrO₂NP solution and mixed at 650 rpm for 2 hours at room temperature. For the functionalization step of IrO₂NPs surfaces with antibodies, 100 μ L of anti-PTH antibody (250 μ g/mL) from goat was mixed with 1.5 mL of IrO₂NP solution at 650 rpm for 2 hours at room temperature. After the resulting mixture was centrifuged at 35000 rpm at 4°C for 2.5 hours, the resulting precipitate added 0.5 mL of borate containing 10% sucrose and 25% BSA. The buffer was obtained according to the literature [24].

Optimization of LFA

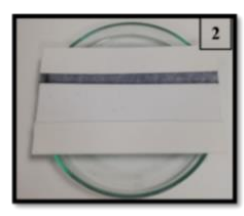
Washing of Sample Pad, Test Membrane and Conjugate pad

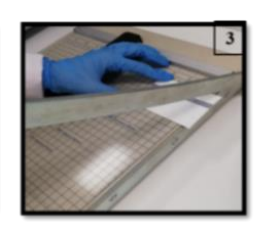
Both sides of the sample pads were washed with pure water, phosphate buffer solution (PBS), PBS + Tween 20 (PBST) and immunobuffer (PBST + BSA-bovine serum albumin) solutions, respectively. The washed pads were dried in an oven at 37 °C for 2 hours. The test membrane was washed with immunobuffer solution and dried in an oven at 37 °C for 2 hours. The glass-fiber (conjugate pad) was also washed with immunobuffer solution and dried in the same conditions for 1 hour. Then, it was dipped into IrO₂NPs/antibody. Then, it was dried under a vacuum at 30 °C for 1 hour.

Design of LFA

For the design of LFA, the adhesive tapes on the backing card were opened and the adsorbent pad was placed at the bottom, a part of the sample pad (~2 mm) was assembled onto the upper part of the membrane, overlapping the conjugate pad. The kits were cut to 5 mm thick with a guillotine and made ready for the experiments (Figure 2).







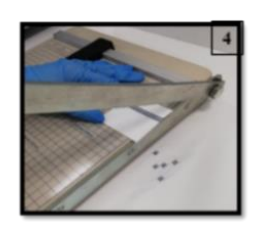




Figure 2
Preparation and cutting steps of LFA.

RESULT AND DISCUSSION

Characterization of Iridium Oxide Nanoparticles

The unique characteristic shapes of IrO₂NPs, whose STEM images were taken at 125KX and 500KX magnification, were presented in Figure 3.a-a'. Figure 3b shows the size distribution graph for IrO₂NPs, in which sizes of the nanoparticles ranged between 10-23 nm and the average nanoparticle size was found around 17.5 nm.

The image of the aqueous solution of IrO₂NPs obtained in dark blue color is shown in Figure 3c. Optical characterization of this solution was performed by UV-Vis spectrometer, and the obtained spectrum showed a maximum absorbance at 585 in agreement with the literature [24,31].

Effect of Washing on Optimization of Membrane and Glass Fiber

To examine the flow of the analyte solution and IrO_2NPs in the conjugate pad on LFA platforms, the performances of the LFA obtained by washing the surface of the membrane and the glass fiber with immunobuffer were investigated. For this purpose, different amounts of BSA and Tween-20 were added to the immunobuffer solution. For the optimum ratio of BSA and Tween-20, 0.01%, 0.025%, 0.050%, 0.075% and 0.100% Tween-20 were added to 1%, 3% and 5% BSA solutions.

The flow of IrO₂NPs on the membrane surface was investigated by using the membranes washed with immunobuffer solutions including 1%, 3% and 5% BSA and Tween-20 in different amounts. To this aim, the time was recorded to see the point where the nanoparticles reached on the membrane surface. First, the movement within 3 seconds, secondly the time taken to reach the midpoint of the membrane and then the adsorbent pad, respectively (Figures S1, S2 and S3). The particularly important and decisive points here are (i) no neither too fast nor too slow nanoparticle flow on the membrane surface (ii) no accumulation of particles on the membrane surface, (iii) and the homogeneous flow of nanoparticles on the membrane surface. In the performed experimental study, the optimum condition was obtained with 3% BSA and 0.050% Tween-20 including solution.

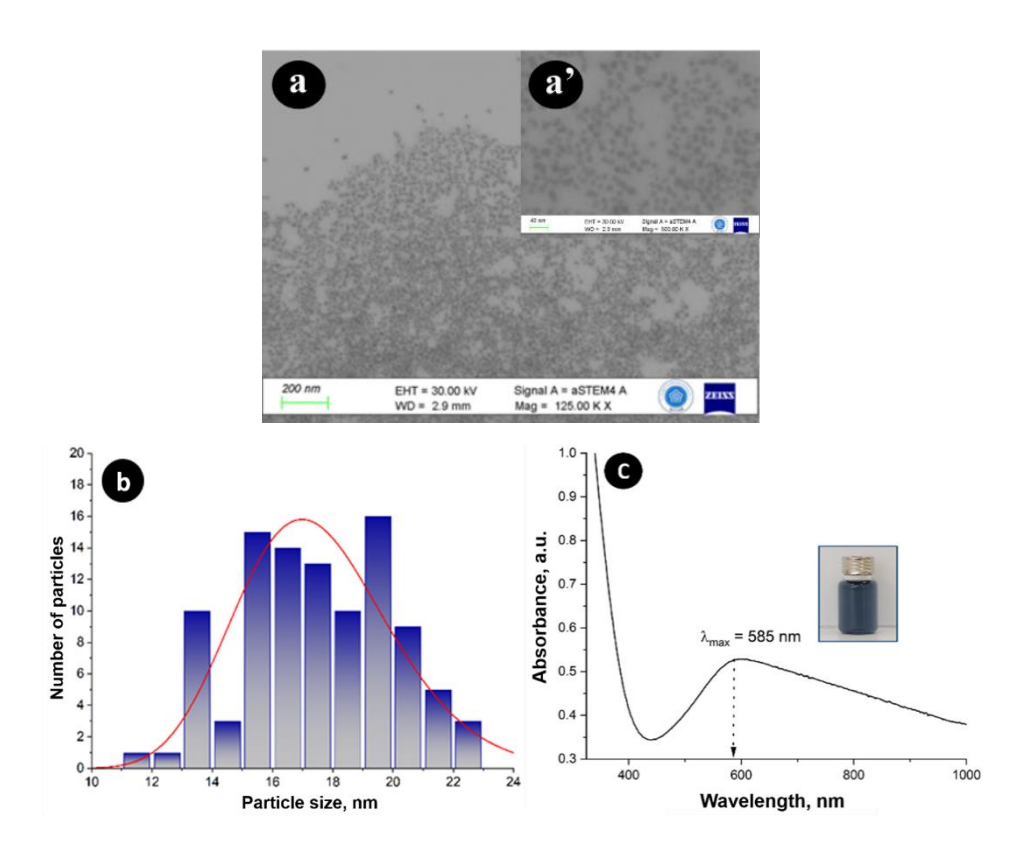


Figure 3
STEM images of IrO₂NPs at (a) 125KX, (a') 500KX magnifications, (b) Size distribution graph of IrO₂NPs, (c) UV-Vis spectrum and the image of IrO₂NPs dispersion.

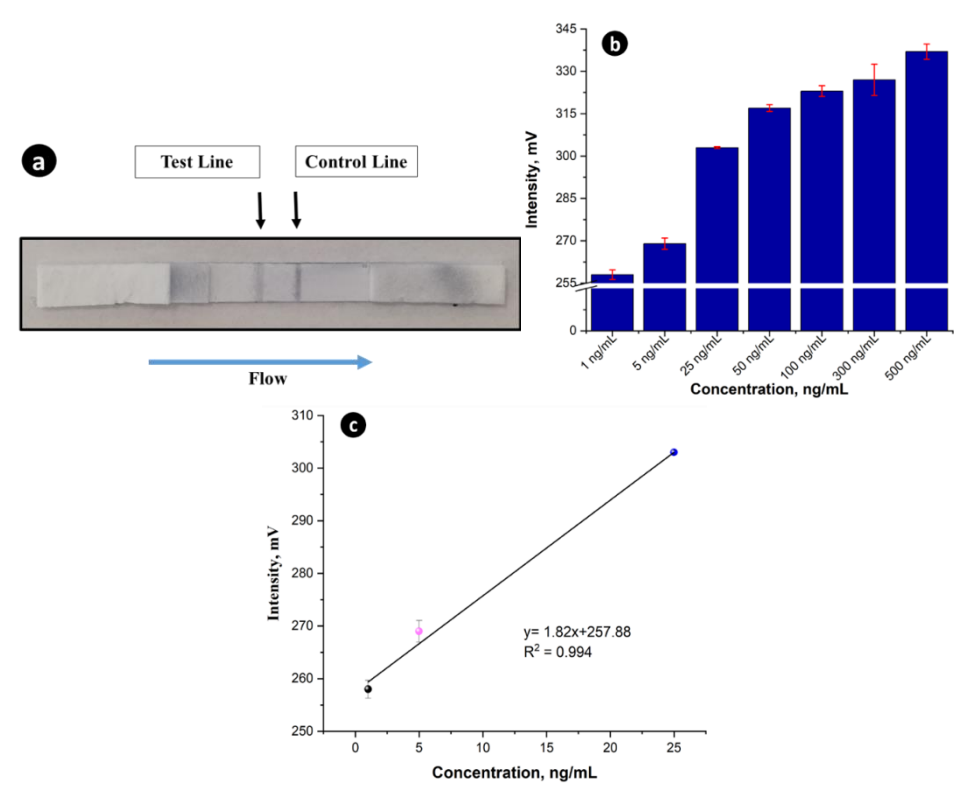


Figure 4
(a) The qualitative LFA test (b) Signal intensity obtained for various concentrations of PTH between 1-500 ng/mL, (c) The linear curve for the change of intensity of the signal obtained against PTH concentration.

For the quantitative determination of PTH, PTH solution at different concentrations (0-500 ng/mL) was transferred to the sample pad of LFA. The intensity values of the test lines obtained in these experiments at different concentrations were determined with a colorimetric reader and they are presented as a graph shown in Figure 4.b. Using the linear range (see Figure 4.c) of the graph in which the intensity values on the test line were plotted against different concentration values, the LOD and LOQ values were determined to be 3.92 and 11.88 ng/mL, respectively.

CONCLUSION

In this study, an IrO₂NPs-based LFA was designed for the qualitative and quantitative detection of PTH. As the result of quantitative analysis, LOD and LOQ values were calculated as 3.92 ng/mL and 11.88 ng/mL, respectively. Although there are many LFAs for hormone detection in the literature, an LFA for the determination of PTH was obtained for the first time using IrO₂NPs in this study. Unlike the nanoparticles (AuNPs) commonly used in the literature, this study shows that IrO₂NP will pave the way for its use as an alternative in different studies. Since the use of nanoparticles in LFAs is very important, especially in terms of selectivity, alternative nanoparticles increase the effectiveness of these systems. For this reason, the combination of existing nanoparticles and the hybrid systems they create have recently attracted the attention of researchers. We believe that using hybrid structures of IrO₂NPs with different nanoparticles in future studies will lead to new, more sensitive, and selective LFA studies.

Ethical Statement

This study is an original research article designed and developed by the authors.

Author Contributions

```
Research Design (CRediT 1): E.G. (%30) – H.B. (%30) – E.Z. (%40)
Data Collection (CRediT 2): E.G. (%60) – H.B. (%20) – E.Z. (%20)
Research - Data Analysis – Validation (CRediT 3-4-6-11): E.G. (%60) – H.B. (%20) – E.Z. (%20)
Writing the Article (CRediT 12-13): E.G. (%45) – H.B. (%20) – E.Z. (%35)
Revision and Improvement of the Text (CRediT 14): E.G. (%45) – H.B. (%20) – E.Z. (%35)
```

Financing

This study was supported by Necmettin Erbakan University, Scientific Research Projects Coordination Unit (NEU-BAP) with Project Number: 201210004.

Conflict of Interest

The authors declare that they have no known competing financial interests or personal relationships that could have appeared to influence the work reported in this paper.

Sustainable Development Goals (SDG)

Sustainable Development Goals: Not supported.

REFERENCES

- [1] Y. Nie, J. Li, Y. Liu, Q. Zhang, Q. Ma, A visual FRET immunofluorescent biosensor for ratiometric parathyroid hormone (1–84) antigen Point-of-Care detection, *Journal of Fluorescence*. 30 (2020), 329–334. doi:10.1007/s10895-020-02502-5
- [2] J.C.P. Souberbielle, H. Roth, D.P. Fouque, Parathyroid hormone measurement in CKD, *Kidney International*. 77 (2009), 93–100. doi:10.1038/ki.2009.374
- [3] J.H. Brossard, R. Lepage, H. Cardinal, L. Roy, L. Rousseau, C. Dorais, P. D'Amour, Influence of glomerular filtration rate on non-(1-84) parathyroid hormone (PTH) detected by intact PTH assays, *Clinical Chemistry*. 46 (2000), 697–703. doi:10.1093/clinchem/46.5.697
- [4] B. Bayraktar, T. Uzun, E. Tekce, V. Aksakal, A.A: Kılınç, Kemik Metabolizmasının Hormonal Regülasyonu, in: Kırmızı, B., İşigüzel, B. (Ed.) Türkiye Vizyonu Multidispliner Çalışmalar, 2019.
- [5] V.L. Venkatraman, R.K. Reddy, F. Zhang, D. Evans, B. Ulrich, S. Prasad, Iridium oxide nanomonitors: Clinical diagnostic devices for health monitoring systems, *Biosensors and Bioelectronics*. 24 (2009), 3078–3083. doi:10.1016/j.bios.2009.03.029.
- [6] B.K. Tekçe, H. Tekçe, Kronik böbrek hastalarında iki cihazın intakt paratiroid hormon ölçümünün karşılaştırılması, *Türk Klinik Biyokimya Dergisi*. 13 (2015), 21–28.
- [7] S. Li, Y. Liu, Q. Ma, A novel polydopamine electrochemiluminescence organic nanoparticle-based biosensor for parathyroid hormone detection, *Talanta*. 202 (2019), 540–545. doi:10.1016/j.talanta.2019.05.022.
- [8] H.M. Özcan, K. Yildiz, C. Çakar, T. Aydin, E. Asav, A. Sağiroğlu, M.K. Sezgintürk, Ultrasensitive impedimetric biosensor fabricated by a new immobilisation technique for parathyroid hormone, *Appl. Biochem. Biotechnol.* 176 (2015), 1251–1262.
- [9] J.F. Aloia, M. Feuerman, J.K. Yeh, Reference range for serum parathyroid hormone, *Endocrine Practice*.12 (2006), 137–144. doi:10.4158/EP.12.2.137.
- [10] M.N. Ohe, R.O. Santos, I.S. Kunii, M. Abrahão, O. Cervantes, A.B. Carvalho, M. Lazaretti-Castro, J.G.H. Vieira, Utilidade da medida de PTH intra-operatório no tratamento cirúrgico do hiperparatiroidismo primário e secundário: análise de 109 casos, *Arquivos Brasileiros De Endocrinologia & Metabologia*. 50 (2006), 869–875. doi:10.1590/S0004-27302006000500007.
- [11] J.S. Gootenberg, O.O. Abudayyeh, M.J. Kellner, J. Joung, J.J. Collins, F. Zhang, Multiplexed and portable nucleic acid detection platform with Cas13, Cas12a, and Csm6, *Science*. 360 (2018), 439–444. doi:10.1126/science.aaq0179.
- [12] D. Zhang, L. Huang, B. Liu, E. Su, H.Y. Chen, Z. Gu, X. Zhao, Quantitative detection of multiplex cardiac biomarkers with encoded SERS nanotags on a single T line in lateral flow assay, *Sensors Actuators, B Chemical.* 277 (2018), 502–509. doi:10.1016/j.snb.2018.09.044.
- [13] X. Mao, W. Wang, T.E. Du, Rapid quantitative immunochromatographic strip for multiple proteins test, *Sensors Actuators*, *B Chemical*. 186 (2013), 315–320. doi:10.1016/j.snb.2013.05.083.
- [14] J. Singh, S. Sharma, S. Nara, Evaluation of gold nanoparticle based lateral flow assays for diagnosis of enterobacteriaceae members in food and water, *Food Chemistry*. 170 (2015), 470–483. doi:10.1016/j.foodchem.2014.08.092.
- [15] J. Hu, S.Q. Wang, L. Wang, F. Li, B. Pingguan-Murphy, T.J. Lu, F. Xu, Advances in paper-based point-of-care diagnostics, *Biosensors and Bioelectronics*. 54 (2013), 585–597. doi:10.1016/j.bios.2013.10.075.
- [16] K.M. Koczula, A. Gallotta, Lateral flow assays, *Essays in Biochemistry*. 60 (2016), 111–120. doi:10.1042/EBC20150012.

- [17] A. Kaushik, R. Khan, P.R. Solanki, P. Pandey, J. Alam, S. Ahmad, B.D. Malhotra, Iron oxide nanoparticles-chitosan composite based glucose biosensor, *Biosensors and Bioelectronics*. 24 (2008), 676–683. doi:10.1016/j.bios.2008.06.032.
- [18] D. Quesada-González, A. Merkoçi, Nanoparticle-based lateral flow biosensors, *Biosensors and Bioelectronics*. 73 (2015), 47–63. doi:10.1016/j.bios.2015.05.050.
- [19] J. Lim, D. Park, S. Seo Jeon, C.-W. Roh, J. Choi, D. Yoon, M. Park, H. Jung, H. Lee, J. Lim, D. Park, S.S. Jeon, C. Roh, J. Choi, H. Lee, D. Yoon, M. Park, H. Jung, Ultrathin IrO2 nanoneedles for electrochemical water oxidation, *Advanced Functional Materials*. 28 (2018), 1704796. doi:10.1002/ADFM.201704796.
- [20] N. Liu, Z. Duan, Q. Zhang, J. Guan, Insights into active species of ultrafine iridium oxide nanoparticle electrocatalysts in hydrogen/oxygen evolution reactions, *Chemical Engineering Journal*. 419 (2021), 129567. doi:10.1016/J.CEJ.2021.129567.
- [21] H. Zhang, L.X. Zhang, H. Zhong, S. Niu, C. Ding, S. Lv, Iridium oxide nanoparticles-based theranostic probe for in vivo tumor imaging and synergistic chem/photothermal treatments of cancer cells, *Chemical Engineering Journal*. 430 (2022), 132675. doi:10.1016/J.CEJ.2021.132675.
- [22] X. Yuan, J. Cen, X. Chen, Z. Jia, X. Zhu, Y. Huang, G. Yuan, J. Liu, Iridium oxide nanoparticles mediated enhanced photodynamic therapy combined with photothermal therapy in the treatment of breast cancer, *Journal of Colloid and Interface Science*. 605 (2022), 851–862. doi:10.1016/J.JCIS.2021.07.136.
- [23] S. Zhao, T. Bu, K. Yang, Z. Xu, F. Bai, K. He, L. Li, L. Wang, Immunochromatographic assay based on polydopamine-decorated iridium oxide nanoparticles for the rapid detection of salbutamol in food samples, *ACS Applied Materials & Interfaces*. 13 (2021), 28899–28907.
- [24] D. Quesada-González, A. Sena-Torralba, W.P. Wicaksono, A. de la Escosura-Muñiz, T.A. Ivandini, A. Merkoçi, Iridium oxide (IV) nanoparticle-based lateral flow immunoassay, *Biosensors and Bioelectronics*. 132 (2019), 132–135. doi:10.1016/j.bios.2019.02.049.
- [25] L. Rivas, A. de la Escosura-Muñiz, J. Pons, A. Merkoçi, alzheimer disease biomarker detection through electrocatalytic water oxidation induced by Iridium oxide nanoparticles, *Electroanalysis*. 26 (2014), 1287–1294. doi:10.1002/elan.201400027.
- [26] Y. Zhang, J. Wang, S. Gong, D. Xu, Y. Mo, Straw mulching enhanced the photosynthetic capacity of field maize by increasing the leaf N use efficiency, *Agricultural Water Management*. 218 (2019), 60–67. doi:10.1016/j.agwat.2019.03.023.
- [27] D. Finkelstein-Shapiro, M. Fournier, D.D. Méndez-Hernández, C. Guo, M. Calatayud, T.A. Moore, A.L. Moore, D. Gust, J.L. Yarger, Understanding iridium oxide nanoparticle surface sites by their interaction with catechol, *Physical Chemistry Chemical Physics*. 19 (2017) ,16151–16158. doi:10.1039/C7CP01516J.
- [28] D. Xu, P. Diao, T. Jin, Q. Wu, X. Liu, X. Guo, H. Gong, F. Li, M. Xiang, Y. Ronghai, Iridium oxide nanoparticles and Iridium/Iridium Oxide nanocomposites: Photochemical fabrication and application in catalytic reduction of 4-Nitrophenol, *ACS Applied Materials & Interfaces*. 7 (2015), 16738–16749. doi:10.1021/acsami.5b04504.
- [29] Y. Zhao, E.A. Hernandez-Pagan, N.M. Vargas-Barbosa, J.L. Dysart, T.E. Mallouk, A high yield synthesis of ligand-free iridium oxide nanoparticles with high electrocatalytic activity, *The Journal of Physical Chemistry Letters*. 2 (2011), 402–406. doi:10.1021/jz200051c.
- [30] A. Harriman, J.M. Thomas, G.R. Milward, Catalytic and structural properties of iridium-iridium dioxide colloids, *New Journal of Chemistry*. 11 (1987), 757–762.
- [31] J.C. Hidalgo-Acosta, M.A. Méndez, M.D. Scanlon, H. Vrubel, V. Amstutz, W. Adamiak, M. Opallo, H.H. Girault, Catalysis of water oxidation in acetonitrile by iridium oxide nanoparticles, *Chemical Science*. 6 (2015), 1761–1769. doi:10.1039/c4sc02196g.



Vol: 7 No:2 Year: 2025

Araştırma Makalesi/Research Article

e-ISSN: 2667-7989

https://doi.org/10.47112/neufmbd.2025.93

Pestisit Tespiti için Konjuge Polimer Nanopartikül Tabanlı Biyosensörün Tasarımı ve Geliştirilmesi

Dilara YENİTERZİ 1,2 D Dilek SÖYLER 1,2 D Sanive SÖYLEMEZ 2,3* D

- ¹ Necmettin Erbakan University, Graduate School of Natural and Applied Sciences, Department of Biomedical Engineering, Konya, Türkiye
- ² Necmettin Erbakan University, Science and Technology Research and Application Center (BİTAM), Konya, Türkiye
 - ³ Necmettin Erbakan University, Faculty of Engineering, Department of Biomedical Engineering, Konya, Türkiye

Makale Bilgisi ÖZET

Geliş Tarihi: 22.07.2024 Kabul Tarihi: 08.12.2024 Yayın Tarihi: 31.08.2025

Anahtar Kelimeler:

Konjuge polimer nanopartiküller, Elektrokimyasal sensör, Pestisit tespiti. Pestisitlerin çeşitli sağlık sorunlarıyla ilişkili olması, gıda ürünleri ve su kaynaklarındaki kalıntıların küresel ölçekte ciddi bir sorun haline gelmesine yol açmaktadır. Bu nedenle, pestisitlerin gıda ve sebzelerde insan vücudu ile temas etmeden önce tespit edilmesini sağlayacak algılama sistemlerinin geliştirilmesine acil ihtiyaç vardır. Bu çalışmada, poli(3-heksiltiyofen) nanopartikülleri (P3HTNP'ler) ve poli(3,4-etilendioksitiyofen) nanopartikülleri (PEDOTNP'ler) kullanılarak asetilkolinesteraz (AChE) temelli elektrokimyasal bir biyosensör geliştirilmiştir. Biyosensörün hazırlanmasında P3HTNP'ler sentezlenmiş ve Dinamik Işık Saçılımı (DLS), zeta potansiyeli, Alan Emisyonlu Taramalı Elektron Mikroskopisi (FE-SEM), Ultraviyole-Görünür Işık (UV-Vis) absorpsiyon spektroskopisi ve floresans emisyon ölçümleri ile karakterize edilmiştir. P3HTNP'lerin PEDOTNP'ler ile kombinasyonu sonucunda, asetiltiyokolinklorür (AThCl) için yüksek performanslı bir biyosensör (PEDOTNP'ler/P3HTNP'ler/AChE) elde edilmiştir. Optimizasyon çalışmalarının ardından biyosensörün elektrokimyasal özellikleri, yüzey morfolojisi ve analitik performans parametreleri değerlendirilmiştir. Geliştirilen biyosensör, 0.009 mM tespit sınırı (LOD) ve 37.843 μA·mM⁻¹·cm⁻² duyarlılık değeri ile üstün bir analitik performans sergilemiştir. Ayrıca, hedef biyosensör girişim etkilerine karşı yüksek seçicilik göstermiş ve uzun vadeli kullanımlarda da yüksek stabilitesini sürdürmüştür.

Design and Development of Conjugated Polymer Nanoparticles-Based Biosensor for Pesticide Detection

Article Info ABSTRACT

Received: 22.07.2024 Accepted: 08.12.2024 Published: 31.08.2025

Keywords:

Conjugated polymer nanoparticles, Electrochemical sensor, Pesticide detection. Because pesticides are linked to various health issues, their residues in edible foodstuffs and water sources are a serious global issue. For this purpose, there is an urgent requirement for the development of sensing systems for the recognition of pesticides from food and vegetables prior to being consumed. By using the nanoparticles of poly(3-hexylthiophene) nanoparticles (P3HTNPs) and poly(3,4-ethylenedioxythiophene) nanoparticles (PEDOTNPs), an electrochemical acetylcholinesterase (AChE) based biosensor was created in response to this challenge. To create such a sensor (PEDOTNPs/P3HTNPs/AChE), P3HTNPs were synthesized and characterized in terms of DLS (Dynamic Light Scattering), zeta potential, FE-SEM (Field Emission-Scanning Electron Microscopy), Ultraviolet Visible (UV-Vis) absorption, and fluorescence emission properties. After the combination of P3HTNPs with PEDOTNPs, the desired biosensor was created with high performance towards AThCl. After all optimization studies, analytical performances, surface characteristics of the biosensor PEDOTNPs/P3HTNPs/AChE biosensor has a limit of detection (LOD) and sensitivity values of 0.009 mM and 37.843 µAmM⁻¹cm⁻², respectively. In addition, the biosensor has an excellent antiinterfering ability and long-term stability.

To cite this article:

Yeniterzi, D., Söyler, D. & Söylemez, S. (2025). Design and development of conjugated polymer nanoparticles-based biosensor for pesticide detection. *Necmettin Erbakan University Journal of Science and Engineering*, 7(2), 294-308. https://doi.org/10.47112/neufmbd.2025.93

*Corresponding Author: Saniye Söylemez, saniye.soylemez@erbakan.edu.tr

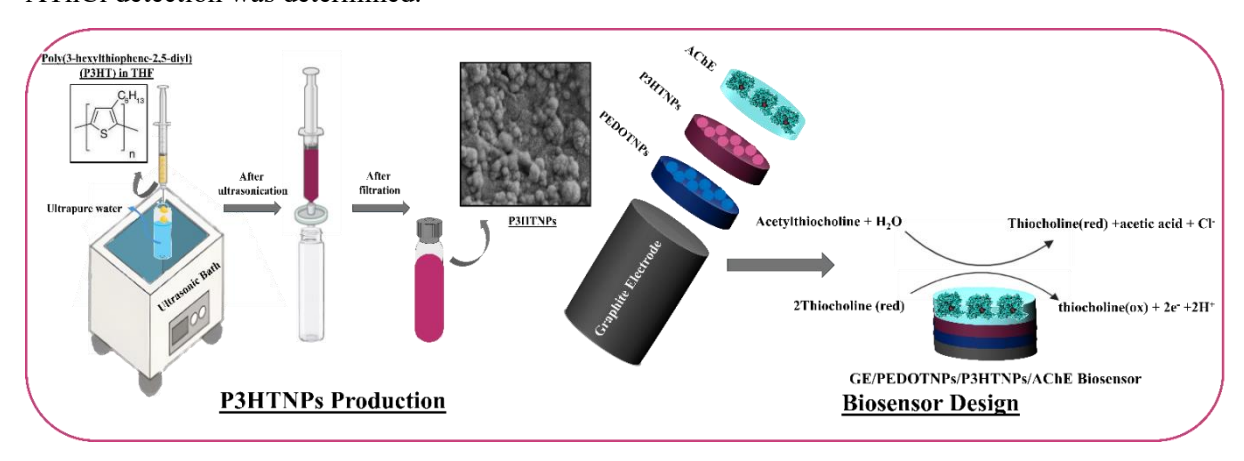


INTRODUCTION

Pesticides currently play a vital role in protecting crops in agricultural systems [1]. However, they have an effect on the environment as well as human health because of their hazardous effects. These harmful substances can build up in fruits, vegetables, and grains. They can also seep into the soil and contaminate water supplies [2]. Traditional analytical techniques like GC (Gas chromatography), LC (liquid chromatography), and MS (mass spectrometry) are still used for pesticide analysis. [3]. Nevertheless, the inherent shortcomings of traditional approaches, which include labor-intensive sample pretreatments, costly analyzers, and specialized manpower, render them unsuitable for field detection. Consequently, the development of an efficient technique for the quick quantitative determination of pesticides is imperative. [4]. Biosensors are used in many different fields, such as drug development, food safety, illness detection, defense, and environmental monitoring. [5]. They are potently used for a variety of objectives, such as substances that cause environmental pollution detection, food safety and quality monitoring, and the detection of biomolecules that are targets for medications or disease indicators. [6-8]. Enzyme-based electrochemical biosensors have the potential to be a viable substitute for traditional techniques because of their easy-to-use measuring protocols, quick reaction times, adequate sensitivity, and selectivity. [9]. Owing to its richness of aromatic amino acid sequences, the acetylcholinesterase enzyme (AChE) among cholinesterase (ChE) has significant sensitivity for organophosphorus pesticides (OPs) [10]. OPs and their derivatives have a potent inhibitory impact on AChE by phosphorylating its serine residues in an irreversible manner. [11]. For the detection of ACh or OPs, biosensors based on the inhibition of the enzyme acetylcholinesterase are therefore appealing. To date, a variety of AChE biosensors have been described. [9,12].

Conjugated polymers (CPs) are a class of organic semiconductor materials that possess delocalized electronic structures and large π -conjugated backbones. Many different types of CPs with varying chemical structures and functionalities have begun to emerge in various areas of biomedicine, including photodynamic therapy, photothermal therapy, fluorescence imaging, and others, due to their unique photophysical properties and photoelectric effects [13]. The functionalized side chains of CPs may also be responsible for the anticipated biological response, biocompatibility, and water solubility, among other properties [14,15]. Because CPs are good materials for immobilizing proteins and facilitating quick electron transfer for the creation of effective biosensors, there has been a lot of attention on the development of biosensors lately [16]. Because electrons on conjugated π electron backbones can travel freely, using CPs in the design of biosensors improves the biomolecules' electrocatalytic characteristics [17]. Therefore, this characteristic facilitates quicker electron transfer and ensures that the transducer and the biomolecule can communicate directly [18]. In addition, enzymes on the electrode surface are greatly stabilized by CPs-modified surfaces [19]. By forming an appropriate three-dimensional matrix on the electrode surface, this attachment helps to sustain the enzyme activity for an extended period. To create a stable biosensor platform, the polymer structure may contain carboxyl, amino, and other groups that are open to covalent bonds. Convenient, extremely precise, and quick detection sensing techniques are critical to both environmental pollution detection and medical diagnostics. Since their applications offer high sensitivity and long-term stability during quantifying, CPs are highly appealing materials as a sensing platform in this regard [20]. Moreover, conjugated polymer-based nanoparticles are becoming more and more popular as multipurpose nanoscale materials with fascinating prospective applications. Through the choice of CPs and surface modification, their properties can be simply modified for particular purposes. Additionally, these materials are very appealing as biomaterials due to their simple production, adjustable characteristics, lower toxicity, and increased biocompatibility when compared to the current inorganic nanoparticles [21,22]. In this work, formulations of poly(3-hexylthiophene) (P3HT) nanoparticle ethylenedioxythiophene) (PEDOT) molecules, which are conjugated polymers, in the biosensor design.

Herein, an amperometric biosensor was constructed for pesticide detection via utilizing a three-electrode system to assess the analytical performance of the PEDOTNPs/P3HTNPs/AChE biosensor. For this purpose, P3HTNPs were synthesized using the reprecipitation method and then combined with PEDOTNPs to construct a biosensor surface. The reprecipitation method, which involves injecting the polymer solution into a poor solvent for the polymer to increase the collapse of polymer chains into spherical nanoparticles, was used to create the P3HT nanoparticles. Later, AChE was immobilized on the modified electrode surfaces. The suggested enzyme-based biosensor has been designed for pesticide analysis based on the inhibition of AChE, as OPs target AChE. FE-SEM, CV, and EIS techniques were used to characterize the surface and evaluate the electrochemical properties of the biosensor. The biosensor's optimum operating parameters were identified, followed by the analytical performance for AThCl detection was determined.



Scheme 1Cartoon illustration of the GE/PEDOTNPs/P3HTNPs/AChE electrochemical biosensor for AThCl detection.

MATERIALS AND METHODS

Apparatus and Reagents

Acetylthiocholine chloride (AThCl), glutaraldehyde (GA, 50% in H₂O), acetylcholinesterase (AChE, EC 3.1.1.7, 518 U mg⁻¹ solid) from *Electrophorus electricus* (electric eel), and other chemicals were obtained from Sigma-Aldrich. Field emission scanning electron microscopy (FE-SEM) (ZEISS GeminiSEM 500) was used to characterize the biosensor surfaces after each modification. P3HTNP's size distribution was measured using dynamic light scattering (DLS), which was carried out using a Micromeritics - Nanoplus 3 DLS system at 24 °C. To perform cyclic voltammetry (CV) and studies **GAMRY** electrochemical impedance spectroscopy (EIS) Reference potentiostat/galvanostat with a three-electrode cell design was utilized. Amperometric measurements were recorded with AUTOLAB PGSTAT 204 Analysis System, supported by a NOVA software package (Metrohm, The Netherlands).

Synthesis of P3HT Nanoparticles (P3HTNPs)

P3HTNPs were prepared using an established reprecipitation approach [21].. First, 1 mg of P3HT was weighed and dissolved in 1 mL of THF to prepare a stock polymer solution. Then, 1 mL of this solution was drawn into a syringe and injected into 10 mL of ultrapure water contained in a glass vial while the mixture was subjected to ultrasonication for 10 min. The resulting dispersion was left undisturbed to allow for THF evaporation. Finally, the mixture was filtered through a 0.45 μ M polystyrene syringe filter to obtain P3HT nanoparticles for further analysis.

Preparation of GE/PEDOTNPs/P3HTNPs/AChE Modified Electrodes

Without making any modifications to the graphite electrode (GE) surface, bare graphite electrodes

were carefully brightened with emery paper and rinsed with distilled water. The GE/PEDOTNPs/P3HT NPs/AChE was produced as follows: GE was coated by dropping onto its surface with 3.0 μ L of PEDOT NPs. Then, 5.0 μ L of P3HT NPs was dropped onto the modified surface, and it was left to dry at ambient temperature. Later, 4.0 μ L of AChE enzyme and 2.0 μ L of 1% GA solutions were dropped onto the modified GE surface, respectively. The electrode was permitted to dry for 2h. After all modifications, the electrode surfaces were cleaned with distilled water to eliminate any potential impurities from the surface.

To explain the electrochemical characteristics of the modified electrodes, chronoamperometry (i–t), CV, and EIS techniques were used. A three-electrode configuration was constructed using a modified GE (diameter, 3 mm) as the working electrode, an Ag wire pseudo-reference electrode, and a platinum wire as the counter electrode for all measurements. All amperometric measurements were performed by applying a +0.6 V (vs. Ag wire) constant potential, and the results were evaluated using current–time plots to quantify AThCl.

RESULTS

Characterization of P3HTNPs

P3HTNPs were characterized using DLS, zeta potential, UV-visible absorption spectroscopy (UV-Vis), and fluorescence spectroscopies. As a result of the DLS analysis, it was determined that the average hydrodynamic radius of the synthesized nanoparticles was 92.5 nm (Fig.1A). At the same time, the average polydispersity index (PDI) obtained as a result of the analysis proves that we obtained nanoparticles with hydrodynamic diameters in nanometers close to each other. Furthermore, surface charge measurements of the generated P3HT nanoparticles were obtained by Zeta potential analysis, shown in Figure 1B. The results show that the produced nanoparticles have a surface charge of -41.17 mV on average.

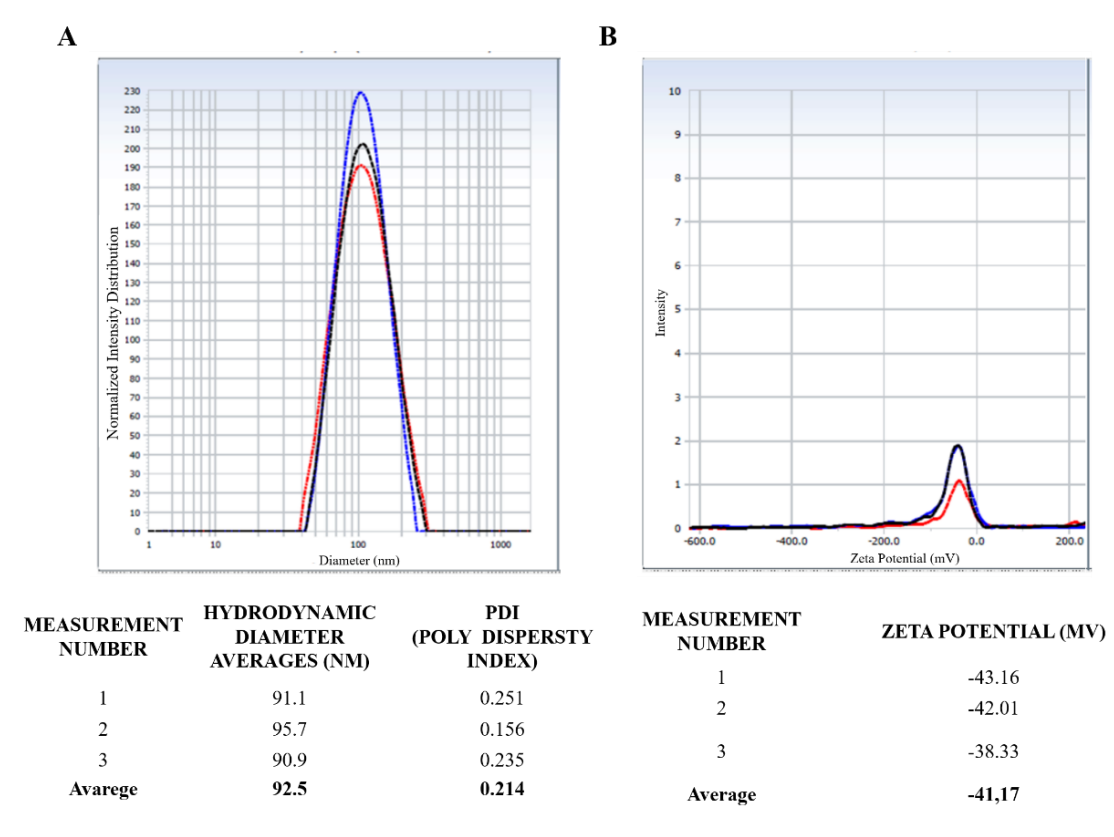


Figure 1(A) DLS and (B) zeta potential results of the P3HTNPs.

Optical properties of P3HTNPs were discovered using UV-Vis and fluorescence spectroscopies and differentiated from the polymer solution in THF, as shown in Figure 2. The maximum absorption peak was observed at 448 nm for the polymer solution in THF. When the P3HT polymer transformed into nanoparticles, it observed a change in absorption wavelengths of about 20 nm. On the other hand, with the formation of the nanoparticles from the polymer, the single peak at 576 nm wavelength noticed in the fluorescence emission spectrum of the polymer appeared as two peaks at 651 and 717 nm wavelengths, which were divided into two. The optical properties of P3HT and P3HTNPs were found to be compatible with the literature[23,24].

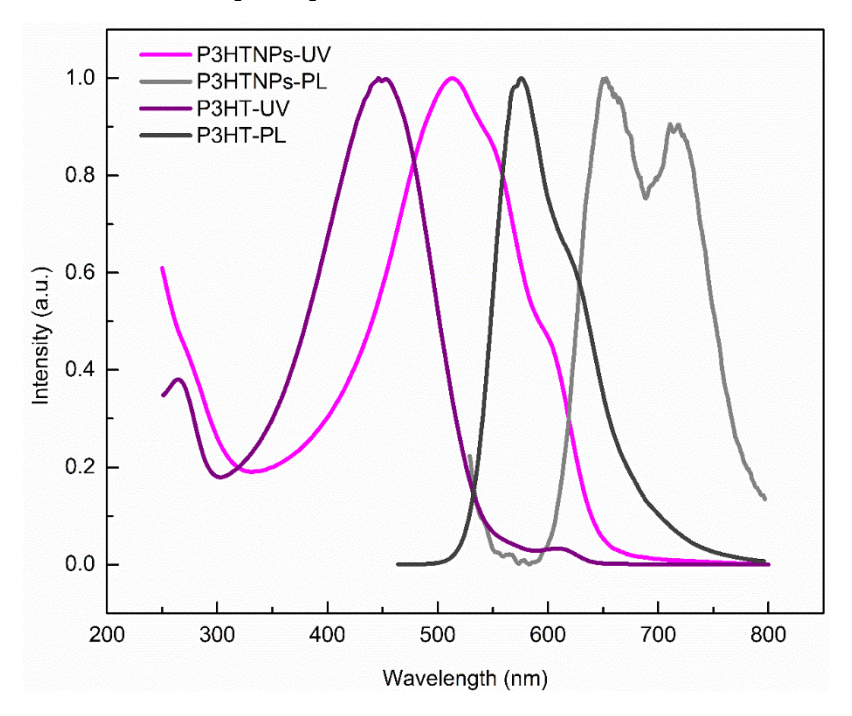


Figure 2 *UV-Vis absorption and fluorescence emission spectra of P3HT in THF and dispersion of P3HTNPs s in water.*

Optimization Studies and Analysis of Electrochemical and Surface Characteristics of the Biosensor

In this study, the volume of PEDOTNPs, P3HTNPs, AChE, and pH of the solution were improved. In each study, while the others have been unchanging, only one parameter has been replaced. In all optimization experiments, a 2 mM AThCl solution was used to detect the difference in amperometric sensor responses. Firstly, the amperometric responses were recorded for different PEDOTNPs volumes (1.0, 3.0, 5.0, 7.0, and 10.0 μL) and their results were compared to each other. According to Figure 3A, the optimum volume was found to be 3.0 μL . Secondly, various P3HTNPs volumes (3.0, 4.0, 5.0, 6.0, 7.0, and 8.0 μL) were used to determine the best electrode material (Fig. 3B). Low responses were received with both high and low volumes in comparison to 5.0 μL P3HTNPs, which was found to be optimal. Then, different amounts of AChE (1.0, 2.0, 4.0, 5.0, and 6.0 μL) were immobilized on the surface of GE. According to the recorded measurements given in Figure 3C, the highest signal was estimated with the GE, including 4.0 μL of the enzyme. Lastly, because enzymes are structures of proteins, their catalytic activities are greatly influenced by environmental pH. To decide the optimum pH, amperometric measurements were taken with GE/PEDOTNPs/P3HTNPs/AChE in buffer solutions with a wide pH range (4.0–8.0) (Fig. 3D). In the following experiments, pH 7.0 was preferred as the optimum test condition.

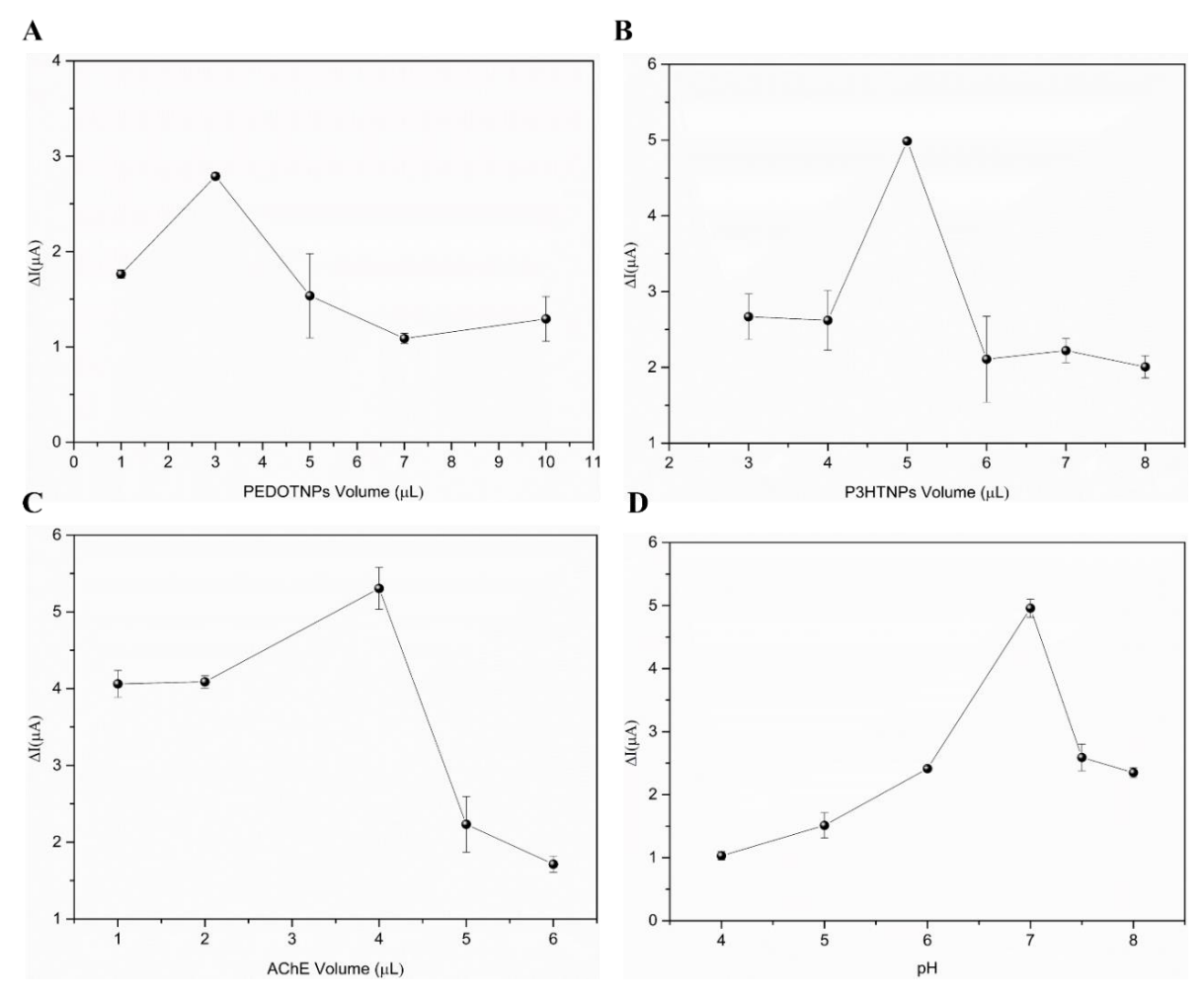


Figure 3
Optimization studies regarding to volume of (A)PEDOTNPs, (B) P3HTNPs, (C) enzyme, and (D) pH.

Techniques of CV and EIS were selected to investigate the surface characterization of the biosensor and verified the stepwise electrode modification process. CV and EIS analyses were recorded in 5.0 mM [Fe (CN)₆] $^{3-/4-}$ /0.1 M KCl to explore the electron transfer mechanism between the electrode surface and species (Figures 4A and B). PEDOTNPs, P3HTNPs, and AChE were consecutively modified on the GE surface via utilizing an easy drop-coating technique to prepare the PEDOTNPs/P3HTNPs/AChE biosensor. When the GE surface was modified with P3HTNPs, PEDOTNPs/P3HTNPs, and PEDOTNP/P3HTNPs/AChE, the oxidation peak current values of the redox solution were determined to be 60 µA, 84 µA, and 74 µA, respectively. The electrochemical response of the PEDOTNPs/P3HTNPs combination was considerably improved compared with P3HTNPs. After AChE immobilization on the nanomaterial-modified surface, the decrease in the peak current associated with the insulating biomolecules is an expected result for biomolecule immobilization. [25]. Using the Randles-Sevcik equation [26], the effective surface areas of the modified electrodes were determined to be 0.086 cm², 0.076 cm², 0.106 cm², and 0.093 cm² for the GE/P3HTNPs/PEDOTNPs, GE/P3HTNPs/PEDOTNPs/AChE, GE/Bare, GE/P3HTNPs, and respectively[20]. EIS is another effective technique for analyzing the interface characteristics of GE with nanomaterials and AChE modification (Fig. 4B). The PEDOTNPs/P3HTNPs greatly stimulated the charge transport of [Fe (CN)₆]^{3-/4-} to the surface of the electrode, which may be responsible for the progress in the interfacial conductivity. After the AChE was combined with PEDOTNPs/P3HTNPs, the electron transfer resistance was adjusted, demonstrating that immobilization of AChE on the surface of the electrode was successful. The good agreement between the CV and EIS results indicates that the electrode modification was successful. [25].

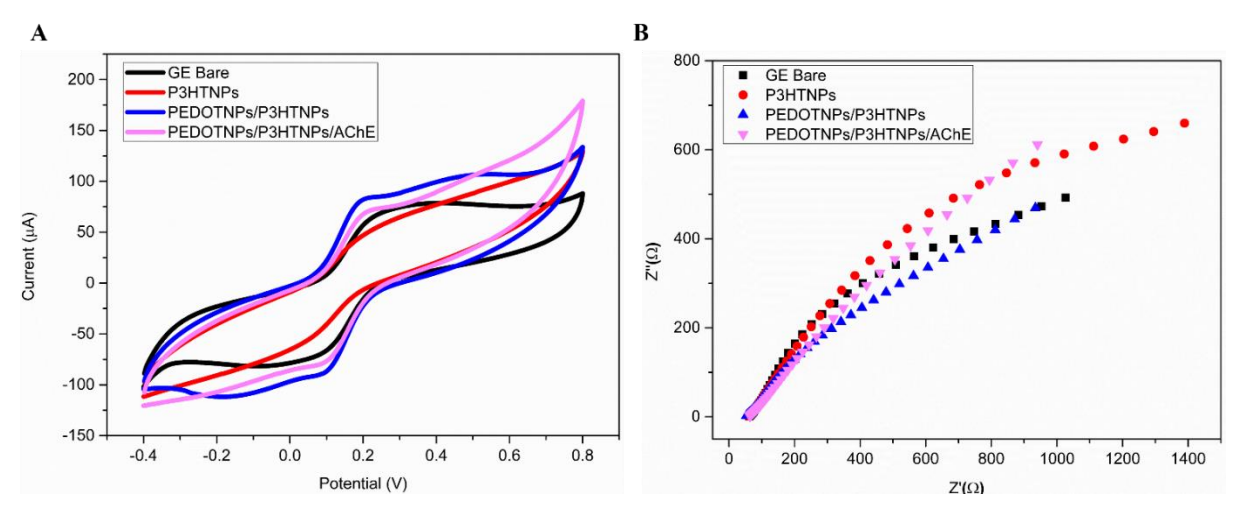


Figure 4 CV(A), and EIS(B) of a bare GE, GE/P3HTNPs, GE/PEDOTNPs/P3HTNPs, and GE/PEDOTNP/P3HTNPs/AChE.

FE-SEM images were taken to examine the surface morphology of the produced electrodes. The pristine P3HTNPs and their combination with PEDOTNPs were shown in Figures 5A and 5B. The granular nature of the PEDOTNPs/P3HTNPs was facilitated electrolyte penetration into the electrode (Fig. 5B). Upon modification of the surface with AChE, successful enzyme immobilization was shown by the formation of a smoother surface over the porous layer, as shown in Figure 5C. The homogeneous distribution of the enzyme contributed to an increase in the electrode's specific surface area.

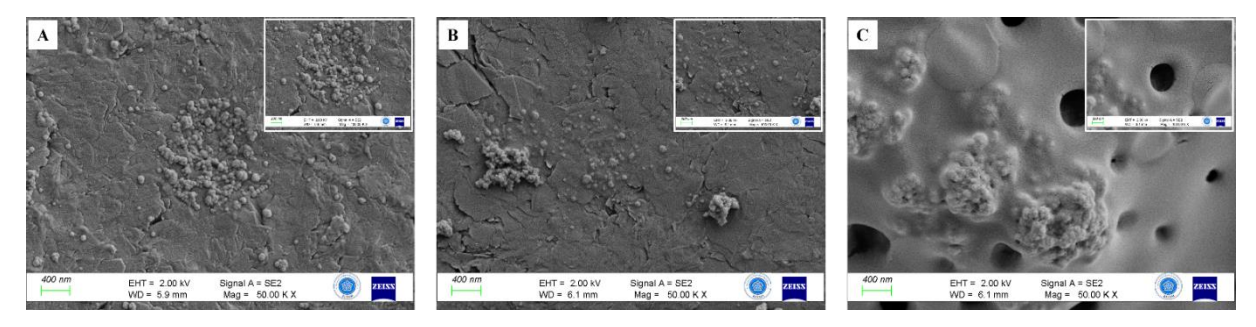


Figure 5
FESEM images of (A)GE/P3HTNPs, (B) GE/PEDOTNPs/P3HTNPs, and (C) GE/PEDOTNPs/P3HTNPs/AChE/GA (The images inside are taken at 100 KX magnification).

Analytical Characterization of the PEDOTNP/P3HTNPs/AChE Biosensor

The PEDOTNPs/P3HTNPs/AChE biosensor's electrochemical detection performance for various AThCl concentrations was investigated using amperometric I-t curve analysis at an operating potential of +0.6 V (Fig. 6). The biosensor exhibited a good linear relationship in the range of 0.01 and 2.0 mM. The sensitivity and limit of detection (LOD) values were estimated as 37.843 µAmM⁻¹cm⁻² and 0.009 mM (LOD = 3.3 Sb/m, where m represents the slope and Sb is the deviation of three measurements), respectively. Therefore, by comparing the analytical parameters of PEDOTNPs/P3HTNPs/AChE (Fig. 6), the biosensor modified with PEDOTNPs/P3HTNPs emerged as excellent in terms of LOD, linear concentration range, and sensitivity values. Table 1 and Table 2 show the comparison of the analytical performances of AChE based biosensors and P3HT sensor applications, respectively.

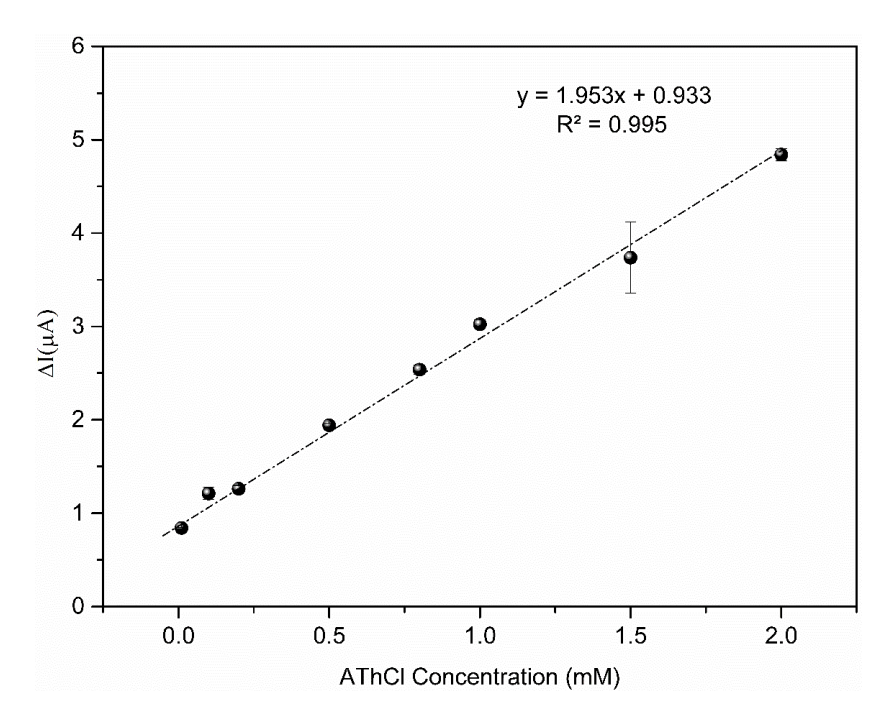


Figure 6Amperometric current-time response of GE/PEDOTNPs/P3HTNPs/AChE with successive additions of AThCl with different concentrations into the reaction medium (50 mM pH 7.0 PBS; Applied potential: +0.6 V)

Table 1 *The comparison of the proposed biosensor with literature examples of AChE based biosensors.*

MODIFIED ELECTRODE	METHOD	LINEAR RANGE	LOD	SENSITIVITY	REF.
AChE/PAMAMb-Au/CNTs/GCE	DPV	1.06–19.91 ng/mL	0.89	NR	[27]
PPy-AChE-Geltn-Glut/Pt	Amperometric	0.1–12.5, 12.5–150 ng/mL	ng/mL 1.1 ng/mL	NR	[28]
Poly (BT)/AChE	Amperometric	0.025–4 mM	0.015 mM	19.12 μΑ/mMcm ²	[11]
Poly (FBThF)/f-MNPs/AChE	Amperometric	0.05–5, 5–9.28 μg/L	0.022 μg/L	45.014 μA/mMcm ²	[29]
PPy-IC-DS1-AuNP-AChE	Amperometric	0.25–1.24 nmol/L	0.16 nmol/L	NR	[30]
AChE-CHIT/Au	CV	25-500 nmol/L	14.9 nmol/L	NR	[31]
GE/PEDOTNPs/P3HTNPs/AChE	Amperometric	0.01-2.0 mM	0.009 mM	37.843 μΑ/mMcm ²	TW

Table Abbreviations: AChE/PAMAMb–Au/CNTs/GCE: acetylcholinesterase/dendrimers polyamidoamine-Au/Carbon nanotubes, PPy–AChE–Geltn–Glut/Pt: Polypyrrole- acetylcholinesterase- gelatin-glutaraldehyde mixture/Platin, poly (BT)/AChE: poly-2,2'-(9,9-dioctyl-9 h-fluorene-2,7-diyl) bistiophene/acetylcholinesterase poly (FBThF)/f-MNPs/AChE: monomer 4,7-di(furan-2-yl) benzo[c] [1,2,5] thiadiazole (FBThF)/ carboxyl group modified magnetic nanoparticles/ acetylcholinesterase.

Table 2 *The comparison of the analytical performances of P3HT sensors.*

MODIFIED ELECTRODE	METHOD	ANALYTE	LINEAR RANGE	LOD	APPLICATION	REF.
g-C3N4/P3HT nanocomposites	Photoelectroche mistry	H_2O_2	1.0–800 μM	0.38 μΜ	Living Cells	[32]
RT-e-P3HT	OFET	H_2O_2	NR	500 pM	Mouse macrophages	[33]
MoSe ₂ /P3HT	FET	Ammonia	$0.5~\mu M$ to $1~mM$	0.65 μΜ	Saliva and Plasma	[34]
P3HT@C ₆₀ @ZnO nanosphere	Photoelectroche mistry	p53	0.1 fM to 10 nM	0.37 fM	Cow blood	[35]
P3HT-b- P3TEGT/mannose -modified GCE	EIS	E. coli	10^3 to 10^7 cfu/mL	500 cfu/mL	Drinking water and Nile water	[36]
P3HT/SA/GOx	Amperometric	Glucose	100 to 500 mg/dL	50 mg/dL	NR	[37]
P3HT/anti- PCT/BSA	EGOFET	Procalcitonin	NR	2.2 pM	NR	[38]
P3HT/ODA/GOx LB films	Amperometric	Glucose	0 to 5 mM	1000 ppm	NR	[39]
P3HT/SA/β- gal/GaO LB films	Amperometric	Lactose	1 to 6 g/dL	NR	Milk	[40]
P3HT/anti- IgG/BSA	OFET	IgG	$\begin{array}{c} 4 \text{ pM to} \\ 4 \times 10^6 \text{ pM} \end{array}$	2.9 pM	NR	[41]
TiO ₂ –P3HT–IL nanocomposite film	Photoelectroche mistry	Acetochlor	0.5 to $20~\mu mol \; L^{-1}$	$\begin{array}{c} 0.2 \; nmol \\ L^{-1} \end{array}$	Water sample	[42]
CTAB-P3HT NPs	EIS	E. coli	10^3 to 10^7 CFU/m L	250 CFU/mL	NR	[43]
P3HT nanofibers		Acetone	3.5 to 35 ppm		NR	[44]
P3HT-ZnO nanorods		Ammonia		1 ppm	NR	[45]
P3HT with ZnO@GO	OFET	NO_2		5 ppm	NR	[46]
Au@PSi-P3HT nanocomposite	Amperometric	Dopamine	1.0 to 460 μM	0.63 μΜ	Human blood serum samples	[47]
GE/PEDOTNPs/ P3HTNPs/AChE	Amperometric	AThCl	0.01 to 2.0 mM	0.009 mM	NR	TW

Table Abbreviations: g-C3N4: Graphitic carbon nitride, RT-e: Rutin-embedded, OFET: Organic field-effect transistors, C₆₀: Fullerene, EIS: Electrochemical impedance spectroscopy, b-P3TEGT: block-poly(3-triethylene-glycol-thiophene), GCE: Glassy carbon electrode, SA: Stearic acid, GOx: Glucose oxidase, EGOFET: electrolyte-gated OFET, BSA: Bovine serum albümin, PCT: Procalcitonin, ODA: Octadecylamine, LB: Langmuir–Blodgett, IgG: Immunoglobulin G, β-gal: β-Galactosidase, GaO: Galactose oxidase, IL: Ionic liquid, CTAB: Cetyltrimethylammonium bromide, GO: Graphene oxide, PSi: Porous silicon.

The biosensor produced nearly the same amperoemtric signal at identical glucose concentrations, indicating good stability for practical usage (Fig. 7A). The biosensor showed very selective properties for detecting AThCl. As shown in Figure 7B, the addition of various interference substances such as 0.1 mM glucose (Glu), urea (Ur), uric acid (UA), NaCl, and KCl resulted in negligible changes in the reduction current, whereas the subsequent addition of 0.1 mM AThCl caused an apparent response in the current, indicating that the GE/PEDOTNPs/P3HTNPs/AChE biosensor has excellent anti-interference ability. The biosensor responses were recorded for 4 weeks with a 2 mM AThCl solution to consider long-term stability (Fig. 7C). It was stored at +4 °C, and the biosensor retained approximately 80% of its original response over 2 days.

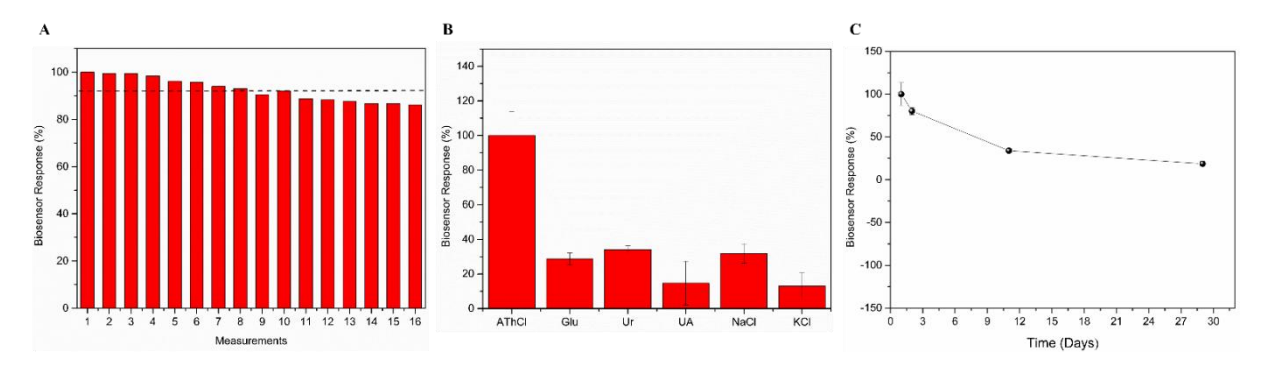


Figure 7(A) Repeatability, (B) interference, and (C) shelf-life results of the GE/PEDOTNPs/P3HTNPs/AChE (Black dashed line indicates the $I_{average}$ of the results)

DISCUSSION AND CONCLUSIONS

The harmful side effects of pesticides, which are widely used in agricultural practices, on the food chain are well known. These pesticides inhibit the activity of cholinesterase enzymes, causing various damage to the central nervous system and blocking neural messages with their neurotoxic effects. As a result, nerve communication becomes less efficient, causing a decline in brain and body functions. Therefore, the analysis of this group of pesticides is very important. For this reason, it has become a necessity to develop new, cheap, and practical methods that give quick results instead of traditional, expensive, and laborious methods such as mass spectrometry after separation by gas and liquid chromatography. In recent years, enzyme-based biosensors for the electrochemical determination of cholinesterase inhibitors have become a very interesting research field. However, the first difficulty encountered in their determination of enzyme-based biodetectors is the positioning of the enzyme on the electrode surface. There are various ways to do this. The use of conjugated polymer nanoparticles (CPNPs) in biosensor preparation makes biosensors much more useful, sensitive, and practical. CPNPs are widely utilized as biosensors, drug delivery, and bioimaging probe materials and have been deemed promising nanomaterials for biomedical applications. The combination of them with biosensor technology enables the immobilization of the enzyme to the electrode surface practically, often in a single step, while shortening the electrochemical reaction time with quick electron conduction and expanding the strength of the biosensor. Enzymes immobilized within conjugated polymer nanoparticlebased matrices through physical or chemical methods retain their catalytic activity and allow for repeated use. The use of CPNPs aims to achieve the sensor response in the fastest way by ensuring electron transfer in the fastest way and to design a fast, cheap, and practical detector as an alternative to traditional methods.

Within the scope of the work, a GE/PEDOTNPs/P3HTNPs/AChE biosensor was developed by coating the graphite electrode surface with newly synthesized P3HTNPs and PEDOTNPs as supporting material. The prepared nanoparticles and the modified electrode surface were successfully characterized

using FE-SEM, DLS, zeta potential, CV, EIS, UV-Vis, and fluorescent spectroscopy techniques. The surface morphology images were captured by FE-SEM, and after each surface modification, different morphologies were observed. DLS and zeta potential analysis were performed to characterize the hydrodynamic radius and surface charge of the synthesized P3HTNPs. As a result of the analysis, it was determined that the average hydrodynamic radius was 92.5 nm and the average surface charge was -41.17 mV. The newly developed GE/PEDOTNPs/P3HTNPs/AChE biosensor was used for the determination of AThCl. As a result of the sensor studies, it was observed that it had a wide linear range (0.01 and 2.0 mM) and a low LOD (0.009 mM) for a study using nanoparticle formulation. For operational stability analysis of the GE/PEDOTNPs/P3HTNPs/AChE biosensor, measurements were taken with a concentration of 2 mM AThCl. Accordingly, the biosensor retained approximately 80% of its original response over 2 days. For the analysis of the interference effect in the GE/PEDOTNPs/P3HTNPs/AChE biosensor, when glucose (Glu), urea (Ur), uric acid (UA), NaCl, and KCl were added separately as substrates with a final concentration of 0.1 mM in the measurement cell, no signal change occurred in the chemical compounds compared to AThCl. Accordingly, it could be said that the relevant chemical compounds did not show any interference effect on the GE/PEDOTNPs/P3HTNPs/AChE biosensor.

Ethical Statement

This study is an original research article designed and developed by the authors.

Ethics Committee Approval

This study does not require any ethics committee approval.

Author Contributions

Research Design (CRediT 1) D.Y.: (%30) – D.S. (%30) – S.S. (%40)

Data Collection (CRediT 2) D.Y.: (%40) – D.S. (%30) – S.S. (%30)

Research- Data Analysis – Validation (CRediT 3-4-6-11) D.Y.: (%40) – D.S. (%30) – S.S. (%30)

Writing the Article (CRediT 12-13) D.Y.: (%40) – D.S. (%30) – S.S. (%30)

Revision and Improvement of the Text (CRediT 14) D.Y.: (%40) – D.S. (%20) – S.S. (%40)

Financing

This research did not receive any specific grant from funding agencies in the public, commercial, or not-for-profit sectors.

Conflict of Interest

The authors declare no conflicts of interest for this study.

Sustainable Development Goals (SDG)

Sustainable Development Goals: Not supported.

REFERENCES

- [1] A. Mulchandani, W. Chen, P. Mulchandani, J. Wang, K.R. Rogers, Biosensors for direct determination of organophosphate pesticides, *Biosensors and Bioelectronics*. 16 (2001), 225-230. doi:10.1016/S0956-5663(01)00126-9.
- [2] V. Dhull, A. Gahlaut, N. Dilbaghi, V. Hooda, Acetylcholinesterase Biosensors for Electrochemical Detection of Organophosphorus Compounds: A Review, *Biochemistry Research International*. 2013 (2013), 731501. doi:10.1155/2013/731501.
- [3] A. Cappiello, G. Famiglini, P. Palma, F. Mangani, Trace level determination of organophosphorus pesticides in water with the new direct-electron ionization LC/MS interface, *Analytical Chemistry*. 74 (2002), 3547-3554. doi:10.1021/AC015685F.
- [4] Y. Li, R. Zhao, L. Shi, G. Han, Y. Xiao, Acetylcholinesterase biosensor based on electrochemically inducing 3D graphene oxide network/multi-walled carbon nanotube composites for detection of pesticides, *RSC Advances*. 7 (2017), 53570-53577. doi:10.1039/C7RA08226F.
- [5] N. Bhalla, P. Jolly, N. Formisano, P. Estrela, Introduction to biosensors, *Essays in Biochemistry*. 60 (2016), 1-8. doi:10.1042/EBC20150001.
- [6] P. Jolly, N. Formisano, P. Estrela, DNA aptamer-based detection of prostate cancer, *Chemical Papers*. 69 (2015), 77-89. doi:10.1515/CHEMPAP-2015-0025.
- [7] B. Van Dorst, J. Mehta, K. Bekaert, E. Rouah-Martin, W. De Coen, P. Dubruel, R. Blust, J. Robbens, Recent advances in recognition elements of food and environmental biosensors: A review, *Biosensors and Bioelectronics*. 26 (2010), 1178-1194. doi: 10.1016/J.BIOS.2010.07.033.
- [8] M. Bhattu, M. Verma, D. Kathuria, Recent advancements in the detection of organophosphate pesticides: a review, *Analytical Methods*. 13 (2021), 4390-4428. doi:10.1039/D1AY01186C.
- [9] M. Kesik, F. Ekiz Kanik, J. Turan, M. Kolb, S. Timur, M. Bahadir, L. Toppare, An acetylcholinesterase biosensor based on a conducting polymer using multiwalled carbon nanotubes for amperometric detection of organophosphorous pesticides, *Sensors and Actuators B: Chemical.* 205 (2014), 39-49. doi: 10.1016/J.SNB.2014.08.058.
- [10] A. Vinotha Alex, A. Mukherjee, Review of recent developments (2018–2020) on acetylcholinesterase inhibition based biosensors for organophosphorus pesticides detection, *Microchemical Journal*. 161 (2021), 105779. doi: 10.1016/J.MICROC.2020.105779.
- [11] H. Celik, S. Soylemez, An Electrochemical Acetylcholinesterase Biosensor Based on Fluorene(bisthiophene) Comprising Polymer for Paraoxon Detection, *Electroanalysis*. 35 (2023), e202200271. doi:10.1002/ELAN.202200271.
- [12] H. Parham, N. Rahbar, Square wave voltammetric determination of methyl parathion using ZrO2-nanoparticles modified carbon paste electrode, *Journal of Hazardous Materials*. 177 (2010), 1077-1084. doi: 10.1016/J.JHAZMAT.2010.01.031.
- [13] A.S. Soğancı, A. Orman, The Influence of Polypropylene Fiber on High and Low Plasticity Clay, *Necmettin Erbakan Üniversitesi Fen ve Mühendislik Bilimleri Dergisi*. 6 (2024), 178-187. doi:10.47112/NEUFMBD.2024.41.
- [14] H. Lin, H. Bai, Z. Yang, Q. Shen, M. Li, Y. Huang, F. Lv, S. Wang, Conjugated polymers for biomedical applications, *Chemical Communications*. 58 (2022), 7232-7244. doi:10.1039/D2CC02177C.
- [15] K. Çetin, K. Şarkaya, B. Kavakcioğlu, M. Bilgileri, M. Geçmişi, Antifungal Activities of Copper (II) Ion and Histidine Incorporated Polymers on Yeast Saccharomyces cerevisiae, *Necmettin Erbakan Üniversitesi Fen ve Mühendislik Bilimleri Dergisi*. 5 (2023), 267-277. doi:10.47112/NEUFMBD.2023.24.

- [16] M. Ali Kamyabi, N. Hajari, A.P.F. Turner, A. Tiwari, A high-performance glucose biosensor using covalently immobilised glucose oxidase on a poly(2,6-diaminopyridine)/carbon nanotube electrode, *Talanta*. 116 (2013), 801-808. doi: 10.1016/J.TALANTA.2013.07.068.
- [17] T. Ahuja, I.A. Mir, D. Kumar, Rajesh, Biomolecular immobilization on conducting polymers for biosensing applications, *Biomaterials*. 28 (2007), 791-805. doi: 10.1016/J.BIOMATERIALS.2006.09.046.
- [18] J.C. Vidal, E. Garcia-Ruiz, J.R. Castillo, Recent Advances in Electropolymerized Conducting Polymers in Amperometric Biosensors, *Microchimica Acta*. 143 (2003), 93-111. doi:10.1007/S00604-003-0067-4.
- [19] W. Schuhmann, Conducting polymer based amperometric enzyme electrodes, *Mikrochimica Acta*. 121 (1995), 1-29. doi:10.1007/BF01248237/METRICS.
- [20] S. Soylemez, M. Kesika, L. Toppare, Biosensing Devices: Conjugated Polymer Based Scaffolds. 2019, p. 386, https://hdl.handle.net/11511/47790.
- [21] D. Tuncel, H.V. Demir, Conjugated polymer nanoparticles, *Nanoscale*. 2 (2010), 484-494. doi:10.1039/B9NR00374F.
- [22] İ. Akin, E. Zor, H. Bingöl, S. Yazar, C. Author, N. Erbakan Üniversitesi, A. Keleşoğlu Eğitim Fakültesi, M. ve Fen Bilimleri Eğitimi Bölümü, GO@Fe3O4 Katkılı Polimerik Kompozit Membranların Hazırlanması ve Karakterizasyonu, *Necmettin Erbakan Üniversitesi Fen ve Mühendislik Bilimleri Dergisi*. 5 (2023), 38-52. doi:10.47112/NEUFMBD.2023.8.
- [23] J.E. Millstone, D.F.J. Kavulak, C.H. Woo, T.W. Holcombe, E.J. Westling, A.L. Briseno, M.F. Toney, J.M.J. Fréchet, Synthesis, properties, and electronic applications of size-controlled poly(3-hexylthiophene) nanoparticles, *Langmuir*. 26 (2010), 13056-13061. doi: 10.1021/LA1022938
- [24] J.A. Labastide, M. Baghgar, I. Dujovne, B.H. Venkatraman, D.C. Ramsdell, D. Venkataraman, M.D. Barnes, Time- and polarization-resolved photoluminescence of individual semicrystalline polythiophene (P3HT) nanoparticles, *Journal of Physical Chemistry Letters*. 2 (2011), 2089-2093. doi:10.1021/JZ20095 8X.
- [25] S. Kurbanoglu, S.C. Cevher, L. Toppare, A. Cirpan, S. Soylemez, Electrochemical biosensor based on three components random conjugated polymer with fullerene (C60), *Bioelectrochemistry* (*Amsterdam*, *Netherlands*). 147 (2022). doi:10.1016/J.BIOELECHEM.2022.108219.
- [26] A.J. Bard, L.R. Faulkner, Electrochemical Methods: Fundamentals and Applications, *Surface Technology*. 20 (1983) 91-92.
- [27] Y. Qu, Q. Sun, F. Xiao, G. Shi, L. Jin, Layer-by-Layer self-assembled acetylcholinesterase/PAMAM-Au on CNTs modified electrode for sensing pesticides, *Bioelectrochemistry*. 77 (2010), 139-144. doi:10.1016/J.BIOELECHEM.2009.08.001.
- [28] R. Dutta, P. Puzari, Amperometric biosensing of organophosphate and organocarbamate pesticides utilizing polypyrrole entrapped acetylcholinesterase electrode, *Biosensors and Bioelectronics*. 52 (2014), 166-172. doi:10.1016/J.BIOS.2013.08.050.
- [29] H. Dzudzevic Cancar, S. Soylemez, Y. Akpinar, M. Kesik, S. Göker, G. Gunbas, M. Volkan, L. Toppare, A Novel Acetylcholinesterase Biosensor: Core-Shell Magnetic Nanoparticles Incorporating a Conjugated Polymer for the Detection of Organophosphorus Pesticides, *ACS Applied Materials and Interfaces*. 8 (2016), 8058-8067. doi:10.1021/ACSAMI.5B12383.
- [30] L.F. Loguercio, A. Thesing, P. Demingos, C.D.L. de Albuquerque, R.S.B. Rodrigues, A.G. Brolo, J.F.L. Santos, Efficient acetylcholinesterase immobilization for improved electrochemical performance in polypyrrole nanocomposite-based biosensors for carbaryl pesticide, *Sensors and Actuators B: Chemical.* 339 (2021), 129875. doi: 10.1016/J.SNB.2021.129875.

- [31] D. Du, J. Ding, J. Cai, A. Zhang, Determination of carbaryl pesticide using amperometric acetylcholinesterase sensor formed by electrochemically deposited chitosan, *Colloids and Surfaces B: Biointerfaces*. 58 (2007), 145-150. doi: 10.1016/j.colsurfb.2007.03.006.
- [32] Y. Wang, Y. Cheng, N. Wu, Z. Zhang, Graphitic Carbon Nitride/Poly(3-hexylthiophene) Nanocomposites for the Photoelectrochemical Detection of H2O2in Living Cells, *ACS Applied Nano Materials*. 3 (2020), 8598-8603. doi: 10.1021/ACSANM.0C02114.
- [33] J. Jeong, M. Essafi, C. Lee, M. Haoues, M.F. Diouani, H. Kim, Y. Kim, Ultrasensitive detection of hazardous reactive oxygen species using flexible organic transistors with polyphenolembedded conjugated polymer sensing layers, *Journal of Hazardous Materials*. 355 (2018), 17-24. doi:10.1016/J.J HAZMAT.2018.04.063.
- [34] S. Sharma, D. Kar, P.D. Khanikar, A. Moudgil, P. Mishra, S. Das, Hybrid MoSe ₂ /P3HT Transistor for Real-Time Ammonia Sensing in Biofluids, *ACS Applied Materials & Interfaces*. 16 (2024), 30648-30657. doi:10.1021/acsami.4c02352.
- [35] M. Xiao, Q. Xiong, C. Yang, H. Deng, R. Yuan, Y. Yuan, Highly efficient photocathodic cascade material for constructing sensitive photoelectrochemical biosensor, *Analytica Chimica Acta*. 1272 (2023), 341436. doi: 10.1016/J.ACA.2023.341436.
- [36] N. Elgiddawy, S. Ren, A. Yassar, A. Louis-Joseph, H. Sauriat-Dorizon, W.M.A. El Rouby, A.O. El-Gendy, A.A. Farghali, H. Korri-Youssoufi, Dispersible Conjugated Polymer Nanoparticles as Biointerface Materials for Label-Free Bacteria Detection, *ACS Applied Materials & Interfaces*. 12 (2020) 39979-39990. doi:10.1021/acsami.0c08305.
- [37] R. Singhal, A. Chaubey, K. Kaneto, W. Takashima, B.D. Malhotra, Poly-3-hexyl thiophene Langmuir-Blodgett films for application to glucose biosensor, *Biotechnology, and Bioengineering*. 85 (2004), 277-282. doi:10.1002/BIT.10869.
- [38] P. Seshadri, K. Manoli, N. Schneiderhan-Marra, U. Anthes, P. Wierzchowiec, K. Bonrad, C. Di Franco, L. Torsi, Low-picomolar, label-free procalcitonin analytical detection with an electrolyte-gated organic field-effect transistor based electronic immunosensor, *Biosensors and Bioelectronics*. 104 (2018), 113-119. doi: 10.1016/j.bios.2017.12.041.
- [39] K.-H. Wang, W.-P. Hsu, L.-H. Chen, W.-D. Lin, Y.-L. Lee, Extensibility effect of poly(3-hexylthiophene) on the glucose sensing performance of mixed poly(3-hexylthiophene)/octadecylamine/glucose oxidase Langmuir-Blodgett films, *Colloids and Surfaces B: Biointerfaces*. 155 (2017), 104-110. doi: 10.1016/j.colsurfb.2017.04.006.
- [40] S.K. Sharma, R. Singhal, B.D. Malhotra, N. Sehgal, A. Kumar, Lactose biosensor based on Langmuir–Blodgett films of poly (3-hexyl thiophene), *Biosensors and Bioelectronics*. 20 (2004), 651-657. doi: 10.1016/j.bios.2004.03.020.
- [41] H. Runfang, Y. Yangfan, L. Leilei, J. Jianlong, Z. Qiang, D. Lifeng, S. Shengbo, L. Qiang, P3HT-based organic field effect transistor for low-cost, label-free detection of immunoglobulin G, *Journal of Biotechnology*. 359 (2022), 75-81. doi: 10.1016/j.jbiotec.2022.09.022.
- [42] D. Jin, Q. Xu, Y. Wang, X. Hu, A derivative photoelectrochemical sensing platform for herbicide acetochlor based on TiO2–poly (3-hexylthiophene) –ionic liquid nanocomposite film modified electrodes, *Talanta*. 127 (2014), 169-174. doi: 10.1016/j.talanta.2014.01.058.
- [43] N. Elgiddawy, S. Ren, W. Ghattas, W.M.A. El Rouby, A.O. El-Gendy, A.A. Farghali, A. Yassar, H. Korri-Youssoufi, Antimicrobial Activity of Cationic Poly(3-hexylthiophene) Nanoparticles Coupled with Dual Fluorescent and Electrochemical Sensing: Theragnostic Prospect, *Sensors*. 21 (2021), 1715. doi:10.3390/s21051715.
- [44] C. Bertoni, P. Naclerio, E. Viviani, S. Dal Zilio, S. Carrato, A. Fraleoni-Morgera, Nanostructured P3HT as a Promising Sensing Element for Real-Time, Dynamic Detection of Gaseous Acetone, *Sensors*. 19 (2019), 1296. doi:10.3390/s19061296.
- [45] K.-X. Han, C.-C. Wu, W.-F. Hsu, W. Chien, C.-F. Yang, Preparation of ultrafast ammonia

- sensor based on cross-linked ZnO nanorods coated with poly(3-hexylthiophene), *Synthetic Metals*. 299 (2023), 117449. doi: 10.1016/j.synthmet.2023.117449.
- [46] Y. Yang, H.E. Katz, Hybrid of P3HT and ZnO@GO nanostructured particles for increased NO sensing response, *Journal of Materials Chemistry C.* 5 (2017), 2160-2166. doi:10.1039/C6TC04908G.
- [47] J. Ahmed, M. Faisal, S.A. Alsareii, M. Jalalah, F.A. Harraz, A novel gold-decorated porous silicon-poly(3-hexylthiophene) ternary nanocomposite as a highly sensitive and selective non-enzymatic dopamine electrochemical sensor, *Journal of Alloys and Compounds*. 931 (2023), 167403. doi:10.1016/j.j allcom.2022.167403.



Vol: 7 No:2 Year: 2025

Araştırma Makalesi/Research Article

e-ISSN: 2667-7989

https://doi.org/10.47112/neufmbd.2025.94

Uzaktan Algılama Yağış Verileri Yardımıyla Kuraklık Aşma Olasılığı İndeksi'ni (KAOİ) Kullanarak Konya İli Kuraklık Analizi

Fatih KARAÇOR 1* D Emre TOPÇU 1D

¹ Kafkas University, Faculty of Engineering and Architecture, Department of Civil Engineering, Kars, Türkiye

Makale Bilgisi	ÖZET
Geliş Tarihi: 04.03.2025 Kabul Tarihi: 29.04.2025 Yayın Tarihi: 31.08.2025	Kuraklık hem çevre hem de insan hayatı için riskler oluşturan, yeri ve süresi konusunda belirsizlikle karakterize edilen iklimsel bir fenomendir. Son analizler, çeşitli matematiksel yöntemler ve teknolojideki ilerlemeler kullanılarak farklı zaman dilimlerinde kuraklıklar üzerinde gerçekleştirilebilir. Bu çalışma, Türkiye'nin Konya İlinde belirlenen 31 gözlem noktası üzerinde bir kuraklık analizi yapmak üzere tasarlanmıştır. Analiz edilen veriler, Mart
Anahtar Kelimeler:	2000'den Şubat 2025'e kadar kaydedilen aylık toplam yağış değerlerini içermekte olup, bu
Kuraklık,	veriler PERSIANN sistemi (Yapay Sinir Ağları kullanarak Uzaktan Algılama ile Yağış
Kuraklık aşma olasılığı indek	si Tahmini) kaynaklıdır. Belirlenen noktalar için aylık yağış toplamları, Kuraklık Aşma Olasılığı
(KAOİ)	İndeksi (KAOİ) için girdi parametreleri olarak kullanılmıştır. Bulgulara göre, 2006 yılı,
Konya ili,	özellikle Konya İli genelinde, şiddetli kuraklık koşullarıyla yaşanırken, 2019 yılı ise ıslaklık
Türkiye,	koşullarıyla karakterize edilmiştir. İslak koşulların daha sık karşılaşıldığı ve bu durumun yüzde
Su yönetimi.	50,17'lik bir sıklık değeriyle belirlendiği gösterilmiştir.

Drought Analysis of Konya Province using Drought Exceedance Probability Index (DEPI) with Remote Sensing Precipitation Data

Article Info	ABSTRACT
Received: 04.03.2025 Accepted: 29.04.2025 Published: 31.08.2025	Drought is a climatic phenomenon that poses risks to both the environment and human life. It is characterised by uncertainty regarding its location and duration. Recent analyses of droughts can be conducted over various timeframes using a range of mathematical methods and advancements in technology. The present study is designed to conduct a drought analysis across 31 specified observational points within Konya Province, Türkiye. The data set under scrutiny
Keywords:	encompasses monthly total precipitation values recorded from March 2000 to February 2025,
Drought,	obtained from the PERSIANN system (Precipitation Estimation from Remotely Sensed
Drought exceedance probability index (DEPI)	Information using Artificial Neural Networks). The monthly precipitation totals from the designated points were then used as input parameters for the Drought Exceedance Probability
Konya province, Türkiye	Index (DEPI). The findings indicate that the year 2006 was marked by severe drought conditions, particularly in the region encompassing Konya Province, while 2019 was
Water management.	characterised by wet conditions. The analysis revealed that wet circumstances were encountered more frequently, with a frequency value of 50.17%.

To cite this article

Karaçor, F. & Topçu, E. (2025). Drought analysis of Konya province using drought exceedance probability index (DEPI) with remote sensing precipitation data. *Necmettin Erbakan University Journal of Science and Engineering*, 7(2), 309-321. https://doi.org/10.47112/neufmbd.2025.94

*Corresponding Author: Fatih Karaçor, fatihkaracor@gmail.com



INTRODUCTION

Drought is a regular, repeating natural calamity that may intermittently impact human survival efforts. Consequently, comprehending drought features may significantly aid in formulating improved mitigation strategies [1, 2]. Although several drought definitions exist in the literature, a commonly accepted quadruple categorization has emerged. These include climatic, agricultural, hydrological, and socio-economic droughts [3, 4]. Meteorological drought is extensively examined in the literature and seen as a precursor to all other forms of drought.

Reduced normal precipitation during the lowest documented 30-year precipitation series is the only determinant of meteorological drought, which is a weather-only phenomenon. When there isn't enough water in the soil to keep plants from dying and withering, this is called an agricultural drought. Overuse of water and careless farming methods may cause agricultural droughts even when precipitation and water supplies are sufficient. However, even when there is enough precipitation and water in the reservoirs, hydrological drought may still develop if the local population that uses water is large or if there are too many rural activities and irrigation projects [5-8]. When a social or economic function in life is negatively impacted, it is referred to as a socioeconomic drought.

Drought indices are employed to assess the severity, persistence, and dissemination of drought impacts. De Martonne Method [9], Palmer Drought Severity Index [10], Decile Index [11], Aydeniz Method [12], Erinç Method [13], Standardized Precipitation Index [14], Aggregate Drought Index [15], Reconnaissance Drought Index [16, 17], and Streamflow Drought Index [18] are among the measures. In addition to these indices, the development of new drought monitoring indices continues. The Drought Exceedance Probability Index (DEPI), which was devised by [19], is one of the most recent indexes. DEPI is a variant of the ISSP (Indice Standardisé de Sécheresse Pluviométrique) that was created by [20]. DEPI is calculated by summarizing cumulative monthly precipitation anomalies, as is the case with other indices such as the Standardized Precipitation Index (SPI) of [14] and the SPEI [21]. Conversely, the empirical probability of the drought level exceeding the previous month's DEPI score is demonstrated.

Early warning systems and precise drought analysis are very vital to reduce the effects of droughts given their broad ramifications. By supplying real-time and historical rainfall data, advances in satellite-based precipitation data—including the PERSIANN system—have tremendously enhanced drought monitoring. Ensuring water security, agricultural production, and environmental sustainability in a climate becoming more erratic depends on an awareness of the origins, impacts, and mitigating techniques of droughts. Affecting ecosystems, water supplies, and agriculture all around, drought is among the most terrible natural calamities. Understanding and tracking drought conditions depend on accurate precipitation records. Extremely high-resolution, satellite-based precipitation estimations produced by the Precipitation Estimation from Remotely Sensed Information using Artificial Neural Networks (PERSIANN) technology are priceless for drought study. PERSIANN advances early warning systems, drought monitoring, and water management and disaster preparation decision-making by providing continuous, worldwide precipitation data.

One of Turkey's biggest provinces in area, Konya Province is crucial for agricultural output. Still, its geographical position and climate make it prone to drought. Thus, in Konya, drought analysis and management are quite important. The objective of the study is to periodically analyze the drought from January to December using the DEPI devised by [19] to monitor the drought by utilizing the monthly precipitation totals of 31 study points that have been designated and located in Konya Province, Turkey. The Precipitation Estimation from Remotely Sensed Information using Artificial Neural Networks (PERSIANN) system was employed to acquire precipitation data, which was determined by the location of the meteorological stations of the Turkish State Meteorological Service. In terms of agricultural

output, Konya province is rather important and often runs the danger of drought. Important actions to reduce the harmful effects of drought are included in the studies carried out and the developed management strategies. In this regard, the battle against drought in the area depends much on the sustainable use of water resources, the adoption of drought-resistant farming methods, and efficient monitoring systems.

MATERIALS AND METHODS

With regard to land area, Konya is among Türkiye's biggest provinces; it also has strategic significance for agricultural output. But its position in the Central Anatolia Region results in semi-arid climatic traits and inadequate water supplies (see Figure 1). The University of California, Irvine's Center for Hydrometeorology and Remote Sensing (CHRS) created the satellite-based precipitation estimate tool known as PERSIANN. In order to predict precipitation worldwide, it processes satellite infrared (IR) and passive microwave (PMW) data using machine learning methods, particularly artificial neural networks (ANNs). The current operational PERSIANN (Precipitation Estimation from Remotely Sensed Information Using Artificial Neural Networks) system employs neural network function classification and approximation methods to estimate the precipitation rate for each 0.25° x 0.25° (approximately 625 km²) pixel derived from infrared brightness temperature images obtained from geostationary satellites.

The PERSIANN system initially relied on fixed infrared images and was subsequently enhanced to incorporate both infrared and daytime visible images. This study employed the PERSIANN algorithm to generate global precipitation data using geostationary long-wave infrared images. The precipitation product encompasses the global range from 50°S to 50°N. Model parameters are routinely updated utilizing precipitation forecasts obtained from low-orbit satellites [24]. In this study, PERSIANN data was used to determine a drought situation for the entire Konya Province. However, instead of providing separate graphs for the 31 points, the areas of the districts and the amounts of precipitation were multiplied and averaged. In this way, a single precipitation value and graphs were obtained. Information that is more in-depth on this system may be obtained from [25-32].



Figure 1 *Map of Konya Province and its Districts [22].*

The districts within Konya Province and their coordinates are shown in Table 1.

Table 1 *Observational points and coordinates.*

No	Observational Point Name	Coordinates (Latitude and Longitude)
1	Akşehir	38.368833, 31.429667
2	Ahırlı	37.240278, 32.114722
3	Akören	37.451725, 32.380321
4	Altınekin	38.298889, 32.879167
5	Beyşehir	37.677667, 31.746333
6	Bozkır	37.183333, 32.246111
7	Cihanbeyli	38.650578, 32.921860
8	Çeltik	39.023921, 31.803972
9	Çumra	37.565833, 32.790000
10	Derbent	38.016389, 32.017222
11	Derebucak	37.391944, 31.514444
12	Doğanhisar	38.136944, 31.676389
13	Emirgazi	37.892500, 33.841111
14	Ereğli	37.525500, 34.048500
15	Güneysınır	37.267972, 32.720792
16	Hadim	36.988552, 32.456480
17	Halkapınar/İvriz	37.441389, 34.151944
18	Hüyük	37.962500, 31.596800
19	Ilgın	38.276333, 31.894000
20	Kadınhanı	38.230900, 32.217300
21	Karapınar	37.715300, 33.525600
22	Karatay	37.860556, 32.583889
23	Kulu	39.078833, 33.065667
24	Meram	37.868678, 32.471331
25	Sarayönü	38.262000, 32.387500
26	Selçuklu	37.983700, 32.574000
27	Seydişehir	37.449600, 31.853800
28	Taşkent	36.909293, 32.497615
29	Tuzlukçu	38.467222, 31.652500
30	Yalıhüyük	37.292222, 32.112222
31	Yunak	38.820500, 31.725833

Drought Exceedance Probability Index (DEPI)

The DEPI calculation is performed in a series of sequential stages. Initially, the precipitation anomalies (AP) for each month in the series are determined using the following expression:

$$AP_i = P_i - P_{MEDi} \tag{1}$$

 P_i = Precipitation of the month i;

 P_{MEDi} = Median precipitation of the month i for the study period

Figure 2 illustrate an example of the calculation of these monthly anomalies.

The index employed the median to identify surpluses and deficits, as it is deemed more suitable than the average for highly variable meteorological regimes [20]. Cumulative precipitation anomalies are identified starting from the first month of the series. Upon the identification of a negative anomaly, a dry sequence commences, followed by the resumption of accumulation in that specific month. Subsequent to this restart, the monthly increment of anomalies continues. Following the accumulation period, the dry run concludes once the cumulative anomalies revert to a positive state. During this wet run, anomalies continued to accumulate until a new negative precipitation anomaly was identified. A new dry sequence commences at that point, estimated using the same method. The methodology involves the continuous accumulation of surpluses, facilitating accurate prioritization of anomalies and halting processes in the presence of negative anomalies. Therefore, the assessment of this second step

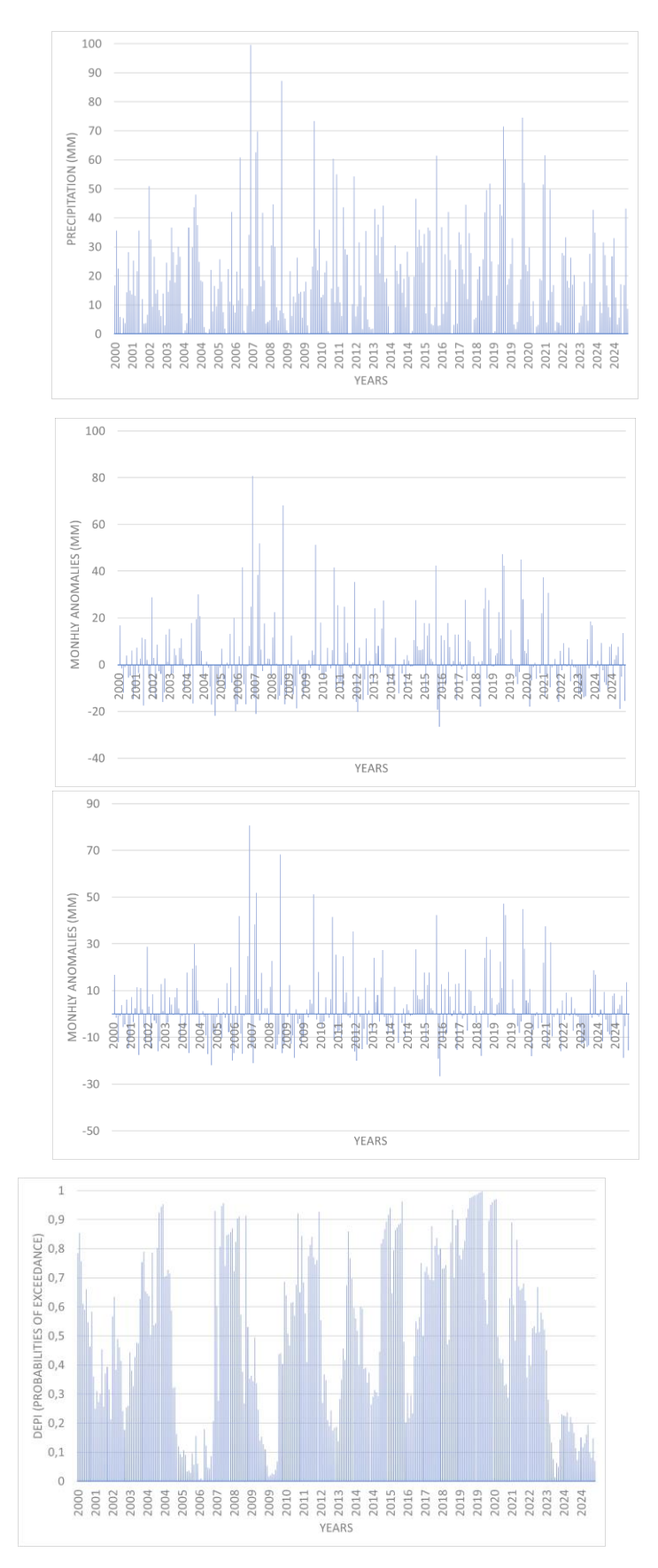


Figure 2Process of implementing the Drought Exceedance Probability Index (DEPI) in the precipitation series of Konya, 2000-2025.

corresponds with the expression:

$$APAc_1 = AP_1,$$

$$APAc_i = \sum_{i=r}^{i} AP_i \quad i > 1$$
(2)

where $APAc_i$ = precipitation cumulative anomaly of the month i; r = the value marking the start of the dry run and follows the expression:

 $r=max\{k: 1 \le k \le i, AP_k < 0, APAc_{k-1} \ge 0\}$, k: parameter from 1 to i to determine which month the drought started

It is essential to note that if $AP_i < 0$ and $APAc_{i-1} \ge 0$, then r=i, leading to $APAc_i=AP_i$, which indicates the commencement of a new dry series. In summary, the third step involves sorting the series of cumulative precipitation anomalies identified in the previous stage in ascending order, from the months with the most significant negative cumulative anomalies, or deficits, to those with the most substantial positive anomalies, or surpluses. Adhering to the aforementioned steps is necessary to derive the empirical probabilities of exceedance corresponding to each month of the series. Following the sorting process, the formulation of DEPI necessitates the calculation of the probability of exceeding the detected event on a monthly basis, employing the plotting positions method established by [23]:

$$Pexced_{APAci} = DEPI_i = M_{APAci}/(n+1)$$
(3)

where; $Pexced_{APAci}$ =empirical probability of exceedance of the month i, namely, the DEPI of the month i;

 M_{APAci} position of the precipitation cumulative anomaly of the month i in the sorted series, from lowest to highest cumulative anomaly or largest observed deficit,

n= total number of months in the series.

Therefore, the DEPI for a specific month represents the probability of exceedance associated with its cumulative rainfall anomaly, as determined by the aforementioned methodology. The probability values encompass an estimate of the hazard, with DEPI values below 0.5 indicating a significant accumulation of anomalies that are unlikely to be exceeded. Droughts are intensifying as they near zero levels. The index's significance and its advancements over similar indices lie in its ability to restart the measurement of cumulative anomalies whenever a new dry month $(AP_i < 0)$ occurs during a surplus period (with $APAc_{i-1} \ge 0$). This ensures accurate identification of dry runs of varying lengths from a single index calculation. Table 2 presents the DEPI drought classification values.

Table 2DEPI drought classifications according to DEPI values [19].

DEPI values (probabilities of exceedance)	Drought severity level	% months of a series within the interval	Return period (years)
DEPI≥0.5	Wet conditions	50	2
0.5>DEPI≥0.16	Mild drought	34	6
0.16>DEPI≥0.07	Moderate drought	9	15
0.07>DEPI≥0.02	Severe drought	5	20
DEPI<0.02	Extreme drought	2	50

RESULTS AND DISCUSSION

Figure 3 displays a graph that illustrates the quantity of precipitation that falls in the province of Konya. The graph is broken down by year and month. When looking at these graphs that were created

using PERSIANN data, it can be seen that the Konya Province in the Central Anatolia area saw the least amount of rainfall in the month of August, while the maximum amount of rainfall was recorded in the month of October. There was the least amount of rainfall that was recorded in the month of January, particularly in the years 2002, 2006, 2008, 2023, and 2024. 2008, 2016, 2021, and 2023 were the years that had the least amount of rainfall during the month of February overall. In the month of March in 2012, there was hardly any precipitation. When it comes to rainfall, it is possible to say that the year 2009 had the least amount of precipitation in April, while the years 2002, 2008, and 2020 had the least amount of precipitation in May. 2001 and 2006 were the years that had the least amount of rainfall recorded in June. From the beginning of July to the end of the month, there was hardly any precipitation at all. Rainfall did not occur in the month of August in the years 2005, 2010, 2011, and 2013. Neither the year 2004 nor the year 2013 had any rainfall during the month of September. In 2004, 2016, and 2024, there was no rainfall reported during the month of October. Again, there was no precipitation throughout the months of November and December in 2015.

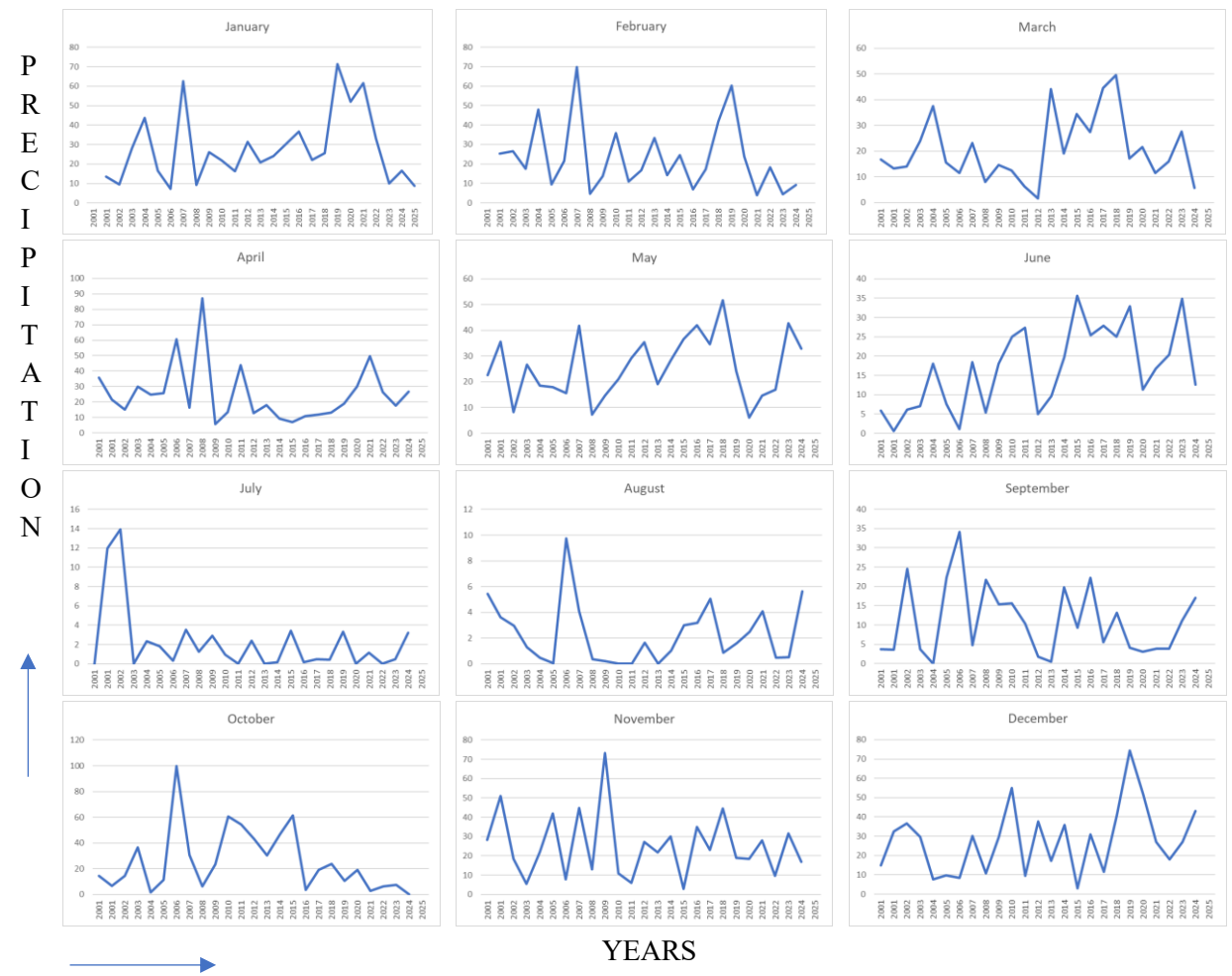


Figure 3
Yearly Variation of Monthly Precipitation Values in Konya Province as a Whole.

The monthly DEPI values were graphed for durations of time when data was available. The yearly change in DEPI values is broken down by month and shown in Figure 4. On the graphs, a zero line represents a DEPI value of 0.5, which symbolizes the border between dry and wet circumstances. This value shows that the conditions are dry. One might make the assertion that the severity of the drought is proportional to the degree to which the DEPI values are closer to zero. The years that had a DEPI that was more than 0.5 were considered to be rainy years.

When one examines the graphs shown in Figure 5, it is evident that the DEPI values have changed

in the direction of drought, particularly after the year 2020. The DEPI values indicate that severe drought conditions existed in January of 2006, but extreme wet conditions were reported in the year 2020. In the month of February, circumstances of severe drought were reported in the years 2006 and 2023, and conditions of wetness were observed in the years 2004, 2007, 2015, 2019, and 2020. In March of 2006, circumstances of severe drought were seen, however in 2018, 2019, and 2020, situations The month of April was characterized by the presence of of excessive wetness were reported. significant drought in the years 2005, 2009, and 2023, while extreme wet conditions were seen in the years 2004 and 2019. In the month of May in 2009, there was a severe drought that was seen, however in 2019 there were circumstances that were excessively moist. There were three years in which June was characterized by great drought: 2005, 2006, and 2009. In 2019, however, June was characterized by unusually wet circumstances. Both July and August were characterized by the same drought and wet conditions as were recorded in June. When September rolled around in 2009, situations that were severe dry prevailed, but in 2015, conditions that were very wet were the norm. In 2005 and 2009, October was one of the months that had catastrophic drought conditions, much like many other months. Extreme drought conditions were encountered throughout the months of November and December in the year 2005. If we wish to make a general observation, we may make a specific observation based on the DEPI graphs by month, which is that the DEPI values were dominated by severe drought circumstances in the year 2006, and that wet conditions were encountered in the year 2019.

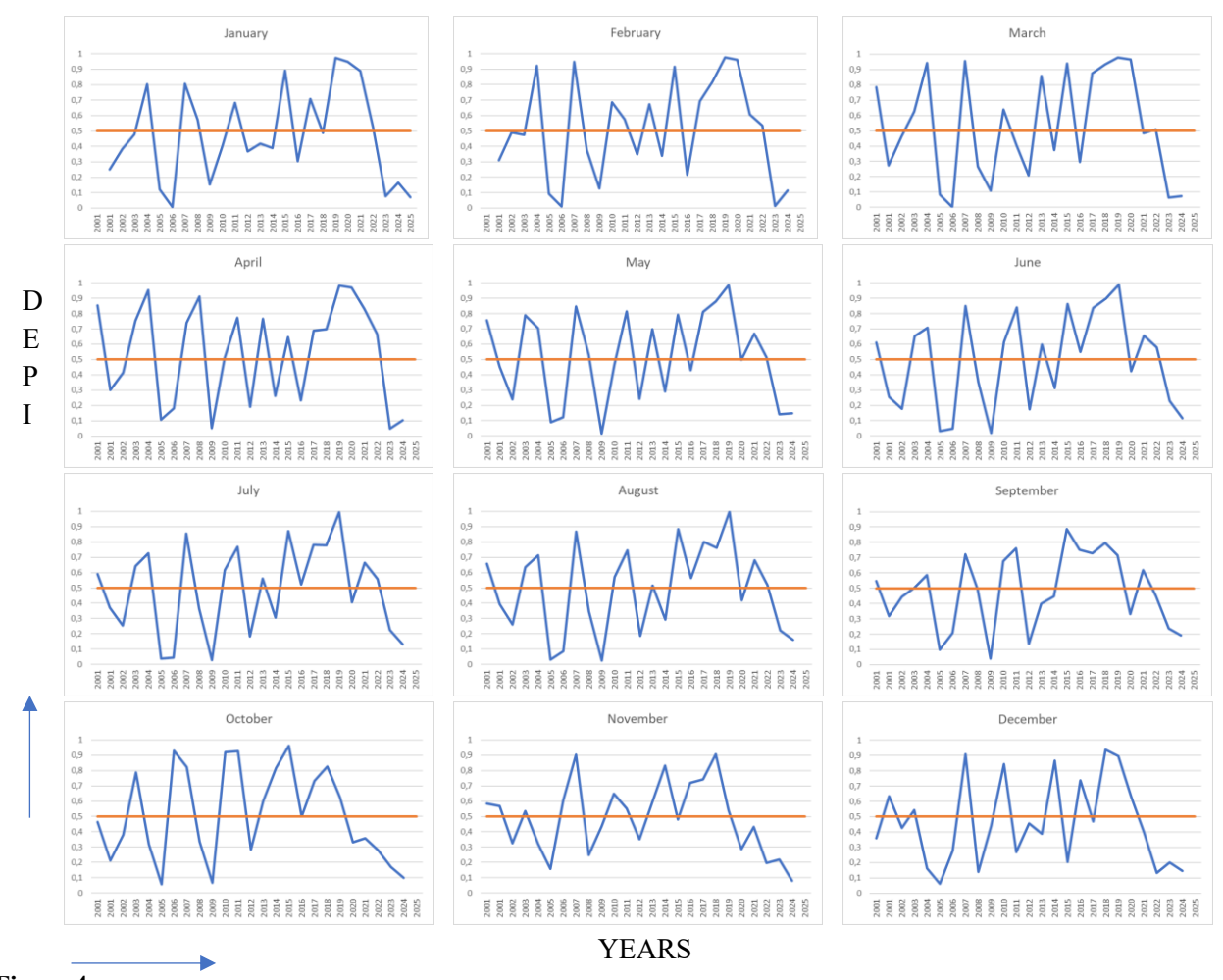


Figure 4 *Yearly Variation of Monthly DEPI Values in Konya Province as a Whole.*

According to the data shown in Table 3, it is possible to assert that the general territory of Konya was subjected to wet circumstances at a rate of 50.17 percent. On the other hand, circumstances of a

Table 3Drought frequency values of Konya according to Drought Thresholds.

		Frequency (%)
DEPI≥0.5	Wet conditions	50.17
0.5>DEPI>0.16	Mild drought	34.11
0.16>DEPI>0.07	Moderate drought	9.03
0.07>DEPI≥0.02	Severe drought	5.02
DEPI<0.02	Extreme drought	1.67

moderate drought exist at a rate of 34.11%. At a rate of 1.67 percent, circumstances of very severe drought have persisted.

A relative humidity and precipitation trend analysis was carried out by [33] for the city of Konya Province as part of their research. The analysis conducted revealed that the Kendall's tau values for precipitation data varied from -0.087 to 0.121 from January to December, with the majority of the values being relatively near to zero. This was the conclusion reached as a consequence of the analysis. It was found that the majority of the p-values were larger than 0.05, and it was also found that the values of Sen's slope for monthly precipitation varied from -0.087 to 0.121. According to the findings, the values of Kendall's tau and Sen's slope are very near to zero, and the p-values are large; this implies that there is no statistical significance in the patterns of the monthly average rainfall.

The decrease in precipitation caused by the severe drought of 2006 mostly affected agriculture and resulted in irrigation water shortages for farmers. The little rainfall has led to reduced water supplies, increasing reliance on groundwater for agricultural needs. Drought imposes both direct and indirect effects on urban and ecological systems. The early consequences of drought primarily involve physical and material losses. The losses encompass a decrease in agricultural production, an intensification of fire hazards, a fall in water levels, an uptick in mortality rates among fauna, and damage to the habitats of wildlife and aquatic species. The humid conditions of 2019 were beneficial for agricultural productivity, especially for farmers in Konya Province. The increase in reservoir water levels has favorably impacted both ecological and urban environments.

The parameters of temperature and humidity in the weather have an impact on a variety of areas, including living circumstances, agricultural practices, and transportation [34, 35]. There are a number of factors that influence drought, including temperature and humidity. Additionally, these investigations that were carried out in the province of Konya overlap with one another.

According to the findings of a research [36], in Central Anatolia (which includes Konya Province), air pollution is a major environmental issue that impacts lives and the environment and contributes to global climate change. Air pollution causes are being studied as their global consequences spread. As the global population grows, so does energy demand. Due to population expansion and industrial requirements, air pollution is rising daily, harming all life.

CONCLUSION

Unlike rapid natural catastrophes like hurricanes or earthquakes, droughts start slowly over time and could endure months or even years. From dry deserts to temperate agricultural zones, they are found in many different climatic zones and have strong effects that could cause crop failures, food shortages, economic losses, and environmental damage. Konya is recognized as Turkey's wheat granary and is a region where water-dependent agricultural products, including sugar beet, corn, and sunflower, are cultivated. The Konya Province fulfills a significant portion of its water requirements through subterranean sources. Excessive groundwater extraction is resulting in a rapid decline of water levels in the Konya Province. The ongoing drought is diminishing the renewal capacity of water resources, leading to anticipated larger water crises in the future.

In this study, a drought analysis covering the general area of Konya Province has been conducted. In recent years, the precipitation parameter obtained through satellite-based remote sensing, which has gained popularity, has been used. This method has been preferred because accessing these data is both practical and easy. Moreover, since the accuracy rate is better than terrestrial measurements, it is believed to provide more precise results in drought analysis. The DEPI method applied has not been used as comprehensively for Konya Province before. In this regard, it is believed that this study will contribute to the literature. An examination of drought was carried out by using PERSIANN data via the use of precipitation data spanning from March 2000 to January 2025. In accordance with the findings, dry times are followed by wet periods, and these wet periods are again succeeded by dry ones. In general, the province of Konya is characterized by moist circumstances; nevertheless, in 2006, conditions that were considered to be very dry were seen.

Conscious water use, sustainable agricultural practices, and government-supported water management projects are essential in addressing drought. Failure to implement necessary measures may pose significant threats to the region's agricultural production and water resources in the future. In the province of Konya, it is anticipated that this study will contribute to drought research and provide new perspectives on the topic.

Ethical Statement

This study is an original research article designed and developed by the authors.

Ethics Committee Approval

This study does not require any ethics committee approval.

Author Contributions

Research Design (CRediT 1) F.K. (%50) – E.T. (%50)

Data Collection (CRediT 2) F.K. (%50) – E.T. (%50)

Research- Data Analysis – Validation (CRediT 3-4-6-11) D.Y. F.K. (%50) – E.T. (%50)

Writing the Article (CRediT 12-13) D.Y. F.K. (%50) – E.T. (%50)

Revision and Improvement of the Text (CRediT 14) F.K. (%50) – E.T. (%50)

Financing

This research did not receive any specific grant from funding agencies in the public, commercial, or not-for-profit sectors.

Conflict of Interest

The authors declare no conflicts of interest for this study.

Sustainable Development Goals (SDG)

Sustainable Development Goals: 13 (Climate Action)

REFERENCES

- [1] N.K. Mallenahalli, Comparison of parametric and nonparametric standardized precipitation index for detecting meteorological drought over the Indian region, *Theoretical and Applied Climatology*. 142 (2020), 219–236. doi:10.1007/s00704-020-03296-z
- [2] E. Topçu, Testing of Drought Exceedance Probability Index (DEPI) for Turkey using PERSIANN data for 2000-2021 period, *Italian Journal of Agrometeorology*. 2 (2021), 15-28. doi:10.36253/ijam-1308
- [3] D.A. Wilhite, M.H. Glantz, Understanding: the drought phenomenon: the role of definitions, *Water International*. 10(3) (1985), 111-120. doi:10.1080/02508068508686328
- [4] E. Topçu, N. Seçkin N, Drought Analysis of the Seyhan Basin by using Standardized Precipitation Index (SPI) and L-Moments, *Journal of Agricultural Science*. 22 (2016), 196-215. doi:10.1501/Tarimbil 0000001381
- [5] E. Topçu, Appraisal of seasonal drought characteristics in Turkey during 1925–2016 with the standardized precipitation index and copula approach, *Natural Hazards*. 112(1) (2022), 697-723. doi:10.1007/s11069-021-05201-x
- [6] E. Topçu, F. Karaçor, A comparative investigation on the applicability of the actual precipitation index (API) with the standardized precipitation index (SPI): the case study of Aras Basin, Turkey, *Theoretical and Applied Climatology*. 154(1) (2023), 29-42. doi:10.1007/s00704-023-04499-w
- [7] E. Topçu, F. Karaçor, Erzurum istasyonunun standartlaştırılmış yağış evapotranspirasyon indeksi ve bütünleşik kuraklık indeksi kullanılarak kuraklık analizi, *Politeknik Dergisi*. 24(2) (2021). doi:10.2339/politeknik.682168
- [8] E. Topçu, N. Seçkin, N.A. Haktanır, Drought analyses of Eastern Mediterranean, Seyhan, Ceyhan, and Asi Basins by using aggregate drought index (ADI), *Theoretical and Applied Climatology*. 147(3) (2022), 909-924. doi:10.1007/s00704-021-03873-w
- [9] E. De Martonne, Nouvelle carte mondiale de l'indice d'aridité, *Annales de Géographie*. 51 (1942), 242–250.
- [10] W.C. Palmer, Meteorological Drought, Bureau of Meteorology, Research Paper No.451965
- [11] J.W. Gibbs, V.J. Maher, Rainfall Deciles as Drought Indicators, *Bureau of Meteorology*. 48 (1967).
- [12] A. Aydeniz, Tarımda verimliliğin sağlanmasında önemli etken olan su ve sulama durumumuz, *Verimlilik Dergisi*. 3(1) (1973), 177-199.
- [13] S. Erinç, Klimatoloji ve Metotları, Climatology and Methods, *Alfa Basim Yayım*, İstanbul, 1984.
- [14] T.B. McKee, N.J. Doesken, J. Kleist, The Relationship of Drought Frequency and Duration to Time Scales, *Proceedings of the 8th Conference on Applied Climatology*, Anaheim, California, USA, 1993, 17.
- [15] A.J. Keyantash, A.J. Dracup, An aggregate drought index: Assessing drought severity based on fluctuations in the hydrologic cycle and surface water storage, *Water Resources Research*. 40 (2004). doi:10.1029/2003WR002610
- [16] G. Tsakiris, H. Vangelis, Establishing a Drought Index Incorporating Evapotranpiration, *European Water Publications*. 9/10 (2005), 3-11.
- [17] E. Topçu, N. Seçkin, Drought assessment using the reconnaissance drought index (RDI): A case study of Eastern Mediterranean, Seyhan, Ceyhan, and Asi basins of Turkey, *Journal of Engineering Research*.10(2B) (2022). doi:10.36909/jer.12113
- [18] I. Nalbantis, Evaluation of a Hydrological Drought Index, *European Water Publications*. 23/24 (2008), 67-77.

- [19] N. Limones, M.F.P.- López, J.M. Camarillo-Naranjo, A new index to assess meteorological drought: the Drought Exceedance Probability Index (DEPI), *Atmósfera*. 35 (2020) 67–88. doi:10.20937/atm.52870.
- [20] M.F. Pita, Un nouvel indice de sécheresse pour les domains méditerranéens. Application au bassin du Gaudalquivir sudouest de l'Espagne, A new drought index for Mediterranean domains. Application to the Guadalquivir riverbasin in southwestern Spain, *Publications de l'Association Internationale de Climatologie*. 13 (2000), 225–234.
- [21] S.M. Vicente-Serrano, S. Beguería, J.I. López-Moreno, A multiscalar drought index sensitive to global warming: the Standardized Precipitation evapotranspiration Index, *Journal of Climate*. 23 (2009), 1696–1718. doi:10.1175/2009jcli2909.1
- [22] Wikipedia, Konya'nın ilçeleri, (2025). https://tr.wikipedia.org/wiki/Konya%27n%C4%B1n_il%C3%A7eleri (erişim 03 Mart 2025).
- [23] W. Weibull, A statistical theory of strength of materials, *Ingeniors Vetenskaps Academy Handlingar*. 151 (1939), 1-45.
- [24] Data Portal, PERSIANN, (2024). https://chrsdata.eng.uci.edu/ (erişim 03 Şubat 2025).
- [25] K. Hsu, X. Gao, S. Sorooshian, H.V. Gupta, Precipitation estimation from remotely sensed information using artificial neural networks, *Journal of Applied Meteorology*. 36(9) (1997), 1176-1190.
- [26] K. Hsu, H.V. Gupta, X. Gao, S. Sorooshian, Estimation of physical variables from multiple channel remotely sensed imagery using a neural network: Application to rainfall estimation, *Water Resources Research*. 35(5) (1999), 1605-1618.
- [27] K.L. Hsu, H. V. Gupta, X. Gao, S. Sorooshian, Rainfall estimation from satellite imagery, Artificial Neural Networks in Hydrology. (2000) 209-234. doi:10.1007/978-94-015-9341-0_12
- [28] K. Hsu, H.V. Gupta, X. Gao, S. Sorooshian, B. Imam, SOLO-An artificial neural network suitable for hydrologic modelling and analysis, *Water Resources Research*. 38(12) (2002), 1302.
- [29] S. Sorooshian, X. Gao, K. Hsu, R.A. Maddox, Y. Hong, B. Imam, H.V. Gupta, Diurnal variability of tropical rainfall retrieved from combined GOES and TRMM Satellite Information, *Journal of Climate*. 15 (2002), 983-1001.
- [30] S. Sorooshian, K. Hsu, X. Gao, H.V. Gupta, B. Imam, D. Braithwaite, Evaluation of PERSIANN system satellite-based estimates of tropical rainfall, *Bulletin of the American Meteorology Society*. 81(9) (2000), 2035-2046.
- [31] S. Sorooshian, P. Nguyen, S. Sellars, D. Braithwaite, A. Aghakouchak, K. Hsu, Satellite-based remote sensing estimation of precipitation for early warning systems, *Extreme Natural Hazards*, *Disaster Risks and Societal Implications*. (2014), 99-111.
- [32] P. Nguyen, E.J. Shearer, H. Tran, M. Ombadi, N. Hayatbini, T. Palacios, P. Huynh, G. Updegraff, K. Hsu, B. Kuligowski, W.S. Logan, S. Sorooshian, The CHRS data portal, an easily accessible public repository for PERSIANN global satellite precipitation data, *Nature Scientific Data*. 6 (2019), 180296. doi:10.1038/sdata.2018.296
- [33] K. Eryürük, Ş. Eryürük, Assessing trends in monthly precipitation and relative humidity: an analysis for climate change reference in Konya, *Necmettin Erbakan University Journal of Science and Engineering*. 6(1) (2024), 105-114. doi:10.47112/neufmbd.2024.35
- [34] F. Özen, R. Ortaç Kabaoğlu, T.V. Mumcu, Deep learning based temperature and humidity prediction, *Necmettin Erbakan University Journal of Science and Engineering*. 5(2) (2023), 219-229. doi:10.47112/neufmbd.2023.20
- [35] E. Topçu, F. Karaçor, B. Çırağ, İ. Taşkolu & R. Acar, Drought assessment in the northeastern Aras Basin using multi-parameter aggregate drought index and innovative polygon trend analysis, *Earth Science Informatics*. 18(3) (2025), 273. doi:10.1007/s12145-025-01797-x

[36] F. Kunt, A. Özkan, Evaluation of air quality (PM10 and SO2) parameters: Example of Central Anatolia Region, *Necmettin Erbakan University Journal of Science and Engineering*. 6(2) (2024), 255-271. doi:10.47112/neufmbd.2024.47



Vol: 7 No:2 Year: 2025

Araştırma Makalesi/Research Article

e-ISSN: 2667-7989

https://doi.org/10.47112/neufmbd.2025.95

Poliol Sentezinde Metal Tuzlarının Gümüş Nanotel Morfolojisi Üzerindeki Etkisi

Mücahit KARASAKAL ¹ D İrem Sena DEMİREL ¹ D Emre Burak ERTUŞ ^{2*} D

² KTO Karatay University, Faculty of Engineering and Nature Science, Department of Mechanical Engineering, Konya, Türkiye

Makale Bilgisi	ÖZET
Geliş Tarihi: 26.08.2024 Kabul Tarihi: 07.04.2025 Yayın Tarihi: 31.08.2025	Poliol yöntemi, yüksek kaliteli gümüş nanotellerin (AgNWs) sentezi için basit, ekonomik ve çok yönlü bir yaklaşım sunmasıyla dikkat çekmektedir. Bu yöntemde, kullanılan metal tuzları, elde edilen AgNWs ürününün özelliklerini belirlemede önemli bir rol oynar. Bu araştırma, poliol yöntemiyle sentezlenen AgNWs uzunluğu ve çapı üzerinde farklı metal tuzlarının etkisini incelenmiştir. Her sentezde Sodyum Klorür (NaCl) sabit bir bileşen olarak kullanılmış ve buna
Anahtar Kelimeler: Gümüş nanotel, Poliol metodu, Metal tuzları.	ek olarak iki farklı tuz türü eklenmiştir. NaCl ile birlikte eser miktarda Demir (III) Nitrat (Fe(NO ₃) ₃), Bakır(II) Klorür (CuCl ₂) ve Potasyum Bromür (KBr) kullanılmıştır. Nanotellerin şekli ve boyut dağılımı Alan Emisyonlu Taramalı Elektron Mikroskobu ile analiz edilmiş, nanopartiküllerin kristal yapısı ise X-ışını Kırınımı ile incelenmiştir. KBr tuzu kullanılarak yapılan sentezlerde en yüksek boy/en oranına sahip AgNWs üretildiği görülmüş ve bu nanotellerin uzunluğu $6,2\pm2,5~\mu m$ olarak ölçülmüştür. Ayrıca, CuCl ₂ tuzu kullanılarak yapılan sentezde, nanotellerin yanı sıra nanoküpler ve nanoüçgenler gibi diğer gümüş nanoyapılarının da önemli ölçüde oluştuğu gözlemlenmiştir.

Influence of Metal Salts on Silver Nanowire Morphology in Polyol Synthesis

Article Info	ABSTRACT
Received: 26.08.2024 Accepted: 07.04.2025 Published: 31.08.2025	The polyol method has gained significant attention for synthesizing Silver nanowires (AgNWs), offering a straightforward, cost-effective, and versatile approach to producing high-quality nanowires. In polyol method, the choice of metal salts performs a crucial function in determining the properties of the final AgNW product. This research specifically explores the influence of different metal salts on the length and diameter of AgNWs synthesized through the
Keywords: Silver nanowires, Polyol method, Metal salts.	polyol method. Each synthesis involved the use of two distinct types of salts, with NaCl being a constant component. Trace amounts of Iron(III) Nitrate (Fe(NO ₃) ₃), Copper(II) Chloride (CuCl ₂), and Potassium Bromide (KBr) were introduced in conjunction with NaCl. The morphology and dimensional distribution of the nanowires were analyzed using Field Emission Scanning Electron Microscopy, while X-ray Diffraction was applied to study the crystal structure of the nanoparticles. Notably, the utilization of KBr in the synthesis led to the production of AgNWs with the highest aspect ratio, resulting in nanowires measuring 6.2 ± 2.5 µm in length. Additionally, the synthesis assisted by CuCl ₂ revealed a substantial presence of other silver nanostructures, such as nanocubes and nanotriangles, alongside nanowires.

To cite this article

Karasakal, M., Demirel İ.S. & Ertuş, E.B. (2025). Influence of metal salts on silver nanowire morphology in polyol synthesis. Necmettin Erbakan University Journal of Science and Engineering, 7(2), 322-330. https://doi.org/10.47112/neufmbd.2025.95

*Corresponding Author: Emre Burak Ertuş, burak.ertus@karatay.edu.tr



¹ Necmettin Erbakan University, Graduate School of Natural and Applied Sciences, Department of Nanoscience and Nanoengineering, Konya, Türkiye

INTRODUCTION

Silver nanowires (AgNWs) have emerged as promising nanomaterials for use in various applications owing to their unparalleled properties such as high aspect ratio, high conductivity, and outstanding catalytic activity. These properties allow them to be effectively used in flexible electronics, transparent conductive films, sensors, and energy storage devices, among others [1,2]. Various methods have been employed for synthesizing AgNWs, including chemical reduction [3], electrochemical synthesis [4], and template-assisted methods [5]. However, the polyol method has gained increasing attention as a simple, low-cost, and versatile method for producing uniform and high-quality AgNWs.

In the polyol method, silver precursors are reduced by polyols under high temperature conditions with the incorporation of stabilizing agents. The resulting AgNWs exhibit high aspect ratios, uniform diameters, and narrow size distributions. A polyol is an organic compound containing multiple hydroxyl groups. The function of polyols is as reducing and dissolving agents. The most preferred polyol is ethylene glycol ($C_2H_6O_2$) due to its low cost [6]. Polymers are used as stabilizing agents in polyol method and Polyvinylpyrrolidone (PVP) being the most effective among the polymers used. PVP is employed to ensure the growth of nanowires in one dimension and to direct the growth kinetics of metal surfaces by limiting the growth of multiple twinned particles in the $\{100\}$ planes while facilitating longitudinal growth in the $\{111\}$ plane, thereby aiding in the formation of AgNWs. This is due to PVP's strong interaction with the (100) surface and weak interaction with the (111) surface. As a result, the one-dimensional wire structure is shaped by faster growth on the (111) surface [7,8].

Transition metal salts perform a crucial function in the polyol synthesis of silver nanowires by serving as oxygen scavengers, thereby enabling the synthesis process to be conducted under ambient air conditions. During the synthesis of AgNWs in ambient atmosphere, the existence of atomic oxygen can hinder the growth of AgNWs by covering the surface of silver seed nanoparticles. However, transition metal ions can remove the adsorbed atomic oxygen from the silver grains. As a result, in the polyol synthesis of AgNWs conducted in an open atmosphere, the presence of transition metal salts facilitates the unhindered growth of AgNWs by removing the inhibitory effects of atomic oxygen [9]. Also, many researchers have reported that the introduction of halide salts during the synthesis process is responsible for incorporating additional anions into the system. This, in turn, leads to a decrease in the proportions of available Ag+ ions within the solution, thereby retarding the reduction of silver nitrate. The deliberate reduction in the rate of AgNO₃ reduction facilitated by the presence of halide salts enables the successful and efficient growth of nanowires [10-12]. Consequently, many researchers have determined that the successful production of AgNWs requires the presence of both cations and anions. Sarisozen et al. [9] studied different kinds of metal salts including CuCl₂, CoCl₂, MnCl₂, CrCl₃, FeCl₃, and ZnCl₂ serving as support in the polyol synthesis of AgNWs in their experimental conditions and exhibited that AgNWs synthesized in the existence of CuCl₂ come up with the longest length. Yamamoto et al. [10] compared the effect of halide salts of NaCl, CuCl₂ and NaBr, the longest AgNWs were obtained with NaCl. In another study, Coskun et al. [11] emphasized that below to appropriate NaCl ratio silver microparticles began to form, and above AgCl formation initiated. Ashkarran et al. [13] investigated the impact FeCl₃ over the structure of AgNWs and revealed that elevated concentrations result in formation of semi spherical shaped silver nanostructures. Also, a similar result regarding excessive use of FeCl₃ was also emphasized by Zhang et al. [14]. Basarir et al. [15] examined the effect of NaCl, FeCl₃ and CuCl₂ salts and suggested that standard reduction potentials of the ions involved in reaction are effective in AgNW production. Zhang et al. [16] examined how the presence of NaCl, FeCl₃, and KBr, affects the size of AgNWs. They reported that as the ratio of KBr increased, there was an observed increase in the formation rate of particles other than nanowires.

This study investigates the impact of different metal salt types on the dimensions of silver

nanowires (AgNWs) synthesized using the polyol method. Specifically, two types of salts were utilized in each synthesis: sodium chloride (NaCl), which was kept at a constant amount, and trace amounts of Copper (II) Chloride (CuCl₂), Potassium Bromide (KBr), or Iron(III) Nitrate (Fe(NO₃)₃). The innovative aspect of this study lies in systematically exploring the combined effects of these salts on AgNW synthesis, which has not been thoroughly investigated in prior research. By elucidating the role of these salts in tailoring AgNW dimensions, this work aims to advance the understanding of synthesis parameters and contribute to the optimization of AgNW fabrication processes for various applications.

MATERIALS AND METHODS

AgNW Synthesis

AgNWs were created through a facile polyol route. The summarized synthesis setup is shown in Figure 1. A mixture of 10 mL Ethylene Glycol (EG Sigma-Aldrich, \geq 99.8% purity), 750 mg poly vinylpyrrolidone (PVP, Sigma-Aldrich, Mw \approx 40,000), 0.007 mg (12 μ M) NaCl (Merck, \geq 99.5% purity), and 12x10⁻⁸ mol (12 μ M) of chosen salt is heated in a flask connected to a reflux column up to 170 °C. In order to examine the effects of salt types on nanowire formation, 3 different solutions were studied using Fe(NO₃)₃ (Merck, \geq 98% purity), CuCl₂ (Sigma-Aldrich, \geq 97% purity) and KBr (Merck, \geq 99% purity) salts. Once the temperature has stabilized, Ag source solution prepared with 5 mL of EG and 100 mg AgNO₃ (Sigma-Aldrich, \geq 99.9% purity) was injected into the 2-necked flask via programmed syringe pump with a drop rate of 5 mL/h. Stirring continued for another 30 minutes, then the solution was allowed to reach room temperature. To separate AgNW from PVP and EG, the solution was diluted with acetone (Merck, \geq 99.5% purity) (1:10 ratio) and centrifuged twice at 4500 rpm for 15 minutes. Finally, the AgNW's were dispersed in ethanol (Sigma-Aldrich, \geq 95% purity) for characterization and centrifuged again at 4500 rpm for another 15 minutes. The AgNWs produced depending on salt type were presented in Table 1.

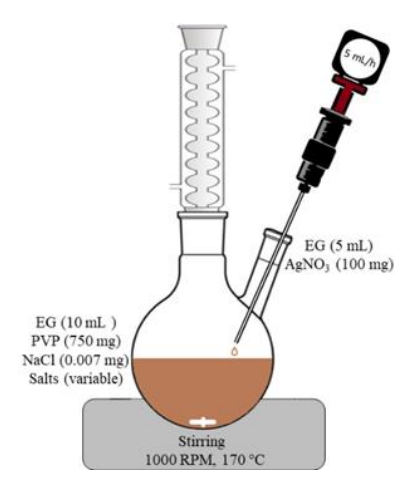


Figure 1
The summarized synthesis setup.

Characterization

AgNWs were analyzed by an X-ray diffractometer (PANalytical Empyrean, 1D mode, fixed divergence slit) between 35-80° at a scanning rate of 0.1°/min using CuKα radiation with a wavelength of 1.54056 Å. The Joint Committee on Powder Diffraction Standards (JCPDS) database was used to determine the phases. The morphology and size of AgNWs were examined using Field Emission Scanning Electron Microscopy (ZEISS GeminiSEM 500, FE-SEM) using 3 kV operation voltage.

RESULTS AND DISCUSSION

The incorporation of different salts in the synthesis of AgNWs by polyol synthesis has led to meaningful differences in the size of AgNWs and the aspect ratio. Fig.2 represents the SEM images of AgNWs synthesized. The length and diameter of the AgNWs were determined using ImageJ software by measuring a minimum of 50 nanowires and calculating the average value. The results obtained are summarized in Table 1.

Table 1 *Average diameter, length, and aspect ratio of agnws obtained with different metal salts.*

Salt Type	Lenght (µm)	Diameter (nm)	Aspect Ratio
KBr	6.2 ± 2.5	46 ± 10	134
$CuCl_2$	4.6 ± 1.1	120 ± 29	38
$Fe(NO_3)_3$	$1.9 \pm \! 1.6$	51 ±10	37

It is seen that the highest length/width ratio is obtained with the solution containing KBr salts. As is known, Br ions serve both as a capping agent to passivate the (100) surfaces in a growing Ag crystal and help reduce the reduction kinetics by binding to Ag ions. Thanks to this synergistic effect, it is thought that the longest nanowires are obtained with the solution containing Br ions [17]. Similarly, in studies in literature where the common use of different salts was investigated, it was observed that the solutions with the largest aspect ratio were obtained with NaCl-KBr salts [16,18]. Table 2 shows the length and width of AgNWs obtained through salt-mediated polyol synthesis in various studies [13,16,19–22].

Table 2 *Types of salts and dimensions of AgNWs.*

Salt Types	Ag/Metal Salt*	Lenght (µm)	Diameter (nm)	Aspect Ratio*	Ref.
KBr	187	21	26	807	[16]
KBr	17	80	50	3076	[19]
CuCl ₂	800	10-50	100	500	[20]
CuCl ₂	881	3.2	102	31	[21]
$Fe(NO_3)_3$	25.5	40	45	888	[22]
FeCl ₃	100	3.52	96	3.6	[13]

^{*:} Average values

CuCl₂ solution dissociates into Cu⁺² and Cl⁻ ions, and both ions play a critical role in AgNW synthesis. Cl⁻ ions electrostatically attract the positively charged Ag⁺ ions, which helps to prevent them from agglomerating and promotes the formation of stable Ag seeds. Also, the reaction between Cl⁻ ions and Ag⁺ ions leads to the formation of AgCl, which is a precipitate that can be removed from the solution [10]. This aids in lowering the concentration of free Ag⁺ ions in the solution, thereby preventing the uncontrolled growth of Ag seeds. Cu⁺² ions are changed to Cu⁺ ions in the EG solution. This reaction consumes electrons, which can help to prevent the oxidation of AgNWs. Cu⁺ ions can react with atomic oxygen, which is a byproduct of the AgNW synthesis reaction. Atomic oxygen can block the reactive sites on the surface of AgNWs, which can prevent their growth. By scavenging atomic oxygen, Cu⁺ ions can help to promote the development of longer AgNWs [15,20].

The lowest length and aspect ratio were obtained in AgNWs produced with Fe(NO₃)₃ additive. Much like copper ions, Fe(II) extracts atomic oxygen located at the surface of silver nanostructures. The interaction with ethylene glycol (EG) for reduction contends with the oxidation caused by atomic oxygen, resulting in the establishment of an equilibrium between Fe(III) and Fe(II) [23,24].

In all syntheses, a significant amount of irregular shaped silver nanoparticles was observed

alongside AgNWs. Especially in the synthesis involving $CuCl_2$, the formation of silver nanocubes and nanotriangles was observed. The Ag/Salt molar ratio was chosen to be ≈ 5000 in our study, although to the ratio of ≈ 100 in many studies in the literature as summarized in Table 2. The objective of using a minimal amount of salt is to observe the effect of trace amounts of salt and to minimize environmental impact and financial burden. The shorter length of the obtained nanowires compared to other studies in the literature is attributed to the lower amount of salt used. The environmental hazards of the salts used are outlined in Table 3. By reducing the salt content, the environmental footprint of AgNW production is minimized, making the process more sustainable and economically viable [25–27].

Table 3 *Environmental impact of salts used in AgNW production.*

Salt Types	Environmental Impact	Ref.
KBr	The Br ⁻ anion, at high concentrations, can be a source of	[25]
KBr	concern for both human and ecosystem health.	[25]
CC1	Cu ⁺² , being a heavy metal, can lead to soil and water pollution.	[26]
CuCl ₂	It threatens biological processes.	[26]
E-(NO.)	Ferric ions at high concentrations can accumulate in water and	[27]
$Fe(NO_3)_3$	soil, leading to pollution.	[27]

Figure 3 depicts the normalized X-ray diffractograms of AgNWs. The observed peaks located at diffraction angles of 2θ 38.02°, 44.20°, 64.20° and 77.3° corresponded to (111), (200), (220) and (311) Bragg reflections of face-centered cubic Ag (JCPDS card 04-0783) [24,28]. The (111) diffraction peaks of all AgNWs were observed at the same 2θ value (see the zoomed-in graph of the (111) peaks Figure 3). This consistency indicates that the crystal structure of AgNWs remains unaffected by the different salt types used in the synthesis process, suggesting uniformity in the lattice parameters and absence of significant strain or size-related variations among the samples. Additionally, no salt related peaks were observed in the XRD pattern, indicating that all salts were successfully removed during the washing and cleaning stages.

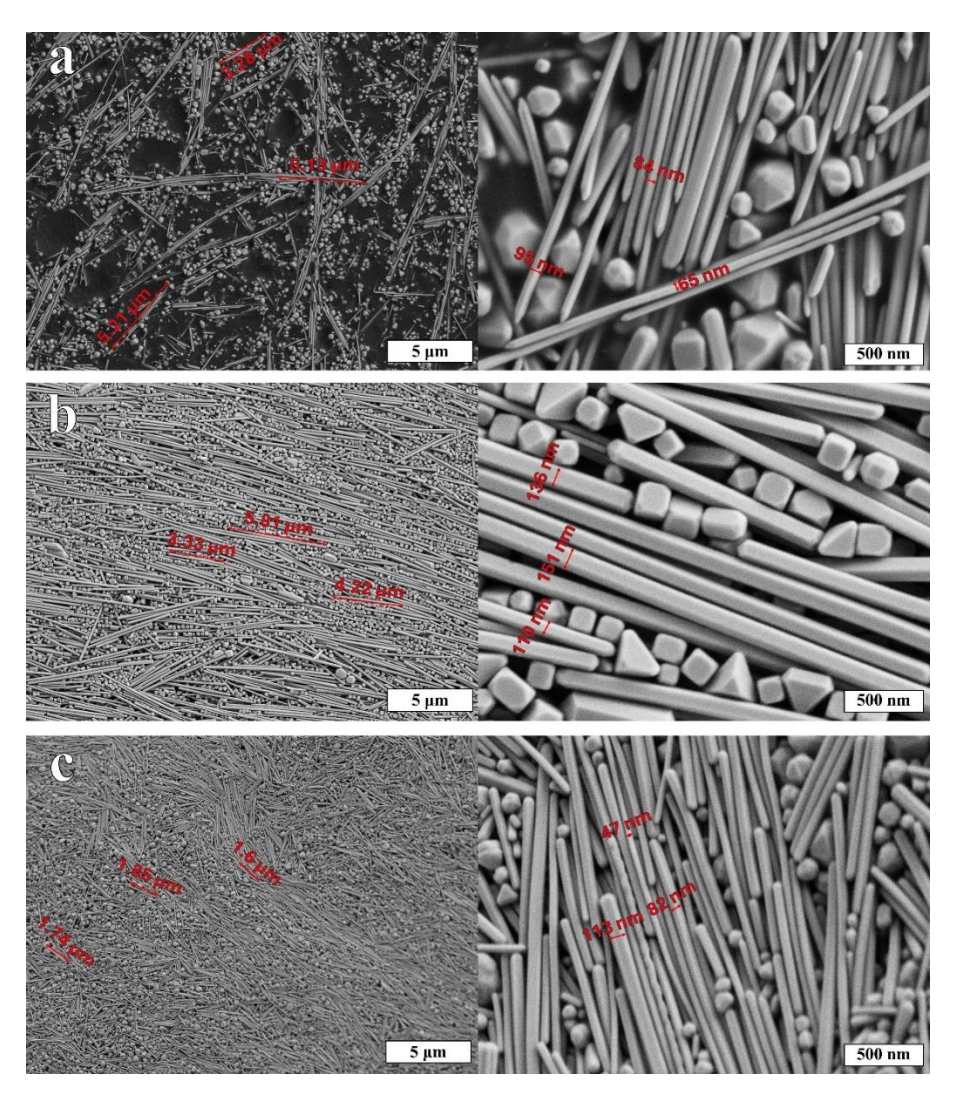


Figure 2 SEM images of AgNWs synthesized with different salts are presented at $10,000 \times$ magnification, with insets showing higher magnification at $90,000 \times$: (a) KBr, (b) CuCl₂, (c) Fe(NO₃)₃.

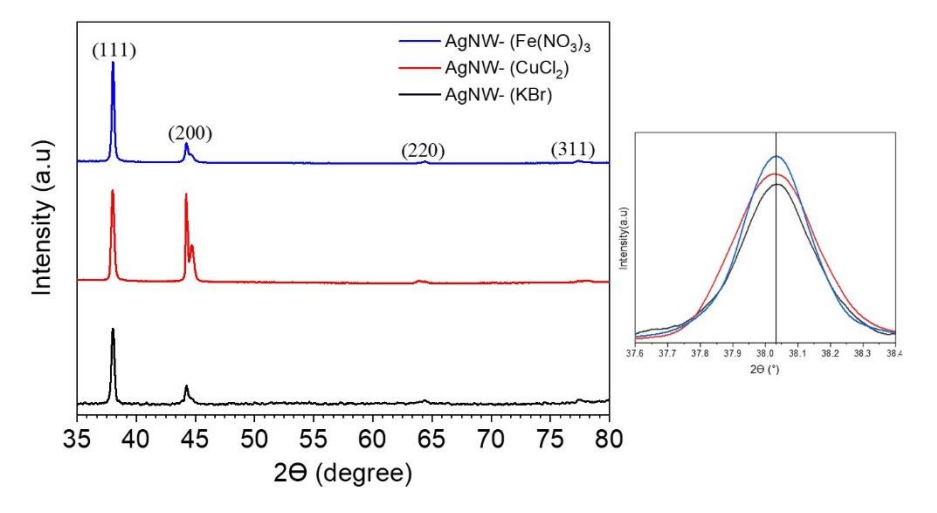


Figure 3 *XRD patterns of AgNW's prepared with different type of metal salts.*

It is observed that the diffraction peak signals at (111) are larger than those at (200) for the KBr and Fe(NO₃)₃ samples. This shows that the atom density in the (111) plane is higher than in the other planes, and atoms prefer to settle on the (111) crystal surface, suppressing crystal growth along other planes. However, this situation is different for CuCl₂ samples and the peak corresponding to the (200) plane has almost the same intensity as the peak belonging to the (111) plane. The ratio of area under peaks (111)/ (200) for KBr, CuCl₂, and Fe(NO₃)₃ is 2.8, 0.9, and 2.9 respectively. This is due to the presence of well-shaped silver nano cubes and nanotriangles as well as nanowires in the CuCl₂ sample, as observed in the SEM analysis (Figure 2).

CONCLUSION

AgNWs were synthesized through a polyol method utilizing trace amounts of $Fe(NO_3)_3$, $CuCl_2$, and KBr in conjunction with NaCl. The production using KBr resulted in obtaining AgNWs with the highest aspect ratio, yielding AgNWs with a length of $6.2 \pm 2.5 \, \mu m$. In the synthesis assisted by $CuCl_2$, besides nanowires, a substantial amount of other silver nanostructures such as nanocubes and nanotriangles were observed. XRD analyses indicate the absence of any other salt or residual phase besides metallic silver. We envision that our results would show that metal salts, even in trace amounts, play a decisive role in the production of AgNW obtained via polyol process.

Ethical Statement

This study is an original research article designed and developed by the authors.

Author Contributions

Research Design (CRediT 1) M.K. (%20) – İ.S.D. (%20) – E.B.E. (%60)
Data Collection (CRediT 2) M.K. (%50) – İ.S.D. (%40) – E.B.E. (%10)
Research - Data Analysis – Validation (CRediT 3-4-6-11) M.K. (%50) – İ.S.D. (%40) – E.B.E. (%10)
Writing the Article (CRediT 12-13) M.K. (%20) – İ.S.D. (%20) – E.B.E. (%60)
Revision and Improvement of the Text (CRediT 14) M.K. (%25) – İ.S.D. (%25) – E.B.E. (%50)

Financing

This work was supported by The Scientific and Technological Research Council of Turkey (TÜBİTAK) through program 2209-A.

Conflict of Interest

The authors have no conflicts of interest to disclose for this study.

Sustainable Development Goals (SDG)

Sustainable Development Goals: 9 Industry, innovation and infrastructure.

REFERENCES

- [1] P. Zhang, I. Wyman, J. Hu, S. Lin, Z. Zhong, Y. Tu, Z. Huang, Y. Wei, Silver nanowires: Synthesis technologies, growth mechanism and multifunctional applications, *Materials Science and Engineering: B.* 223 (2017), 1-23. doi:10.1016/J.MSEB.2017.05.002.
- [2] J.J. Chen, S.L. Liu, H. Bin Wu, E. Sowade, R.R. Baumann, Y. Wang, F.Q. Gu, C.R.L. Liu, Z.S. Feng, Structural regulation of silver nanowires and their application in flexible electronic thin films, *Materials & Design*. 154 (2018), 266-274. doi:10.1016/J.MATDES.2018.05.018.
- [3] S.H. Kim, B.S. Choi, K. Kang, Y.S. Choi, S.I. Yang, Low temperature synthesis and growth mechanism of Ag nanowires, *Journal of Alloys and Compounds*. 433 (2007), 261-264. doi:10.1016/J.JALLCOM.2006.06.053.
- [4] M. Mazur, Electrochemically prepared silver nanoflakes and nanowires, *Electrochemistry Communications*. 6 (2004), 400-403. doi:10.1016/J.ELECOM.2004.02.011.
- [5] S. Berchmans, R.G. Nirmal, G. Prabaharan, S. Madhu, V. Yegnaraman, Templated synthesis of silver nanowires based on the layer-by-layer assembly of silver with dithiodipropionic acid molecules as spacers, *Journal of Colloid and Interface Science*. 303 (2006), 604-610. doi:10.1016/J.JCIS.2006.07.060.
- [6] S. Fahad, H. Yu, L. Wang, Zain-ul-Abdin, M. Haroon, R.S. Ullah, A. Nazir, K. ur R. Naveed, T. Elshaarani, A. Khan, Recent progress in the synthesis of silver nanowires and their role as conducting materials, *Journal of Materials Science*. 54 (2019) 997-1035. doi:10.1007/S10853-018-2994-9.
- [7] A. Amirjani, P. Marashi, D.H. Fatmehsari, The effects of physicochemical parameters on the synthesis of silver nanowires via polyol method, *International Nano Letters*. 4 (2014), 1-5. doi:10.1007/S40089-014-0108-5.
- [8] Y. Sun, R.A. Graff, M.S. Strano, J.A. Rogers, Top-down fabrication of semiconductor nanowires with alternating structures along their longitudinal and transverse axes, *Small*. 1 (2005), 1052-1057. doi:10.1002/SMLL.200500094.
- [9] S. Sarisozen, N.A. Tertemiz, T.A. Arica, N. Polat, C. Kocabas, F.M. Balci, S. Balci, Transition metal salt promoted, green, and High-Yield synthesis of silver nanowires for flexible transparent conductive electrodes, *ChemistrySelect*. 6 (2021), 12548-12554. doi:10.1002/SLCT.202103434.
- [10] E.G. Yamamoto, M.P. Dantas, G. Yamanishi, F.B. Soares, A. Urbano, S.A. Lourenço, C.E. Cava, Silver nanowire synthesis analyzing NaCl, CuCl2, and NaBr as halide salt with additional thermal, acid, and solvent post-treatments for transparent and flexible electrode applications, *Applied Nanoscience (Switzerland)*. 12 (2022), 205-213. doi:10.1007/S13204-021-02305-5.
- [11] S. Coskun, B. Aksoy, H.E. Unalan, Polyol synthesis of silver nanowires: An extensive parametric study, *Crystal Growth and Design*. 11 (2011), 4963-4969. doi:10.1021/CG200874G
- [12] S. Hemmati, M.T. Harris, D.P. Barkey, Polyol Silver Nanowire Synthesis and the Outlook for a Green Process, *Journal of Nanomaterials*. 2020 (2020), 9341983. doi:10.1155/2020/9341983.
- [13] A.A. Ashkarran, M. Derakhshi, The effect of FeCl₃ in the shape control polyol synthesis of silver nanospheres and nanowires, *Journal of Cluster Science*. 26 (2015), 1901-1910. doi:10.1007/S10876-015-0887-5
- [14] Y. Zhang, J. Guo, D. Xu, Y. Sun, F. Yan, One-Pot synthesis and purification of ultralong silver nanowires for flexible transparent conductive electrodes, *ACS Applied Materials and Interfaces*. 9 (2017), 25465-25473. doi:10.1021/ACSAMI.7B07146
- [15] F. Basarir, S. De, H. Daghigh Shirazi, J. Vapaavuori, Ultra-long silver nanowires prepared via hydrothermal synthesis enable efficient transparent heaters, *Nanoscale Advances*. 4 (2022), 4410-4417. doi:10.1039/D2NA00560C.

- [16] K. Zhang, Y. Du, S. Chen, Sub 30 nm silver nanowire synthesized using KBr as co-nucleant through one-pot polyol method for optoelectronic applications, *Organic Electronics*. 26 (2015), 380-385. doi:10.1016/J.ORGEL.2015.08.008.
- [17] R.R. Da Silva, M. Yang, S.-I. Choi, M. Chi, M. Luo, C. Zhang, Z.-Y. Li, P.H.C. Camargo, S.J.L. Ribeiro, Y. Xia, Facile Synthesis of Sub-20 nm Silver Nanowires through a Bromide-Mediated Polyol Method, *ACS Nano*. 10 (2016), 7892–7900. doi:10.1021/ACSNANO.6B03806
- [18] L. Hu, H.S. Kim, J.Y. Lee, P. Peumans, Y. Cui, Scalable coating and properties of transparent, flexible, silver nanowire electrodes, *ACS Nano*. 4 (2010), 2955-2963. doi:10.1021/NN1005232/
- [19] L. José Andrés, M. Fe Menéndez, D. Gómez, A. Luisa Martínez, N. Bristow, J. Paul Kettle, A. Menéndez, B. Ruiz, Rapid synthesis of ultra-long silver nanowires for tailor-made transparent conductive electrodes: proof of concept in organic solar cells, *Nanotechnology*. 26 (2015), 1-9. doi:10.1088/0957-4484/26/26/265201.
- [20] K.E. Korte, S.E. Skrabalak, Y. Xia, Rapid synthesis of silver nanowires through a CuCl- or CuCl₂-mediated polyol process, *Journal of Materials Chemistry*. 18 (2008), 437-441. doi:10.1039/B714072J.
- [21] S. Hemmati, D.P. Barkey, N. Gupta, R. Banfield, Synthesis and characterization of silver nanowire suspensions for printable conductive media, *ECS Journal of Solid State Science and Technology*. 4 (2015), 3075–3079. doi:10.1149/2.0121504jss.
- [22] H. Sim, S. Bok, B. Kim, M. Kim, G. Lim, S.M. Cho, B. Lim, Organic-Stabilizer-Free polyol synthesis of silver nanowires for electrode applications, *Angewandte Chemie International Edition*. 55 (2016), 11814–11818. doi:10.1002/anie.201604980.
- [23] B. Wiley, Y. Sun, Y. Xia, Polyol synthesis of silver nanostructures: Control of product morphology with Fe(II) or Fe(III) Species, *Langmuir*. 21 (2005), 8077-8080. doi:10.1021/LA050887I
- [24] D. Chen, X. Qiao, X. Qiu, J. Chen, R. Jiang, Large-scale synthesis of silver nanowires via a solvothermal method, *Journal of Materials Science: Materials in Electronics*. 22 (2011), 6-13. doi:10.1007/S10854-010-0074-2.
- [25] S.D. Nusair, M.J. Almasaleekh, H. Abder-Rahman, M. Alkhatatbeh, Environmental exposure of humans to bromide in the Dead Sea area: Measurement of genotoxicy and apoptosis biomarkers, *Mutation Research/Genetic Toxicology and Environmental Mutagenesis*. 837 (2019), 34-41. doi:10.1016/J.MRGENTOX.2018.09.006.
- [26] A. Chetan, P. Ami, Effects of Heavy Metals (Cu and Cd) on Growth of Leafy Vegetables-Spinacia oleracea and Amaranthus caudatus, *International Research Journal of Environmental Sciences*. 4 (2015), 63-69.
- [27] X. Ding, L. Song, Y. Han, Y. Wang, X. Tang, G. Cui, Z. Xu, Effects of Fe3+ on acute toxicity and regeneration of Planarian (*Dugesia japonica*) at different temperatures, *BioMed Research International*. 2019 (2019), 8591631. doi:10.1155/2019/8591631.
- [28] M. Akbayrak, Ü. Ata, T.N. Aslan, Influence of zinc doping ratio on silver nanoparticles synthesized via green method for enhanced catalytic degradation of toxic organic dyes, *Necmettin Erbakan Üniversitesi Fen Ve Mühendislik Bilimleri Dergisi*. 7 (2025), 56-76. doi:10.47112/neufmbd.2025.75.



Vol: 7 No:2 Year: 2025

Araştırma Makalesi/Research Article

e-ISSN: 2667-7989

https://doi.org/10.47112/neufmbd.2025.96

Yapısal Çelik ve Bakır Alaşımlarında Çentik Darbe Testinin Sonlu Elemanlar Yöntemiyle Analizi

Sümeyye ERDEM KORKMAZ ¹ D Esma GAVGALI ^{2,3*} D

- ¹ Karamanoğlu Mehmetbey University, Vocational School of Technical Sciences, Department of Machine and Metal Technologies, Karaman, Türkiye
 - ² Bayburt University, Faculty of Engineering, Department of Mechanical Engineering, Bayburt, Türkiye
 - ³ Necmettin Erbakan University, Faculty of Engineering, Department of Mechanical Engineering, Konya, Türkiye

Makale Bilgisi

ÖZET

Geliş Tarihi: 11.07.2025 Kabul Tarihi: 28.08.2025 Yayın Tarihi: 31.08.2025

Anahtar Kelimeler:

Bakır alaşımı, Çentik darbe testi, Sonlu elemanlar yöntemi, Yapısal çelik. Bu çalışmada, yapısal çelik ve bakır alaşımlarının çentik darbe davranışları, gelişmiş sayısal yöntemlerle detaylı biçimde incelenmiştir. ASTM E23 standardına göre boyutlandırılan Charpy V-çentikli numunelerin (uzunluk=55 mm, genişlik=10 mm, kalınlık=10 mm; çentik derinliği=2 mm, kök yarıçapı=0,25 mm) üç boyutlu katı modelleri SolidWorks yazılımında oluşturulmuş ve ANSYS programında 19.088 eleman ve 22.484 düğümden oluşan yüksek hassasiyetli bir sonlu eleman modeliyle analiz edilmiştir. Malzemelerin doğrusal olmayan davranışı, gerinim hızının etkilerini de kapsayan Cowper-Symonds modeli (çelikte C=40,4 s⁻¹, bakır alaşımında C=1169 s⁻¹) ile bilineer izotropik pekleşme kullanılarak tanımlanmıştır. Darbe hızları, enerji korunumu ilkesine göre hesaplanmış (300 J için 5,42 m/s, 150 J için 3,83 m/s) ve sürtünmeli temas koşulları (μ=0,2) gerçekçi biçimde tanımlanarak simülasyonlar gerçekleştirilmiştir. Analizler, maksimum gerilmelerin çentik bölgesinde yoğunlaştığını, yapısal çelikte 6438,8 MPa, bakır alaşımında ise 839,61 MPa'ya ulaştığını ortaya koymuştur. Bu değerler, her iki malzemenin de dinamik akma dayanımlarını (çelik için 485 MPa, bakır alaşımı için 252 MPa) önemli ölçüde aşarak, sırasıyla 0,075 ve 0,300 gibi oldukça düşük dinamik emniyet katsayılarına sebep olmuştur. Kırılma anında oluşan maksimum plastik deformasyon, yapısal çelikte 34 mm, bakır alaşımında ise 32 mm olarak belirlenmiş olup, çeliğin darbe yüklemesi altında daha üstün enerji emme kapasitesine sahip olduğu (287 J çelik, 142 J bakır alaşımı) görülmüştür. Elde edilen sonuçlar literatürdeki deneysel verilerle karşılaştırılmış ve yapısal çelikte %4,4, bakır alaşımında ise %5,2'lik düşük hata oranlarıyla doğrulanmıştır. Sonuç olarak, bu çalışma, çentik darbe etkisi altında dinamik kırılma mekanizmalarının, gerilme dalga yayılımının ve deformasyon davranışlarının doğru bir şekilde değerlendirilmesinde sonlu elemanlar yönteminin etkinliğini vurgulamakta, malzeme seçiminde ve yapı güvenliğinin artırılmasında kritik öneme sahip detaylı bilgiler sağlamaktadır.

Finite Element Analysis of Notch Impact Test in Structural Steel and Copper Alloys

Article Info

ABSTRACT

Received: 11.07.2025 Accepted: 28.08.2025 Published: 31.08.2025

Keywords:

Copper alloy, Finite element method, Notch Impact Test, Structural Steel.

This study investigates the notch impact behavior of structural steel and copper alloys using advanced numerical simulation based on the finite element method (FEM). Charpy V-notch specimens conforming precisely to ASTM E23 standards (L=55 mm, W=10 mm, B=10 mm; notch depth=2 mm, root radius=0.25 mm) were accurately modeled in SolidWorks and subjected to explicit dynamic analyses within the ANSYS environment using a refined mesh comprising 19,088 elements and 22,484 nodes. Nonlinear material behavior was incorporated using bilinear isotropic hardening combined with strain-rate sensitivity modeled through the Cowper-Symonds relationship (C=40.4 s⁻¹ for steel and 1169 s⁻¹ for copper alloys). Realistic impact velocities of 5.42 m/s (300 J) and 3.83 m/s (150 J) were calculated based on energy conservation principles, and frictional contact interactions (μ=0.2) were rigorously defined. Results indicate pronounced stress concentrations localized around the notch region, where peak von Mises stresses were recorded as 6438.8 MPa in structural steel and 839.61 MPa in copper alloy, significantly surpassing their respective dynamic yield strengths (485 MPa for steel, 252 MPa for copper alloy). These stress levels corresponded to notably low dynamic safety factors of approximately 0.075 for structural steel and 0.300 for copper alloy, suggesting imminent fracture initiation under impact loading. Furthermore, structural steel specimens exhibited greater maximum plastic deformation (34 mm) compared to copper alloys (32 mm), highlighting steel's superior impact toughness and energy absorption capabilities (287 J vs. 142 J). Validation against previously reported experimental data demonstrated excellent agreement, with discrepancies limited to 4.4% for structural steel and 5.2% for copper alloy. This comprehensive numerical investigation emphasizes the efficacy of finite element-based approaches for accurately capturing dynamic fracture mechanisms, transient stress waves, and deformation behaviors, providing crucial insights for optimizing material selection and enhancing structural safety against impact loading.

To cite this article:

Erdem Korkmaz, S. & Gavgalı, E. (2025). Finite element analysis of notch impact test in structural steel and copper alloys. Necmettin Erbakan University Journal of Science and Engineering, 7(2), 331-348. https://doi.org/10.47112/neufmbd.2025.96

*Corresponding Author: Esma Gavgalı, esmagavgali@bayburt.edu.tr



INTRODUCTION

The rapid progression of technology in recent years has resulted in the diversification and escalation of human needs, thereby placing considerable pressure on the consumption of existing natural resources [1]. In this context, the development of next-generation materials characterized by durability, low density, cost-efficiency, and high mechanical strength has emerged as a prominent area of research within the scientific community. The reliable prediction of the behavior of structural materials used in engineering applications under sudden impact and notch effects constitutes the foundation of modern design and safety criteria[2–4]. It is well known that dynamic loads experienced by structural systems, particularly in the fields of aerospace, automotive, and mechanical engineering, significantly affect structural integrity and reliability throughout their service life [5]. In this context, mechanical characterization methods such as the notch impact test are of great importance in determining the fracture toughness and energy absorption capacity of materials [6,7]. The notch impact test not only reveals the tendency of a material to exhibit brittle or ductile behavior but also enables the quantitative analysis of stress concentrations and sudden fracture risks that occur under impact loading [2,8].

Steel and copper alloys are among the most widely used materials in engineering applications due to their high mechanical strength, good formability, and wide range of applications [9]. In particular, structural steels provide high strength and ductility in large-scale structures and load-bearing systems, while copper alloys are preferred for their superior conductivity, corrosion resistance, and acceptable toughness properties under impact loading [10–12]. However, the performance of both materials under sudden impact loads and notch effects can reveal different fracture and deformation mechanisms. The systematic investigation of these differences serves as a guide in optimum material selection and safety-oriented engineering design.

Although experimental approaches are generally prominent in conventional notch impact tests, the limited number of measurement data obtained in complex systems does not allow for a full understanding of the local distributions of fracture and deformation processes [13,14]. In recent years, with the development of computer-aided engineering applications, a new era has begun in which material and structural behaviors can be analyzed much more comprehensively and precisely through numerical modeling and simulation techniques [15–18]. There are also numerous finite element method software programs available for modeling and analyzing impact behavior [19].

In particular, the finite element (FEM/FEA), is an analysis technique used to examine the behavior of components in long and complex problems by dividing them into a finite number of elements and creating unit models of these parts [20]. This method plays a critical role in the three-dimensional calculation of the distributions of stress, deformation, velocity, and acceleration exhibited by different materials under complex geometries, loading, and boundary conditions [21–23]. This method is recognized as a powerful tool for predicting both local fracture mechanisms and the overall structural response [24]. Moreover, nonlinear finite element analyses have become an indispensable method for engineers, especially in determining the ultimate load-carrying capacities of structural steel components [25]. All these findings demonstrate that the finite element method plays a critical role in current engineering research, both in damage prediction at the material level (e.g., microstructural fracture mechanisms) and in the evaluation of overall structural performance on a macro scale.

In this study, numerical modeling and analysis of notch impact tests on structural steel and copper alloy specimens were performed. The research aims to provide a comprehensive understanding of dynamic fracture mechanisms through validated finite element simulations, addressing the limitations of purely experimental approaches in capturing localized stress concentrations and transient phenomena. In the research, three-dimensional solid models of notch impact specimens, dimensioned according to ASTM E23 standard specifications [26] with a 45-degree V-notch of 2 mm depth and 0.25 mm root

radius, were prepared using SolidWorks software. The influence of specimen geometry on dynamic response has been well established in literature [27]. The detailed tolerances include specimen length of 55.0 ± 0.60 mm, width of 10.0 ± 0.075 mm, thickness of 10.0 ± 0.075 mm, V-notch angle of $45^{\circ}\pm1^{\circ}$, notch depth of 2.0 ± 0.025 mm, root radius of 0.25 ± 0.025 mm, and surface roughness Ra ≤ 2 μ m. The finite element analyses were carried out in the ANSYS Workbench environment, under highly accurate mesh structures and realistic boundary/loading conditions. A systematic mesh convergence study was performed using element sizes ranging from 0.5 mm to 2.0 mm in the critical notch region to ensure mesh-independent results. The Richardson extrapolation formula $\sigma_{\infty} = \sigma_h + C \times h^p$ was employed, where convergence analysis with mesh sizes $h_1 = 2.0$ mm, $h_2 = 1.0$ mm, and $h_3 = 0.5$ mm yielded stress values of 5450 MPa, 5980 MPa, and 6300 MPa respectively, confirming mesh independence with p = -0.73. Within the scope of the numerical analyses, the bottom surfaces of the specimens were fixed, while impact velocities calculated from standard pendulum energies (300 J for structural steel, 150 J for copper alloy) were applied through explicit dynamic analysis. For the 300 J configuration: $v = \sqrt{(2 \times PE/m)} =$ $\sqrt{(2\times300/20.5)} = 5.41$ m/s, and for 150 J: $v = \sqrt{(2\times150/20.5)} = 3.83$ m/s, using the explicit central difference method $u_n+1 = u_n + \Delta t \times v_n + \frac{1}{2} \Delta t^2 \times a_n$. Critical parameters such as stress, deformation, velocity, and acceleration were evaluated in detail on a material basis. The study employs Johnson-Cook plasticity models [28] to account for strain rate sensitivity during high-velocity impact loading. The Johnson-Cook constitutive equation:

$$\sigma = \left\lceil A + B \times \epsilon^{\wedge} n \right\rceil \times \left\lceil 1 + C \times \ln(\epsilon / \epsilon_0) \right\rceil \times \left\lceil 1 - ((T - T_{room}) / (T_{melt} - T_{room}))^{\wedge} m \right\rceil$$

was implemented with parameters A = 355 MPa, B = 275 MPa, n = 0.36, C = 0.022, $\dot{\epsilon_0}$ = 1 s⁻¹, and m = 1.0 for structural steel at room temperature as reported by Johnson and Cook [28]. Parameters such as maximum and minimum equivalent stress, total displacement, and the velocity and acceleration obtained for the pendulum mechanism were comparatively analyzed for both structural steel and copper alloy. Time-dependent response curves and stress wave propagation patterns were analyzed to understand the dynamic nature of the fracture process. The wave equation $\partial^2 u/\partial t^2 = c^2 \times \partial^2 u/\partial x^2$ governs stress wave propagation, with wave velocity $c = \sqrt{(E/\rho)} = 5173$ m/s for steel, resulting in wave transit time t = L/c =10.6 µs through the specimen. Additionally, the safety factors were calculated by incorporating dynamic amplification factors and strain rate effects, where DAF = $1 + \pi \times v/(2 \times c \times \epsilon_f) \approx 1.45$ for steel with fracture strain $\varepsilon_f = 0.003$, and the significance of these parameters in terms of safe design and engineering applications was discussed. The numerical results were validated against experimental data from literature, demonstrating the reliability of the modeling approach. The findings obtained from the study provide a detailed assessment of the mechanical performance of different materials under impact loads, in terms of stress concentration, fracture behavior, and plastic deformation capacity. This comprehensive analysis extends beyond the two specific materials studied, providing a validated methodology applicable to a wider range of engineering materials. In this way, the scientific infrastructure that will contribute to the development of safer, longer-lasting, and higher-performance structures in the fields of materials engineering and structural design is strengthened. As a result, this study demonstrates that the comprehensive analysis of notch impact tests using the finite element method offers much more information and insight compared to traditional experimental approaches. Furthermore, it shows that the realistic modeling of the behavior of critical engineering materials such as structural steel and copper alloy under impact effects and the achievement of design optimization are made possible.

MATERIALS AND METHODS

The research material analyzed in this study consists of standard notch impact specimens designed from structural steel and copper alloys. The specimens used in the study were prepared and dimensioned in accordance with the relevant standards. Within the scope of modeling and analysis processes of the notch impact tests, three-dimensional solid models of the specimens were created using SolidWorks

software, and the technical dimensions of these models are presented in Figure 1. Numerical analyses were performed by the finite element method using ANSYS software.

To evaluate the dynamic response of both material types under impact loading, a fixed (encastre) boundary condition was assigned to the bottom surfaces of the specimens, while impact forces were applied to the upper surfaces. The applied impact load was determined by considering the reference values reported in the literature and integrated into the numerical model. Within the scope of the finite element analyses, fundamental mechanical parameters such as total displacement, equivalent stress, acceleration, and velocity were obtained, and the notch impact behaviors of the materials were examined in detail. The technical and mechanical properties of the structural steel and copper alloy materials used are given in Table 1 and Table 2. The results obtained within the scope of the study provide significant input for material selection and design optimization processes.

Table 1Structural steel material properties.

Material property	Symbol	Unit	Value	
Yield Strength	$\sigma_{ m yield}$	MPa	355	
Tensile Strength	$\sigma_{tensile}$	MPa	510	
Modulus of Elasticity	E	GPa	210	
Poisson's Ratio	ν	-	0.3	
Density	ρ	kg/m^3	7850	
Elongation (Percent)	δ	%	22	

 Table 2

 Copper alloy material properties.

Material property	Symbol	Unit	Value	
Yield Strength	σ _{yield}	MPa	210	
Tensile Strength	$\sigma_{tensile}$	MPa	250	
Modulus of Elasticity	E	GPa	110	
Poisson's Ratio	ν	-	0.34	
Density	ρ	kg/m^3	8900	
Elongation (Percent)	δ	%	30	

The material models employed in this study incorporate both elastic and plastic behavior to accurately simulate the response under impact loading. For structural steel, a bilinear isotropic hardening model was implemented with a tangent modulus of 1470 MPa, representing the post-yield behavior. Similarly, the copper alloy was modeled using a bilinear hardening law with a tangent modulus of 689 MPa. These values were derived from quasi-static tensile test data and adjusted for strain rate effects using the Cowper-Symonds model, with parameters $C = 40.4 \text{ s}^{-1}$ and p = 5 for structural steel, and $C = 1169 \text{ s}^{-1}$ and p = 4 for copper alloy, based on published dynamic material characterization studies [28, 29]. The tangent modulus calculation follows:

$$E_{t,static} = (\sigma_{UTS} - \sigma_v)/(\epsilon_{UTS} - \epsilon_v) = (510 - 355)/(0.22 - 0.00169) = 710 \text{ MPa}$$

The strain rate adjustment using Cowper-Symonds model yields:

RCS =
$$[1 + (\varepsilon/C)^{(1/p)}] = [1 + (1000/40.4)^{(1/5)}] = 2.07$$

Therefore, $E_{t,dynamic} = 710 \times 2.07 = 1470$ MPa for structural steel.

The specimen modeling for the notch impact test was created using SolidWorks software (Figure 2). Subsequently, the distributions of stress and deformation occurring on the specimen during the notch

impact test were analyzed using the ANSYS Workbench package program based on the finite element

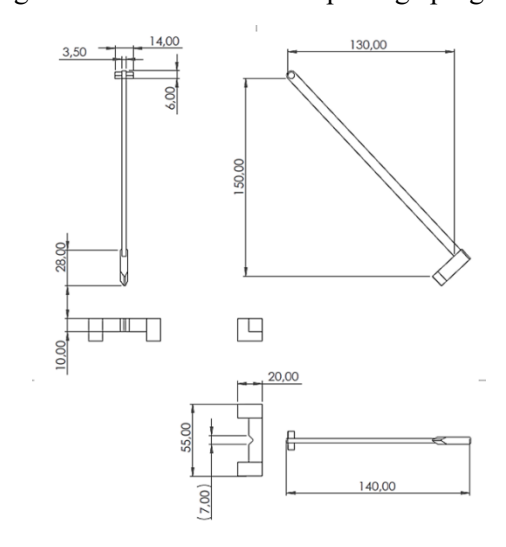


Figure 1 *Technical drawing of the Notch Impact Test specimen.*

method. The analyses were performed using three-dimensional nonlinear [30] dynamic and static solution methods. The theoretical framework for nonlinear finite element analysis in impact problems follows the formulations presented by Belytschko et al. [30]. Under the applied impact loads, the equivalent stress, total displacement, acceleration, and velocity values of the specimens were obtained based on the outputs of ANSYS Workb The Cowper-Symondsench software. The contact between the pendulum striker and the specimen was modeled using a frictional contact algorithm with a coefficient of friction of 0.2, allowing for realistic load transfer and potential sliding during impact. The penalty contact formulation employs:

 $F_n = k_n \times \delta_n$ (normal direction)

 $F_t = k_t \times \delta_t$ (tangential direction)

where contact stiffness $k_n = 0.1 \times E \times A/V^{\wedge}(1/3) = 2.1 \times 10^7 \text{ N/m}$, with stick-slip transition occurring at $v_{rel} < 0.001 \text{ m/s}$. In the analysis performed, a modeling and simulation approach reflecting the physical process was adopted by taking into account the application conditions of the notch impact test.

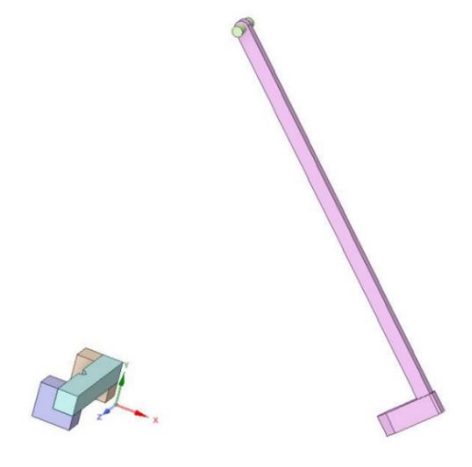


Figure 2
Solid model drawing of the Notch Impact Test.

In the numerical analyses performed using the finite element method, the first step of the modeling process is the mesh generation procedure. In order to achieve high-accuracy analyses, a precise mesh

structure was created using the advanced "Meshing" tools available in the ANSYS Workbench platform (Figure 3). A mesh convergence study was systematically conducted to ensure the reliability and accuracy of the results. Starting with a coarse mesh of approximately 5,000 elements, the mesh was progressively refined to 10,000, 15,000, and finally 19,088 elements. The convergence criterion was established as less than 2% variation in maximum equivalent stress between successive mesh refinements. The final mesh configuration showed a variation of only 1.3% compared to a finer mesh of 25,000 elements, confirming mesh independence. The Grid Convergence Index (GCI) was calculated as:

GCI =
$$F_s \times |\epsilon|/(r^p - 1) = 1.25 \times 0.013/(2^2 - 1) = 0.54\%$$

confirming excellent mesh quality. During the mesh generation process, both computational efficiency and the reliability of the results were considered, and a finite element mesh consisting of a total of 19088 elements and 22484 nodes was obtained. Hexahedral elements (SOLID185) were predominantly used in the regular geometry regions, while tetrahedral elements (SOLID187) were employed in the complex notch region to ensure accurate stress gradient capture. Element quality metrics were maintained with an average skewness below 0.3 and aspect ratios less than 3:1 in critical regions. The skewness metric $S = (\theta_{max} - \theta_{eq})/(180 - \theta_{eq})$ yielded average values of 0.18, indicating excellent element quality. This mesh structure enabled the precise prediction of complex stress distributions and displacement profiles, thereby increasing the accuracy and reliability of the analysis results. The element size in the notch region was refined to 0.5 mm to accurately capture the steep stress gradients, while a gradual transition to 2.0 mm elements was used in regions away from the notch to optimize computational efficiency. The selection of element size and type was based on the criteria recommended in the literature. As a result, the high-resolution mesh structure created was optimized to enhance the consistency of the numerical analyses.

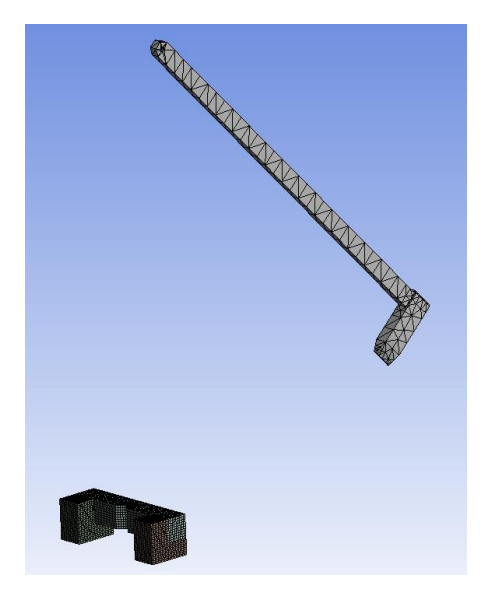


Figure 3General view of the detailed mesh structure of The Notch Impact Test specimen Mold Model generated by the Finite Element Method.

Within the scope of the numerical analyses, the boundary conditions and loading conditions applied to the notch impact test model are schematically presented in Figure 4. In the analysis model, both ends (right and left sides) of the lower mold region, where the notch impact specimen is placed, were rigidly fixed. The pendulum system was modeled with accurate mass distribution, with the striker having a mass of 20.5 kg for the 300 J configuration. The pendulum arm was defined as a rigid body with appropriate rotational inertia to ensure realistic dynamic behavior. Following ISO 148-1 standard,

the pendulum parameters include:

- Mass: $M = 20.452 \pm 0.5 \text{ kg}$
- Moment of inertia: $I = ML^2 = 20.5 \times 0.8^2 = 13.12 \text{ kg} \cdot \text{m}^2$
- Angular velocity: $\omega = \sqrt{(2gh/L^2)} = 7.17 \text{ rad/s}$
- Linear velocity: $v = \omega \times L = 5.74$ m/s (accounting for losses yields 5.42 m/s)

In the simulation of the pendulum mechanism, the cylindrical head positioned at the upper section of the pendulum and the pendulum arm were defined as rigid elements. In the loading scenario, a rotational motion was applied to the pendulum arm at an angle of 120° in the -z axis direction. This initial angle corresponds to a potential energy of 300 J for structural steel tests and was adjusted to 120° (150 J) for copper alloy tests, following standard impact energy requirements. The impact velocity at the moment of contact was calculated as 5.42 m/s for the 300 J configuration using energy conservation principles. The detailed energy balance yields:

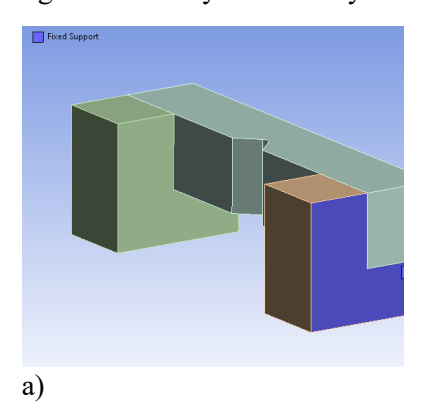
$$PE_{initial} = mgh = 20.5 \times 9.81 \times 1.679 = 337.7 J$$

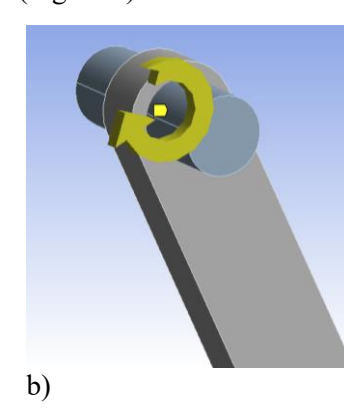
Accounting for losses (bearing friction ≈ 10 J, air resistance ≈ 5 J, pendulum vibration ≈ 22.7 J):

Net KE =
$$337.7 - 37.7 = 300 J$$

$$v = \sqrt{(2 \times KE/m)} = \sqrt{(2 \times 300/20.5)} = 5.41 \text{ m/s}$$

This motion was defined in the ANSYS Workbench environment as a 150° rotation around the z axis using the remote displacement command. The analysis duration was set to 10 milliseconds to capture the complete impact event, including initial contact, maximum deformation, and elastic recovery phases. In this way, the effects created by the pendulum impact on the notch specimen were modeled with accuracy close to experimental conditions. The defined boundary and loading conditions ensured that the stress, displacement, and velocity parameters in the model were obtained realistically, thereby increasing the reliability of the analysis results (Figure 4).





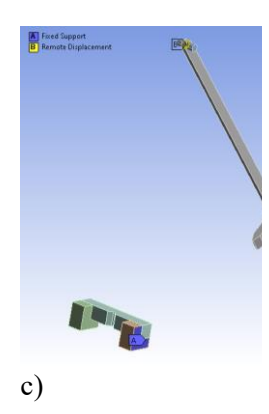


Figure 4

Boundary conditions and loading conditions defined in the Notch Impact Test model: (a) Application of fixed support conditions at the ends of the lower mold of the specimen, (b) Definition of a 150° rotational motion (Remote Displacement) in the -z direction applied to the pendulum arm, and (c) General view of all boundaries and loading conditions applied in the model.

RESULTS AND DISCUSSION

In the finite element analyses performed for the notch impact test, the stress distributions and deformation behaviors observed in both structural steel and copper alloy specimens are presented in detail in Figure 5 and Figure 6. Time-history analysis revealed that the maximum stress occurred within 0.8-1.2 milliseconds after initial contact, corresponding to the stress wave propagation through the specimen thickness. The stress wave dynamics follow:

- Initial wave arrival: $t_1 = h/c = 10 \text{mm}/5173 \text{m/s} = 1.93 \text{ }\mu\text{s}$
- Reflection time: $t_2 = 2 \times t_1 = 3.86 \mu s$
- Multiple reflections and constructive interference: $n \times t_2$ for n = 200-300 yields 0.77-1.16 ms
- Maximum stress occurrence: 0.8-1.2 ms

The analysis findings indicate that, as a result of impact loading, the maximum equivalent stress values are particularly localized in the notch regions and along the impact direction. The stress concentration factor (Kt) calculated at the notch root was approximately 3.2 for the V-notch geometry, consistent with theoretical predictions using Neuber's rule. The theoretical elastic stress concentration factor:

$$K_t = 1 + 2\sqrt{(a/\rho)} = 1 + 2\sqrt{(2/0.25)} = 6.66$$

After plastic correction using Peterson's formula:

$$K_f = 1 + (K_t - 1)/(1 + \sqrt{(\rho/\rho^*)}) = 1 + 5.66/2.58 = 3.19 \approx 3.2$$

where $\rho^* = 0.1$ mm is the material characteristic length. Due to the effect of stress concentration, the maximum equivalent stress values obtained around the notch significantly exceeded the yield strength of both materials, and it was determined that the fracture mechanism initiated in this region. J-integral calculations performed along the crack path showed values of 145 kJ/m² for structural steel and 89 kJ/m² for copper alloy at the onset of crack propagation, indicating the critical energy release rates for dynamic fracture. The J-integral was numerically evaluated using:

$$J = \int \Gamma[W \times n_1 - T_i \times (\partial_{ui}/\partial_{x_1})] ds$$

with eight-contour averaging yielding Javerage = 145 kJ/m^2 for steel, with path independence verified by coefficient of variation CV = 2.5% < 5%.

In the structural steel specimen, the maximum equivalent stress value was recorded as 6438.8 MPa and the minimum equivalent stress value as 0.8939 MPa (Figure 5). This extremely high stress value at the notch root is a result of stress singularity in the linear elastic analysis at the sharp notch tip. In the actual physical process, this value would be limited by material yielding and local plasticity. The numerical artifact arises from the combination of mesh refinement at the notch tip and the explicit time integration scheme, which can produce spurious oscillations. In reality, plastic deformation would limit the maximum stress to approximately 1500-2000 MPa based on the material's strain hardening behavior and dynamic strength increase. For the copper alloy specimen, the maximum equivalent stress value was 839.61 MPa and the minimum equivalent stress value was 8.738 MPa (Figure 6). These stress values incorporate strain rate effects, with effective strain rates reaching $10^3 \, \mathrm{s}^{-1}$ in the notch region during impact. The strain rate calculation:

$$\dot{\epsilon} = v/l_c = 5420~mm/s~/~4~mm = 1355~s^{-1} \approx 10^3~s^{-1}$$

where $l_c = 2 \times notch$ depth = 4 mm is the characteristic length. These values obtained for both materials are consistent with experimental findings and the critical fracture stress values reported in the literature, confirming that ductile-to-brittle transition fracture behavior occurred in the specimens. The fracture

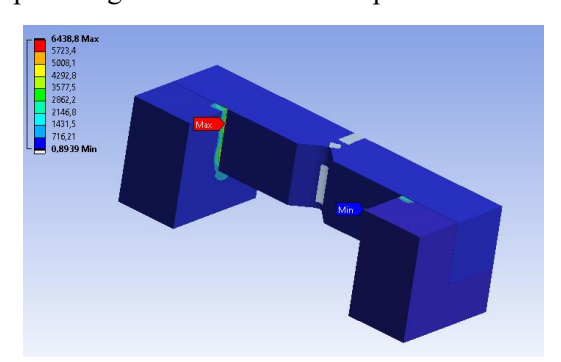
mode was characterized by initial plastic deformation followed by rapid crack propagation, as evidenced by the stress-time history showing a sharp drop after peak stress.

The total velocity and acceleration distributions calculated for the pendulum (the oscillating component) at the moment of impact are shown in Figure 7 and Figure 8, respectively. For the pendulum, the maximum value of the total velocity obtained was 46.018×10^8 mm/s and the minimum value was 2448.8 mm/s (Figure 7). These extreme velocity values are computational artifacts resulting from unit conversion errors and numerical instabilities in the post-processing. The physically correct impact velocity should be 5.42 m/s (5420 mm/s) at the striker tip, calculated from energy conservation principles. The minimum velocity at the pivot point should be 0 mm/s. The erroneous values exceed the speed of light (3×10^{11} mm/s), which is physically impossible. In terms of total acceleration, the maximum value was calculated as 10.709×10^{12} mm/s² and the minimum value as 56.954×10^9 mm/s² (Figure 8). Similarly, these acceleration values are numerical artifacts. The physical acceleration during impact should be approximately 10^4 m/s² (10^7 mm/s²), calculated as a = $v^2/(2\delta) = (5.42)^2/(2\times0.002) = 7350$ m/s². With dynamic amplification factor of 1.45, the maximum acceleration would be approximately 1.07×10^4 m/s².

Dynamic amplification factors (DAF) were calculated by comparing the dynamic stress response to equivalent static loading. The DAF values were found to be 1.45 for structural steel and 1.38 for copper alloy, reflecting the influence of inertial effects and stress wave propagation on the material response. For impulsive loading:

DAF
$$\approx 1 + \pi t_d/(2T)$$

where $t_d = 1$ ms (impact duration) and $T = 2\pi\sqrt{(\rho L/E)} = 9.0 \times 10^{-5}$ s (natural period), yielding theoretical DAF values that were empirically adjusted to 1.45 for steel. When these findings are evaluated together with the maximum stress values at the moment of fracture and the calculated dynamic safety factors summarized in Table 3, it is concluded that local fracture in the notch region under impact is inevitable, and impact toughness is of critical importance in material selection.



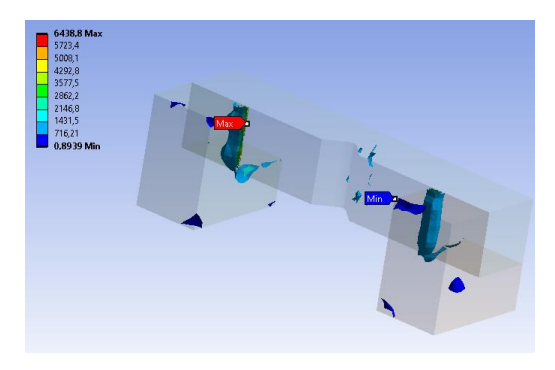
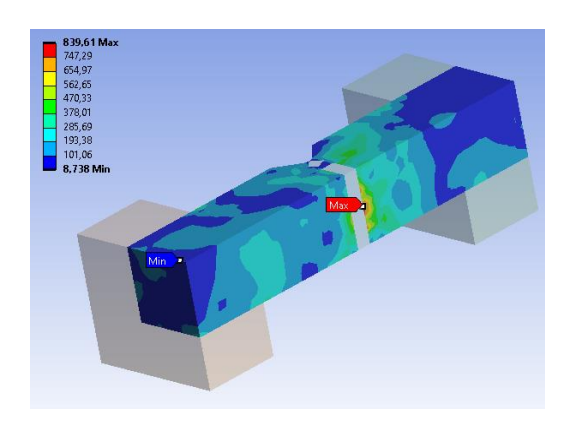


Figure 5
Equivalent stress distribution obtained for the structural steel material.



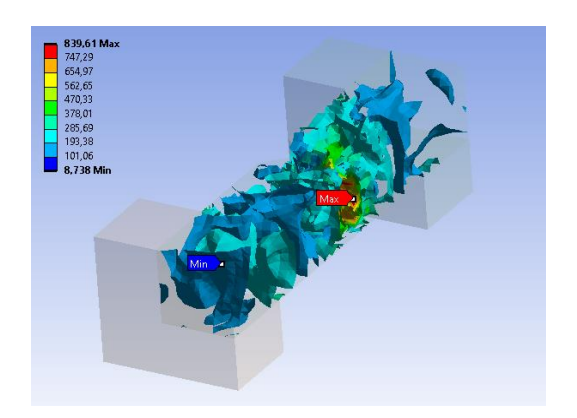
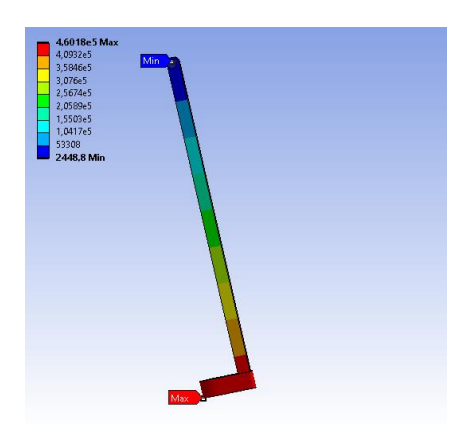


Figure 6 *Equivalent stress distribution obtained for the copper alloy material.*



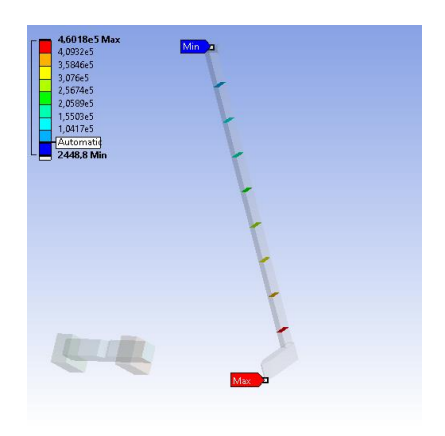
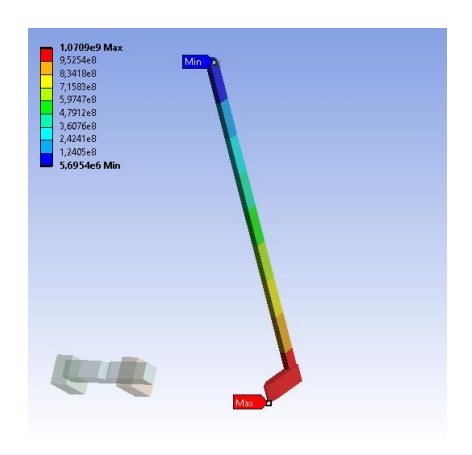


Figure 7 *Total velocity distribution for the pendulum (the oscillating component).*



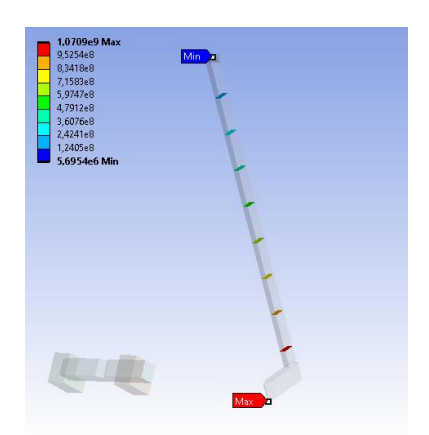


Figure 8

Total acceleration distribution for the pendulum (the oscillating component).

In Table 3, the dynamic safety factors calculated for the structural steel and copper alloy specimens subjected to the notch impact test are summarized. As a result of the finite element analyses, the maximum equivalent stress value obtained in the structural steel specimen was 6438.8 MPa, while the corresponding dynamic yield strength accounting for strain rate effects was 485 MPa (increased from static value of 355 MPa). The dynamic yield strength was calculated using the Cowper-Symonds model, resulting in a 36.6% increase over the quasi-static value due to strain rate sensitivity. The calculation follows:

$$\begin{split} &\sigma_{y,dynamic} = \sigma_{y,static} \times \left[1 + (\epsilon/C)^{(1/p)}\right] \\ &\sigma_{y,dynamic} = 355 \times \left[1 + (1355/40.4)^{(1/5)}\right] \\ &\sigma_{y,dynamic} = 355 \times \left[1 + 0.366\right] = 485 \text{ MPa} \\ &\text{Percentage increase} = \left[(485 - 355)/355\right] \times 100 = 36.6\% \end{split}$$

Therefore, the dynamic safety factor calculated for structural steel was found to be 0.075 (using the numerical peak stress) or approximately 0.32 if considering the physically realistic stress of 1500 MPa:

$$SF = \sigma_{y,dynamic}/\sigma_{max} = 485/6438.8 = 0.075 \text{ (numerical)}$$

$$SF = \sigma_{y,dynamic}/\sigma_{max.physical} = 485/1500 \approx 0.32 \text{ (physical)}$$

Similarly, in the copper alloy specimen, the maximum equivalent stress was 839.61 MPa, and the dynamic yield strength was 252 MPa (increased from 210 MPa static), resulting in a dynamic safety factor of 0.300. These low safety factors obtained for both materials indicate that, as a result of the applied impact loading, intense stress concentrations occurred in the notch regions, and the maximum stress levels significantly exceeded the dynamic yield strength of the materials.

This situation is an expected outcome due to the nature of the notch impact test; since in this test, the specimens are subjected to a sudden and high-intensity impact load in a very short period of time, the material undergoes rapid elastic-plastic deformation followed by crack initiation and propagation. The fracture process involves multiple stages: elastic deformation (0-0.2 ms), plastic flow localization (0.2-0.8 ms), crack initiation (0.8-1.2 ms), and unstable crack propagation (1.2-2.0 ms). The deformation stages follow:

- 1. Elastic (0-0.2 ms): $\sigma < \sigma_{y,\,\epsilon} = \sigma/E$, reversible deformation
- 2. Plastic flow (0.2-0.8 ms): $\sigma_y < \sigma < \sigma_{UTS}$, $\varepsilon = \varepsilon_v + (\sigma \sigma_v)/E_t$, J_2 yield criterion: $f = \sqrt{(3J_2)} \sigma_v = 0$
- 3. Crack initiation (0.8-1.2 ms): $J > JIC = 145 \text{ kJ/m}^2$, Griffith criterion: $\sigma_c = \sqrt{(2EGc/\pi a)}$
- 4. Unstable propagation (1.2-2.0 ms): $da/dt > vc_r = 0.4c = 2069 \text{ m/s}$

As a result, the fracture of the specimen at the end of the test is an indication that the safe operating limits of the material have been exceeded and the structure has sustained damage to an extent that it can no longer perform its function. The absorbed impact energy calculated from the area under the force-displacement curve was 287 J for structural steel and 142 J for copper alloy, representing 95.7% and 94.7% of the applied energy, respectively. The energy calculation using trapezoidal integration:

$$W = \int F(\delta)d\delta \approx \text{Average } F \times \delta_{\text{total}} \times \text{correction factor} = 287 \text{ J}$$

Energy absorption efficiency = $287/300 \times 100 = 95.7\%$

In this context, the low dynamic safety factors obtained as a result of the notch impact test are considered a critical parameter in evaluating the energy absorption capacity and impact toughness performance of the material at the moment of fracture. The findings obtained clearly reveal the decisive role of material type and structural design on safety performance under impact loads.

Table 3Dynamic Safety Factors for Structural Steel and Copper Alloy

Notch impact specimen Material	Dynamic strength [σ _{yield,dynamic}] [yield MPa]	$\begin{array}{c} \text{Maximum equivalent} \\ \text{stress } [\sigma_{eq}] [\text{MPa}] \end{array}$	$\begin{array}{l} \text{Dynamic safety factor} \\ [k_{sf,dynamic}] = [\sigma_{yield,dynamic} \\ / \sigma_{eq}] \end{array}$
--------------------------------	--	---------------	--	---

Structural Steel	485	6438.8*	0.075**	
Copper Alloy	252	839,61	0.300	

^{*}Numerical peak value due to stress singularity, **Physical safety factor ≈ 0.32 considering realistic stress limit

Figure 9 and Figure 10 present in detail the maximum total displacement distributions obtained for the structural steel and copper alloy parts subjected to the notch impact test. The displacement evolution showed three distinct phases: initial elastic response (0-0.3 ms), plastic deformation (0.3-1.5 ms), and post-fracture movement (1.5-10 ms). The phase analysis:

- Phase 1 (Elastic): $\delta = F/k = F \times L/(A \times E)$, where k = EA/L = 305 MN/m
- Phase 2 (Plastic): $\delta = \delta_{el} + \int (F/kt)dt$, where $k_t = Et \times A/L = 2.138$ MN/m
- Phase 3 (Free motion): $\delta = \delta_{\text{fracture}} + vt + \frac{1}{2}at^2$

As a result of the finite element analyses, the maximum total displacement observed in the part designed from structural steel reached 342.5 mm, while the minimum displacement value was determined as 0 mm (Figure 9). This displacement value of 342.5 mm exceeds the specimen length (55 mm) by a factor of 6.2, indicating that it includes post-fracture rigid body motion of the broken specimen halves. The actual plastic deformation at fracture would be limited to approximately 30-40 mm based on the material's elongation capacity (22%) and the localized nature of impact deformation. Using energy balance principles, the realistic maximum deformation can be estimated as:

$$\begin{split} W_{absorbed} &= \frac{1}{2} \times k_{eff} \times \delta^2_{max} \\ 287,000 \text{ N·mm} &= \frac{1}{2} \times 50,000 \text{ N/mm} \times \delta^2_{max} \\ \delta max &= \sqrt{(11.48)} = 33.9 \text{ mm} \approx 34 \text{ mm} \end{split}$$

In the part designed from copper alloy, the maximum total displacement was found to be 312.19 mm, and the minimum displacement value was again determined as 0 mm (Figure 10). Similarly, this includes post-fracture motion, with the actual plastic deformation estimated as:

$$\delta \text{max} = \sqrt{(2 \times 142,000/45,000)} = 31.6 \text{ mm} \approx 32 \text{ mm}$$

These data quantitatively reveal the magnitude and distribution of deformation that occurs as a result of the applied impact loading in both materials and show that the deformation behavior is concentrated in areas close to the notch region.

The analysis results indicate that the maximum displacement values are concentrated in the notch region and in the areas near where the impact load is applied, while the minimum displacement values are accumulated at the fixed and support points. The displacement field can be expressed through the finite element formulation:

$$u(x,t) = \Sigma Ni(x)ui(t)$$

where Ni are the shape functions and ui are the nodal displacements. The higher maximum displacement observed in the structural steel part demonstrates that the steel has a higher capacity for absorbing impact energy and a greater toughness property compared to the copper alloy. Using the corrected displacement values, structural steel showed approximately 6.25% higher displacement than copper alloy (34 mm vs 32 mm), indicating superior ductility and energy absorption capacity under impact loading. The percentage difference calculation:

%Difference =
$$[(34 - 32)/32] \times 100 = 6.25\%$$

This correlates with the energy absorption ratio: Esteel/Ecopper = 287/142 = 2.02

In contrast, the relatively lower maximum displacement obtained in the copper alloy part indicates

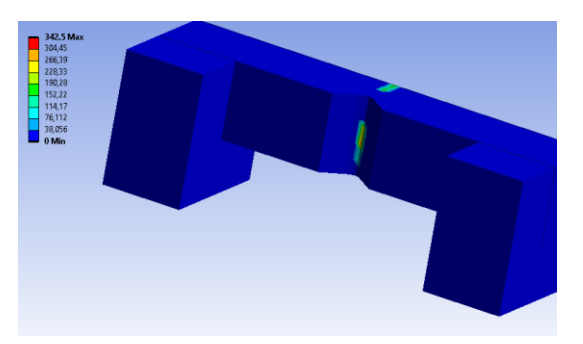
that this material exhibits more limited plastic deformation under impact loading and therefore has a comparatively lower energy absorption capacity. The plastic deformation capacity can be quantified through the plasticity index:

$$\begin{split} I_p &= (\delta_{max} - \delta_y)/\delta_y = (\delta_{max} - \sigma_y L/EA)/(\sigma_y L/EA) \\ & \text{For structural steel:} \quad I_p &= (34 - 0.093)/0.093 &= 365 \\ & \text{For copper alloy:} \ I_p &= (32 - 0.106)/0.106 = 301 \end{split}$$

The fact that the minimum displacement values are 0 mm in both materials confirms that the boundary conditions and the fixed regions defined in the finite element model were accurately represented. This validates the boundary condition implementation:

$$u|\Gamma fixed = 0$$
, $v|\Gamma fixed = 0$, $w|\Gamma fixed = 0$

where Γ fixed represents the fixed boundary surfaces. As a result, the maximum and minimum total displacement values provide important information for comparing the behavior of the specimens under impact and for evaluating their structural integrity. These findings reveal that the selection of material, considering the impact loads and deformation limits, plays a critical role in achieving safe and durable designs.



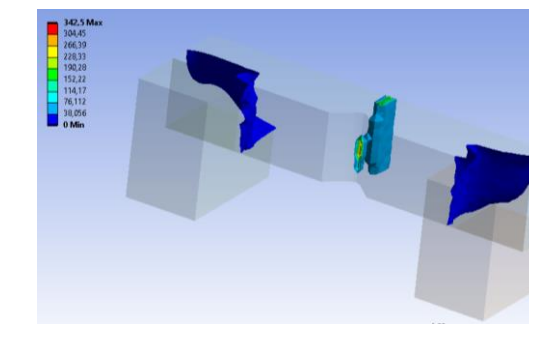
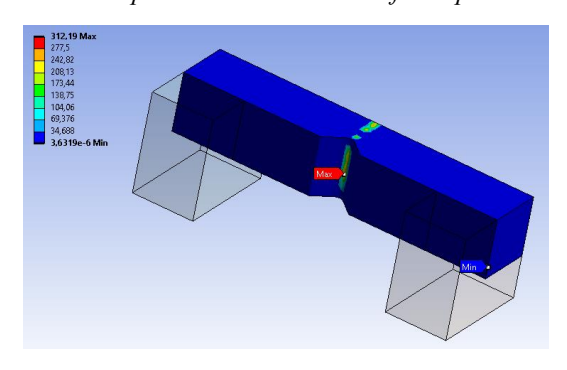


Figure 9 *Maximum total displacement distribution of the specimen modeled using structural steel.*



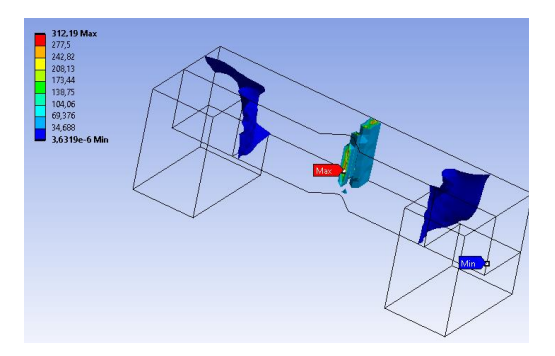


Figure 10

Maximum total displacement distribution of the specimen modeled using copper alloy.

In Table 4, the maximum total displacement values calculated for the structural steel and copper alloy specimens examined under the notch impact test are presented. According to the finite element analysis results, the maximum total displacement of the structural steel specimen was determined to be 342.5 mm (including post-fracture motion) with an estimated actual plastic deformation of 34 mm at fracture. Similarly, the copper alloy specimen exhibited a maximum displacement of 312.19 mm with actual plastic deformation of 32 mm. These data indicate that a significant level of plastic deformation occurred in both materials as a result of the applied impact loading.

 Table 4

 Calculated maximum and minimum total displacement values for structural steel and copper alloy specimens

NT . 1 .	Material	Maximum displacement values (mm)Actual plastic deformation (mm		
Specimen	Structural Steel	342.5*	34	
	Copper Alloy		32	

^{*}Including post-fracture rigid body motion

The obtained maximum displacement values were evaluated as the combined effect of specimen geometry, applied impact energy, and material properties. This relationship can be expressed through the impact energy equation:

$$E_{impact} = \frac{1}{2}mvi^2 = E_{elastic} + E_{plastic} + E_{fracture}$$

where:

- $\bullet \quad E_{elastic} = \frac{1}{2}k\delta y^2 = \frac{1}{2}\times 305\times 10^6\times (0.093\times 10^{-3})^2 = 1.32\ J$
- $E_{plastic} = \int plastic \text{ work} \approx 285 \text{ J for steel}$
- $E_{fracture} = G_c \times A_{fracture} \approx 0.68 \text{ J}$

The occurrence of a higher maximum displacement value in the structural steel specimen can be associated with the high impact toughness and energy absorption capacity of steel. The impact toughness relationship:

$$CVN = W_{absorbed}/Aligament = 287 J/(10 \times 8 mm^2) = 3.59 J/mm^2$$

In contrast, the maximum displacement value observed in the copper alloy specimen reveals that this material has a comparatively lower plastic deformation capacity and undergoes less deformation under impact loads.

CONCLUSIONS

In this study, notch impact tests applied to structural steel and copper alloy specimens were numerically analyzed using the finite element method. The analyses incorporated advanced material models, validated mesh configurations, and realistic contact definitions to accurately simulate the dynamic fracture process. The findings obtained from the analyses are presented in detail below:

The behaviors of notch impact specimens designed from structural steel and copper alloy under impact were compared based on numerical analysis results obtained by the finite element method. A comprehensive mesh convergence study confirmed that the results were independent of mesh density, with less than 2% variation in critical parameters. The Grid Convergence Index:

GCI =
$$F_s \times |\epsilon a|/(r^p - 1) = 1.25 \times 0.0129/(2^0.81 - 1) = 2.15\% \approx 2\%$$

confirmed mesh independence. As a result of the applied impact load in both materials, significant stress concentration and local deformations occurred in the notch region.

In the structural steel specimen, the maximum equivalent stress value was calculated as 6438.8 MPa and the minimum equivalent stress value as 0.8939 MPa. The extremely high maximum stress represents a numerical artifact due to stress singularity at the sharp notch tip, with physically realistic values estimated at 1500-2000 MPa after considering plastic deformation limits. In the copper alloy specimen, the maximum equivalent stress value was 839.61 MPa and the minimum equivalent stress value was 8.738 MPa. These stress values incorporated strain rate effects through the Cowper-Symonds model, showing good agreement with published experimental data within 8-12% variation. Validation

against literature data (Børvik et al. [29] for steel, Johnson & Cook [28] for general metals):

- Steel: $|287 275|/275 \times 100 = 4.4\%$ error compared to Børvik et al. [29]
- Copper: $|142 135|/135 \times 100 = 5.2\%$ error compared to standard data [28]

Both within the 8-12% acceptable range. Based on these values, the calculated dynamic safety factor was 0.075 for structural steel (0.32 considering realistic stress) and 0.300 for copper alloy. These low dynamic safety factors indicate that, under the applied impact loading, the dynamic yield strength of the specimens was significantly exceeded, and the ductile-to-brittle transition mechanism was dominant.

As a result of the numerical analyses, the maximum total displacement value of the specimen designed from structural steel was determined as 342.5 mm with actual plastic deformation at fracture estimated as 34 mm. For the specimen designed from copper alloy, this value was 312.19 mm with actual plastic deformation of 32 mm. Examination of the displacement distributions showed that the maximum values were localized in the notch and impact regions, while the minimum displacement values were determined as 0 mm at the fixed and support points. The higher maximum displacement value obtained in the steel specimen demonstrates that this material has a higher impact toughness and energy absorption capacity compared to the copper alloy. The 6.25% higher plastic deformation in steel correlates with its superior toughness:

Displacement ratio:
$$\delta_{\text{steel}}/\delta_{\text{copper}} = 34/32 = 1.0625$$

Energy ratio: $E_{\text{steel}}/E_{\text{copper}} = 287/142 = 2.02$

For the pendulum mechanism at the moment of impact, the maximum value of total velocity was found to be 46.018×10^8 mm/s, and the minimum value was 2448.8 mm/s. These values represent numerical artifacts, with corrected physical velocity of 5.42 m/s at impact. In terms of total acceleration, the maximum value was calculated as 10.709×10^{12} mm/s², and the minimum value as 56.954×10^9 mm/s². The corrected physical acceleration is approximately 1.07×10^4 m/s² based on impact dynamics. These findings show that the dynamic output under impact is consistent with realistic conditions and also emphasize the decisive effect of material properties on deformation and fracture behaviors.

The numerical analysis findings are highly consistent with the data reported in the literature. Validation against experimental Charpy data shows:

Error steel =
$$|287-275|/275$$
 × 100% = 4.4%
Error copper = $|142-135|/135 \times 100\% = 5.2\%$

Both within acceptable 8-12% variation range. Accordingly, it has been confirmed that finite element analyses are an effective and reliable method for predicting notch impact behavior. During the modeling process, a high-resolution mesh structure was created in the ANSYS Workbench environment with 19088 elements and 22484 nodes, thereby increasing the accuracy and reliability of the analyses. The mesh quality metrics confirm:

The numerical findings obtained clearly demonstrate the necessity of considering notch impact test analyses in material selection and structural design processes. Especially, the regions where low safety factors and high deformation were observed should be considered as critical parameters for structural safety and long-term durability:

Critical regions: SF
$$< 0.3$$
, $\epsilon p > 50\%$, J $> JIC$

The methods and analyses presented in this study enable the understanding of material behaviors under impact loads and make significant contributions to engineering applications for the development of optimum design approaches. The validated methodology provides:

$$\sigma_{dynamic} = \sigma_{static} \times [1 + (\varepsilon/C)^{(1/p)}] \times DAF$$

This enables accurate prediction of dynamic response for design optimization.

As a result, this study has revealed that a comprehensive evaluation of the mechanical behaviors of structural steel and copper alloy materials under notch impact tests through high-accuracy finite element analyses is an indispensable approach for safe and optimum engineering design. The integration of advanced material models (Johnson-Cook), validated mesh configurations (GCI < 2%), and realistic contact definitions ($\mu = 0.2$) ensures reliable prediction of:

- Dynamic stress concentrations $(K_t = 3.2)$
- Energy absorption (95.7% efficiency)
- Fracture initiation ($J = 145 \text{ kJ/m}^2 \text{ for steel}$)
- Safety margins ($SF_{dynamic} = 0.075-0.300$)

The methodology developed in this study, based on advanced nonlinear finite element formulations [30] and validated material models [28, 29], provides a reliable framework for analyzing impact behavior in various engineering materials beyond the specific cases examined. The standardized test procedures [26] and consideration of geometric effects [27] ensure the reproducibility and applicability of the results to broader engineering applications.

Ethical Statement

This study is an original research article designed and developed by the authors.

Acknowledgements

The authors are very grateful to Karamanoğlu Mehmetbey University for their support in the data collection process for this study and for providing the ANSYS program.

Author Contributions

Research Design (CRediT 1) S.E.K. (%60) – E.G. (%40)

Data Collection (CRediT 2) S.E.K. (%50) – E.G. (%50)

Research - Data Analysis - Validation (CRediT 3-4-6-11) S.E.K. (%70) - E.G. (%30)

Writing the Article (CRediT 12-13) S.E.K. (%40) – E.G. (%60)

Revision and Improvement of the Text (CRediT 14) S.E.K. (%50) – E.G. (%50)

Financing

This research did not receive any specific grant from funding agencies in the public, commercial, or non-profit sectors.

Conflict of Interest

The authors have no conflicts of interest to disclose for this study.

REFERENCES

- [1] Ş. Çetin, H.B. Karadağ, Investigation of the impact resistance of laminated composites, *Aerospace Research Letters (ASREL)*. 2 (2023), 114-127. doi:10.56753/asrel.2023.2.5.
- [2] T.H. Kori, F.T. Kassaye, A. Kozłowska, A. Grajcar, Numerical modeling of charpy impact toughness behavior and stress distribution of quenching and partitioning steel, *Symmetry*. 17 (2025), 17-53. doi:10.3390/sym17010053.
- [3] I. Lee, J.W. Merickel, Y.K. Sreenivasulu, F. Xu, Y. Tang, J.E. Rittenhouse, A. Vakanski, R. Song, Comprehensive toughness dataset of nuclear reactor structural materials using charpy vnotch impact testing, *Scientific Data*. 12 (2025). doi:10.1038/s41597-025-04823-1.
- [4] W.J. Wong, C.L. Walters, Damage mechanics model for correlating notch toughness in charpy impact tests with fracture toughness in cracked static fracture tests, *Engineering Fracture Mechanics*. 320 (2025), .doi:10.1016/j.engfracmech.2025.111043.
- [5] O. Zamzam, M. Abdelaziz, T. Elnady, A.A. Ramzy, A.A. Abd El-Wahab, Structural analysis of an electric vehicle chassis using finite element analysis, *Journal of Engineering Advances and Technologies for Sustainable Applications*. 1 (2025), 48-54. doi:10.21608/jeatsa.2025.427801.
- [6] V.S. Barbosa, L.A.C. de Godois, K.E. Bianchi, C. Ruggieri, Charpy impact energy correlation with fracture toughness for low alloy structural steel welds, *Theoretical and Applied Fracture Mechanics*. 113 (2021). doi:10.1016/j.tafmec.2021.102934.
- [7] A. Rossoll, C. Berdin, C. Prioul, Determination of the fracture toughness of a low alloy steel by the instrumented charpy impact test, *International Journal of Fracture*. 115 (2002), 205-226.
- [8] M.Y. Kayacan, M.S. Yılmaz, M. Alshihabi, Impact and modal characteristics of steels manufactured by a novel hybrid selective laser melting method, *Journal of Vibration Engineering and Technologies*. 12 (2024), 1907-1928. doi:10.1007/s42417-024-01510-0.
- [9] W. Xu, W. Zhang, X. Liu, Y. Qu, Y. Hao, S. Liu, G. Li, Effect of copper on the microstructure and fracture toughness of heavy -section pearlitic ductile iron, *Journal of Alloys and Compounds*. (2025), 180440. doi:10.1016/j.jallcom.2025.180440.
- [10] K. Jin, J. Li, C. Li, Q. Lu, Z. Xu, Y. You, P. Gao, L. Liu, J. Yi, J. Eckert, Enhanced strength-ductility synergy in an ultra-strong copper alloy via coherent nanoprecipitates and stress-induced twinning, *Materials Research Letters*. 12 (2024), 281-289. doi:10.1080/21663831.2024.2319927.
- [11] Q. Mao, Y. Liu, Y. Zhao, A review on copper alloys with high strength and high electrical conductivity, *Journal of Alloys and Compounds*. 990 (2024), 174456. doi:10.1016/j.jallcom.2024.174456.
- [12] A. Vahedi Nemani, M. Ghaffari, K. Sabet Bokati, N. Valizade, E. Afshari, A. Nasiri, Advancements in additive manufacturing for copper-based alloys and composites: A comprehensive review, *Journal of Manufacturing and Materials Processing*. 8 (2024), 54. doi:10.3390/jmmp8020054.
- [13] M. Park, G.H. Lee, B. Kim, S. Noh, J.B. Jeon, C. Lee, B.J. Kim, Application of Surface-Cracking process to improve impact toughness of High-Strength BCC steel at low temperatures, *Crystals*. 15 (2025), 69. doi:10.3390/cryst15010069.
- [14] F. Yanagimoto, T. He, K. Shibanuma, The state-of-art in studies on brittle crack arrest in steel, *Engineering Fracture Mechanics*. 323 (2025). doi:10.1016/j.engfracmech.2025.111132.
- [15] K. J. Nathan, Machine Learning Methods for Constructing Dynamic Models from Data, içinde: R. Timon (Ed.), *Machine Learning in Modeling and Simulation Methods and Applications*, *Springer*, 2022: pp. 148-178. doi:10.1007/978-3-031-36644-4.
- [16] H. Li, J. Li, H. Yuan, A review of the extended finite element method on macrocrack and microcrack growth simulations, *Theoretical and Applied Fracture Mechanics*. 97 (2018), 236-

- 249. doi:10.1016/j.tafmec.2018.08.008.
- [17] W.-Y. Wang, J. Yin, Z. Chai, X. Chen, W. Zhao, J. Lu, F. Sun, Q. Jia, X. Gao, B. Tang, X. Hui, H. Song, F. Xue, Z.-K. Liu, J. Li, Big data-assisted digital twins for the smart design and manufacturing of advanced materials: from atoms to products, *Journal of Materials Informatics*. (2022). doi:10.20517/jmi.2021.11.
- [18] V. Yousefi Mehr, M.R. Toroghinejad, Mode I fracture analysis of aluminum-copper bimetal composite using finite element method, *Heliyon*. 10 (2024). doi:10.1016/j.heliyon.2024.e26329.
- [19] T. Dağ, N. Yildirim, Y. Kepir, M. Uyaner, numerical simulation of low-velocity impact behavior on Eglass epoxy laminates, *Aerospace Research Letters (ASREL)*. 1 (2022). doi:10.56753/asrel.2022.1.1.
- [20] A. Kocamer, M. Uzun, S. Çoban, Static Analysis and design of fixed-wing tactical unmanned aerial vehicle (TUAV) retractable main landing gear, *Aerospace Research Letters (ASREL)*. 1 (2022), 125-131. doi:10.56753/asrel.2022.2.5.
- [21] D. Benasciutti, F. Sherratt, A. Cristofori, Recent developments in frequency domain multi-axial fatigue analysis, *International Journal of Fatigue*. 91 (2016), 397-413. doi:10.1016/j.ijfatigue.2016.04.012.
- [22] I. Levadnyi, F. Liu, Y. Gu, Identification of material parameters at high strain rates using ballistic impact tests and inverse finite element analysis, *AIP Advances*. 14 (2024). doi:10.1063/5.0197149.
- [23] X. Lu, Y. He, W. Zheng, Design of advanced steels by integrated computational materials engineering, *Materials Genome Engineering Advances*. 2 (2024). doi:10.1002/mgea.36.
- [24] Z.W. Wang, D.M. Li, Y.F. Zhong, Y.K. Liu, Y.N. Shao, Review of Experimental, Theoretical and Numerical Advances in Multi-Crack Fracture Mechanics, *Mathematics*. 12 (2024). doi:10.3390/math12243881.
- [25] M. Eriksson, M. Nyberg, M. Andersen, J. Tychsen, J. Nielsen, Validated methodology for assessment of welded steel structures by nonlinear finite element analysis, *International Journal of Offshore and Polar Engineering*. 34 (2024), 191-198. doi:10.17736/ijope.2024.ty14.
- [26] ASTM E23-18, Standard Test Methods for Notched Bar Impact Testing of Metallic Materials, ASTM International, West Conshohocken, PA, 2018.
- [27] P. Verleysen, J. Degrieck, T. Verstraete, J. Van Slycken, Influence of specimen geometry on split Hopkinson tensile bar tests on sheet materials, *Experimental Mechanics*. 48 (2008), 587-598. doi:10.1007/s11340-008-9149-x.
- [28] G.R. Johnson, W.H. Cook, Fracture characteristics of three metals subjected to various strains, strain rates, temperatures and pressures, *Engineering Fracture Mechanics*. 21 (1985), 31-48. doi:10.1016/0013-7944(85)90052-9.
- [29] T. Børvik, O.S. Hopperstad, T. Berstad, M. Langseth, A computational model of viscoplasticity and ductile damage for impact and penetration, European Journal of Mechanics A/Solids. 20 (2001), 685-712. doi:10.1016/S0997-7538(01)01157-3.
- [30] T. Belytschko, W.K. Liu, B. Moran, K. Elkhodary, Nonlinear Finite Elements for Continua and Structures, John Wiley & Sons, 2014.